AWARD NUMBER:

W81XWH-06-2-0067

PROJECT TITLE:

Alliance for NanoHealth Competitive Research Program

PRINCIPAL INVESTIGATOR:

Jodie L. Conyers, PhD

CONTRACTING ORGANIZATION:

The University of Texas Health Science Center at Houston
Houston, Texas 77030

REPORT DATE:

October 2008

TYPE OF REPORT:

Annual

PREPARED FOR:

U.S. Army Medical Research and Materiel Command
Fort Detrick, Maryland 21702-5012

DISTRIBUTION STATEMENT:

Approved for Public Release;
Distribution Unlimited

REPORT DOCUMENTATION PAGE

Form Approved
OMB No. 0704-0188

1. REPORT DATE *(DD-MM-YYYY)*	**2. REPORT TYPE**	**3. DATES COVERED** *(From - To)*
01-10-2008	Annual	29 Sep 2007-28 Sep 2008

4. TITLE AND SUBTITLE
Alliance for NanoHealth Competitive Research Program

5a. CONTRACT NUMBER

5b. GRANT NUMBER
W81XWH-06-2-0067

5c. PROGRAM ELEMENT NUMBER

6. AUTHOR(S)
Jodie L. Conyers, PhD

E-Mail: Jodie.L.Conyers@uth.tmc.edu

5d. PROJECT NUMBER

5e. TASK NUMBER

5f. WORK UNIT NUMBER

7. PERFORMING ORGANIZATION NAME(S) AND ADDRESS(ES)

The University of Texas Health Science Center at Houston
Houston, Texas 77030

8. PERFORMING ORGANIZATION REPORT NUMBER

9. SPONSORING / MONITORING AGENCY NAME(S) AND ADDRESS(ES)
U.S. Army Medical Research and Materiel Command
Fort Detrick, Maryland 21702-5012

10. SPONSOR/MONITOR'S ACRONYM(S)

11. SPONSOR/MONITOR'S REPORT NUMBER(S)

12. DISTRIBUTION / AVAILABILITY STATEMENT
Approved for Public Release; Distribution Unlimited

13. SUPPLEMENTARY NOTES

14. ABSTRACT

Through the work performed within the T5 program, Houston will become well prepared for the adverse effects of terrorism and natural disasters. The University of Texas Health Science Center at Houston has organized a highly qualified team within the Texas Medical Center for addressing the plurality of concerns that arise during public health crises. The ultimate goal of the T5 program will be to solve a wide variety of public health, scientific, and medical issues that will eventually lead to enhanced community preparedness. As part of the T5 program, training and education as well as predictive strategies will be explored to enhance disaster response. Diagnostic and therapeutic measures will be developed to assess and treat injury and disease. Fundamental scientific research will also be performed in order to better understand the physiological response to injury and disease. No other comprehensive program matches the combined technology, medical expertise, fundamental science, and training that encompass the T5 program. Under the direction of Dr. S. Ward Casscells and other leaders of the Texas Medical Center, the T5 program will provide the blueprint that other cities will use to better prepare their communities for public health disasters.

15. SUBJECT TERMS
No subject terms

16. SECURITY CLASSIFICATION OF:			**17. LIMITATION OF ABSTRACT**	**18. NUMBER OF PAGES**	**19a. NAME OF RESPONSIBLE PERSON**
a. REPORT	**b. ABSTRACT**	**c. THIS PAGE**			USAMRMC
U	U	U	UU	163	**19b. TELEPHONE NUMBER** *(include area code)*

TABLE OF CONTENTS

On-command control of blood pool residence time for nanoparticle-based molecular imaging

Vikas Kundra, MD, PhD (M.D. Anderson Cancer Center)
Ananth Annapragada, PhD (UT Health Science Center at Houston)

Specific Aims:

1. *Construct Nanoparticles:* To construct "on-command" Stealth nanoparticles, targeted by octreotide to the somatostatin receptor.
2. *Test Localization:* To test the localization of these nanoparticles in tumors overexpressing the somatostatin receptor.
3. *Test on-command cleavability:* To test the on-command clearance of these nanoparticles from the blood pool, and demonstrate the enhancements in contrast at the target achievable by the on-command clearance technique.

Stealth liposomes were created that bind cells expressing somatostatin receptor type 2 via incorporation of octreotide into the PEG moiety of the liposome. Binding was competed by somatostatin. Binding did not occur in cells that did not express SSTR2.

For the "On command" portion of the work, a cleavable linker was needed. We concentrated on spdp (Sulfosuccinimidyl 6-(3'-[2-pyridyldithio]-propionamido)hexanoate) and dtb (dithiobenzyl). Cleavage of conjugate alone was tested in solution at 30 mM of conjugate with increasing concentrations of cysteine and glutathione for different time points in phosphate buffered saline, pH 7.2 at 37 ^{o}C. To stop the reaction, the samples were rapidly frozen and lyophilized and then extracted with 500 ml of MeOH, centrifuged and 100 ml analyzed by HPLC for the presence of conjugate. The spdp conjugate was more susceptible to cleavage by cysteine than glutathione and was less susceptible to cleavage than dtb. Approximately 50% cleavage of a 30 mM solution of spdp conjugate occured with 10 mM cysteine concentration within thirty minutes.

Stability of the cleavable linkers in fetal bovine serum was evaluated. .01 mM final concentration of the cleavable linker was incubated in fetal bovine serum for 37 ^{o}C for different periods of time (0-12 hours). At each time point, 1 ml of the serum solution was withdrawn, frozen and lyophilized. The spdp conjugate was noted to be relatively more stable in serum with approximately 80% without cleavage at 12 hours. The DTB conjugate, on the other hand, was less stable with approximately 30% without cleavage at 2 hours and approximately 23% without cleavage at 12 hours.

When animal studies with the linker were begun, it was noted that the amount of signal obtained from per liposome was low for MR imaging, particularly given that one needed to create an agent that would not saturate the reticuloendothelial (RES) system of the mouse model. Conceptually, upon cleavage of the cleavable linker, the liposome would lose its stealth properties; and then, it would be taken up by the RES. If too much liposome was given to the animal, the RES would become saturated and would not be able to "clear" the excess liposomes; in essence, voiding the ability to clear the cleaved liposomes. Thus, it was decided that making a liposome particle with increased signal/particle needed to be addressed first. To do so, a new liposome-gadolinium agent was created for T1-weighted for MR imaging. The new agent, named Dual-Gd, combined features of two previously described agents, CE-Gd (encapsulating Gd inside a liposome) and SC-Gd (with Gd on the surface of the liposome) to create a new entity with improved T1-relaxivity per particle. The Dual Gd agent had an improved relaxation rate at various lipid concentration compared to either CE-Gd or SC-Gd. Moreover, Dual-Gd had improved relaxivity/particle compared to the either of the other two agents. The new agent was then tested in vivo. Importantly, the Dual-Gd resulted in both improved signal to noise (SNR) and contrast to noise (CNR). Among other applications, the Dual-Gd agent should find use in vascular imaging, particularly for evaluation of small features that can be critical for clinical decision making in humans and for imaging of small animals; as well as, in molecular imaging, where the number of imaging agents per particle bound to the target is critical for creating enough signal for target identification. A manuscript describing the Dual-Gd agent has been prepared and is about to be submitted.

This ANH grant was a seed grant. It has resulted in a manuscript and cooperation between Investigators, including those in different fields and institutions. It has generated a team-centered approach and significant preliminary data that has been used to submit additional proposals. A new proposal to carry forward this work will be submitted to the NIH this summer.

Nanomagnetic Biosensors for Cancer Diagnosis

Dmitri Litvinov, PhD (University of Houston)
Mini Kapoor, PhD (M.D. Anderson Cancer Center)

Drs. Litvinov and Kapoor finished their seed project during the original performance period (June 20, 2006 – September 20, 2007) and therefore did not carry out experiments or incur expenses during the performance period being reported in this Annual Report.

Modulation of Inner Ear Nanomechanics

John S. Oghalai, MD, Baylor College of Medicine
Bahman Anvari, Ph.D., Rice University (now at UC-Riverside)

A) Introduction/Abstract

The auditory portion of the mammalian inner ear, the cochlea, transduces sound waves into electrical energy. There are progressive changes in the basilar membrane, the dominant vibratory element of the cochlea, that create a tonotopic organization. Thus, one end of the cochlea resonates at high frequencies and the other at low frequencies. At normal speech intensities, the magnitude of basilar membrane vibrations ranges from 0.1 – 1 nm. Loud sounds, aging, and ototoxic medications cause hearing loss by damaging the sensory hair cells that sit on top of the basilar membrane. These insults predominantly cause hair cell death in the high frequency region of the cochlea while the hair cells in the low frequency region remain essentially intact. We propose to use laser irradiation to re-tune the resonant frequency map of the basilar membrane by modulating the nano-scale organization of its constituent collagen molecules. The clinical significance of this technique is the potential for development of a novel treatment for patients with hearing loss by making the low frequency region of the cochlea that contains functional hair cells to be more sensitive to high frequency sounds. We have already demonstrated using histological techniques that laser irradiation can induce molecular changes in the structure of collagen within the basilar membrane. In other tissues, similar laser-induced changes in collagen change the tissue stiffness. We hypothesize that laser-induced nano-scale structural changes within the basilar membrane will similarly change the stiffness of the basilar membrane and subsequently alter the resonant frequency map. We will test this hypothesis by using a laser Doppler vibrometer to measure basilar membrane resonance in the mouse cochlea before and after laser irradiation. Additionally, auditory brainstem evoked responses, an *in vivo* measure of hearing, will be measured before and after irradiation. Finally, light and electron microscopy will be used to assess for histological changes in the irradiated cochlea. This proposal involves the use of novel bioengineering technology to modulate the nano-mechanical properties of collagen within a biologic organ that functions to detect nano-scale vibrations.

B) Results and Discussion

As a result of this grant, we have made substantial strides in our ability to use laser photoirradiation to modulate the mechanical properties of the basilar membrane within the cochlea. While achievable with a low-power, long-pulse laser, a problem we noted was trauma to surrounding tissues. This trauma includes partial loss of hair cells and scar tissue formation.

In order to get around this issue, we were lucky to achieve additional sources of funding and purchased a high-power, femptosecond laser to provide a more targeted irradiation to the basilar membrane. An important benefit of using a femptosecond laser is that we can apply the laser energy to the cochlea in a non-invasive manner. Thus, we no longer need to apply a dye inside to cochlea to stain tissues that we desire to target. This is expected to dramatically reduce trauma to surrounding tissues. At this point, we are continuing this work beyond the scope of the original grant using these additional sources of funding.

As part of our additional goal of making nanoscale measurements of the cochlear basilar membrane, we are in the process of building an optical coherence tomography setup. By using it in a Doppler mode, nanoscale movements can be detected from discrete structures. This novel setup will be used to assess the biophysical impact of the femptosecond laser on basilar membrane tuning.

C) Key Research Accomplishments

- Development of the methodology to optically irradiate the mammalian cochlea.
- Development of an optical coherence tomography device to measure movements of cochlear membranes.

D) Conclusions

Laser irradiation of the mammalian cochlea can alter basilar membrane mechanics and structure.

E) Translation to military medicine

Our hope is to be able to use this technique as the basis for treating high frequency hearing loss.

F) Publications

Wenzel, G.I., Anvari, B., Mazhar, A., Pikkula, B. & Oghalai, J.S. Laser-induced collagen remodeling and deposition within the basilar membrane of the mouse cochlea. *J Biomed Opt* **12**, 021007 (2007).

G) Funding received as a result of the seed funds

- The Virginia and L.E. Simmons Family Foundation Collaborative Research Fund. Stimulation of Auditory Neurons by Multi-Photon Laser Targeting
- The Clayton Foundation. Stereotactic Stimulation of the Cochlea for the Treatment of Hearing Loss

Journal of Biomedical Optics 12(2), 1 (March/April 2007)

Laser-induced collagen remodeling and deposition within the basilar membrane of the mouse cochlea

Gentiana I. Wenzel
Baylor College of Medicine
Bobby R. Alford Department of Otolaryngology
Head and Neck Surgery
One Baylor Plaza, NA102
Houston, Texas 77030

Bahman Anvari
Amaan Mazhar
Brian Pikkula
Rice University
Department of Bioengineering
Houston, Texas 77005-1892

John S. Oghalai
Baylor College of Medicine
Bobby R. Alford Department of Otolaryngology
Head and Neck Surgery
One Baylor Plaza, NA102
Houston, Texas 77030
and
Rice University
Department of Bioengineering
Houston, Texas 77005-1892
E-mail: jso@bcm.edu

Abstract. The cochlea is the mammalian organ of hearing. Its predominant vibratory element, the basilar membrane, is tonotopically tuned, based on the spatial variation of its mass and stiffness. The constituent collagen fibers of the basilar membrane affect its stiffness. Laser irradiation can induce collagen remodeling and deposition in various tissues. We tested whether similar effects could be induced within the basilar membrane. Trypan blue was perfused into the scala tympani of anesthetized mice to stain the basilar membrane. We then irradiated the cochleas with a 600-nm pulsed dye laser at 15 or 180 J/cm^2. The mice were sacrificed 14 to 16 days later and collagen organization was studied. Polarization microscopy revealed that laser irradiation increased the birefringence within the basilar membrane in a dose-dependent manner. Electron microscopy demonstrated an increase in the density of collagen fibers and the deposition of new fibrils between collagen fibers after laser irradiation. As an assessment of hearing, auditory brainstem response (ABR) thresholds were found to increase moderately after 15 J/cm^2 and substantially after 180 J/cm^2. Our results demonstrate that collagen remodeling and new collagen deposition occurs within the basilar membrane after laser irradiation in a similar fashion to that found in other tissues. [DOI: 10.1117/1.2714286]

Keywords: collagen; resonant frequency; hearing; photocoagulation; remodeling.

Paper 06130SSR received May 19, 2006; revised manuscript received Sep. 5, 2006; accepted for publication Sep. 7, 2006.

1 Introduction

The cochlea is the organ of hearing (Fig. 1). It transduces the mechanical energy of sound pressure waves into electrical energy, which is then carried to the brain via the auditory nerve. Sensation occurs when the sound pressure waves induce nanoscale vibrations of the structures within the inner ear. The dominant vibratory mechanical component of the cochlea is the basilar membrane. Its mass and stiffness vary systematically in a reciprocal fashion along the length of the cochlea, and hence acts as a cascade of passive filters.[1–4] This spatial variation in mechanical properties of the basilar membrane creates a tonotopic organization to the cochlea, with the base sensitive to high-frequency tones and the apex sensitive to low-frequency tones. Thus, there is a spatial representation of frequency.

The basilar membrane consists of a filamentous layer consisting primarily of collagen fibers that run radially from medial to lateral[5,6] (i.e., perpendicular to the length of the cochlear duct). Collagen is regarded as a main source of basilar membrane stiffness and therefore plays a critical role in establishing its tuned resonant frequency map.[7–10] Collagen molecules are packed together in a hexagonal manner to form fibrils, which are covalently bound together with groups of other fibrils to form collagen fibers.[11,12] Ground substance fills in the spaces between fibers.

The sensory epithelium of the inner ear, located on top of the basilar membrane, is called the organ of Corti.[13,14] It contains the sensory hair cells that perform the actual sound transduction process (for review, see Ref. 14). The mechanical properties of the hair cells, as well as the other structures of the organ of Corti (the tectorial membrane, supporting cells, pillar cells, etc.) play important roles in refining cochlear tuning. However, these contributions are not as critical as that of the basilar membrane itself in determining the overall tonotopic frequency map of the cochlea.[15–20]

Lasers can induce conformational changes in collagen in many different tissues including the cornea,[21] the periodontal ligament,[22] the medial collateral ligament,[23] the femoropatellar joint capsule,[24,25] and skin.[26]. Initially, there is a decrease in tissue stiffness due to photocoagulation of collagen.[23,24] Previously, we demonstrated that immediate photocoagulative effects similarly occur within the basilar membrane after laser irradiation.[27] Studies in other tissues have shown that there are also delayed effects of laser irradiation on collagen.[28–30] In the subsequent days to weeks after irradiation, there is an increase in tissue stiffness as existing collagen remodels and new collagen is synthesized. Ongoing changes can occur even up to 2 yr after laser treatment.[28] Increases in tissue stiffness of up

Address all correspondence to John S. Oghalai, Baylor College of Medicine, Bobby R. Alford Department of Otolaryngology, Head and Neck Surgery, One Baylor Plaza, NA102, Houston, Texas 77030; Tel: 713-798-3234; Fax: 713-798-5078; E-mail:jso@bcm.edu

1083-3668/2007/12(2)/1/0/$25.00 © 2007 SPIE

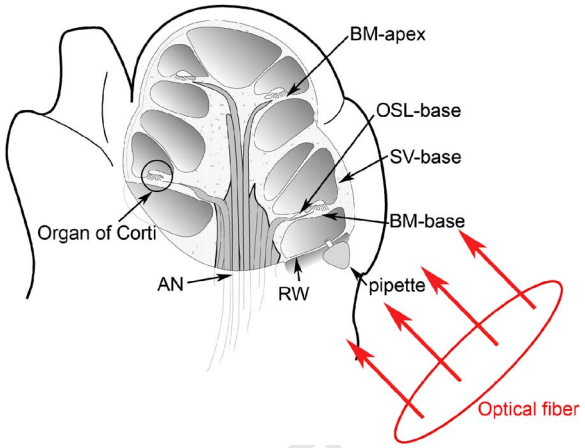

Fig. 1 Diagram of the mouse cochlea with the orientation of the optical fiber. A midmodiolar cross section through the cochlea cuts perpendicular to the organ of Corti. The pipette used to perfuse trypan blue to stain the basilar membrane at the base of the cochlea (BM-base) was inserted through the round window membrane (RW): basilar membrane at the apex of the cochlea (BM-apex), osseous spiral lamina (OSL-base), stria vascularis (SV-base), and auditory nerve (AN).

to 100% have been shown in tendon connective tissue after laser irradiation.[23]

We hypothesized that cochlear laser irradiation would induce delayed changes in basilar membrane collagen similar to that found in other tissues. Using polarized light and transmission electron microscopy, we examined the effects of laser irradiation on basilar membrane collagen. Herein, we demonstrate that, 2 weeks after the irradiation procedure, collagen remodeling and new collagen deposition can be detected within the basilar membrane. Additionally, we assessed the impact of the laser irradiation procedure on auditory thresholds by measuring the auditory brainstem response (ABR).

2 Material and Methods

2.1 *Surgical Technique*

The Baylor College of Medicine Institutional Animal Care and Use Committee approved the study protocol. C57BL/6 mice, weighing 20 to 30 g, age 4 to 8 weeks were anesthetized with an intraperitoneal (IP) injection of ketamine hydrochloride (100 mg/kg) and xylazine hydrochloride (5 to 10 mg/kg). Body temperature was maintained at 39°C using an electric heating pad (FHC, Bowdoinham, Maine). A retroauricular incision extending ventrally was made and the soft tissues divided to expose the tympanic bulla. The bulla was then opened and the round window membrane exposed. ABR thresholds were then measured (see the following).

The membranous structures within the cochlea are nearly transparent and are bathed in an aqueous environment. To enhance laser energy absorption and achieve optical selectivity for the basilar membrane, an exogenous chromophore was applied. We chose trypan blue (Gibco Laboratories, New York), a water-soluble stain that has maximal optical absorption at 607 nm, with an absorption coefficient 0.25 cm^{-1}. At the laser wavelength of 694 nm available to us (see details following), the absorption coefficient of trypan blue is[31] less than 0.05 cm^{-1}. Trypan blue was diluted to 0.1% in artificial perilymph (containing, in mM: 130 NaCl, 4 HCl, 1 $MgCl_2$, 2 $CaCl_2$, 10 HEPES, 10 glucose). The pH was titrated to 7.3 and the osmolarity was 293 mOsm. A flexible micropipette (Microfil, World Precision Instruments, Sarasota, Florida) was inserted through the round window and directed up the duct of scala tympani about 1.5 mm. Trypan blue (0.3 ml) was gently perfused in over 5 min. As the fluid drained out the round window, it was aspirated with a cotton wisp. Thus, only the basal region of the cochlea was stained. ABR thresholds were remeasured and the cochlea was then irradiated.

After laser irradiation, the incision was closed with sutures and the mouse was monitored until fully awake. The animal was then returned to its cage and maintained for another 14 to 16 days. At that point, the mouse was reanesthetized and the incision reopened. Any fluid within the middle ear space was aspirated and ABR thresholds were measured for a third time. The mouse was then sacrificed, perfused systemically with fixative, and its temporal bones harvested.

2.2 *Laser Irradiation*

A 694-nm-long pulsed (3 ms) ruby laser (Epilaser, Palomar Medical Technologies, Inc., Burlington, Massachusetts) was used to irradiate the cochlea. The light was coupled from the articulated arm of the laser into a 600-μm-core-diam fiber optic probe to facilitate light delivery to the basilar membrane through the exposed cochlea. Light output from the optical fiber was measured with an Ophir (30A, Wilmington, Massachusetts) power meter. It was estimated that the spot size was 1 mm in diameter at the cochlea. The radiant exposure applied at the focal spot was selected to be either 15 J/cm^2 (one pulse of 15 J/cm^2) or 180 J/cm^2 (six pulses of 30 J/cm^2) with a repetition rate of 1 Hz). We chose the 180-J/cm^2 dosage because it was the lowest dose used in our previous *ex vivo* study that caused statistically significant decreases in basilar membrane birefringence.[27] We chose the 15-J/cm^2 dose as the lowest in this set of experiments because it is a dose commonly used in clinical practice to induce collagen changes for skin rejuvenation.[32,33]

2.3 *Measurement of ABR Thresholds*

Sine wave stimuli were generated using a digital signal processing system. The stimuli were attenuated to the appropriate intensity, and delivered acoustically to the ear by an electrostatic speaker (RP-2, PA-5, ED-1, and EC-1 Tucker-Davis Technologies). The speaker was calibrated across the frequency range of 1 to 80 kHz prior to each experiment using a probe-tip microphone (microphone type 8192, NEXUS conditioning amplifier, Bruel and Kjar, Demark). This was performed after connecting the microphone and speaker to an earbar inserted into the animal's ear canal.

The ABR was recorded using needle electrodes positioned at the vertex of the skull and along the ventral surface of the tympanic bulla. A ground electrode was placed in the hind leg. The signals were amplified 10,000 times using a biological amplifier (HS4/DB4, Tucker-Davis Technologies, Alachua, Florida), digitized at 100 kHz (RP-2, Tucker-Davis Technologies), and digitally filtered to pass frequency components in the 300 to 3000-Hz range.

The stimulus for eliciting the ABR was a 5-ms sine wave tone with $\cos^2$ envelope rise and fall times of 0.5 ms. The repetition time was 50 ms and 250 trials were averaged. The peak-to-peak ABR signal was measured at stimulus intensities ranging from 10 to 80 dB sound pressure level (SPL) in 10-dB steps for each frequency. These data were interpolated using a cubic spline algorithm (MATLAB, Release 13, The Mathworks, Natick, Massachusetts) off-line to identify where the signal crossed the average noise floor plus four standard deviations to determine frequency-specific thresholds. We measured ABR thresholds at frequencies between 4 to 80 kHz. If no ABR was detected even at our equipment limits of 80 dB SPL, we arbitrarily defined the threshold to be 80 dB when calculating average thresholds.

Statistical analysis was performed using Excel (Microsoft, Redmond, Washington). ABR thresholds in the same mice before and after trypan blue perfusion were compared using the Student's two-tailed paired t test. The mean ABR thresholds in each group of irradiated mice were compared to each other and to ABR thresholds of all the mice before trypan blue perfusion using the Student's two-tailed nonpaired t test. Statistical significance was defined as $p < 0.05$. All presented values are mean ± SEM (standard error of the mean).

2.4 *Polarized Light Microscopy*

After harvesting the cochleas, they were immersed in 4% paraformaldehyde for 2 days, decalcified in 0.2-M EDTA for 2 weeks, embedded in paraffin, and cut perpendicular to the organ of Corti in 7-μm sections. To enhance the native birefringence of collagen, the sections were stained with picrosirius red (Sigma Aldrich, St. Louis, Missouri). Picrosirius red is a strongly elongated, birefringent molecule that binds parallel to collagen molecules.[21,34–37] It was originally used in the textile industry to analyze fiber orientation,[38] and it has been used to assess collagen organization[35,39] since the 1960s. We additionally stained the sections with hemotoxylin (Thermo Shandon, Pennsylvania) to visualize regions with minimal collagen.

Once all of the cochlear cross sections were cut and stained, they were visualized using polarized light microscopy to highlight parallel arrays of collagen. Before starting this procedure, one control specimen was placed on the microscope stage and the two polarizers were rotated to maximize the birefringence of the tissue. Once this was done, the polarizers were locked into place and all of the specimens were studied in the same anatomic orientation. Thus, polarization settings were held constant for all sections. Images were captured digitally using a 6.3-Mpixel camera (Canon, EOS 10D, Tokyo 146-8501, Japan) connected to an upright microscope (Zeiss, Axioskop 2, Germany). The applied light, aperture size, and time exposure were also held constant for all images.

ImageJ [National Institute of Health (NIH), http://rsb.info.nih.gov/ij/] was used to quantify the intensity of the birefringence within different collagen-containing areas of the cochlea. The color images of each turn of each cochlea were converted to 8-bit gray scale. After conversion, areas of high birefringence were white and areas of low birefringence were gray or black. Within each region to be analyzed, the area with the strongest birefringence was chosen and the signal intensity determined by averaging at least 60 pixels. The two-tailed nonpaired Student's t test was used to compare the birefringence between different regions and laser dosages.

2.5 *Transmission Electron Microscopy*

The harvested cochleas were fixed in 2.5% glutaraldehyde in 0.1-M cacodylate buffer containing 2-mM CaCl at a pH 7.4, and decalcified in 0.2-M EDTA for 2 weeks. They were then washed several times with 0.1-M cacodylate buffer. The samples were postfixed in 1% osmium tetroxide in 0.1-M cacodylate buffer and then washed with cacodylate buffer. Gradual dehydration was performed from 25 to 50% ethanol and the cochleas were then stained with 2% uranyl acetate in 50% ethanol for an hour. The cochleas were further dehydrated in 100% ethanol, followed by the transitional dehydrating agent propylene oxide.

The cochleas were gradually infiltrated with propylene oxide resin (Durucupan ACM Resin). This process was repeated using progressively higher resin concentrations until pure resin was infiltrated. The cochleas were oriented in resin-filled blocks, cured for 2 days at 55°, and then cut into 80-nm thin sections with an ultramicrotome. The sections were stained with 2% uranyl acetate in 50% ethanol for 7 min and with Reynold's lead citrate for 1 min. The specimens were imaged using a transmission electron microscope (H-7500, Hitachi).

2.6 *Animals*

We studied a total of 18 mice. The first 11 mice were used to develop the technique of *in vivo* laser irradiation. From these 11 animals, we present only the ABR data collected prior to laser irradiation (i.e., after the surgical exposure of the cochlea and after perfusion of trypan blue into the cochlea). After the laser irradiation procedure was perfected, four mice were irradiated at 15 J/cm^2 and 3 mice were irradiated at 180 J/cm^2. One cochlea from each of these groups was prepared for electron microscopy analysis, and the others (three and two cochleas, respectively) underwent ABR threshold testing and polarized light microscopy analysis.

Four contralateral cochleas were used as controls. They were not operated on, and so were not stained with trypan blue or irradiated. One was studied with electron microscopy and three were studied with polarized light microscopy.

3 Results

3.1 *Polarized Light Microscopy*

Polarized light microscopy revealed that the birefringence of the basilar membrane of the basal turn 2 weeks after irradiation was higher than in controls (Fig. 2). In a cochlea irradiated at 15 J/cm^2, the organ of Corti architecture appeared normal 2 weeks following laser irradiation. Both the inner and outer hair cells were maintained throughout the cochlea at this laser dosage. At 180 J/cm^2, the basilar membrane demonstrated even more birefringence than that at the lower laser dosage. However, intracochlear fibrosis and inflammatory tissue filled the scalae. The cells that normally make up the organ of Corti (hair cells and supporting cells) were not evident.

We quantified the tissue birefringence from four different regions in each cochlea (Fig. 3). The basilar membrane from the basal turn near the round window (BM-base) was the area

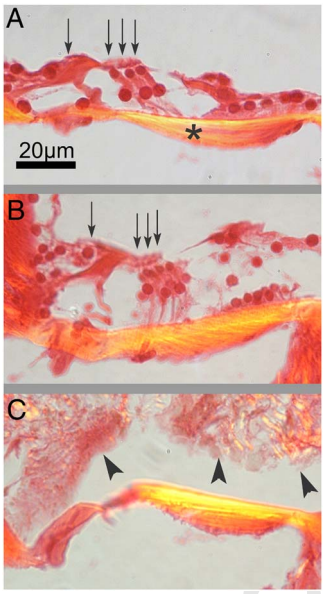

Fig. 2 Organ of Corti. Paraffin-embedded cochlear cross sections stained with picrosirius red and hemotoxylin were visualized using polarization microscopy to highlight collagen arrays. (A) A representative control section (cochlea not perfused or irradiated). The normal basilar membrane birefringence can be noted (*). Inner and outer hair cells are also visible (arrows). (B) A representative section of a cochlea 14 days after the laser irradiation with 15 J/cm^2. Note the continued presence of hair cells (arrows) and the normal architecture of the organ of Corti. (C) A representative section of a cochlea 14 days after irradiation with 180 J/cm^2. The basilar membrane birefringence appears brighter (more yellow) than that of the control cochlea. Hair cells are no longer present and scar tissue fills the intracochlear scalae (arrowheads).

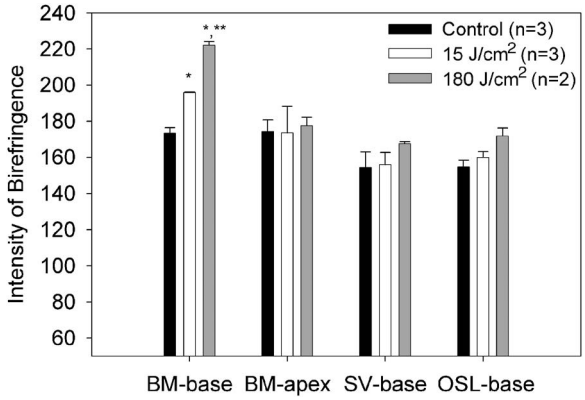

Fig. 3 Quantification of collagen birefringence. Measurements were taken from the basilar membrane in the basal turn (BM-base), the basilar membrane in the apical turn (BM-apex), the stria vascularis in the basal turn (SV-base), and the osseous spiral lamina in the basal turn (OSL-base). The intensity of birefringence is the average pixel intensity on a scale of 0 to 255. At both 15- and 180-J/cm^2 laser dosages, there were statistically significant increases in the collagen birefringence in the BM-base compared to controls (*). Additionally, the collagen birefringence in the BM-base after 180 J/cm^2 was larger than that after 15 J/cm^2 (**). No changes occurred in the other regions of the cochlea.

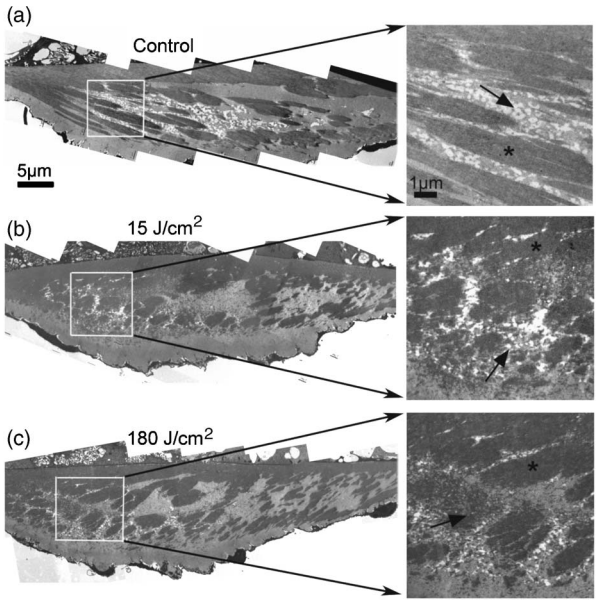

Fig. 4 Transmission electron microscopy of the basilar membrane. A cross section of the basilar membrane from the basal turn is shown. (a) A representative control section demonstrates the normal organization of the basilar membrane. There are collagen fibers (*) separated by loose connective tissue, which appear predominantly as white vacuoles. (b) Fourteen days after irradiation with 15 J/cm^2. The collagen fibers are slightly denser than in the control section. There are also an increased amount of thin collagen fibrils within the loose connective tissue between the fibers (arrow). (c) Fourteen days after irradiation with 180 J/cm^2. At this level of irradiation, the collagen fibers remain denser than in the control section. In many areas, the fibers seem wider with less crisp borders. Thus, there is less space between adjacent collagen fibers and almost no vacuolated space. This is due to the substantial amount of thin collagen fibrils within the loose connective tissue between fibers (arrow).

stained with trypan blue and was directly in the path of the laser beam. The basilar membrane of the apical turn (BM-apex) was likely not stained by the trypan blue. The stria vascularis (SV-base) is the tissue along the lateral wall of the cochlea that produces the electrochemical gradients within the scala media necessary for normal cochlear function. The osseous spiral lamina (OSL-base) is the bone to which the basilar membrane makes its medial attachment. We only analyzed the stria vascularis and osseous spiral lamina within the basal turn of the cochlea.

We found statistically significant increases in the average birefringence of the BM-base in cochleas irradiated with either laser dosage compared to controls (173±3, 196±0.4, and 222±2 for controls, 15 J/cm^2, and 180 J/cm^2, respectively; $P<0.05$). Additionally, the effect was dose dependent in that the mean birefringence of cochleas irradiated at 180 J/cm^2 was larger than that of the cochlea irradiated at 15 J/cm^2 ($P<0.05$). There were no statistically significant changes in tissue birefringence in the BM-apex, SV-base, or OSL-base for cochleae irradiated with either laser dosage compared to controls.

3.2 *Transmission Electron Microscopy*

Transmission electron microscopy of the basilar membrane of a control cochlea revealed the expected normal architecture

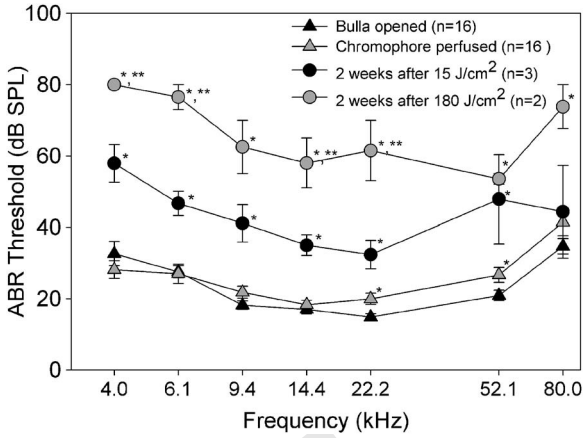

Fig. 5 ABR thresholds. After initially opening the bulla, the mice had normal thresholds across the frequency spectrum. After perfusing trypan blue through the round window, there were only statistically significant increases in the ABR threshold at 22 and 52 kHz. Two weeks after irradiating with 15 J/cm^2, there were 17 to 27-dB increases in ABR thresholds that were statistically significant compared to baseline at every frequency except at 80 kHz. After irradiating with 180 J/cm^2, there were 32 to 59-dB increases in ABR thresholds across the frequency spectrum compared to baseline. SPL was defined using a standard reference that is approximately the intensity of a 1000-Hz sinusoid that is just barely audible to a human with normal hearing[42] (20 μPa). Postirradiation thresholds that were statistically elevated from baseline are marked (*). Thresholds statistically higher after 180 compared to 15 J/cm^2 are marked (**).

(Fig. 4). There were large collagen fibers oriented in a radial fashion with loose connective tissue and ground substance between them. The space between the fibers was filled with white vacuoles. This indicates that the material within these spaces leeched out of the basilar membrane during fixation, and thus did not consist of collagen.

In the irradiated cochleas, the collagen fibers were denser than in controls, suggesting that remodeling of the existing collagen had occurred. Also, there were substantial numbers of new collagen fibrils within the loose connective tissue regions between the fibers. These fibrils were irregularly organized in between adjacent fibers. However, the new fibrils also appeared to condense around the borders of the preexisting collagen fibers. This may perhaps reflect the early incorporation of these new collagen fibrils into the fibers. Thus, there was a reduced amount of the vacuolated space between the fibers after 15 J/cm^2, and almost no vacuolated space after 180 J/cm^2. Together, these findings are consistent with new collagen deposition within the basilar membrane.[40,41]

3.3 *ABR Threshold Shifts*

ABR thresholds were measured after opening the tympanic bulla, following perfusion of the cochlea with trypan blue, and just prior to sacrifice 14 to 16 days later (Fig. 5). Normal thresholds were found after opening the bulla, as expected. There were no changes in ABR thresholds after trypan blue perfusion, except for 4 to 6-dB increases in the ABR threshold at 22 and 52 kHz that were statistically significant. This indicates that the perfusion procedure and the chromophore application had only minimal effects on cochlear function. This finding is consistent with data from the guinea pig cochlea, in which only a slight high-frequency threshold shift develops when artificial perilymph is perfused through scala tympani in a careful fashion.[43,44] Presumably, this hearing loss reflects inadvertent cochlear trauma or cooling of the cochlea because of its exposure to the outside environment.

Two weeks after laser irradiation with 15 J/cm^2, there were increases in ABR thresholds ranging from 17 to 27 dB that were statistically significant at every frequency except at 80 kHz. After laser irradiation with 180 J/cm^2, there were larger increases in ABR thresholds ranging from 32 to 59 dB across the frequency spectrum. Statistically significant increases in ABR thresholds were found in mice irradiated with 180 J/cm^2 compared to those irradiated with 15 J/cm^2 at 4, 6, 14, and 22 kHz that ranged from 22 to 30 dB.

4 Discussion

In this paper we show that 2 weeks after laser irradiation, there are histologic changes consistent with collagen remodeling and new collagen deposition both by polarized light and electron microscopy. We previously demonstrated that there is a decrease in basilar membrane birefringence acutely.[27] This process has been well-studied in other tissues and been found to reflect a photocoagulative effect that changes the properties of individual collagen molecules so that interpeptide hydrogen bonds break and result in collapse of their normal linear structure.[21,28–30,45,46] This breakage of normal linear structure causes an acute decrease in stiffness, which likely also occurs within the basilar membrane. These studies have also shown that with time, there is new collagen deposition and reorganization that leads to an increase in tissue birefringence and stiffness. Our findings suggest that collagen within the basilar membrane undergoes similar changes.

There are two potential explanations for the delayed increase in basilar membrane birefringence measured by polarization microscopy after laser irradiation. First, the new collagen fibrils that were deposited would be expected to bind additional picrosirius red molecules. This binding will increase the tissue birefringence only if the molecules are organized into arrays. Presumably, the irregularly organized fibrils between collagen fibers did not substantively detract from organization of the fibrils that were condensing around the preexisting collagen fibers. If more than 14 days of wound healing was permitted, we would expect the tissue birefringence to continue to increase as the newly deposited collagen organizes further. Second, it is possible that there was recruitment of additional binding sites for picrosirius red molecules to pre-existing molecules because of collagen remodeling.[21]

In any case, changes in collagen birefringence were noted only within the basal turn of the basilar membrane. Since only the basal turn was perfused with the exogenous chromophore trypan blue, the basilar membrane within the apical turn likely remained unstained and hence did not absorb the laser energy. In our previous study with an excised cochlear preparation, the entire length of the cochlea was perfused with trypan blue, and irradiation effects were noted within the basilar membrane of every turn.[27]

We believe the reason that significant changes in tissue birefringence did not occur within the stria vascularis and the osseous spiral lamina is that the chromophore did not substantially stain those tissues. However, in our previous study, we

did note staining of these tissues and measured changes in their birefringence after laser irradiation. The reason for this difference is probably because the experimental preparations are not the same. *In vivo*, there is continuous perilymph flow out of the open round window since mice have a patent cochlear aqueduct. This permits the entry of cerebrospinal fluid into the inner ear from the subarachoid space.[47] Therefore, the chromophore is rapidly washed out from the cochlea during perfusion and likely does not have time to penetrate into these thicker tissue structures.

At the laser energy of 180 J/cm^2, intense intrascalar fibrosis occurred and ABR thresholds were raised across the frequency spectrum. The normal auditory frequency range of the mouse is 1 to 91 kHz, and there is an exponential pattern to the basilar membrane frequency-place map of 1.2 mm/octave (Refs. 48 and 49). Based on the area targeted by the laser (~1 mm of basilar membrane at the basal end of the cochlea), one might expect that only frequencies >45 kHz would be affected by the laser. However, the elevation in low-frequency thresholds is not surprising given the longitudinal coupling within the cochlea that is needed to sustain traveling waves.[1,14] Modeling studies have confirmed that intrascalar scarring at the base of the cochlea can cause reduced cochlear responses at the apex.[50] Additionally, we did not assess for spiral ganglion cell damage in this study, and it is possible that the entire auditory nerve could have been affected as it courses through the lower portion of the modiolus near the round window. Finally, changes in the endocochlear potential could have occurred, producing broad-spectrum hearing loss.

Clearly, reducing the laser dosage appears to be critical in minimizing side effects. No evidence of intrascalar fibrosis was found at 15 J/cm^2, and there were normal-appearing hair cells and organ of Corti architecture, which is quite encouraging. However, there was still a moderate elevation in ABR thresholds across the frequency spectrum. There are many potential explanations for this. As discussed, damage to spiral ganglion cells or a reduced endocochlear potential could be a factor. Additionally, changes in the tectorial membrane or hair cell mechanics could have occurred. Although difficult to prove, some of the changes in ABR thresholds that we measured may actually reflect a change in the biomechanics of the basilar membrane.

Interestingly, this lower laser dosage is within a more clinically relevant range. The typical range of laser dosage used for skin rejuvination is 2 to 15 J/cm^2, a technique based on the same concept of acutely photocoagulating collagen to stimulate delayed collagen remodeling and new collagen deposition.[28–30,32,33] The mouse basilar membrane is much thinner and more delicate than human skin, and it is probable that lower irradiation dosages may still stimulate changes in basilar membrane collagen with a lower risk of toxicity.

Ultimately, our goal is to use cochlear laser irradiation to change the biomechanical properties of the basilar membrane by changing collagen organization and density. It remains to be studied if these types of laser-irradiation-induced changes within the basilar membrane do increase its stiffness, as described in other tissues.[23,28–30] Obviously, it will be important to measure the stiffness and resonant frequency of the basilar membrane before and after irradiation to determine whether the tonotopic frequency map of the cochlea can be modulated. We predict that there should be a decrease in the resonant frequency of an irradiated region acutely because the photocoagulative effect should decrease basilar membrane stiffness. However, with time, there should be a gradual increase in the resonant frequency of that region as collagen remodeling and deposition occurs, increasing basilar membrane stiffness.

If laser irradiation can safely "retune" the resonant frequency map of the cochlea, it may provide the basis for a novel therapeutic approach for the treatment of hearing loss. The most common type of sensorineural hearing loss is age-related hair cell degeneration in the high-frequency region of the cochlea.[51–54] It is conceivable that using this technique, a low-frequency region of the cochlea with functional sensory hair cells might be made to resonate at a higher frequency in an effort to partially compensate for this high-frequency hearing loss.

Acknowledgments

We wish to acknowledge Parmeswaran Diagaradjane for technical assistance with some experiments, Isaac Ayala for the artwork, NIH Grant No. DC006671 (to JSO), and a grant from the Alliance for NanoHealth/U.S. Department of Defense (USDOD) (to JSO and BA).

References

1. G. von Bekesy, *Experiments in Hearing*, McGraw-Hill, New York (1960).
2. R. C. Naidu and D. C. Mountain, "Measurements of the stiffness map challenge a basic tenet of cochlear theories," *Hear. Res.* **124**(1–2), 124–131 (1998).
3. E. S. Olson, "Direct measurement of intra-cochlear pressure waves," *Nature (London)* **402**(6761), 526–529 (1999).
4. E. S. Olson, "Intracochlear pressure measurements related to cochlear tuning," *J. Acoust. Soc. Am.* **110**(1), 349–367 (2001).
5. S. Iurato, "Functional implications of the nature and submicroscopic structure of the tectorial and basilar membranes," *J. Acoust. Soc. Am.* **34**, 1386–1395 (1962).
6. D. J. Lim and H. N. Kim, "The canaliculae perforantes of Schuknecht," *Adv. Oto-Rhino-Laryngol.* **31**, 85–117 (1983).
7. L. Voldrich, "Mechanical properties of basilar membrane," *Acta Oto-Laryngol.* **86**(5–6), 331–335 (1978).
8. C. E. Miller, "Structural implications of basilar membrane compliance measurements," *J. Acoust. Soc. Am.* **77**(4), 1465–1474 (1985)
9. W. Plassmann, W. Peetz, and M. Schmidt, "The cochlea in gerbilline rodents," *Brain Behav. Evol.* **30**(1–2), 82–101 (1987).
10. G. Ehret, "Stiffness gradient along the basilar membrane as a basis for spatial frequency analysis within the cochlea," *J. Acoust. Soc. Am.* **64**(6), 1723–1726 (1978).
11. L. Stryer, Biochemistry, W. H. Freeman, San Francisco (1975).
12. F. H. Silver, *Biological Materials: Structure, Mechanical Properties, and Modeling of Soft Tissues*, New York University Press, New York (1987).
13. J. S. Oghalai, "The cochlear amplifier: augmentation of the traveling wave within the inner ear," *Curr. Opin. Otolaryngol. Head Neck Surg.* **12**(5), 431–438 (2004).
14. C. D. Geisler, *From Sound to Synapse: Physiology of the Mammalian Ear*, Oxford University Press, New York (1998).
15. P. K. Legan, A. Rau, J. N. Keen, and G. P. Richardson, "The mouse tectorins. Modular matrix proteins of the inner ear homologous to components of the sperm-egg adhesion system," *J. Biol. Chem.* **272**(13), 8791–8801 (1997).
16. M. Cohen-Salmon, A. El-Amraoui, M. Leibovici, and C. Petit, "Otogelin: a glycoprotein specific to the acellular membranes of the inner ear," *Proc. Natl. Acad. Sci. U.S.A.* **94**(26), 14450–14455 (1997).
17. D. J. Lim, "Fine morphology of the tectorial membrane. Its relationship to the organ of Corti," *Arch. Otolaryngol.* **96**(3), 199–215 (1972).

PROOF COPY 008702JBO

18. D. J. Lim, "Development of the tectorial membrane," *Hear. Res.* **28**(1), 9–21 (1987).
19. R. J. Goodyear and G. P. Richardson, "Extracellular matrices associated with the apical surfaces of sensory epithelia in the inner ear: molecular and structural diversity," *J. Neurobiol.* **53**(2), 212–227 (2002).
20. K. Legan, R. J. Goodyear, V. Lukashkina, and A. N. Lukashkin, "Loss of striated-sheet matrix, aberrant collagen fibril organization, and changes in the tectorial membrane's frequency and level-dependent properties in the beta-tectorin null mutant mouse," in Abstracts of the 26th Meeting of the Association for Research in Otolaryngology, p. 207, (2003).
21. M. N. Asiyo-Vogel, R. Brinkmann, H. Notbohm, R. Eggers, H. Lubatschowski, H. Laqua, and A. Vogel, "Histologic analysis of thermal effects of laser thermokeratoplasty and corneal ablation using Sirius-red polarization microscopy," *J. Cataract Refractive Surg.* **23**(4), 515–526 (1997).
22. G. Kesler, R. Koren, A. Kesler, D. Kristt, and R. Gal, "Differences in histochemical characteristics of gingival collagen after ER:YAG laser periodontal plastic surgery," *J. Clin. Laser Med. Surg.* **18**(4), 203–207 (2000).
23. D. T. Fung, G. Y. Ng, M. C. Leung, and D. K. Tay, "Therapeutic low energy laser improves the mechanical strength of repairing medial collateral ligament," *Lasers Surg. Med.* **31**(2), 91–96 (2002).
24. K. Hayashi, P. Hecht, G. Thabit, 3rd, D. M. Peters, R. Vanderby Jr., A. J. Cooley, G. S. Fanton, J. F. Orwin, and M. D. Markel, "The biologic response to laser thermal modification in an in vivo sheep model," *Clin. Orthop. Relat. Res.* **373**, 265–276 (2000).
25. K. Hayashi, J. A. Nieckarz, G. Thabit, 3rd, J. J. Bogdanske, A. J. Cooley, and M. D. Markel, "Effect of nonablative laser energy on the joint capsule: an in vivo rabbit study using a holmium:YAG laser," *Lasers Surg. Med.* **20**(2), 164–171 (1997).
26. J. Tang, F. Zeng, H. Savage, P. P. Ho, and R. R. Alfano, "Fluorescence spectroscopic imaging to detect changes in collagen and elastin following laser tissue welding," *J. Clin. Laser Med. Surg.* **18**(1), 3–8 (2000).
27. G. I. Wenzel, B. Pikkula, C. H. Choi, B. Anvari, and J. S. Oghalai, "Laser irradiation of the guinea pig basilar membrane," *Lasers Surg. Med.* **35**(3), 174–180 (2004).
28. M. A. Trelles, L. Garcia, J. Rigau, I. Allones, and M. Velez, "Pulsed and scanned carbon dioxide laser resurfacing 2 years after treatment: comparison by means of scanning electron microscopy," *Plast. Reconstr. Surg.* **111**(6), 2069–2078; discussion 2079–2081 (2003).
29. B. R. Moody, J. E. McCarthy, and G. J. Hruza, "Collagen remodeling after 585-nm pulsed dye laser irradiation: an ultrasonographic analysis," *Dermatol. Surg.* **29**(10), 997–999; discussion 999–1000 (2003).
30. E. L. Tanzi, C. M. Williams, and T. S. Alster, "Treatment of facial rhytides with a nonablative 1,450-nm diode laser: a controlled clinical and histologic study," *Dermatol. Surg.* **29**(2), 124–128 (2003).
31. G. Marque and L. V. Wang, "White light oblique incidence reflectometer for measuring absorption and reduced scattering spectra of tissue-like turbid media," *Opt. Express* **1**(13), 454–460 (1997).
32. M. W. Lee, "Combination 532-nm and 1064-nm lasers for noninvasive skin rejuvenation and toning," *Arch. Dermatol.* **139**(10), 1265–1276 (2003).
33. M. H. Tan, J. S. Dover, T. S. Hsu, K. A. Arndt, and B. Stewart, "Clinical evaluation of enhanced nonablative skin rejuvenation using a combination of a 532 and a 1,064 nm laser," *Lasers Surg. Med.* **34**(5), 439–445 (2004).
34. L. C. Junqueira, W. Cossermelli, and R. Brentani, "Differential staining of collagens type I, II and III by Sirius red and polarization microscopy," *Arch. Histol. Jpn.* **41**(3), 267–274 (1978).
35. L. C. Junqueira, G. Bignolas, and R. R. Brentani, "Picrosirius staining plus polarization microscopy, a specific method for collagen detection in tissue sections," *Histochem. J.* **11**(4), 447–455 (1979).
36. B. C. Vidal, M. L. Mello, and E. R. Pimentel, "Polarization microscopy and microspectrophotometry of Sirius red, picrosirius and chlorantine fast red aggregates and of their complexes with collagen," *Histochem. J.* **14**(6), 857–878 (1982).
37. G. E. Pierard, "Sirius red polarization method is useful to visualize the organization of connective tissues but not the molecular composition of their fibrous polymers," *Matrix* **9**(1), 68–71 (1989).
38. J. M. Preston and P. C. Tsien, "The cellulose-dye complex. Part V-A: comparison of orientation factors derived from dichroism and other parameters," *J. Soc. Dyers Colour.* **66**, 361–365 (1950).
39. F. Sweat, H. Puchtler, and S. I. Rosenthal, "Sirius red F3BA as a stain for connective tissue," *Arch. Pathol.* **78**, 69–72 (1964).
40. D. Goldberg, M. Tan, M. D. Sarradet, and M. Gordon, "Nonablative dermal remodeling with a 585-nm, 350-microsec, flashlamp pulsed dye laser: clinical and ultrastructural analysis," *Dermatol. Surg.* **29**(2), 161–163; discussion 163–164 (2003).
41. C. W. van Wyk, H. A. Seedat, and V. M. Phillips, "Collagen in submucous fibrosis: an electron-microscopic study," *J. Oral Pathol. Med.* **19**(4), 182–187 (1990).
42. C. A. Smith and J. A. Vernon, *Handbook of Auditory and Vestibular Research Methods*, C. C. Thomas, Springfield, IL (1976).
43. J. S. Oghalai, "Chlorpromazine inhibits cochlear function in guinea pigs," *Hear. Res.* **198**(1–2), 59–68 (2004).
44. A. L. Nuttall, D. M. Marques, and M. Lawrence, "Effects of perilymphatic perfusion with neomycin on the cochlear microphonic potential in the guinea pig, *Acta Oto-Laryngol.* **83**(5–6), 393–400 (1977).
45. D. T. Fung, G. Y. Ng, M. C. Leung, and D. K. Tay, "Investigation of the collagen fibril distribution in the medial collateral ligament in a rat knee model," *Connect. Tissue Res.* **44**(1), 2–11 (2003).
46. D. T. Fung, G. Y. Ng, M. C. Leung, and D. K. Tay, "Effects of a therapeutic laser on the ultrastructural morphology of repairing medial collateral ligament in a rat model," *Lasers Surg. Med.* **32**(4), 286–293 (2003).
47. J. F. Willott, *Handbook of Mouse Auditory Research: From Behavior to Molecular Biology*, CRC Press, Boca Raton, FL (2001).
48. R. R. Fay, "Comparative psychoacoustics," *Hear. Res.* **34**(3), 295–305 (1988).
49. M. Muller, K. von Hunerbein, S. Hoidis, and J. W. Smolders, "A physiological place-frequency map of the cochlea in the CBA/J mouse," *Hear. Res.* **202**(1–2), 63–73 (2005).
50. C. H. Choi and J. S. Oghalai, "Predicting the effect of post-implant cochlear fibrosis on residual hearing," *Hear. Res.* **205**(1–2), 193–200 (2005).
51. R. Jonsson and U. Rosenhall, "Hearing in advanced age. A study of presbyacusis in 85-, 88- and 90-year-old people," *Audiology* **37**(4), 207–218 (1998).
52. J. S. Milne, "Hearing loss in the elderly: a 17-year longitudinal study," *Clin. Otolaryngol. Allied Sci.* **14**(5), 457 (1989).
53. E. K. Moscicki, E. F. Elkins, H. M. Baum, and P. M. McNamara, "Hearing loss in the elderly: an epidemiologic study of the Framingham Heart Study Cohort," *Ear Hear.* **6**(4), 184–190 (1985).
54. K. E. Pedersen, U. Rosenhall, and M. B. Moller, "Changes in pure-tone thresholds in individuals aged 70–81: results from a longitudinal study," *Audiology* **28**(4), 194–204 (1989).

Development of Asymmetric Liposomal Particles

Final Report

February, 2009

S. Thevananther, Baylor College of Medicine

C. Vipulanandan, K. K. Mohanty, University of Houston

Introduction

It is estimated that hepatocellular carcinoma (HCC) is the fifth most common type of cancer and is the fourth leading cause of cancer-related deaths worldwide.[1] Systemic chemotherapy treatment has been marginally beneficial because of its low response rate (0%-25%), lack of increased survival rate, and harmful toxicity.[2,3] Advances in the molecular understanding of hepatocarcinogenesis have raised the possibility of targeting cellular pathways involved in the formation and progression of HCC. [4,5] Cyclin D1 gene silencing by cyclin D1 specific siRNAs may provide an improved therapy over systemic chemotherapy for HCC treatment.

The delivery of therapeutic quantities of siRNA to HCC is challenging. One method of delivery is the use of liposomal encapsulation. Liposomes are lipid bilayer vesicles that can encapsulate siRNA and other therapeutics for targeted and enhanced delivery. Liposomes have advantages over other delivery systems in that, if composed of naturally occurring lipids and other compounds, they are biodegradable and nontoxic. In the conventional process, however, the encapsulation efficiency is not very high. Approximately 80% of the therapeutic is not encapsulated and must be removed by diafiltration or other techniques and recycled, which can be costly if the therapeutic is valuable. In addition, the conventional method cannot produce SUVs with a heterogeneous distribution of lipid types between the leaflets of the bilayers, which can improve the design and efficacy of the liposomal delivery system. The goal of this project was to produce asymmetric liposomes for drug and siRNA delivery.

Methods

Liposomes are produced in three steps. In step 1, cationic lipids are dissolved by sonication in an oil medium such as dodecane. A small amount of aqueous solution containing the siRNA or other therapeutic is added to the oil-lipid solution. The resulting oil-water system is sonicated and extruded through a polycarbonate membrane of particular pore size to produce inverse emulsion nanoparticles. In step 2 of the production process, neutral lipids are dissolved and sonicated in an oil medium to provide the outer leaflet lipids. This oil-lipid solution, called the intermediate phase, is then placed on top of an aqueous solution that does not contain any siRNA or other therapeutic, because it will become the final medium for the produced asymmetric liposomes. The outer leaflet lipids will align at the oil-water interface, again with the head groups in the aqueous phase and the fatty acid chains in the oil phase. In the final step, the inverse emulsion solution is placed on top of the intermediate phase, which is on top of the aqueous phase, and then entire system is centrifuged at an excess of 120 × *g* for 10 to 60 min. The density difference between the aqueous core of the inverse emulsion particles and the oil medium will be amplified under centrifugation and will drive the inverse emulsion particles through the intermediate and aqueous phase interface. As the particles travel though the interface, they will pick up the outer leaflet of lipids forming a bilayer vesicle, which is now suspended in the bottom aqueous phase. The final product should be asymmetric liposomes containing siRNA or other therapeutics.

Figure depicts the entire production process and illustrates how the outer leaflet is formed around the inverse emulsion particles by centrifugation. Commercially available DMPC and DOTAP are used in this study along with a few fluorescent-tagged lipids.

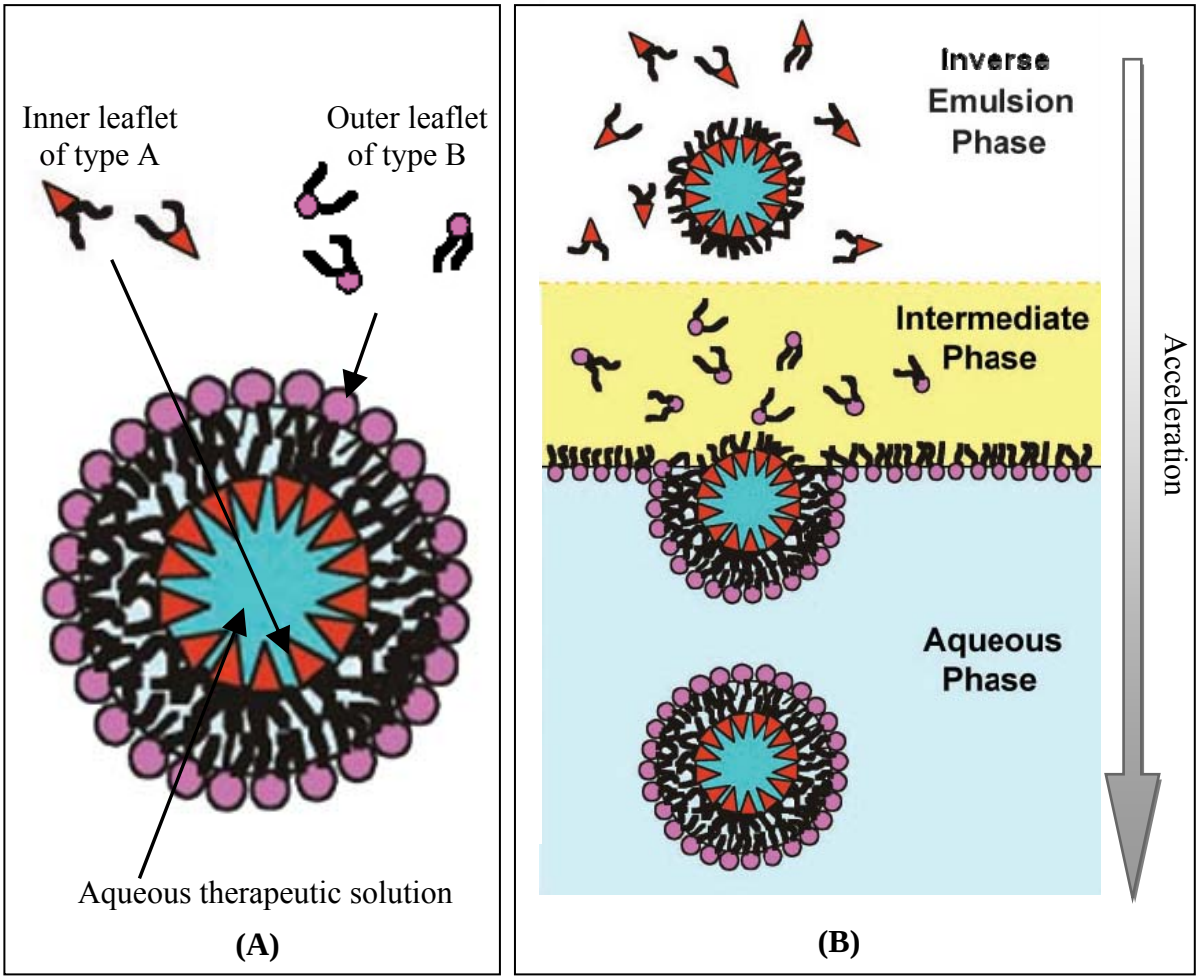

Figure 1. (A) Asymmetric liposome composition. Lipid type A is cationic and lipid type B is neutral or slightly anionic. (B) Asymmetric liposome production scheme.

Results and Discussion

Inverse emulsion. The first step in making asymmetric lipid bilayer vesicles is to produce an inverse emulsion consisting of an oil-lipid solution with encapsulated aqueous droplets of the polynucleotides of interest (DNA, siRNA, plasmid, *etc.*). Figure , shows an inverse emulsion prepared in dodecane (C_{12}) with 94.0 μM POPC (neutral), 100.0 μM DOTAP (cationic), 2.1 μM NBD-PC (neutral fluorescent lipid), and extruded at 5000 nm with 1.25 v/v% aqueous droplets containing 37.0 μM non-fluorescent 21-mer DNA oligo, 37.0 μM Cy3-tagged 21-mer DNA oligo, and 457.0 μM Alexa Fluor 350 salt. The images in the figure correspond to the inverse

emulsion layer shown in **Error! Reference source not found.**, taken within 30 min of emulsion preparation. The lipid layer covering the particles is illuminated by the NBD-PC, as observed in the top image. The amount of NBD-lipid was chosen to maximize fluorescence intensity while avoiding self-quenching. The aqueous core is illuminated by the addition of Alexa Fluor 350 salt, as observed in the middle image. Lastly, the polynucleotide cargo is observed in the bottom image by the encapsulation of Cy3-tagged 21-mer DNA oligo. The white arrows illustrate an inverse emulsion particle present in all three images.

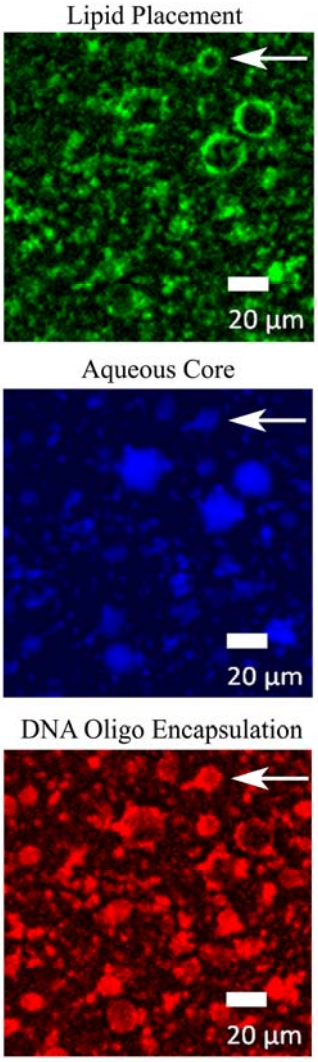

Figure 2. Fluorescent images of the same view field of inverse emulsion containing fluorescent markers. Top: Fluorescence indicates placement of NBD-PC in lipid leaflet; Middle: Fluorescence indicates encapsulated Alexa Fluor 350 Salt; Bottom: Fluorescence indicates

encapsulation of Cy3-tagged 21-mer DNA oligo. The arrows indicate an inverse emulsion particle present in all three images. This inverse emulsion was extruded at 5000 nm.

Similar inverse emulsion results were observed for both mineral oil (mainly C_{15}-C_{40}) and squalene ($C_{30}H_{50}$), a branched hydrocarbon, indicating that inverse emulsion can be easily and consistently produced to contain an outer lipid layer and encapsulate a polynucleotide (negatively charged) cargo. However a wide distribution of particle size is also observed as demonstrated in the images by the scale bar in Figure . This is due to coalescence of the inverse emulsion particles and is discussed later in this article.

Liposome Products Using Dodecane and Mineral Oil. A dodecane intermediate phase was prepared with 211.0 μM DMPC (neutral) and 2.1 μM NBD-PC (neutral fluorescent lipid) and placed on top of an aqueous TBS solution to allow the lipids to align at the oil-water interface as depicted in **Error! Reference source not found.**. An equilibration time of 1.5 hr was used as suggested by Pautot *et al.*[6] to allow the interface to become saturated with lipids. Next, an inverse emulsion phase was prepared with 205.0 μM DOTAP (cationic) and 2.1 μM NBD-PC (neutral fluorescent lipid) and contained 2.1 v/v% aqueous cargo of 80 μM Cy3-tagged 21-mer DNA oligo and 716.0 μM Alexa Fluor 350 salt. The inverse emulsion was extruded through a 1000 nm membrane, then directly placed on top of the intermediate phase and centrifuged at 115 × *g* for 30 min to form liposomes.

Fluorescent images of the liposome products, which are contained in aqueous TBS, are shown in Figure . The images in the figure correspond to the asymmetric lipid bilayer vesicle at the bottom of **Error! Reference source not found.**. The top image in Figure shows the placement of NBD-PC lipids in the liposomes' bilayer. The middle image shows the encapsulation of the aqueous cargo, Alexa Fluor 350, used to form the inverse emulsion. The bottom image shows the placement of the Cy3-tagged DNA oligo. The white circles mark the only particles that exhibit a lipid membrane, aqueous core, and DNA oligo encapsulation. Similar results were observed using a mineral oil.

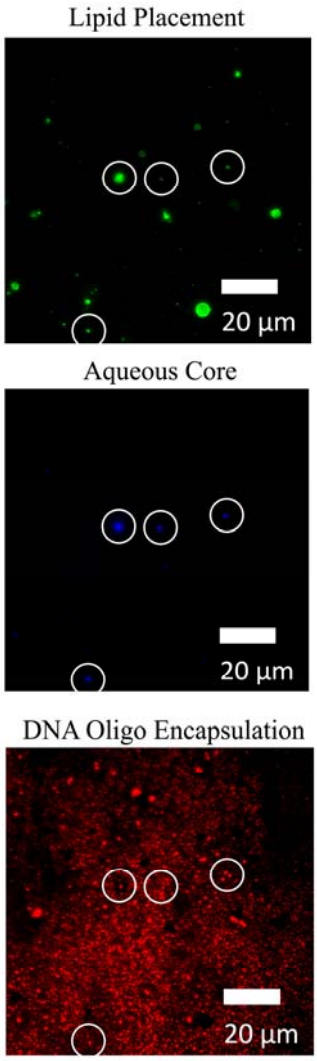

Figure 3. Fluorescent images of the same view field of asymmetrically produced liposomes from dodecane. Top: Fluorescence indicates placement of NBD-PC in a lipid leaflet; Middle: Fluorescence indicates encapsulated Alexa Fluor 350 Salt; Bottom: Fluorescence indicates encapsulation of Cy3-tagged 21-mer DNA oligo. The white circles indicate liposomes containing all three fluorescent markers. The inverse emulsion for these liposome products was extruded at 1000 nm.

Several conclusions can be drawn from Figure . First, the majority of the lipid vesicles in the top image do not contain a detectable amount of Alexa Fluor 350 as shown in the middle image. It is possible, as suggested by Yamada *et al.*, that multi-lipid-layer inverse emulsion particles containing an oil interior are forming in the inverse emulsion phase.[7] As these undesired particles

cross the intermediate and aqueous phase interface, they shed a lipid layer to release a vesicle that does not contain the intended aqueous core. It is also possible that perturbations (perhaps caused by impinging inverse emulsion particles) at the intermediate and aqueous phase interface could cause monolayer or multi-layer vesicles to pinch off, again producing undesired vesicle products that could contain an oil interior. Pautot *et al.*[6] report that aqueous-oil interfaces such as with dodecane and POPC or POPS can spontaneously form water-in-oil or oil-in-water particles by the swelling of lipid liquid-crystalline structures at oil-water interfaces. Such formation of undesired particles could produce liposomes that contain NBD lipids but not the intended cargo. Rather they would contain aqueous phase from the bottom aqueous layer. Second, the total number of liposome particles observed is less than the total number of inverse emulsion particles produced (Figure), which suggests that not all of the inverse emulsion particles were converted into liposomes. Third, the bottom image shows a large number of Cy3-tagged DNA oligo particles across the view field. This distribution does not correspond to lipid vesicles in the top image nor the encapsulated Alexa Fluor 350 in the middle image. This indicates that the intended cargo inside the inverse emulsion particles was released into the bottom aqueous phase during transport through the aqueous phase-intermediate phase boundary. In order to increase cargo encapsulated liposome yield, which is necessary for this process to be competitive with conventional liposome production techniques, the limiting factors must be identified, investigated, and overcome.

3.3. Comparison of Dodecane and Squalene Liposome Products. Many attempts were made to form liposomes from inverse emulsions, but all resulted in extremely low yields with the majority of the cargo unencapsulated and free floating in solution (see Figure). These attempts included changing the lipid concentration in the inverse emulsion and intermediate phase from 0.13 to 1 mM, adding cholesterol to increase lipid layer stability, varying the temperature from 20 to 50 °C (transition temperature of various lipids), removing salt from the aqueous core, and changing the oil type. The only parameter that noticeably affected the efficiency of liposome formation was the oil. Liposome yield was highest using squalene.

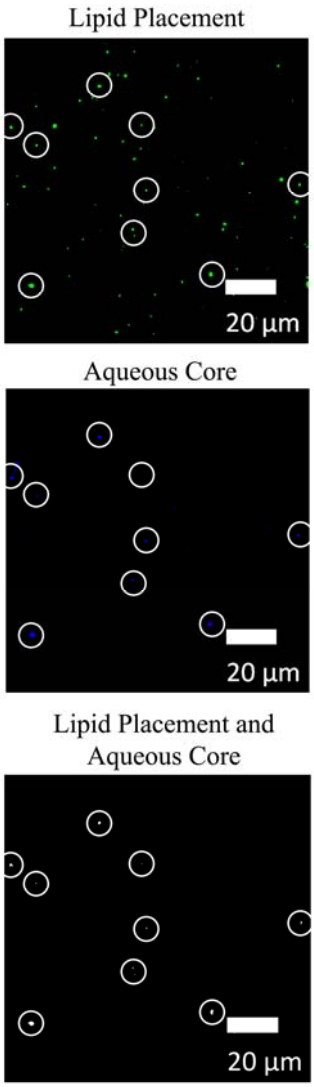

Figure 4. Fluorescent images of the same view field of asymmetrically produced liposomes from squalene which contain fluorescent markers. Top: Fluorescence indicates placement of NBD-PC in a lipid leaflet; Middle: Fluorescence indicates encapsulated Alexa Fluor 350 Salt; Bottom: White dots indicate the liposomes that show *both* NBD and Cy3 fluorescence. The bottom image is a product of the top two images. The white circles indicate liposomes present in all three images. The inverse emulsion for these liposome products was extruded at 200 nm.

The following experiment was done using squalene as the oil. The inverse emulsion contained 113.0 µM POPC, 20.5 µM DOTAP, 1.3 µM NBD-PC, and 0.6 v/v% aqueous droplets containing Alexa Fluor 350 salt and was extruded at 200 nm. The intermediate phase contained 125.0 µM POPC and 1.4 µM NBD-PC. Fluorescent images of the liposome products were acquired after

centrifugation and are shown in Figure . The top image shows the placement of the NBD lipids, the middle image shows the encapsulation of the Alexa Fluor 350 salt, and the bottom image shows liposomes that appear in *both* the top and middle images. Similar to the images of the dodecane system shown in Figure , there are a number of particles that contain NBD lipids in the top image which do not appear to contain the Alexa Fluor 350 salt cargo, as shown in the middle image. However, there are a larger number of liposomes that contain NBD lipids and Alexa Fluor cargo as indicated by the number of white circles outlining liposomes that appear in all three images in the figure.

Table 1. Image analysis of inverse emulsion and asymmetric liposome products. Fluorescent images were captured of inverse emulsion and liposomes and the number of particles in each images was counted.

	# of Inverse Emulsion Vesicles (per mm^2)	**# of Lipid Vesicles** (per mm^2)	**# of Alexa Fluor Encapsulated Vesicles** (per mm^2)	**Encapsulated Liposome Yield**
Dodecane	2,547	8,680	355	13.9%
Squalene	3,582	13,006	651	18.2%

To confirm that squalene produces higher yields, five images were randomly acquired from the dodecane and squalene systems for both the liposomes and the inverse emulsions they derived from. The number of particles in each image was counted (per mm^2 of image area) and shown in **Error! Reference source not found.**. For comparison, the values for the number of lipid vesicles and number of encapsulated vesicles were obtained by dividing the counted particles by the appropriate dilution factor of converting 100 μL of inverse emulsion to 2 mL of liposome product. For both the dodecane and squalene systems, over three times as many lipid vesicles are produced than emulsion particles. This result further supports that undesired or unintentional particles are being formed as discussed above by the formation of oil-in-water droplets at the intermediate and aqueous phase interface either spontaneously or by perturbations caused by the impingement of accelerated inverse emulsion particles at the interface. Of the particles counted in the liposome products, 5% or less were observed to encapsulate the intended Alexa Fluor cargo. Squalene had a higher inverse emulsion to liposome conversion of 18.2% compared to

dodecane at 13.9%. Such a low yield in either oil system must be improved for this technique to be a viable way a producing therapeutic quantities of polynucleotide encapsulated liposomes.

The formation of inverse emulsion particles and the acceleration of these particles through an oil-water interface is dependent on the fluid and interfacial properties of the system. The terminal velocity of an inverse emulsion particle under acceleration can be modeled from Stokes' Law,

$$v_t = (\rho_a - \rho_o)\frac{d_p^2 \omega^2 r_c}{18\mu_o}, \qquad (1)$$

where $(\rho_a - \rho_o)$ is the density difference between the oil and aqueous inverse emulsion particle, d_p is the diameter of the inverse emulsion particle, ω is the rational speed of the centrifuge, r_c is the length of the centrifuge arm, and μ_o is the viscosity of the oil. The terminal velocity, and hence the force at which the inverse emulsion particle impinges on the oil-water interface, is dependent on the oil's density and viscosity, as well as the rational speed of the centrifuge. The interfacial tension at the interface also affects how the inverse emulsion particle passes through it. The density, viscosity, surface tension, and interfacial tension, with or without 113.0 μM POPC and 20.5 μM DOTAP, of the dodecane and squalene systems were measured and are shown in Table 2.

Table 2. Density, viscosity, surface tension, and interfacial tension of dodecane and squalene. Variations are standard error with $n \geq 4$. [a] Measurement done by du Nouy ring method. [b] Measurement done by the pendant drop method. [c] Measurement done by the pendant drop method using time evolution up to 90 min and lipid concentrations of 113.0 μM POPC and 20.5 μM DOTAP.

	Density (g/cm^3)	**Viscosity** (cP)	**Surface Tension** [a] (dynes/cm)	**Interfacial Tension No Lipids** [b] (dynes/cm)	**Interfacial Tension with Lipids** [c] (dynes/cm)
Dodecane	0.856	1.1 ± 0.1	25.3 ± 0.08	44.5 ± 1.3	18.4 ± 1.1
Squalene	0.748	11.0 ± 0.2	32.2 ± 0.04	31.9 ± 1.6	6.9 ± 1.1

The oil density and viscosity affect the terminal velocity of the inverse emulsion particle, but can be compensated for by adjusting the rotational speed of the centrifuge. The interfacial tension cannot be compensated for and is a function of oil type, lipid concentration, and temperature. Higher interfacial tension creates an interface that is more rigid and less elastic than lower interfacial tension. The time evolution of the interfacial tension between TBS and dodecane or squalene containing 113.0 μM POPC and 20.5 μM DOTAP at room temperature is shown in Figure . The first data point of both series was measured separately in the absence of lipids. As the lipid surface concentration increases, the interfacial tension decreases, changing the shape of the droplet. Therefore, the interfacial tension (remaining data points) decreases over time as the POPC and DOTAP lipids diffuse and absorb to the interface of the droplet. The time evolution of the interfacial tension of squalene shows that it has a lower interfacial tension and that it reaches equilibrium faster than with dodecane.

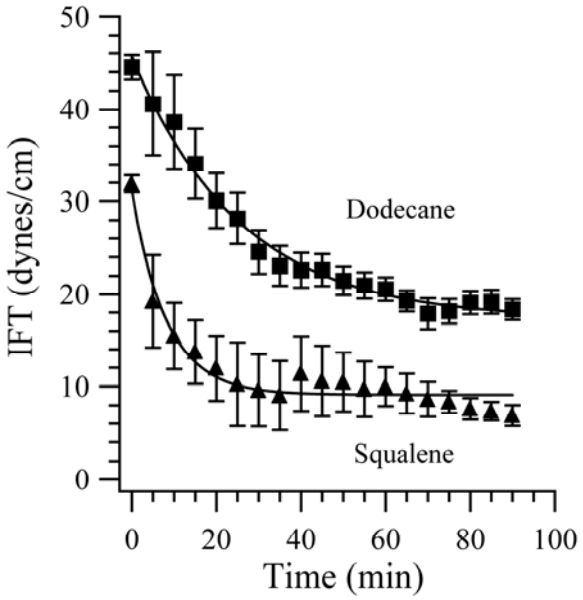

Figure 5. Time evolution of the interfacial tension of an aqueous pendant drop in oil-lipid solutions. Dodecane and squalene solutions contained 113.0 μM POPC and 20.5 μM DOTAP. The measurements were done at room temperature and at least in triplicate. The error bars represent standard error.

Squalene may have a higher liposome yield compared to dodecane because of its lower interfacial tension and higher viscosity. As an inverse emulsion particle contacts the second oil-water interface, the interface may bend more readily around the inverse emulsion particle if the

interfacial tension is lower. Increase in oil viscosity may increase the residence time of the inverse emulsion particle passing through it. An increase in residence time would increase the outer lipid leaflet coverage by the second oil-water interface and increase the likelihood of a bilayer liposome forming. Therefore the efficiency of liposome production from inverse emulsion can be improved by using oils that achieve low interfacial tension and high viscosity. To further study the interactions at the intermediate and aqueous phase interface, a fluorescent microscopy visualization cell was developed.

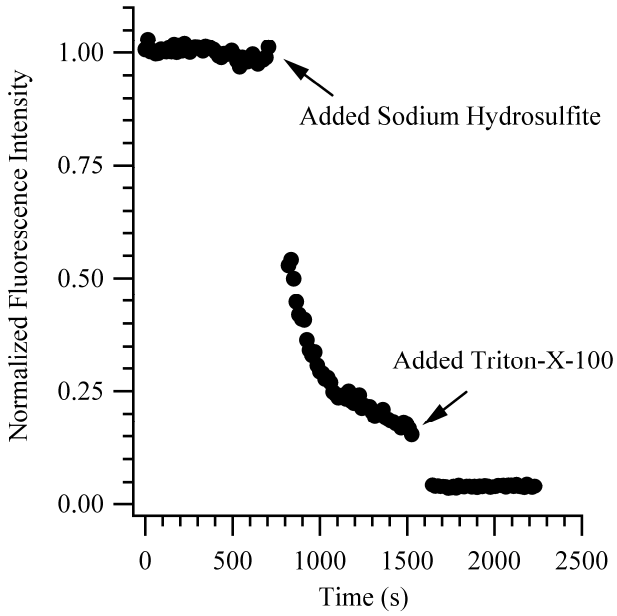

Figure 6. Fluorescence quenching of asymmetrically produced liposomes (with NBD-PC in only the outer leaflet) with 1 M sodium hydrosulfite ($Na_2S_2O_4$). After quenching, the liposomes were lysed with Triton-X-100 (1.25 v/v) and any remaining fluorescence was quenched. Liposomes were produced with 15 mol% DOTAP and 85 mol% POPC in the inner leaflet and 99 mol% POPC and 1 mol% NBD-PC in the outer leaflet. Inverse emulsion was extruded at 200 nm diameter.

Liposome Bilayer Asymmetry. To demonstrate asymmetry in the formed liposomes an experiment was done in which fluorescently asymmetric liposomes were produced with NBD-PC in only the outer leaflet. Sodium hydrosulfite (1 M $Na_2S_2O_4$ in TBS, pH 9.9) was added, as shown in Figure , to the fluorescently asymmetric liposomes and the fluorescence was quenched > 80% by chemical reduction of the NBD group.[8] This demonstrates at least 80% asymmetry and is in agreement with Pautot *et al*. results.[9] After the outer leaflet was quenched, Triton-X-100 was added to lyse the liposomes to allow the sodium hydrosulfite to react with any NBD labeled

lipids in the inner leaflet. The fluorescence intensity was reduced another 16% indicating that a small fraction of the outer leaflet NBD-PC lipids were incorporated into the inner leaflet.

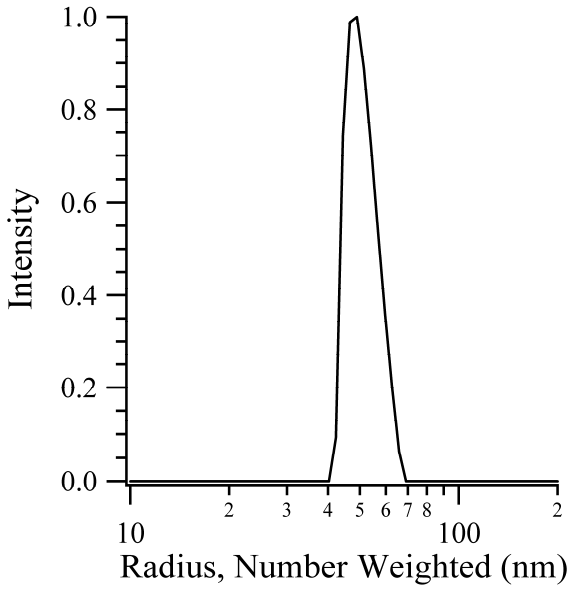

Figure 7. Particle size distribution (from DLS) of inverse emulsion immediately after extrusion at 200 nm. The inverse emulsion was prepared using with 113.0 μM POPC, 20.5 μM DOTAP, 1.3 μM NBD-PC, and 0.06 v/v% aqueous droplets.

3.6. Stability of Inverse Emulsion and Liposome Products using DLS. It is important to know the size stability of the inverse emulsion because it is the base component from which the asymmetric liposomes are constructed. If the size distribution of the inverse emulsion changes before passage through the second oil-water interface, then the formed liposomes would not have the desired size distribution. Dynamic light scattering (DLS) experiments were done to quantify the stability of inverse emulsion and asymmetric liposome products over a week.

Inverse emulsion in squalene was prepared using with 113.0 μM POPC, 20.5 μM DOTAP, 1.3 μM NBD-PC, 0.6 v/v% aqueous droplets, and was extruded at 200 nm. The inverse emulsion size distribution was immediately analyzed by DLS. The results showed monodisperse distributions as shown in Figure for freshly extruded inverse emulsion. However, the distributions indicate the mean radius of the freshly extruded inverse emulsion is about half that expected from a 200 nm diameter extrusion. This suggests that other factors besides extrusion membrane pore size influence inverse emulsion size. Such factors may include extrusion

pressure, oil viscosity, or number of passes. The consistent and reliable production of monodisperse and desired size inverse emulsion is currently under investigation.

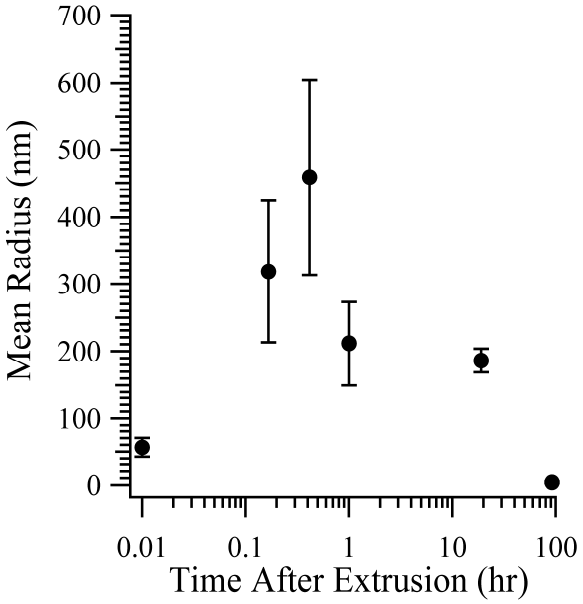

Figure 8. Time evolution of mean particle size in the inverse emulsion, which was prepared using with 113.0 μM POPC, 20.5 μM DOTAP, 1.3 μM NBD-PC, and 0.06 v/v% aqueous phase. Error bars represent standard error of replicate readings of the same sample.

The inverse emulsion was analyzed by DLS over a time of 100 hr. During this period it was kept at room temperature. The time-elapsed size stability results are shown in Figure . The mean radius of the inverse emulsion increased rapidly from 56.4 nm to 458.8 nm after 24 min, then decreased to 211.5 nm after 1 hr and eventually tended toward zero after 100 hr. This trend might be explained by coalescence and settling velocity. After extrusion, the inverse emulsion particles began to coalesce. The coalescences of the inverse emulsion particles increased the mean radius as measured by DLS. The inverse emulsion particles continued to increase in size as did their settling velocity (see Equation 1). After approximately 30 min after extrusion, coalesced inverse emulsion particles began to fall out of the DLS sample volume as defined by the incident laser light on the sample. Therefore a decrease in inverse emulsion size was observed. The process continued until all of the suspended inverse emulsion particles coalesced and settled to the bottom of the cuvette as evidenced by the nearly zero mean radius after 100 hr. In order for the size controlled production of asymmetric liposomes from inverse emulsion, extruded inverse

emulsion must be converted to bilayer liposomes as soon as possible (< 1 min) to avoid coalescence.

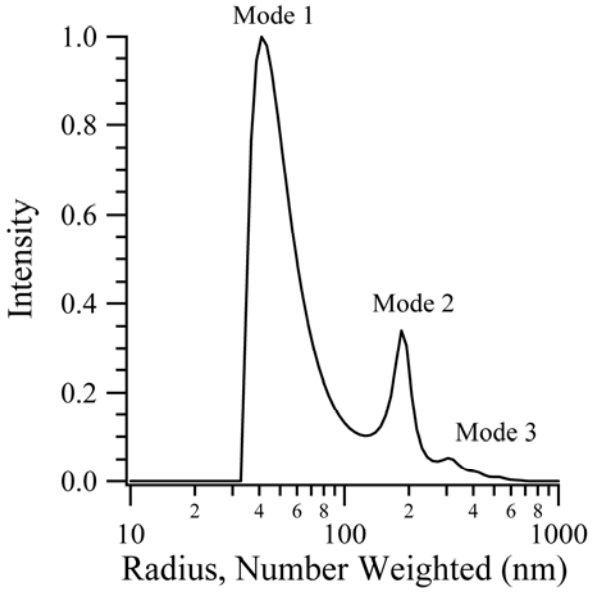

Figure 9. Particle size distribution (from DLS) of liposomes immediately after formation using inverse emulsion extruded at 200 nm. The inverse emulsion was prepared using with 113.0 μM POPC, 20.5 μM DOTAP, 1.3 μM NBD-PC, and 0.06 v/v% aqueous phase. Intermediate phase was prepared with squalene using 125.0 μM POPC and 1.4 μM NBD-PC.

Liposomes were prepared immediately after extrusion from the inverse emulsion described above. The intermediate phase used to produce the liposomes was composed of squalene with 125.0 μM POPC and 1.4 μM NBD-PC. Interestingly, the liposome product produced a trimodal distribution as shown in Figure . The first and most prominent mode has a mean radius of 44 nm followed by a mode of 188 nm and 489 nm. The three modes suggest, as did previous image data above, that various populations of lipid vesicles are forming, some of which are not the intended product. In terms of size stability however, the three modes remain relatively constant over a 160 hr period (Figure 1), especially in comparison to the stability of the inverse emulsion (Figure). The increased liposome stability is expected because the lipid bilayer vesicles are thermodynamically more stable than lipid monolayer inverse emulsions. In order to produce a viable and therapeutic asymmetric liposomal delivery vector for polynucleotides, the end product must have an adequate shelf-life. Longer time periods are currently being investigated to fully characterize shelf-life.

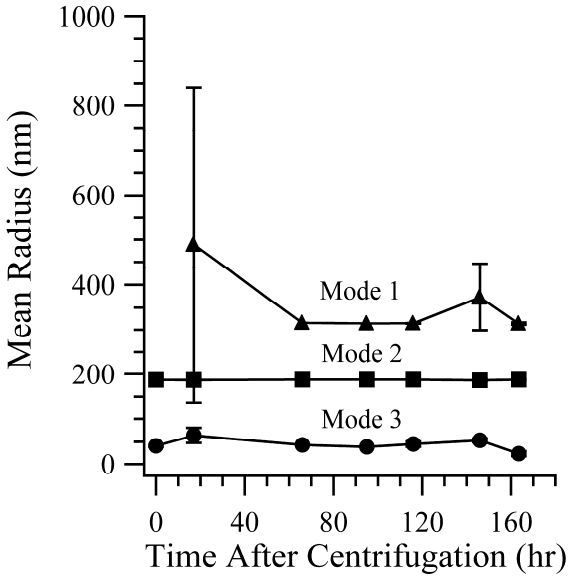

Figure 1. Time evolution of liposome size. The three data series represent the three modes observed in Figure .

Key Research Accomplishments

Production of asymmetric liposomes for drug delivery

Conclusions

Production of liposomes from inverse emulsion allows the design and construction of compositionally different (asymmetric) inner and outer leaflets of the lipid bilayer liposome. Contrary to conventional liposome production techniques, this is done by independently forming each leaflet, one at a time, around an aqueous cargo by the use of oil-water interfaces. Inverse emulsion particles can be produced with a lipid coating and an aqueous core encapsulating a 21-mer DNA oligo polynucleotide cargo. Monodisperse inverse emulsion can be consistently made, but quickly undergoes coalescence to increase mean particle size by an order of magnitude within 30 min of extrusion. Therefore, freshly extruded inverse emulsion must immediately be used if a controlled liposome size distribution is desired.

A low yield was observed for inverse emulsion to liposome conversion with this technique, especially using the unbranched hydrocarbons dodecane (C_{12}) and mineral oil (mainly C_{15}-C_{40}) as the lipid solvent. The yield is higher with squalene as the oil. Presumably because squalene has a significantly higher viscosity and lower interfacial tension than dodecane, which may

increase stability as droplets pass through the interface. The asymmetry of liposomes was demonstrated with a fluorescence quenching assay.

Although most of the inverse emulsion particles are not converted to liposomes, some are. The liposome product had a trimodal size distribution, which remained relatively stable over a 160 hr period.

Translation to Military Medicine

Present medicinal treatments deliver the medicine to all the cells. Targeted drug/gene delivery can deliver medicines to specific tissues which would increase effectiveness and decrease side effects. Many military patients can benefit from targeted delivery. The development of asymmetric liposomes is the first step of developing targeted delivery of siRNAs.

Scientific Publications

Whittenton, J., Harendra, S., Pitchumani, R., Mohanty, K., Vipulanandan, C. & Thevanther, S., "Evaluation of Asymmetric Liposomal Nanoparticles for Encapsulation of Polynucleotides," *Langmuir*, DOI: 10.1021/la801133j (2008).

Funding Received

K. K. Mohanty, "Nanofluid Stability in Carbonate Rocks," Aramco, $45,837, 2008-2009.

References

1. Parkin, D. M.; Bray, F.; Ferlay, J.; Pisani, P., Global cancer statistics, 2002. *CA Cancer J Clin* **2005,** 55, (2), 74-108.
2. Thomas, M. B.; Zhu, A. X., Hepatocellular carcinoma: the need for progress. *J Clin Oncol* **2005,** 23, (13), 2892-9.
3. Zhu, A. X., Systemic therapy of advanced hepatocellular carcinoma: how hopeful should we be? *Oncologist* **2006,** 11, (7), 790-800.
4. Avila, M. A.; Berasain, C.; Sangro, B.; Prieto, J., New therapies for hepatocellular carcinoma. *Oncogene* **2006,** 25, (27), 3866-84.

5. Romano, P. R.; McCallus, D. E.; Pachuk, C. J., RNA interference-mediated prevention and therapy for hepatocellular carcinoma. *Oncogene* **2006,** 25, (27), 3857-65.
6. Pautot, S.; Frisken, B. J.; Weitz, D. A., Production of unilamellar vesicles using an inverted emulsion. *Langmuir* **2003,** 19, (7), 2870-2879.
7. Yamada, A.; Yamanaka, T.; Hamada, T.; Hase, M.; Yoshikawa, K.; Baigl, D., Spontaneous transfer of phospholipid-coated oil-in-oil and water-in-oil micro-droplets through an oil/water interface. *Langmuir* **2006,** 22, (24), 9824-8.
8. Pautot, S.; Frisken, B. J.; Weitz, D. A., Engineering asymmetric vesicles. *Proc Natl Acad Sci U S A* **2003,** 100, (19), 10718-21.
9. Ahmed, F.; Discher, D. E., Self-porating polymersomes of PEG-PLA and PEG-PCL: hydrolysis-triggered controlled release vesicles. *J Control Release* **2004,** 96, (1), 37-53.

Evaluation of Asymmetric Liposomal Nanoparticles for Encapsulation of Polynucleotides

Jeremiah Whittenton[1], Sivaram Harendra[2], Ramanan Pitchumani[3], Kishore Mohanty[1*], Cumaraswamy Vipulanandan[2] and Sundararajah Thevananther[4]

[1] Chemical and Biomolecular Engineering, University of Houston, S222 Engineering Bldg. 1, Houston, TX 77204-4004
[2] Civil and Environmental Engineering, University of Houston, N107 Engineering Bldg. 1, Houston, TX 77204
[3] Biomedical Engineering, University of Houston, N207 Engineering Bldg. 1, Houston, TX 77204
[4] Pediatrics, Baylor College of Medicine & Texas Children's Liver Center, One Baylor Plaza, MC3-3391, Houston, TX 77030
* Corresponding author

Abstract

Conventional lipid bilayer liposomes have similar inner and outer leaflet compositions; asymmetric liposomes have different lipid leaflet compositions. The goal of this work is to place cationic lipids in the inner leaflet to encapsulate negatively charged polynucleotides and to place neutral/anionic lipids on the outer leaflet to decrease non-specific cellular uptake/toxicity. Inverse emulsion particles have been developed with a single lipid leaflet of cationic and neutral lipids surrounding an aqueous core containing a negatively charged 21-mer DNA oligo. The particles are accelerated through an oil-water interface entrapping a second neutral lipid to form oligo encapsulated unilamellar liposome nanoparticles. Inverse emulsion particles can be consistently produced to encapsulate an aqueous environment containing negatively charged oligo. The efficiency of encapsulated liposome formation is low and depends on the hydrocarbon used as the oil phase. Dodecane, mineral oil, and squalene were tested, and squalene, a branched hydrocarbon, yielded the highest efficiency.

Keywords: Liposomes, drug delivery, encapsulation, gene delivery, emulsion stability

1. Introduction

Delivery of negatively charged polynucleotides (DNA, siRNA) into cancer cells can change intracellular pathways thereby reducing their progression.[2] Conventional techniques using liposomes and cationic polymers have low encapsulation efficiencies and/or high toxicity. The goal of this study was to develop asymmetric liposomal nanoparticles to overcome some of these deficiencies.

Liposomes are vesicular colloidal particles (*ca.* 50-500 nm) composed of self-assembled amphiphilic molecules. Single chain amphiphiles, such as soaps and detergents, typically form micelles. These are small (~2 nm), single layered, spherical structures in which the surface polar heads shield the nonpolar interior from water. Many natural amphipiles, such as lecithin (diacyl phosphotidylcholine), have two nonpolar tails and due to a bulky nonpolar part cannot be packed into micelles. These molecules normally self-assemble into lipid bilayers in which the inner and outer polar surfaces shield the non-polar bilayer interior to form closed spherical structures with an aqueous core and aqueous exterior.[1-3] Conventionally prepared liposomes are symmetric, i.e., the inner and outer lipid layers have the same composition. Biological lipid bilayers, such as the cell plasma membrane, have compositionally different (asymmetric) inner and outer lipid leaflets which are important for coagulation, membrane transport processes, cell signaling, and membrane stability.[4] Asymmetrically designed liposomes may have unique and advantageous properties as delivery vectors and membrane models.

Liposomes have been utilized in a variety of settings including cosmetic, pharmaceutical, cellular, and membrane research.[5] They are able to deliver large amounts of drugs to specific sites, spare healthy tissue from toxic effects, and increase a drug's systematic circulation time.

Over the past two decades, progress in liposomal drug delivery has led to the commercialization of liposomal anticancer drug formulations (*e.g.* Doxil, DaunoXome), which improve their therapeutic index by decreasing toxicity associated with non-specific drug distribution while also increasing drug localization in malignant tissues by attachment of tumor targeting agents to the liposomes' surface. [6,7]

There are many methods for producing liposomes, including extrusion,[8,9] supercritical reverse phase evaporation,[10] and coacervation (phase separation),[11] *etc*. All of these techniques produce symmetric vesicles where the composition of inner and outer leaflets of the bilayer are identical. Production of asymmetric liposomes from inverted emulsion was recently studied by Pautot *et al.*[12] and Yamada *et al*.[12,13] In this process, the encapsulated material remains distinct from the hosting buffer, while allowing an asymmetric design.

It is hypothesized that encapsulation of negatively charged oligos (DNA, siRNA) can be enhanced by having cationic lipids in the inner leaflet, while the non-specific cellular uptake of the liposomes can be minimized by constructing the outer leaflet of neutral or slightly negatively charged lipids. The objective of this study is to evaluate the production of these asymmetric liposomes using the inverted emulsion technique for encapsulation of polynucleotides.

2. Materials and Methods

2.1. Materials. Dodecane (Sigma, #D221104), mineral oil (Sigma, #330779), or squalene (Sigma, #S3626) were used as the oil phase. TBS was prepared with 100 mM NaCl (Sigma, S5886) and 5 mM tris base (Promega, #H5131) at pH 7.4. The cargo used to produce the inverse emulsion contained either TBS or dionized water with Alexa Fluor 350 hydrazide sodium salt (Molecular Probes, #A10439) or 21-mer DNA oligo with 5' covalently bound Alexa Fluor 350 or Cy3 (MWG-Biotech) for fluorescent visualization. The 21-mer oligo is used here as a proxy

for the more expensive siRNA, whose delivery is the goal of the overall project. POPC *(*1-palmitoyl-2-oleoyl-sn-glycero-3-phosphocholine), NBD-PC (1-oleoyl-2-[6-[(7-nitro-2-1,3-benzoxadiazol-4-yl)amino]hexanoyl]-sn-glycero-3-phosphocholine), POPS (1-palmitoyl-2-oleoyl-sn-glycero-3-[phospho-L-serine]), NBD-PS (1-oleoyl-2-[6-[(7-nitro-2-1,3-benzoxadiazol-4-yl)amino]hexanoyl]-sn-glycero-3-phospho-L-serine), DOTAP (1,2-dioleoyl-3-trimethylammonium-propane), and DMPC (1,2-dimyristoyl-sn-glycero-3-phosphocholine) lipids were obtained in chloroform from Avanti Lipids. Lyophilized cholesterol was obtained from Sigma (#362794) and chloroform from EM Science (#CX1055-9). Thirty milliliter syringes were obtained from BD (#309650) and 15 mL centrifuge tubes from Corning (#430052). Extrusion was done by a LiposoFast-Basic extruder with polycarbonate membranes (200 nm to 5 μm pore size) from Avestin. Fluorescent quenching was done with sodium hydrosulfite ($Na_2S_2O_4$) (#157953) from Sigma-Aldrich and liposome lysing was done with Triton-X-100 (#BP151) from Fisher Scientific.

2.2. Liposome Formation. Neutral and cationic lipids (DMPC, DOTAP) to comprise the inner leaflet of the asymmetric bilayer were dissolved in oil (dodecane, mineral oil, or squalene) to a concentration of 0.13 to 1.0 mM. The aqueous phase containing the fluorescently-tagged DNA oligo (0.05 to 0.1 mM) and/or Alexa Fluor 350 salt (0.57 to 0.72 mM) were mixed with the oil to form an inverse emulsion with water droplets (0.5-5 volume%) suspended in the continuous oil phase. As the water droplets form, the lipid molecules adsorb at the oil-water interface of the droplets to form a monolayer with their hydrophilic head groups pointed inward and the hydrophobic tails pointed outward. The lipid monolayer helps stabilize the inverse emulsion by reducing droplet coalescence. To control inverse emulsion particle size, the inverse emulsion was sonicated for 10-60 min and then extruded by hand through a polycarbonate membrane of small

pore size (*e.g.* 0.2-5 μm). A second lipid-oil solution, termed the intermediate phase, was prepared separately by dissolving neutral lipids to comprise the outer leaflet of the bilayer (DMPC, POPC with NBD-PC *etc*.) in the same oil used for the inverse emulsion. The intermediate phase was placed on top of an aqueous phase as shown in Figure 1 and allowed to equilibrate. Since the oil is less dense than water, it remains above the aqueous phase. The outer leaflet lipid molecules in the oil phase diffuse from the bulk to the oil-water interface, again forming a monolayer with the heads groups pointed downward and the fatty acid tails pointed upward. The inverse emulsion is then gently poured on top of the intermediate phase (Figure 1). The water droplets slowly fall through the oil phase and approach the oil-water interface owing to their higher density. Upon crossing the interface, the emulsion droplets pick up a second layer of lipid forming a bilayer and transforming the emulsion droplets into unilamellar vesicles.[12] The above process can be hastened by centrifugation.

2.3. Characterization. Surface and interfacial tensions of the pure oils (dodecane and mineral oil) and oil-lipid solutions were measured by either the du Nouy ring or the pendant drop method. The ring method was performed using a Fisher Scientific Surface Tensiometer 20 and was done by measuring the force needed to pass a 6 cm diameter ring through the air-oil interface. The pendant drop method was performed using a Krüss GmbH G10 contact angle measuring instrument by acquiring a time series of images of a pendant drop of TBS submersed into an oil phase. The pendant drop images were analyzed with software from Krüss. The oil viscosity was measured with a Brookfield LVDVII+CP cone and plate viscometer after calibration with a 4.9 cP @ 25 °C standard.

Particle size distribution was measured for both the inverse emulsion and liposome products by dynamic light scattering with a Malvern ZET 5004 (λ = 633 nm) or ALV-5000 (λ = 514.5

nm). Images of the inverse emulsion and liposomes were taken using a horizontally mounted Nikon Optiphot-2 epifluorescence microscope equipped with a QImaging QICAM Fast 12-bit color camera and Prior ProScan II automated stage. For fluorescence detection, NBD-PC lipids (ex: 465 nm, em: 535 nm), Alexa fluor 350 (ex: 345 nm, em: 440 nm), and Cy3 (ex: 553, em: 565) were used.

Measurement of liposome bilayer asymmetry was done by monitoring the intensity of fluorescent NBD-labeled lipids incorporated into only the outer leaflet of the liposome with a SpectraMax Gemini EM microplate spectrofluorimeter from Molecular Devices. Fluorescence quenching of the outer leaflet NBD-labeled lipids was achieved by adding 2 μL of 1 M sodium hydrosulfite to 50 μL liposome product. Sodium hydrosulfite quenches NBD fluorescence by chemically reducing the NO_2 off the NBD ring to an NH_2 group. Inner leaflet quenching was achieved by lysing 50 μL liposome product with 2 μL of 25% v/v of Triton-X-100 in TBS, pH 7.4. Once the liposomes were broken apart, the sodium hyrosulfite was able to access and quench the inner leaflet NBD labeled lipids to further reduce fluorescence intensity.

2.4. Visualization Cell. A visualization cell was designed to allow the observation of falling inverse emulsion particles across an oil-water interface in real-time by an epifluorescence microscope. The visualization cell was designed to fit inside a Corning 50 mL centrifuge tube (26.5 mm inner diameter, #430290). This allows the system to be imaged before and after centrifugation without the need or disruption of extracting samples from the system. In addition, the cell was designed with a temperature controlled water flow-through module to heat or cool the visualization cell to the desired temperature. The system's temperature may be important for the formation of liposomes above or below the transition temperature of the lipids used. Figure 2 provides the schematic of the visualization cell, which is composed of a temperature control

module, an outer frame, and two 22 × 22 mm glass cover slips, and a 1 mm thick U-shaped gasket.

Prior to use, the visualization cell was cleaned with methanol and dried with N_2 gas. A specialized stand was constructed to mount the Nikon Optiphot-2 microscope horizontally on its side. It was necessary to mount the microscope in this way to have a vertical view of the falling inverse emulsion particles from the intermediate phase through the oil-water interface into the aqueous phase.

A 22 gauge hypodermic needle (Nipro, #AH2238) was inserted from the top into the compartment created by the compression of a U-shaped gasket between two cover slips. Attached to the needle was silastic tubing (Dow Corning, #508-006) which delivered Tris Buffered Saline (TBS) or deionized water. The cell was filled approximately half way with aqueous solution. Then a layer of intermediate phase was placed on top of the aqueous phase, filling the cell another third of the way, with a separate 22 gauge hypodermic needle attached to a 5 mL leur-lok tip syringe (BD, #309603). The two phases were allowed to equilibrate for at least 30 min in order for the lipid molecules dissolved in the intermediate phase to align at the oil-water interface. A small amount of inverse emulsion was placed on top of the intermediate phase using a 30 gauge hypodermic needle and 5 mL syringe. Due to the density difference of the inverse emulsion particles and the surrounding oil phase, the particles moved downward towards the intermediate and aqueous phase interface. Sequential images of the falling inverse emulsion particles and their fate were captured as the particles contacted the interface.

The desired liposome size for drug delivery is about 200 nm or less, but these small particles sediment very slowly (without centrifugation) and are too small to visualize. Therefore, the visualization experiments were conducted with larger particles (> 1μm). The gravitational /

interfacial force ratio changes with particle size. The transport of larger inverse emulsion particles through the oil-water interface is not identical to those of smaller particles, but it provides some insight about the transport process.

3. Results and Discussion

3.1. Inverse emulsion. The first step in making asymmetric lipid bilayer vesicles is to produce an inverse emulsion consisting of an oil-lipid solution with encapsulated aqueous droplets of the polynucleotides of interest (DNA, siRNA, plasmid, *etc.*). Figure 3, shows an inverse emulsion prepared in dodecane (C_{12}) with 94.0 μM POPC (neutral), 100.0 μM DOTAP (cationic), 2.1 μM NBD-PC (neutral fluorescent lipid), and extruded at 5000 nm with 1.25 v/v% aqueous droplets containing 37.0 μM non-fluorescent 21-mer DNA oligo, 37.0 μM Cy3-tagged 21-mer DNA oligo, and 457.0 μM Alexa Fluor 350 salt. The images in the figure correspond to the inverse emulsion layer shown in Figure 1, taken within 30 min of emulsion preparation. The lipid layer covering the particles is illuminated by the NBD-PC, as observed in the top image. The amount of NBD-lipid was chosen to maximize fluorescence intensity while avoiding self-quenching.[14] The aqueous core is illuminated by the addition of Alexa Fluor 350 salt, as observed in the middle image. Lastly, the polynucleotide cargo is observed in the bottom image by the encapsulation of Cy3-tagged 21-mer DNA oligo. The white arrows illustrate an inverse emulsion particle present in all three images.

Similar inverse emulsion results were observed for both mineral oil (mainly C_{15}-C_{40}) and squalene ($C_{30}H_{50}$), a branched hydrocarbon, indicating that inverse emulsion can be easily and consistently produced to contain an outer lipid layer and encapsulate a polynucleotide (negatively charged) cargo. However a wide distribution of particle size is also observed as

demonstrated in the images by the scale bar in Figure 3. This is due to coalescence of the inverse emulsion particles and is discussed later in this article.

3.2. Liposome Products Using Dodecane and Mineral Oil. A dodecane intermediate phase was prepared with 211.0 μM DMPC (neutral) and 2.1 μM NBD-PC (neutral fluorescent lipid) and placed on top of an aqueous TBS solution to allow the lipids to align at the oil-water interface as depicted in Figure 1. An equilibration time of 1.5 hr was used as suggest by Pautot *et al.*[12,15] to allow the interface to become saturated with lipids. Next, an inverse emulsion phase was prepared with 205.0 μM DOTAP (cationic) and 2.1 μM NBD-PC (neutral fluorescent lipid) and contained 2.1 v/v% aqueous cargo of 80 μM Cy3-tagged 21-mer DNA oligo and 716.0 μM Alexa Fluor 350 salt. The inverse emulsion was extruded through a 1000 nm membrane, then directly placed on top of the intermediate phase and centrifuged at 115 × *g* for 30 min to form liposomes.

Fluorescent images of the liposome products, which are contained in aqueous TBS, are shown in Figure 4. The images in the figure correspond to the asymmetric lipid bilayer vesicle at the bottom of Figure 1. The top image in Figure 4 shows the placement of NBD-PC lipids in the liposomes' bilayer. The middle image shows the encapsulation of the aqueous cargo, Alexa Fluor 350, used to form the inverse emulsion. The bottom image shows the placement of the Cy3-tagged DNA oligo. The white circles mark the only particles that exhibit a lipid membrane, aqueous core, and DNA oligo encapsulation. Similar results were observed using a mineral oil.

Several conclusions can be drawn from Figure 4. First, the majority of the lipid vesicles in the top image do not contain a detectable amount of Alexa Fluor 350 as shown in the middle image. It is possible, as suggested by Yamada *et al.*, that multi-lipid-layer inverse emulsion particles containing an oil interior are forming in the inverse emulsion phase.[13] As these

undesired particles cross the intermediate and aqueous phase interface, they shed a lipid layer to release a vesicle that does not contain the intended aqueous core. It is also possible that perturbations (perhaps caused by impinging inverse emulsion particles) at the intermediate and aqueous phase interface could cause monolayer or multi-layer vesicles to pinch off, again producing undesired vesicle products that could contain an oil interior. Pautot *et al.*[15] report that aqueous-oil interfaces such as with dodecane and POPC or POPS can spontaneously form water-in-oil or oil-in-water particles by the swelling of lipid liquid-crystalline structures at oil-water interfaces. Such formation of undesired particles could produce liposomes that contain NBD lipids but not the intended cargo. Rather they would contain aqueous phase from the bottom aqueous layer. Second, the total number of liposome particles observed is less than the total number of inverse emulsion particles produced (Figure 3), which suggests that not all of the inverse emulsion particles were converted into liposomes. Third, the bottom image shows a large number of Cy3-tagged DNA oligo particles across the view field. This distribution does not correspond to lipid vesicles in the top image nor the encapsulated Alexa Fluor 350 in the middle image. This indicates that the intended cargo inside the inverse emulsion particles was released into the bottom aqueous phase during transport through the aqueous phase-intermediate phase boundary. In order to increase cargo encapsulated liposome yield, which is necessary for this process to be competitive with conventional liposome production techniques, the limiting factors must be identified, investigated, and overcome.

3.3. Comparison of Dodecane and Squalene Liposome Products. Many attempts were made to form liposomes from inverse emulsions, but all resulted in extremely low yields with the majority of the cargo unencapsulated and free floating in solution (see Figure 4). These attempts included changing the lipid concentration in the inverse emulsion and intermediate phase from

0.13 to 1 mM, adding cholesterol to increase lipid layer stability, varying the temperature from 20 to 50 °C (transition temperature of various lipids), removing salt from the aqueous core, and changing the oil type. The only parameter that noticeably affected the efficiency of liposome formation was the oil. Liposome yield was highest using squalene.

The following experiment was done using squalene as the oil. The inverse emulsion contained 113.0 μM POPC, 20.5 μM DOTAP, 1.3 μM NBD-PC, and 0.6 v/v% aqueous droplets containing Alexa Fluor 350 salt and was extruded at 200 nm. The intermediate phase contained 125.0 μM POPC and 1.4 μM NBD-PC. Fluorescent images of the liposome products were acquired after centrifugation and are shown in Figure 5. The top image shows the placement of the NBD lipids, the middle image shows the encapsulation of the Alexa Fluor 350 salt, and the bottom image shows liposomes that appear in *both* the top and middle images. Similar to the images of the dodecane system shown in Figure 4, there are a number of particles that contain NBD lipids in the top image which do not appear to contain the Alexa Fluor 350 salt cargo, as shown in the middle image. However, there are a larger number of liposomes that contain NBD lipids and Alexa Fluor cargo as indicated by the number of white circles outlining liposomes that appear in all three images in the figure.

To confirm that squalene produces higher yields, five images were randomly acquired from the dodecane and squalene systems for both the liposomes and the inverse emulsions they derived from. The number of particles in each image was counted (per mm^2 of image area) and shown in Table 1. For comparison, the values for the number of lipid vesicles and number of encapsulated vesicles were obtained by dividing the counted particles by the appropriate dilution factor of converting 100 μL of inverse emulsion to 2 mL of liposome product. For both the dodecane and squalene systems, over three times as many lipid vesicles are produced than

emulsion particles. This result further supports that undesired or unintentional particles are being formed as discussed above by the formation of oil-in-water droplets at the intermediate and aqueous phase interface either spontaneously or by perturbations caused by the impingement of accelerated inverse emulsion particles at the interface. Of the particles counted in the liposome products, 5% or less were observed to encapsulate the intended Alexa Fluor cargo. Squalene had a higher inverse emulsion to liposome conversion of 18.2% compared to dodecane at 13.9%. Such a low yield in either oil system must be improved for this technique to be a viable way a producing therapeutic quantities of polynucleotide encapsulated liposomes.

The formation of inverse emulsion particles and the acceleration of these particles through an oil-water interface is dependent on the fluid and interfacial properties of the system. The terminal velocity of an inverse emulsion particle under acceleration can be modeled from Stokes' Law,

$$v_t = (\rho_a - \rho_o)\frac{d_p^2 \omega^2 r_c}{18\mu_o}, \tag{1}$$

where $(\rho_a - \rho_o)$ is the density difference between the oil and aqueous inverse emulsion particle, d_p is the diameter of the inverse emulsion particle, ω is the rational speed of the centrifuge, r_c is the length of the centrifuge arm, and μ_o is the viscosity of the oil. The terminal velocity, and hence the force at which the inverse emulsion particle impinges on the oil-water interface, is dependent on the oil's density and viscosity, as well as the rational speed of the centrifuge. The interfacial tension at the interface also affects how the inverse emulsion particle passes through it. The density, viscosity, surface tension, and interfacial tension, with or without 113.0 μM POPC and 20.5 μM DOTAP, of the dodecane and squalene systems were measured and are shown in Table 2.

The oil density and viscosity affect the terminal velocity of the inverse emulsion particle, but can be compensated for by adjusting the rotational speed of the centrifuge. The interfacial tension cannot be compensated for and is a function of oil type, lipid concentration, and temperature. Higher interfacial tension creates an interface that is more rigid and less elastic than lower interfacial tension. The time evolution of the interfacial tension between TBS and dodecane or squalene containing 113.0 μM POPC and 20.5 μM DOTAP at room temperature is shown in Figure 6. The first data point of both series was measured separately in the absence of lipids. As the lipid surface concentration increases, the interfacial tension decreases, changing the shape of the droplet. Therefore, the interfacial tension (remaining data points) decreases over time as the POPC and DOTAP lipids diffuse and absorb to the interface of the droplet. The dodecane data agrees well with Pautot *et al.*'s results of a similar system.[15] The time evolution of the interfacial tension of squalene shows that it has a lower interfacial tension and that it reaches equilibrium faster than with dodecane.

Squalene may have a higher liposome yield compared to dodecane because of its lower interfacial tension and higher viscosity. As an inverse emulsion particle contacts the second oil-water interface, the interface may bend more readily around the inverse emulsion particle if the interfacial tension is lower. Increase in oil viscosity may increase the residence time of the inverse emulsion particle passing through it. An increase in residence time would increase the outer lipid leaflet coverage by the second oil-water interface and increase the likelihood of a bilayer liposome forming. Therefore the efficiency of liposome production from inverse emulsion can be improved by using oils that achieve low interfacial tension and high viscosity. To further study the interactions at the intermediate and aqueous phase interface, a fluorescent microscopy visualization cell was developed.

3.4. Visualization Cell. A visualization cell for fluorescent image microscopy was designed to observe the conversion of inverse emulsion particles as they move in real-time across the oil-water interface in order to identify the cause of the low conversion yield. An experiment was done in which inverse emulsion, composed of 300.0 μM POPC (neutral) and 3.0 μM NBD-PC (neutral fluorescent lipid) in mineral oil with 0.57 mM Alexa Fluor 350 salt as the aqueous cargo, was placed into the visualization cell on top of already equilibrated intermediate and aqueous phases. The intermediate phase was compositionally identical to the inverse emulsion but without cargo. The visualization experiments were done with relatively large (> 1 μm) particles because smaller particles remain suspended and tend not to move towards the oil-water interfacial under gravitational forces.

Real-time fluorescent images of an inverse emulsion particle as it moved across the oil-water interface are shown in Figure 7. The first image of the sequence shows the inverse emulsion particle (IEP) in the intermediate phase (IP) above the oil-water interface, which appears as a dark region in the middle of the image. Below the interface is the bottom aqueous phase (AP). Over the course of approximately 40 seconds, the inverse emulsion particle traveled 225 μm where it met the interface. As the particle pressed against the interface, it deformed until its lipid monolayer fused with the interface, causing the particle to rupture instead of passing through the interface to form a bilayer liposome vesicle. Not all of the observed inverse emulsion particles fused with the interface. Some particles passed through the interface and many remained stationary at interface and did not pass through (or fuse with it) within 30 min of observation.

Inverse emulsion particle fusion with the intermediate and aqueous phase interface was observed under a variety of conditions, including: the use of 0.13-1.0 mM lipid concentration in both the inverse emulsion and intermediate phases; the use of dodecane, mineral oil, or squalene

as the oil; the addition of cholesterol (0.17 mM) to both oil phases to increase stability; and varying the temperature of the system from 20-50°C to be below or above the transition temperature of the lipid membrane system.

To test if the electrostatic interaction of negatively charged DNA oligo and the positively charged inner leaflet of lipids would increase the stability of the inverse emulsion particles, an experiment was done using a combination of DOTAP (cationic) and DMPC (zwitterionic, but neutral at pH 7.4) in the inverse emulsion with Alexa Fluor 350-tagged DNA oligo as the cargo. The intermediate phase was solely composed of DMPC. However, imaging with the visualization cell again showed membrane fusion rather than bilayer formation. This suggests that the electrostatic interactions are not sufficient enough to stabilize the large inverse emulsion particles to the extent necessary to remain intact as they pass through the oil-water interface.

3.5 Liposome Bilayer Asymmetry. To demonstrate asymmetry in the formed liposomes an experiment was done in which fluorescently asymmetric liposomes were produced with NBD-PC in only the outer leaflet. Sodium hydrosulfite (1 M $Na_2S_2O_4$ in TBS, pH 9.9) was added, as shown in Figure 8, to the fluorescently asymmetric liposomes and the fluorescence was quenched $>$ 80% by chemical reduction of the NBD group.[16] This demonstrates at least 80% asymmetry and is in agreement with Pautot *et al*. results.[17] After the outer leaflet was quenched, Triton-X-100 was added to lyse the liposomes to allow the sodium hydrosulfite to react with any NBD labeled lipids in the inner leaflet. The fluorescence intensity was reduced another 16% indicating that a small fraction of the outer leaflet NBD-PC lipids were incorporated into the inner leaflet.

3.6. Stability of Inverse Emulsion and Liposome Products using DLS. It is important to know the size stability of the inverse emulsion because it is the base component from which the

asymmetric liposomes are constructed. If the size distribution of the inverse emulsion changes before passage through the second oil-water interface, then the formed liposomes would not have the desired size distribution. Dynamic light scattering (DLS) experiments were done to quantify the stability of inverse emulsion and asymmetric liposome products over a week.

Inverse emulsion in squalene was prepared using with 113.0 μM POPC, 20.5 μM DOTAP, 1.3 μM NBD-PC, 0.6 v/v% aqueous droplets, and was extruded at 200 nm. The inverse emulsion size distribution was immediately analyzed by DLS. The results showed monodisperse distributions as shown in Figure 9 for freshly extruded inverse emulsion. However, the distributions indicate the mean radius of the freshly extruded inverse emulsion is about half that expected from a 200 nm diameter extrusion. This suggests that other factors besides extrusion membrane pore size influence inverse emulsion size. Such factors may include extrusion pressure, oil viscosity, or number of passes. The consistent and reliable production of monodisperse and desired size inverse emulsion is currently under investigation.

The inverse emulsion was analyzed by DLS over a time of 100 hr. During this period it was kept at room temperature. The time-elapsed size stability results are shown in Figure 10. The mean radius of the inverse emulsion increased rapidly from 56.4 nm to 458.8 nm after 24 min, then decreased to 211.5 nm after 1 hr and eventually tended toward zero after 100 hr. This trend might be explained by coalescence and settling velocity. After extrusion, the inverse emulsion particles began to coalesce. The coalescences of the inverse emulsion particles increased the mean radius as measured by DLS. The inverse emulsion particles continued to increase in size as did their settling velocity (see Equation 1). After approximately 30 min after extrusion, coalesced inverse emulsion particles began to fall out of the DLS sample volume as defined by the incident laser light on the sample. Therefore a decrease in inverse emulsion size was observed. The

process continued until all of the suspended inverse emulsion particles coalesced and settled to the bottom of the cuvette as evidenced by the nearly zero mean radius after 100 hr. In order for the size controlled production of asymmetric liposomes from inverse emulsion, extruded inverse emulsion must be converted to bilayer liposomes as soon as possible (< 1 min) to avoid coalescence.

Liposomes were prepared immediately after extrusion from the inverse emulsion described above. The intermediate phase used to produce the liposomes was composed of squalene with 125.0 μM POPC and 1.4 μM NBD-PC. Interestingly, the liposome product produced a trimodal distribution as shown in Figure 11. The first and most prominent mode has a mean radius of 44 nm followed by a mode of 188 nm and 489 nm. The three modes suggest, as did previous image data above, that various populations of lipid vesicles are forming, some of which are not the intended product. In terms of size stability however, the three modes remain relatively constant over a 160 hr period (Figure 12), especially in comparison to the stability of the inverse emulsion (Figure 10). The increased liposome stability is expected because the lipid bilayer vesicles are thermodynamically more stable than lipid monolayer inverse emulsions. In order to produce a viable and therapeutic asymmetric liposomal delivery vector for polynucleotides, the end product must have an adequate shelf-life. Longer time periods are currently being investigated to fully characterize shelf-life.

4. Conclusions

Production of liposomes from inverse emulsion allows the design and construction of compositionally different (asymmetric) inner and outer leaflets of the lipid bilayer liposome. Contrary to conventional liposome production techniques, this is done by independently forming each leaflet, one at a time, around an aqueous cargo by the use of oil-water interfaces. Inverse

emulsion particles can be produced with a lipid coating and an aqueous core encapsulating a 21-mer DNA oligo polynucleotide cargo. Monodisperse inverse emulsion can be consistently made, but quickly undergoes coalescence to increase mean particle size by an order of magnitude within 30 min of extrusion. Therefore, freshly extruded inverse emulsion must immediately be used if a controlled liposome size distribution is desired.

A low yield was observed for inverse emulsion to liposome conversion with this technique, especially using the unbranched hydrocarbons dodecane (C_{12}) and mineral oil (mainly C_{15}-C_{40}) as the lipid solvent. The yield is higher with squalene as the oil. Presumably because squalene has a significantly higher viscosity and lower interfacial tension than dodecane, which may increase stability as droplets pass through the interface. The asymmetry of liposomes was demonstrated with a fluorescence quenching assay.

To investigate the low conversion of the inverse emulsion as it passed through the intermediate and aqueous phase interface, a fluorescent microscopy visualization cell was built and used to observe the conversion in real-time. It was observed that large inverse emulsion particles (> 1 μm) settle at the intermediate and aqueous phase interface, deform, and often fuse with the outer leaflet lipids already aligned at the interface. When this occurs the aqueous interior core of the inverse emulsion particle is released into the bulk of the bottom aqueous phase. Inverse emulsion particle fusion was seen under various conditions, including the use of dodecane, mineral oil, and squalene (branch hydrocarbon) as the oil phase, addition of cholesterol, and at temperatures above and below the lipid membrane transition temperature.

Smaller inverse emulsion particles (< 1 μm) may remain intact as they pass through the intermediate and aqueous interface. Visualization of these smaller particles in the visualization

cell is challenging because the particles do not move under the influence of gravity. Other methods of acceleration are being investigated.

Although most of the inverse emulsion particles are not converted to liposomes, some are. The liposome product had a trimodal size distribution, which remained relatively stable over a 160 hr period.

Acknowledgment. This research program is a collaboration among the University of Houston, Baylor college of Medicine, and Texas Children's Liver Center and was supported by the Alliance for Nanohealth with a grant from the Department of Defense.

Supporting Information. We have included a movie version of the Figure 7 that shows an inverse emulsion particle coalescing with the bottom aqueous phase at the interface. This information is available free of charge via the Internet at http://pubs.acs.org.

References

1. Bangham, A. D.; Horne, R. W., Negative Staining of Phospholipids and Their Structural Modification by Surface-Active Agents as Observed in the Electron Microscope. *J Mol Biol* **1964,** 8, 660-8.
2. Kawakami, S.; Munakata, C.; Fumoto, S.; Yamashita, F.; Hashida, M., Novel galactosylated liposomes for hepatocyte-selective targeting of lipophilic drugs. *J Pharm Sci* **2001,** 90, (2), 105-13.
3. Papahadjopoulos, D.; New York Academy of Sciences., *Liposomes and their uses in biology and medicine*. New York Academy of Sciences: New York, 1978; p 462 p.
4. Roy, M. T.; Gallardo, M.; Estelrich, J., Bilayer distribution of phosphatidylserine and phosphatidylethanolamine in lipid vesicles. *Bioconjug Chem* **1997,** 8, (6), 941-5.

5. Phayre, A. N.; Vanegas Farfano, H. M.; Hayes, M. A., Effects of pH Gradients on Liposomal Charge States Examined by Capillary Electrophoresis. *Langmuir* **2002,** 18, (17), 6499-6503.
6. Bohl Kullberg, E.; Bergstrand, N.; Carlsson, J.; Edwards, K.; Johnsson, M.; Sjoberg, S.; Gedda, L., Development of EGF-conjugated liposomes for targeted delivery of boronated DNA-binding agents. *Bioconjug Chem* **2002,** 13, (4), 737-43.
7. Roux, E.; Lafleur, M.; Lataste, E.; Moreau, P.; Leroux, J. C., On the characterization of pH-sensitive liposome/polymer complexes. *Biomacromolecules* **2003,** 4, (2), 240-8.
8. Graff, A.; Winterhalter, M.; Meier, W., Nanoreactors from Polymer-Stabilized Liposomes. *Langmuir* **2001,** 17, (3), 919-923.
9. Pysher, M. D.; Hayes, M. A., Examination of the Electrophoretic Behavior of Liposomes. *Langmuir* **2004,** 20, (11), 4369-4375.
10. Otake, K.; Shimomura, T.; Goto, T.; Imura, T.; Furuya, T.; Yoda, S.; Takebayashi, Y.; Sakai, H.; Abe, M., Preparation of Liposomes Using an Improved Supercritical Reverse Phase Evaporation Method. *Langmuir* **2006,** 22, (6), 2543-2550.
11. Ishii, F.; Takamura, A.; Ishigami, Y., Procedure for preparation of lipid vesicles (liposomes) using the coacervation (phase separation) technique. *Langmuir* **1995,** 11, (2), 483-486.
12. Pautot, S.; Frisken, B. J.; Weitz, D. A., Production of unilamellar vesicles using an inverted emulsion. *Langmuir* **2003,** 19, (7), 2870-2879.
13. Yamada, A.; Yamanaka, T.; Hamada, T.; Hase, M.; Yoshikawa, K.; Baigl, D., Spontaneous transfer of phospholipid-coated oil-in-oil and water-in-oil micro-droplets through an oil/water interface. *Langmuir* **2006,** 22, (24), 9824-8.
14. Chattopadhyay, A., Chemistry and biology of N-(7-nitrobenz-2-oxa-1,3-diazol-4-yl)-labeled lipids: fluorescent probes of biological and model membranes. *Chem Phys Lipids* **1990,** 53, (1), 1-15.
15. Pautot, S.; Frisken, B. J.; Cheng, J.-X.; Xie, X. S.; Weitz, D. A., Spontaneous Formation of Lipid Structures at Oil/Water/Lipid Interfaces. *Langmuir* **2003,** 19, (24), 10281-10287.
16. McIntyre, J. C.; Sleight, R. G., Fluorescence assay for phospholipid membrane asymmetry. *Biochemistry* **1991,** 30, (51), 11819-27.

17. Pautot, S.; Frisken, B. J.; Weitz, D. A., Engineering asymmetric vesicles. *Proc Natl Acad Sci U S A* **2003,** 100, (19), 10718-21.
18. Ahmed, F.; Discher, D. E., Self-porating polymersomes of PEG-PLA and PEG-PCL: hydrolysis-triggered controlled release vesicles. *J Control Release* **2004,** 96, (1), 37-53.
19. Temming, K.; Schiffelers, R. M.; Molema, G.; Kok, R. J., RGD-based strategies for selective delivery of therapeutics and imaging agents to the tumour vasculature. *Drug Resist Updat* **2005,** 8, (6), 381-402.
20. Ochsenhirt, S. E.; Kokkoli, E.; McCarthy, J. B.; Tirrell, M., Effect of RGD secondary structure and the synergy site PHSRN on cell adhesion, spreading and specific integrin engagement. *Biomaterials* **2006,** 27, (20), 3863-74.

Table 1. Image analysis of inverse emulsion and asymmetric liposome products. Fluorescent images were captured of inverse emulsion and liposomes and the number of particles in each images was counted.

	# of Inverse Emulsion Vesicles (per mm^2)	**# of Lipid Vesicles** (per mm^2)	**# of Alexa Fluor Encapsulated Vesicles** (per mm^2)	**Encapsulated Liposome Yield**
Dodecane	2,547	8,680	355	13.9%
Squalene	3,582	13,006	651	18.2%

Table 2. Density, viscosity, surface tension, and interfacial tension of dodecane and squalene. Variations are standard error with $n \geq 4$. [a] Measurement done by du Nouy ring method. [b] Measurement done by the pendant drop method. [c] Measurement done by the pendant drop method using time evolution up to 90 min and lipid concentrations of 113.0 μM POPC and 20.5 μM DOTAP.

	Density (g/cm^3)	**Viscosity** (cP)	**Surface Tension** [a] (dynes/cm)	**Interfacial Tension No Lipids** [b] (dynes/cm)	**Interfacial Tension with Lipids** [c] (dynes/cm)
Dodecane	0.856	1.1 ± 0.1	25.3 ± 0.08	44.5 ± 1.3	18.4 ± 1.1
Squalene	0.748	11.0 ± 0.2	32.2 ± 0.04	31.9 ± 1.6	6.9 ± 1.1

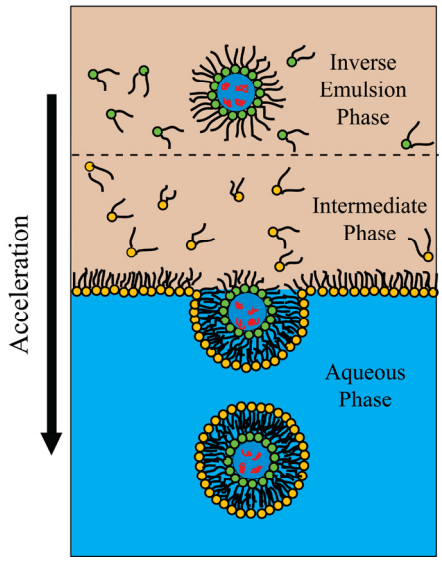

Figure 1. A sketch of asymmetric liposome production from inverse emulsion. The inverse emulsion phase (top layer) is an oil-lipid solution with suspended aqueous droplets containing polynucleotides. The intermediate phase (middle layer) is also an oil-lipid solution, but with a different lipid. The lipids in this phase align at the interface with the bottom aqueous phase layer. The aqueous phase is where the final asymmetric liposomes are produced. An acceleration is applied to move the lipid-coated inverse emulsion particles through the intermediate phase and the aqueous interface to collect the outer leaflet of lipids to form lipid bilayer vesicles.

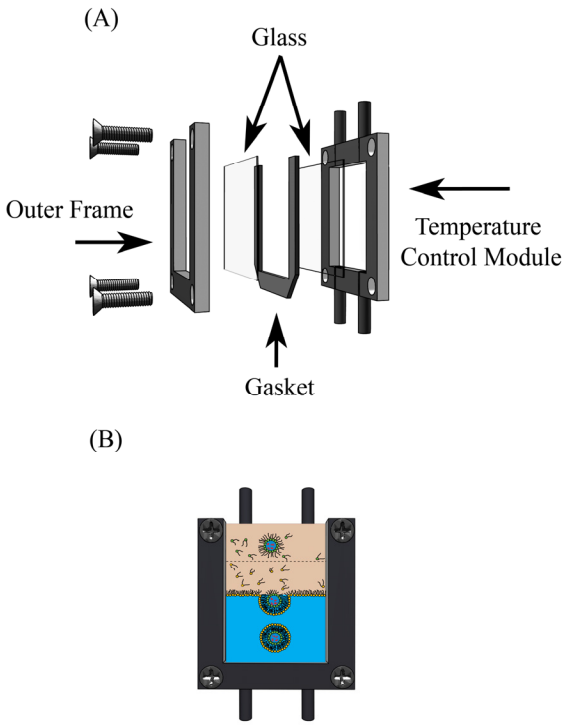

Figure 2. Visualization cell schematic. (A) Three dimensional expanded view. The cell is composed of two glass cover slips separated by a U-shaped gasket. The assembly is compressed together by an outer frame and the temperature control module. Water is circulated through the temperature control module. (B) Assembled view of the visualization cell with sample.

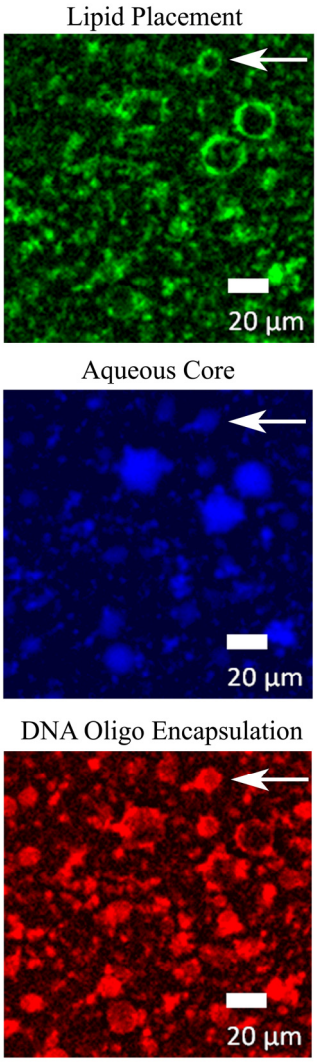

Figure 3. Fluorescent images of the same view field of inverse emulsion containing fluorescent markers. Top: Fluorescence indicates placement of NBD-PC in lipid leaflet; Middle: Fluorescence indicates encapsulated Alexa Fluor 350 Salt; Bottom: Fluorescence indicates encapsulation of Cy3-tagged 21-mer DNA oligo. The arrows indicate an inverse emulsion particle present in all three images. This inverse emulsion was extruded at 5000 nm.

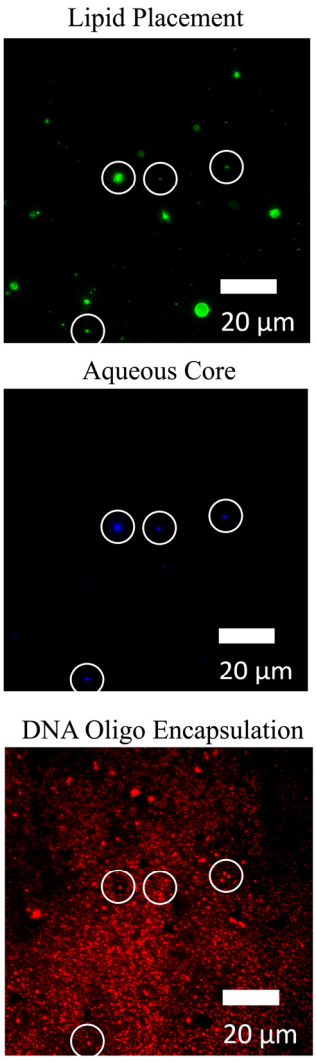

Figure 4. Fluorescent images of the same view field of asymmetrically produced liposomes from dodecane. Top: Fluorescence indicates placement of NBD-PC in a lipid leaflet; Middle: Fluorescence indicates encapsulated Alexa Fluor 350 Salt; Bottom: Fluorescence indicates encapsulation of Cy3-tagged 21-mer DNA oligo. The white circles indicate liposomes containing all three fluorescent markers. The inverse emulsion for these liposome products was extruded at 1000 nm.

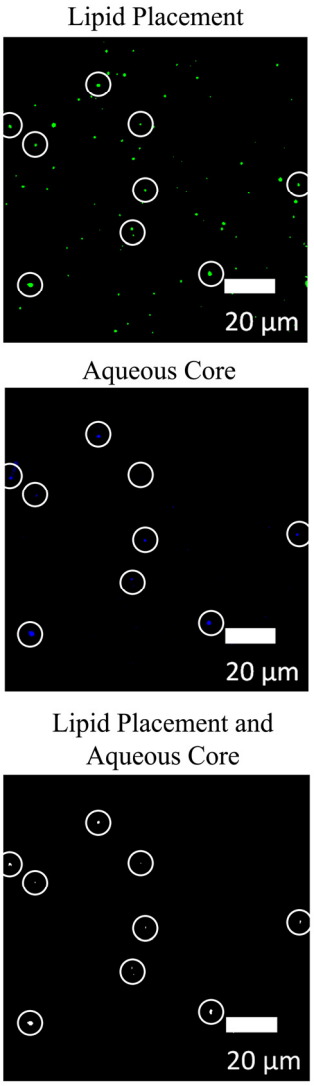

Figure 5. Fluorescent images of the same view field of asymmetrically produced liposomes from squalene which contain fluorescent markers. Top: Fluorescence indicates placement of NBD-PC in a lipid leaflet; Middle: Fluorescence indicates encapsulated Alexa Fluor 350 Salt; Bottom: White dots indicate the liposomes that show *both* NBD and Cy3 fluorescence. The bottom image is a product of the top two images. The white circles indicate liposomes present in all three images. The inverse emulsion for these liposome products was extruded at 200 nm.

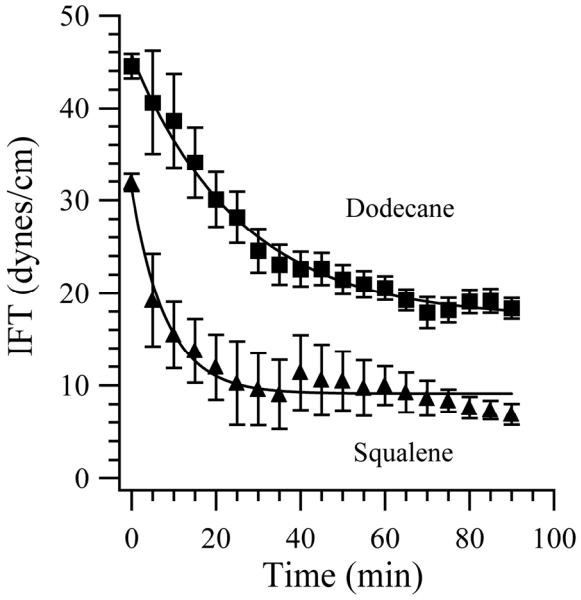

Figure 6. Time evolution of the interfacial tension of an aqueous pendant drop in oil-lipid solutions. Dodecane and squalene solutions contained 113.0 μM POPC and 20.5 μM DOTAP. The measurements were done at room temperature and at least in triplicate. The error bars represent standard error.

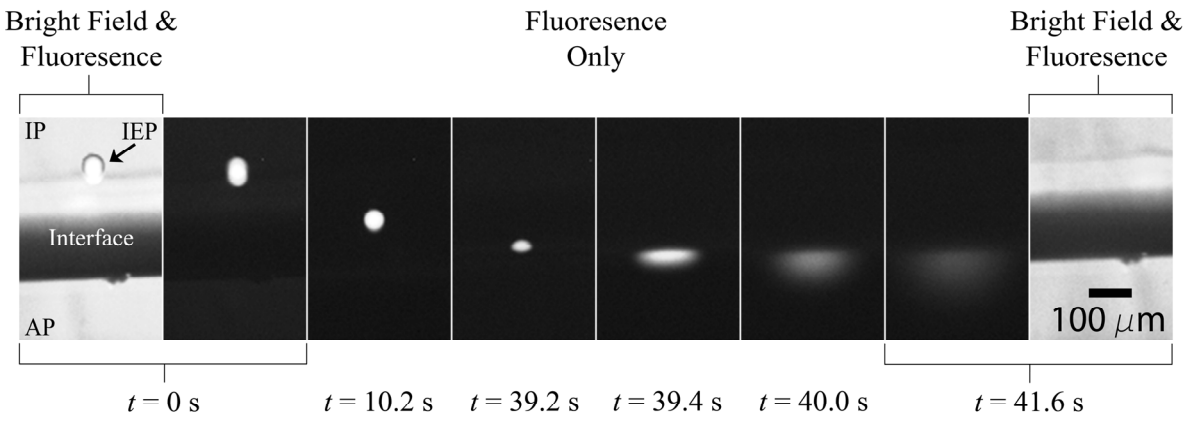

Figure 7. Time series of an inverse emulsion particle containing Alexa Fluor 350 hydrazide sodium salt (570.0 μM) as it fuses with the intermediate phase (IP) and aqueous phase (AP) interface to release its contents into the aqueous phase. Inverse emulsion and intermediate phases were made with POPC (0.3 mM) and NBD-PC (2.0 μM) in mineral oil. The first and last images are simultaneous bright field (BF) and fluorescence light (FL) images of the image adjacent to it. The remaining images are solely fluorescence light (FL) images of Alexa Fluor 350 within the inverse emulsion particle.

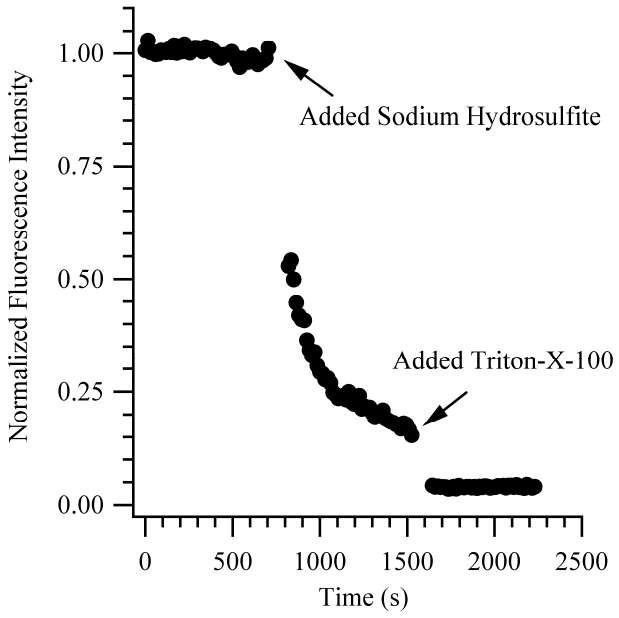

Figure 8. Fluorescence quenching of asymmetrically produced liposomes (with NBD-PC in only the outer leaflet) with 1 M sodium hydrosulfite ($Na_2S_2O_4$). After quenching, the liposomes were lysed with Triton-X-100 (1.25 v/v) and any remaining fluorescence was quenched. Liposomes were produced with 15 mol% DOTAP and 85 mol% POPC in the inner leaflet and 99 mol% POPC and 1 mol% NBD-PC in the outer leaflet. Inverse emulsion was extruded at 200 nm diameter.

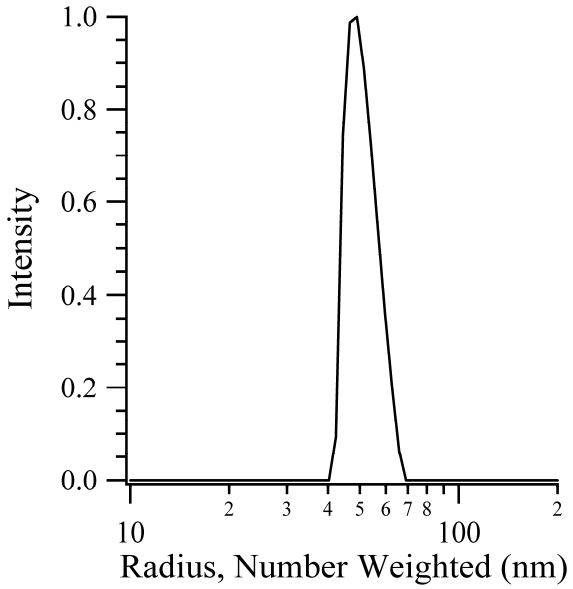

Figure 9. Particle size distribution (from DLS) of inverse emulsion immediately after extrusion at 200 nm. The inverse emulsion was prepared using with 113.0 μM POPC, 20.5 μM DOTAP, 1.3 μM NBD-PC, and 0.06 v/v% aqueous droplets.

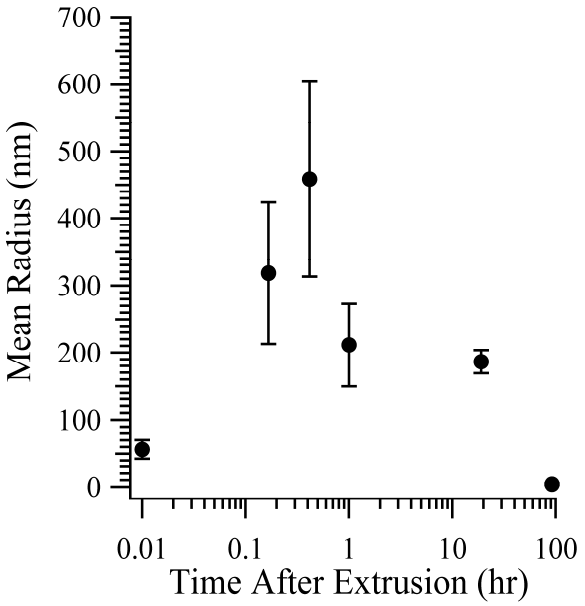

Figure 10. Time evolution of mean particle size in the inverse emulsion, which was prepared using with 113.0 μM POPC, 20.5 μM DOTAP, 1.3 μM NBD-PC, and 0.06 v/v% aqueous phase. Error bars represent standard error of replicate readings of the same sample.

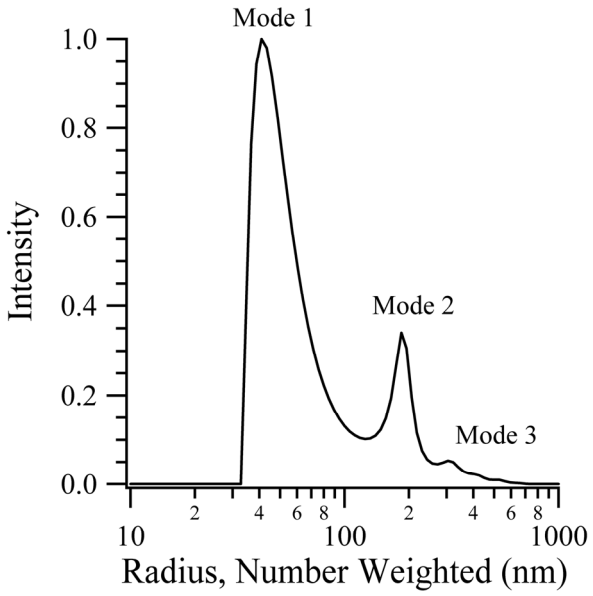

Figure 11. Particle size distribution (from DLS) of liposomes immediately after formation using inverse emulsion extruded at 200 nm. The inverse emulsion was prepared using with 113.0 μM POPC, 20.5 μM DOTAP, 1.3 μM NBD-PC, and 0.06 v/v% aqueous phase. Intermediate phase was prepared with squalene using 125.0 μM POPC and 1.4 μM NBD-PC.

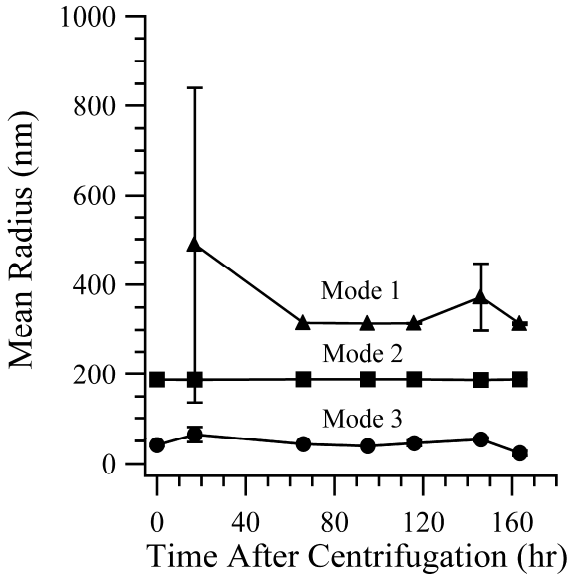

Figure 12. Time evolution of liposome size. The three data series represent the three modes observed in Figure 11.

TOC Graphic.

Nanorods-mediated gene therapy in bladder cancer

Liana Adam, PhD (M.D. Anderson Cancer Center)
Jason Hafner, PhD (Rice University)

Manuscripts submitted

B. C. Rostro, K. M. Mayer, S. Lee, C. M. Payne, E S. Day, L.R. Bickford, L Adam, C. Dinney, T Zal, R.A. Drezek, J.L. West and J. H. Hafner. Covalent Stabilization and Targeting of Surfactant-Synthesized Gold Nanorods. *Manuscript submitted to Chemical Bioconjugates Journal.*

L. Adam, M. Zhong, W. Choi, M. Nicoloso, G. Calin, D. McConkey, M. Bar-Eli, and C. Dinney. miR-200c Expression Regulates Epithelial to Mesenchymal Transition in Bladder Cancer Cells and Reverses Resistance to EGFR Therapy. *Manuscript submitted to Clinical Cancer Research.*

A third manuscript derived from the abstract presented at AACR, please see below, is currently in preparation.

Patents

Liana Adam, MD, Invention Disclosure Report (IDR) submitted to the office of technology and commercialization UT-MD Anderson CC, entitled: A Programmed non-viral delivery of genetic material as a new treatment modality in cancer, United States, Pending.

Abstracts

Adam L, Zhong BC, Rostro B, McIntyre J, McGinnis J, Hafner LE, Dinney CPN. Safe and efficient delivery of non-coding RNAs in bladder cancer cells using near-infra-red irradiated gold nanorods. American Association of Cancer Research (AACR). e-Pub 4/2008.

Magnetic Drug-Loaded Nanoparticles for Targeted Therapy

Jim Klostergaard, PhD (M.D. Anderson Cancer Center)
Joan Bull, MD (UT Health Science Center at Houston)
David Gorenstein, PhD (University of Texas Medical Branch)

A) Introduction

Breast cancer is the most common cancer in women in the U.S. Although combination chemotherapy improves survival in some metastatic breast cancer patients, this disease is generally currently incurable and new treatment approaches are needed. A subtype of breast cancer, inflammatory breast cancer (IBC), currently has no novel therapeutic options and has high rates of recurrence after conventional treatment. Both drug-resistance and inadequate drug delivery to the tumor have been proposed to contribute to this dilemma. The use of magnetically-vectorable, drug-loaded nanoparticles (NP) is proposed to be capable of achieving superior tumor pharmacokinetics compared to that of free drugs as currently practiced. The initial clinical presentation of IBC is superficial, in the skin, and the skin is known to harbor residual disease as it is the primary site of loco-regional recurrence after maximal therapy. The proposed approach using magnetic vectoring of magnetically-responsive NPs (MNPs) would exploit this superficial presentation, accessible to the required magnetic field strengths and gradients inherent in currently available permanent magnets: thus, being translatable to clinical application if validated pre-clinically.

Macromolecular drug delivery systems have been developed as one approach to overcome drug resistance and improve drug therapeutic index. Such polymeric drug conjugates are internalized by endocytosis, resulting in lysosomal accumulation and release of drug from polymer (activation). Drug copolymers may have key advantages over free drugs, including reduced toxicity. High plasma Cmax values and rapid extravasation, which contribute to the toxicity of free drugs, should be largely abrogated with copolymer prodrugs, whose size limits diffusion rates. However, the enhanced permeability and retention (EPR) effect should still allow copolymer accumulation and retention within the tumor interstitium, followed by prodrug activation. These pharmacological principles also generally apply to NP drug carriers, whether serving as components of prodrugs or simply requiring degradation at the tumor.

NPs hold several potential advantages over other carriers for drug delivery to tumors. Drugs with diverse physical-chemical properties can be incorporated, depending on the matrix or linker chemistry selected. In addition, NPs tend to have markedly higher drug loading capacities than other delivery systems. The drug payload can be embedded in matrices whose physical-chemical properties dictate the characteristics of drug release. Finally, NP surfaces can be easily modified with targeting ligands, such as the anti-CD44 thioaptamers we propose herein.

The concept of using MNPs for driving a desired physiological event, such as drug delivery, originated in the late 70's, but has heretofore faced significant technical issues that have hindered advancement of this technology. First, macroparticles attract each other in a magnetic field, causing aggregation, an undesirable outcome. Second, achieving both sufficient therapeutic drug loading levels and chemical functionality have proven to be difficult technical hurdles to overcome. Finally, the technology for effective control of the MNPs in a physiological environment has not been available. However, recent significant technological advancements have occurred to bring targeted magnetic therapies within the realm of functional potential, including: 1) dense, spherical, single domain magnetite MNPs can now be produced uniformly and economically, 2) novel methods now exist for attachment of functional groups to NPs, and 3) new electromagnetic instrumentation is available for vectored NP navigation and positioning.

The application of nanotechnology, and NPs in particular, to breast cancer is only in its infancy. One relevant development is the recently FDA-approved Abraxane™, a Cremophor-free,

albumin-NP-bound paclitaxel formulation, for second-line breast cancer treatment. It achieved superior response rates compared to the 175 mg/m^2 Taxol arm in its registration trial; however, comparisons to Taxotere remain to be conducted, and other indications have not yet been explored.

The CD44 proteoglycan family, including the standard (S) form and 10 or more known splice variants, is expressed on most human breast cancer cell lines. Among a panel of 110 breast carcinomas, 60% were positive for CD44s, 79% for v5, 74% for v6, 54% for v7 and 95% for v3-10. Its wide expression makes it an attractive candidate for targeting breast cancer, including IBC.

Thus, we introduced the concept of bimodal vectoring: an initial phase driven by the magnetic field influence on MNP localization to the tumor; and a secondary, diffusion-controlled, post-magnetic vectoring phase, driven by a binding moiety (anti-CD44 thioaptamer) that will bind to cell-surface CD44 and precipitate an internalization event.

B) Results & Discussion

THIOAPTAMERS TARGETING CD44

Synthesis of CD44 HABD (Hyaluronan Binding Domain) protein by cell free expression.
Due to the poor yields of protein using a bacterial *in vivo* expression system, we used a cell-free expression system to produce the CD44 HABD domain (residues 20-172). Cell-free expression methods offer tremendous advantages over the traditional, *in vivo* expression systems. The main advantages of cell-free expression methods include rapid, often one-step purification of the protein of interest, small working volumes (µL of volumes compared to mL-L of volumes of bacterial cell cultures), and elimination of laborious procedures of cloning and cell culture.

Combinatorial Selection of Monothio DNA aptamers targeting CD44 HABD
The initial library was constructed by PCR-amplification of a chemically synthesized, 73-nt DNA template (a 30-nt random region flanked by a 22-nt and a 21-nt PCR primer regions). Before PCR amplification, the single-stranded DNA template was subjected to Klenow reaction to yield a double-stranded DNA template. During the PCR, dATP(αS) was used along with dCTP, dGTP and dTTP, so the resulting DNA library will have monothio-substituted phosphoryl groups at the 5'-end of each dA residue.

5'-GAGATTCATCACGCGCATAGTC-N_{30}-CGACTATGCGATGATGTCTTC-3'

Selection of thioaptamers was performed on the His-tagged CD44 HABD that was bound to the Ni-NTA (Nickel Nitrolo Triacetic Acid) beads (Qiagen). Before the initial round of selection, the thioapatamer library was screened against the bare Ni-NTA beads to eliminate the DNA sequences that would bind to the beads themselves. After 10 rounds of selection, the sequences of the selected thioaptamers showed convergence.

The selected sequences are shown below.

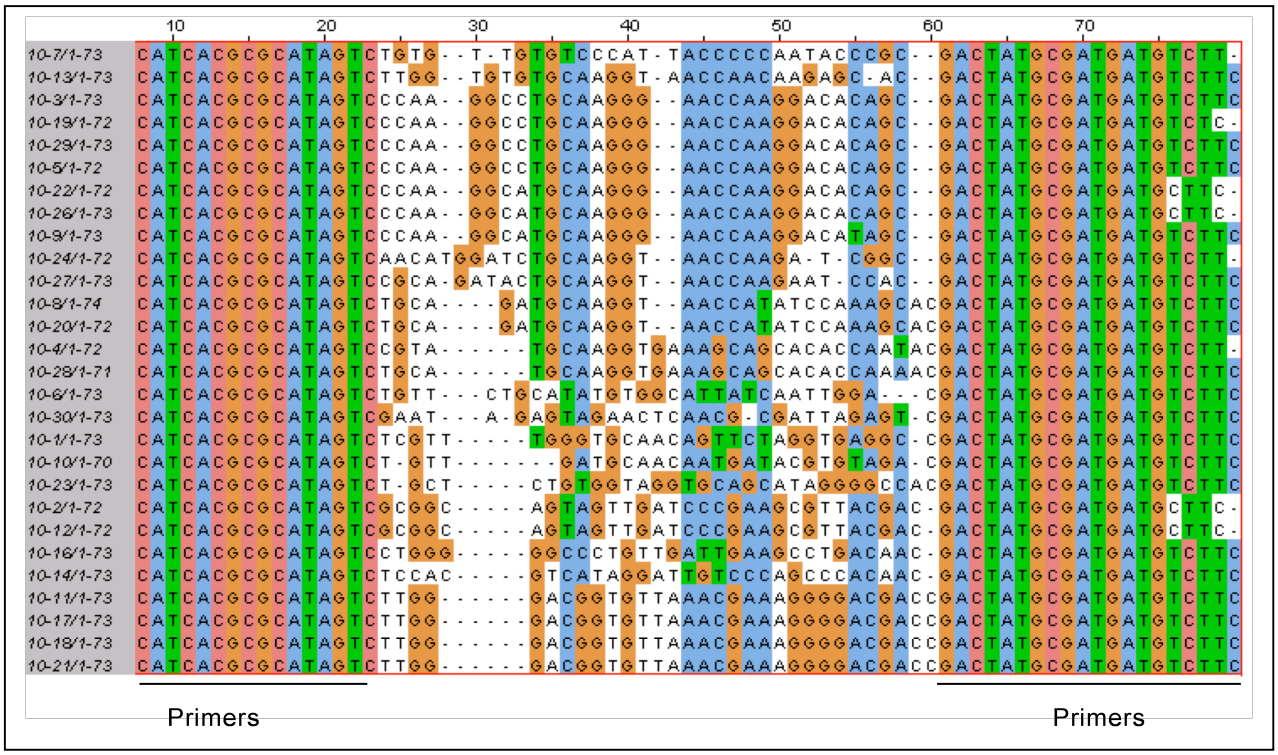

Based on the random region sequences, the selected thioaptamers were grouped into six groups. The sequence for each group is shown below

1. ***Primer-region-CCAAGGCCTGCAAGGGAACCAAGGACACAGC-primer-region***
2. ***Primer-region-CCAAGGCATGCAAGGGAACCAAGGACACAGC-primer-region***
3. ***Primer-region-TGCAGATGCAAGGTAACCATATCCAAAGCA-primer-region***
4. ***Primer-region-CGTATGCAAGGTGAAAGCAGCACACCAATAC-primer-region***
5. ***Primer-region-GCGGCAGTAGTTGATCCCGAAGCGTTACGAC-primer-region***
6. ***Primer-region-TTGGGACGGTGTTAAACGAAAGGGGACGACC-primer-region***

The consensus sequence of the selected thioaptamers, after 10 rounds of selections, is shown below.

dGAGATTCATCACGCGCATAGTCCCAAGGCCTGCAAGGGAACCAAGGACACAGCGACTATGCGATGATGTCTTC

The primer regions are shown in blue and the random region is in black. The binding affinities of these selected thiaptamers will be tested in 96-well ELISA plates and the tightest binding thioaptamer used for the nanoparticle conjugation. We will also identify a dithioate (PS2)-modified variation of the top monothioate-backbone modified (PS) thioaptamer to further enhance the affinity and nuclease resistance of the CD44 targeting thioaptamer. We will utilize our bead-based thioaptamer combinatorial library with FACS selection targeting the CD44 HABD.

Synthesis, Characterization and Biocompatibility of SiMNP and TXL Constructs

SiMNP, magnetite in composition and surface-coated with silica (SiO_2), were synthesized according to a modification of the Massart procedure, which enabled the subsequent formation of discrete silica-coated MNP (20 – 30nm diameter) nanodispersions. Silica coatings were achieved through the stoichiometric addition of sodium silicate to an MNP nanodispersion under controlled conditions of decreasing pH, designed to control shell thickness by silica deposition. The chemical/physical properties were characterized by X-ray diffraction to confirm magnetite composition and crystal structure, by energy dispersive x-ray spectroscopy (EDS) to confirm the presence of silica coatings, by TEM to confirm particle size and size distributions for MNP and SiMNP (10–20nm and 20-30nm) respectively, and by Vibrating Sample Magnetometry (VSM) to provide a quantitative measure of magnetic susceptibility. The magnetic susceptibility is useful for assessing the potential for MNP (~65 emu/g) and SiMNP (~45 emu/g) to be influenced by an external magnetic field.

Several parameters were considered in arriving at the choice of magnetite as the initial vectoring material for evaluation. First, the magnetic susceptibility of our synthesized SiMNP has been shown in our preliminary data to be sufficient to respond to magnetic field gradients achievable with commercially available magnet configurations. Second, while other types of magnets exist with higher magnetic moments, such as those utilizing Ni or Co, our approach eliminates the issues of carrier toxicity and difficult syntheses, allowing the focus to be on SiMNP behavior as the delivery vehicle.

Biocompatibility and hermeticity of SiMNP were assessed by several methods that assessed the potential for free radical generation, which included Electron Spin Resonance (ESR), based on the Fenton system known to generate free radicals in the presence of DMPO (5,5-dimethyl-1-pyrroline-N-oxide). Results indicated no evidence for free radical generation with our synthesized SiMNP.

To better understand SiMNP toxicity, female nude mice were injected with 150 µL of 1000 µg/ml solutions of FITC-labeled SiMNP and held for six months prior to sacrifice (Klostergaard et al., unpublished). Routine hematological (complete CBC and differential) and chemistry (bilirubin, electrolytes, creatinine, BUN, glucose, calcium, phosphorous, serum enzymes, LDH, and total protein) assays were conducted and did not reveal any significant alterations in the SiMNP-treated mice compared to age-matched controls. Histopatholgoical evaluation by a board-certified veterinary pathologist was unremarkable, revealing only aging-associated alterations, not unique to the MNP-treated mice. **These results provide evidence of SiMNP biocompatibility and resistance to physiological degradation.**

Figure 1: SiMNP/TXL Construct

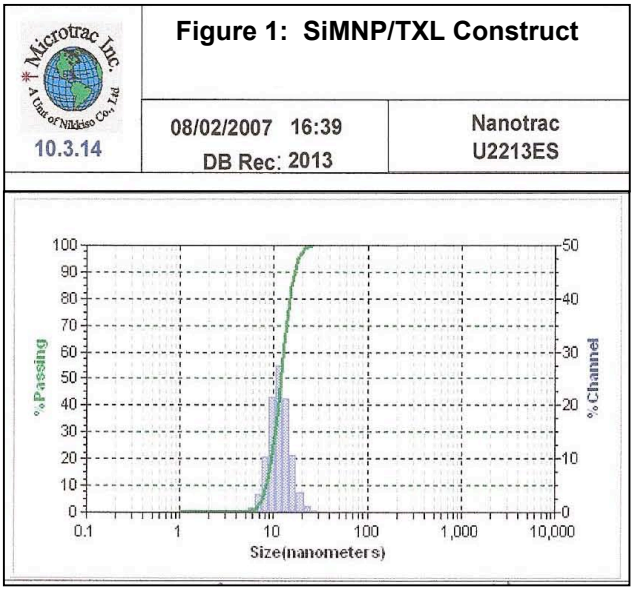

SiMNP-TXL constructs, as stable nanodispersions, have also been synthesized and characterized by dynamic light scattering (**Figure 1**) to show the SiMNP-TXL construct in a narrow size distribution around 10nm diameter. Carbon analyses of the SiMNP-linker and the SiMNP-TXL construct showed 6.15 wgt % and 9.66 wgt %, respectively. SiMNP sites, fully saturated with linker moieties, based on steric assumptions, would show a maximum carbon due to TXL to be ~10% (0.5gram TXL per gram of SiMNP for a 10nm particle), after accounting for the carbon contribution from the linker. Data developed from synthesized SiMNP constructs showed 3.5% TXL content (0.05g TXL per gram SiMNP) again after accounting for the carbon contribution from the linker. These results indicate that approximately 15% of the available sites on SiMNP (10nm diam.) were consumed by TXL, which would allow for delivery of ~15ug of TXL, a significant dose, to the tumor.

Thus, we provide evidence below that SiMNP nanomaterials used in our small animal nude mouse xenograft models were nanoscale in character and that this delivery system has the potential to target an effective dose of TXL.

In Vivo Localization of MNPs to Human Breast tumor Xenografts

To validate the feasibility of magnetically vectoring MNPs, we evaluated the concept in orthotopic human MDA-IBC-1 nude mouse xenografts. The cells for these xenografts were obtained from Dr. Wendy Woodward, MD Anderson Cancer Center. They were established from fresh pleural effusions obtained under an MD Anderson IRB-approved protocol from a patient with metastatic and therapy-resistant IBC. Fresh pleural effusion cells and mammospheres derived therefrom were PAP stained and analyzed by a breast pathologist to confirm that growing cells were tumor and resembled the original pathology. Attached cells demonstrated tube formation with mobile projections connecting foci of attached cells and had mesenchymal morphology. MDA-IBC-1 cells were transplanted in Matrigel into the cleared mammary fatpads of 3-week old Nod/Beige mice ($2x10^6$ cells/gland). Ten of ten injected glands

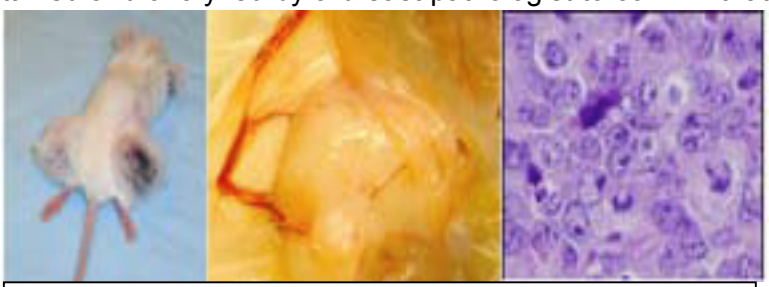

Figure 2: Orthotopic transplantation of MDA-IBC-1 cells resulted in tumor formation with gross skin involvement (left), gross angiogenesis

developed tumors at 14 days. One tumor had gross skin change at the time of sacrifice (**Figure 2, left panel**). Most had mild/moderate erythema. All tumors had evident tumor vasculature (**Figure 2, middle panel**). H & E staining was performed and compared to the patient's original primary tumor by a breast pathologist. Histology resembled patient primary: high grade and malignant (**Figure 2, right panel**). Immunohistochemistry confirmed maintenance of initial receptor phenotypes, ER(+), PR(-), Her-2-neu(-).

To conduct the MNP localization studies, female nude mice were orthotopically (mammary fatpad) implanted with the MDA-IBC-1 cell line using matrigel, and tumors were allowed to grow until their longest diameter reached between 4-10 mm. Then, following i.v. administration protocols, 50 μl of a 25 mg/ml solution of carboxy-silane-modified MNPs were injected with the point of a pyramid-crowned, tandem magnet (**Figure 3**) juxtaposed over the orthotopic tumor. Pre- (left panels) and post (right panels)-magnetic vectoring (magnet in place for 30 min) MR images (T1MSME, top panels; T2FSE, bottom panels) were acquired (**Figure 4**). The evidence for MNP-induced susceptibility artifacts is clear using either the T1- or T2- weighted images. There was no MR evidence for MNP localization without the magnet in place (data not shown).

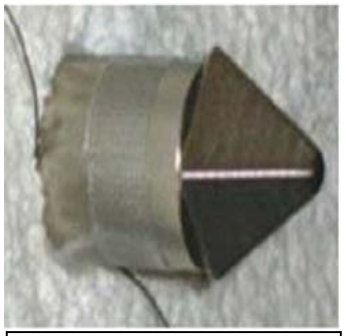

Figure 3: Permanent magnet combination where the small susceptor face is juxtaposed on the mouse abdomen

To begin to assess the kinetics of the retention mechanism in the IBC-1 xenograft, mice with IBC-1 tumors were subjected to the same protocol as described for the experiment in **Figure 4**, and then subjected to repeated MR imaging 24 and 48 hr later. The results are shown in **Figure 5**, and clearly demonstrate diminished signal by 24 hr, and essentially complete equivalence to pre-injection images by 48 hr, suggesting protracted clearance compard to that expected for free drugs.

Figure 4: Pre- (left panels) and post (right panels)-magnetic vectoring (magnet in place for 30 min) MR images (T1MSME, top panels; T2FSE, bottom panels)

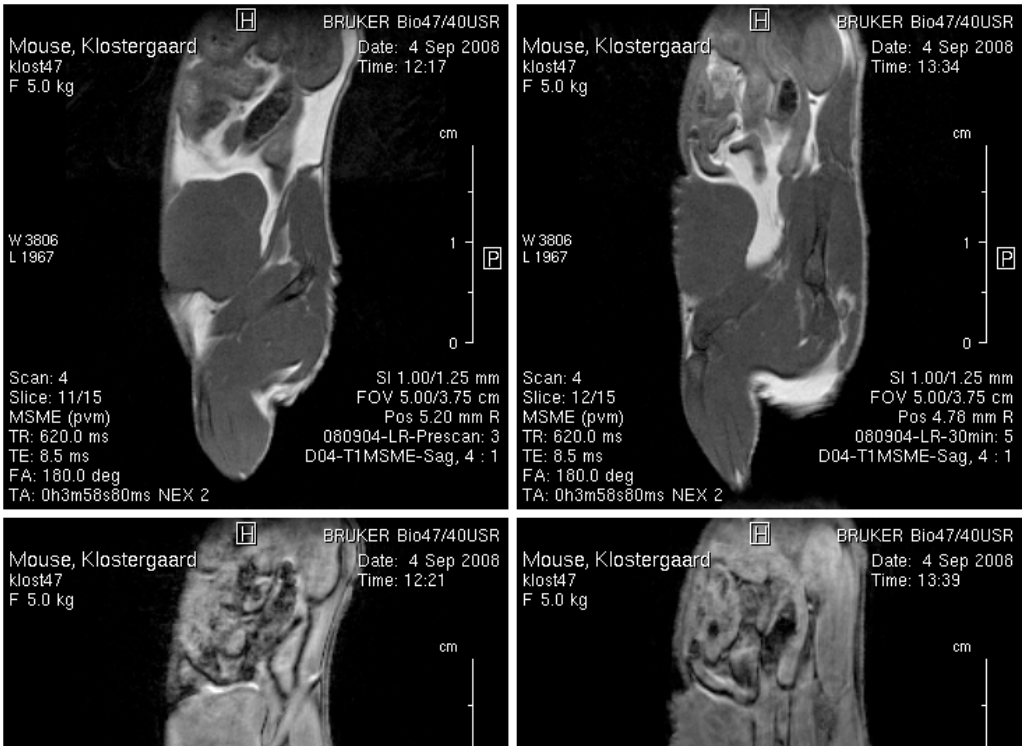

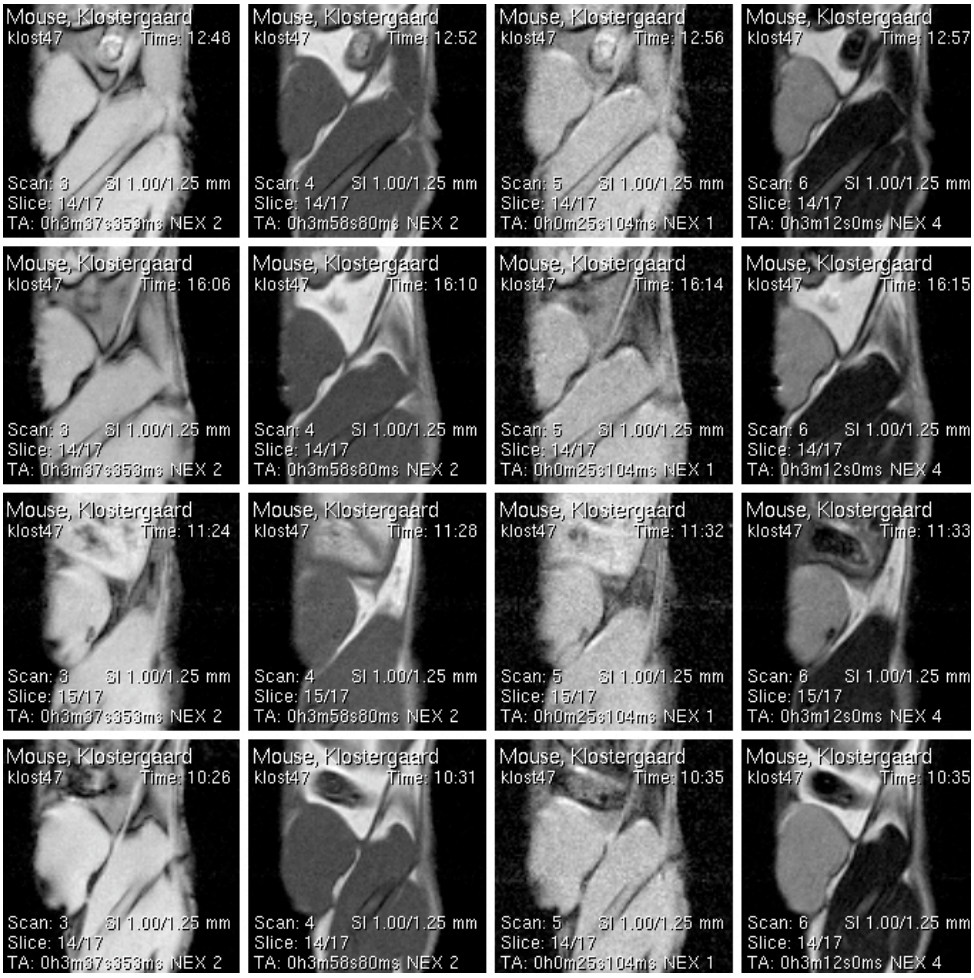

Figure 5: Top row is prescan, 2nd from top is after injection, 3rd row is +24h, bottom row is +48h. Leftmost column is lightly T2*-weighted, 2nd column from left is T1-weighted spin-echo, 3rd column is T13D gradient echo, and rightmost column is T2-weighted spin echo.

C) Key Research Accomplishments

1) Selection of six families of anti-CD44 HABD thioaptamer sequences using bead selection approach.

2) Synthesis and characterization of lead monodispersed MNP-TXL conjugate.

3) Demonstration of magnetically-enhanced localization of MNPs to human orthotopic tumor models, including breast.

D) Conclusions

We have been successful in achieving some key elements needed for construction of a lead anti-CD44-HABD-MNP-TXL construct, as well as in achieving localization of a parental MNP formulation to orthotopic human breast tumor xenografts. The next steps will include 1) validating HABD binding in solid-phase binding assays by the candidate anti-CD44 HABD thioaptamers; 2) if successful, subsequent analysis by competitive binding assays on CD44(+) human breast tumor cells (e.g., SKBR-3 or HBL-100); 3) synthesis of a lead conjugate of anti-CD44 HABD-thioaptamer-MNP, and repetition of the competitive binding assays performed for the free anti-CD44 HABD-thioaptamer; 4) synthesis of a lead conjugate of anti-CD44 HABD-thioaptamer-MNP-TXL and determining CD44-dependent cytotoxicity of this conjugate on CD44(+) tumor cells defined above; 5) evaluation of toxicity and anti-tumor efficacy of this lead formulation in orthotopic nude/SCID mouse human tumor xenografts.

E) Translation to Military Medicine

Breast cancer mortality is influenced by access to health care as well as by genetic and other factors. This is true in the civilian population, but women in the armed services should be able to access appropriate medical care, irrespective of their socio-economic status as civilians. With this technology currently under development, the desired endpoint is delivery of this therapy in an ambulatory treatment center or clinic, or at bedside if required for other reasons; we fully anticipate that this should be feasible at any sophisticated hospital offering oncology care to active or retired service personnel.

F) Scientific Publications, Abstracts, & Presentations

Numerous poster presentations at international meetings, including the 2006 EORTC/AACR/NCI meeting, entitled “Magnetic localization of magnetically-responsive nanoparticles to human ovarian carcinoma peritoneal xenografts”, by Jim Klostergaard, James Bankson, William Yuill and Charles E. Seeney, the 2007 9th US-Japan Symposium on Drug Delivery Systems entitled “Bimodally-targeted, magnetically-responsive nanoparticles as drug carriers”, by Jim Klostergaard, Joan Bull, David Gorenstein and Charles Seeney, and the 2008 First International Meeting on Inflammatory Breast Cancer, entitled “Localization of magnetically-responsive nanoparticles (MNPs) to orthotopic human IBC xenografts”, by Jim Klostergaard, James Bankson, Wendy Woodward, and Charles Seeney.

G) Funding Received as a result of the seed funds

The ANH funding helped provide preliminary data on thioaptamer development that was used to successfully renew a U54 grant between MD Anderson Cancer Center and the University of Puerto Rico Cancer Center.

Similarly, this data has been used in pending proposals, including an Ovarian Cancer SPORE Development Proposal, as well as in response to a solicitation for projects to include in the renewal of the Ovarian Cancer SPORE at MD Anderson.

Alliance for NanoHealth- Department of Defense, TATRC Grant Report

Guided Microvascular Formation and Cellular Infiltration for Tissue Regeneration Applications in Nano-Structured Silk Fibroin-Chitosan Scaffolds

Grant Period: September 2006-Present

Grant Amount: $109,971

Principal Investigator: Anshu B. Mathur, Ph.D.

Department of Plastic Surgery, The University of Texas M. D. Anderson Cancer Center

Manuscript in submission to the journal "Biomaterials" is submitted as Grant Report.

Report Outline

Section A-D are covered in the attached manuscript.

A) Introduction, B) Results & Discussion, C) Key Research Accomplishments, D) Conclusions,

- We have a novel patentable method for fabrication of 3-D nano-fibrillar scaffolds that affect endothelial and stem cell migration and adhesion and guide cells in vivo
- We have submitted for further support from the NIH as an R01 and it is currently under review. This was our last task on the timeline and we have accomplished it.
- Award from the Plastic Surgery Research Council (2006) and Recognition from the American Society of Plastic Surgeons (2007); Gordon et al. Cellular Guidance on NanoStructured Scaffolds

E) Translation to Military Medicine,

The design and development of biodegradable matrices that will replace the native tissue without necrosis or scar formation is a challenging area of research. The composition, architecture, and mechanical properties of the scaffold or matrix are important criteria for bone formation due to its load bearing properties. The structural and biological characteristics also control the initial inflammatory response, cell conductivity or infiltration, generation of the neo-ECM, biodegradation of the biomaterial scaffold, mechanical properties of the remodeled or regenerated tissue, vascularization, mineralization, and differentiation of bone cells. The critical balance that needs to be maintained in the wound healing of load bearing tissues such as bone, is that the degradation rate of the implanted biomaterial should equal the deposition of new matrix so that mechanical strength is not compromised.

The hurdles in regenerative tissue engineering can be overcome by developing structurally engineered 3-D scaffolds using biological sources whose micro and macro structure, mechanical properties, and chemical composition can be designed based on the clinical need. The present funded work provides such strategy to design regenerative biomaterials from nano to macro level per patient specific need for guided regeneration of tissues. In the military, patients that have major injuries due to trauma or other accidents in the battlefield will benefit from this research since many of these injuries are in the maxillofacial region. This work provides an unique way to promote Vascularization and guide the regeneration of critical sized defects in patients with maxillofacial injuries.

F) Scientific Publications, Abstracts, & Presentations

Publication is attached.

Gordon AC, Gascoyne PRC, Mathur AB. Dielectrophoretic alignment in silk fibroin-chitosan scaffolds. Society for Physical Regulation in Biology and Medicine, 2006.

Three dimensional engineering of nano-structured scaffolds for guided microvascular assembly, Plastic Surgery Research Council, Laguna Cliffs, CA, 2006

Engineering the regeneration of tissue at the nanoscale, Advances in Oncology Grand Rounds, Translational Nano- and Micro-technology, The University of Texas MD Anderson Cancer Center, Houston, TX, 2007

Guidance of tissue regeneration in biologically derived materials, Institutional Grand Rounds, Biomedical Engineering, The University of Texas MD Anderson Cancer Center, Houston, TX, 2007

Solutions for a nanoscale world, Atomic Force Microscope Workshop Seminar, Houston, TX, 2007

Engineering biologically derived materials for therapeutic applications, Department of Thoracic and Cardiovascular Surgery, The University of Texas MD Anderson Cancer Center, Houston, TX, 2008

Engineering the regeneration of tissue at the nanoscale, Division of Surgery Grand Rounds, The University of Texas MD Anderson Cancer Center, Houston, TX, 2008

G) Funding Received as a result of the seed funds.

- We have submitted for further support from the NIH as an R01 and it is currently under review. This was our last task on the timeline and we have accomplished it.

Endothelial and Stem Cell Interactions on Dielectrophoretically Engineered Silk Fibroin-Chitosan Scaffolds to Guide Tissue Formation

Vishal Gupta[a], Alexander Gordon[b], Greg Davis[b], Andrew M. Altman[a,c], Gregory P. Reece[a], Peter R. Gascoyne[c], Anshu B. Mathur[a,]*

[a]Department of Plastic Surgery and Biomedical Engineering, University of Texas M.D. Anderson Cancer Center, Houston, TX

[b]Department of Bioengineering, Rice University, Houston, TX

[c]Department of Molecular Pathology, University of Texas M.D. Anderson Cancer Center, Houston, TX

* Corresponding Author:

Anshu B. Mathur, PhD

Director of Research

Tissue Regeneration and Molecular Cell Engineering Labs (TRAMCEL)

Department of Plastic Surgery, Unit 602

University of Texas MD Anderson Cancer Center

PO Box 301402

Houston TX 77230-1402

Phone: (713) 563-7568

FAX: (713) 563-0231

e-mail: amathur@mdanderson.org

Abstract

Cellular interactions in engineered scaffolds are important to elucidate the parameters for the formation of complex tissues. The effect of scaffold structure (nano versus micro) on endothelial cells and stem cells adhesion, proliferation, and migration were studied in silk fibroin (SF) and chitosan (CS) blend three-dimensional scaffolds. The nanostructure of SFCS scaffolds were molecularly engineered using dielectrophoresis. Human adipose-derived mesenchymal stem cells (hASCs) and human umbilical vein endothelial cells (HUVEC) were seeded on either SFCS (microstructured) or E-SFCS (nanostructured) scaffolds and imaged using SEM and time-lapse confocal microscopy to study the cell adhesion, migration, and interactions in vitro. The SFCS and E-SFCS were implanted in an *in vivo* rat mesentery animal model to study the effect of structure on neo-vasculature formation. SEM imaging showed that aligned nano-fibers

was compared to smooth surface of SFCS. Adhesion of hASCs within 30 minutes was higher than HUVEC on either type of scaffolds. The number of moving cells and average speed was highest for hASCs seeded alone on SFCS scaffolds compared to hASC seeded with HUVEC. HUVEC interacts with hASC and appear to slow the speed of hASC migration (in co-culture) on scaffolds. *In vivo* study show that cells interact with nano-fibers and blood vessels align to the fibers on E-SFCS scaffold. In conclusion, aligned micro and nano-fibers were created on E-SFCS scaffold surface for cell guidance and show potential for complex tissue formation.

Keywords: Silk fibroin, Regeneration, Stem cells, Dielectrophoresis, Scaffold, Cell migration, Nano-fiber

1. Introduction

The design and development of biodegradable matrices that will reconstruct and regenerate the native tissue without scar formation is a challenging area of research. Most currently available biomaterials used in the area of reconstruction are not designed to regenerate tissue but to cover or fill defects and/or perform a mechanical function. A regenerative biomaterial is the one that recruits wound healing and precursor cells to form new viable and vascularized tissue *in vivo*.

The composition, architecture, and the mechanical properties of the biodegradable matrices are important criteria since they control the initial inflammatory response, endothelial and stem cell infiltration, generation of new extracellular matrix (ECM), degradation, vascularization, and mechanical properties of the remodeled tissue. The blend of two biologically-derived materials silk fibroin (SF) and chitosan (CS) was developed to repair and regenerate abdominal wall musculofascia and support regeneration of bone in two different *in vivo* models (1, 2).

Recent research has shown that during *in vivo* angiogenesis, capillary sprout endothelial cells and pericytes preferentially migrate along elastic fibers found in the extracellular matrix in order to form neovessels (3). The critical point to note from this study was the fact that capillary sprout endothelial cells (ECs) can use existing fibers in the ECM as substrate to guide microvascular growth. Since silk fibroin is a fiber forming polymer and has shown in vivo regenerative capacity in our previous studies, we used the technique of dielectrophoresis to align silk fibroin fibers within a three-dimensional scaffold and study endothelial cell guidance for vascularization in vivo and endothelial cell-stem cell interactions in vitro.

The use of dielectrophoresis to achieve the nano-fiber formation and alignment of silk fibers in a three-dimensional scaffold is a novel approach. Previously, dielectrophoretic forces have been used for the manipulation of microparticles and cells (4, 5), collection of macromolecules (6), nanoparticles (7), and nanotubes (8). Nano-fibrous structures have been shown to have many applications in tissue engineering, biomedicine and biotechnology (9, 10).

Recently our group published on use of SFCS scaffold for the mesenchymal stem cells' delivery to promote tissue regeneration(11) (12). In this study, we investigated the adhesion and migration behavior of human adipose tissue derived stem cells and endothelial cells on engineered SFCS scaffolds (E-SFCS) with aligned nano-fibers in a three-dimensional scaffold and compared it to our conventional first generation scaffolds that had features of smooth sheets with microfibril extensions. In order to study the guidance of endothelial cells by aligned SF fibrils in the engineered scaffold, we implanted the scaffolds in an *in vivo* rat mesentery model because the mesentery provides a bed of fine blood capillary network as a source for migrating endothelial cells. Mesentery has been used widely for *in vivo* model of angiogenesis (13). This is the first study to use dielectrophoresis for silk fiber alignment and characterize E-SFCS for tissue regeneration.

2. Materials and methods

2.1 Silk-fibroin and chitosan scaffold preparation

Raw silk was kindly donated by Dr. Sam Hudson (North Carolina State University, Raleigh, NC) and high molecular weight chitosan (82.7% deacetylation) was obtained from

Sigma-Aldrich (St. Louis, MO). The blend of 75:25 SF and CS was prepared as described previously [Gobin et al., 2005]. Briefly, raw silk was degummed (removal of sericin coating) in 0.25% (w/v) sodium carbonate and 0.25% (w/v) sodium dodecylsulfate (Sigma-Aldrich) for 1 hour at 100°C. The degummed silk (silk fibroin) was then dissolved in calcium nitrate tetrahydrate and methanol solution (molar ratio of 1:4:2 $Ca:H_2O:MeOH$) at 65°C. Chitosan was dissolved in 2% acetic acid solution at the same concentration as silk fibroin solution and was mixed together in a ratio of 1:3 (1 part chitosan and 3 parts silk fibroin) to prepare 75:25 SFCS. The SFCS scaffolds (controls) were prepared by freezing 75:25 SFCS blend at -80°C overnight and then lyophilizing for 24 hours. The dry scaffolds were treated with 50:50 (v/v) methanol:sodium hydroxide (1 N) solution for 15 minutes to crystallize the silk fibroin and left overnight in 1 N sodium hydroxide solution. The scaffolds were washed several times in phosphate buffer saline (PBS) solution (Lonza, Walkersville, MD) to equilibrate the pH to 7.0. The SFCS scaffolds were sterilized in ethanol solution overnight under the laminar flow hood and again washed with PBS several times to bring the pH equal to 7.0.

2.2 Engineered scaffold preparation

Engineered silk fibroin and chitosan scaffolds (E-SFCS) were prepared using dielectrophoresis technique (4). The electrodes were made of periodic triangular arrays fabricated by microlithography techniques (Fig. 1). A thin film coating of gold on a glass microscope slide was used as a substrate, and patterned using UV photolithography and gold etching [Reference]. SFCS blend solution (0.5 ml) was pipetted on to the interdigitated bar electrode. The electrode was connected to an AC power supply (Agilent 33220A 20MHz

Function/Arbitrary Waveform Generator), and a 100 kHz, 10 V(p-p) sine wave was applied across the sample for 45 minutes. The electrode voltage, field frequency and time were optimized for better alignment. The fibers collect to the electrode tips of the triangular micropattern and move to the gaps by repulsion of fibers. The scaffold was then frozen in liquid N_2 vapors and lyophilized. E-SFCS scaffold was then crystallized and sterilized as mentioned above for SFCS scaffolds. The dimensions of the electrode used for in vitro study are Larger micro-electrodes were used for *in vivo* study because bigger scaffolds were needed for implantation into the animal (Fig. 1).

2.3 Cell culture

Human adipose-derived stromal mesenchymal stem cells (hASCs) were obtained from InGeneron Inc. (Houston, TX) and cultured in α-minimum essential medium (Gibco, Grand Island, NY) containing 20% fetal bovine serum, 2 mM L-glutamine, 100 U/ml penicillin and 100 μg/ml streptomycin (12, 14). Human umbilical vein endothelial cells (HUVEC) were obtained from Cascade Biologics (Portland, OR) and cultured in Medium 200 containing low serum growth supplements (Cascade Biologics). Both hASC and HUVEC were cultured at 37°C in 100% humidified atmosphere with 5% CO_2 supply. Passages from 3 to 6 were used for both cell types in all the experiments.

2.4 Polarized light microscopy

SFCS and E-SFCS were imaged using polarizer, analyzer, and a red retardation plate attached to Olympus IX70 (Olympus, Center Valley, PA) microscope. Polarized light microscopy was used to assess the alignment and orientation of the fibrils within the scaffold.

2.5 Scanning electron microscopy (SEM)

SFCS and E-SFCS scaffolds were cut to fit 96-well cell culture plate and kept at the bottom of the plate. The scaffolds were seeded with 300,000 cells (hASCs or HUVEC or both cell types together) per well and incubated for 30 minutes at 37°C. The scaffolds were washed 2 times with PBS to remove unattached cells and then fixed in 2% paraformaldehyde and 3% glutaraldehyde solution. Unattached cells were counted to calculate the percent adhesion of cells to scaffolds. The cell-seeded scaffolds were imaged using JSM-590 scanning electron microscope (JEOL, USA, Inc., Peabody, MA) as described before (12).

2.6 Cytokinetic study using time-lapse confocal microscopy

The hASCs were transfected with green fluorescent protein (GFP) and HUVEC were labeled with DiI dye (Invitrogen, Carlsbad, CA), which bind to cell membrane. First, 2 million HUVEC were suspended in 2 ml of Hanks Balanced Salt solution (Lonza) and 0.5 µl of DiI (from 10 mg/ml DiI stock in EtOH) was added in dark. Both hASC and HUVEC were also labeled for nucleus stain using Hoechst dye (Sigma-Aldrich; 5 µg per million cells). After the addition of dyes in dark, the cell suspension was incubated at 37°C for 5 minutes then at 4°C for 15 minutes and again at 37°C for 30 minutes ending with 30 minutes at room temperature. The cell suspension was centrifuged at 1500g for 10 minutes and the pellet was suspended in the

culture medium. The ethanol sterilized E-SFCS and SFCS scaffolds were cut and kept at the bottom of 96-well plate. Fluorescently labeled hASC and HUVEC (total 100,000 cells per well) were seeded on top of scaffolds either single or in co-culture. After 30 minutes, unattached cell were washed with PBS and the cell-seeded scaffolds were imaged using confocal fluorescence microscope Olympus IX81 (Olympus, Center Valley, PA, USA) every 15 minutes for 4 hours. Later, the images were processed for cytokinetic data calculations (cell speed and persistence time) using Slidebook software (Intelligent Imaging Innovations GmbH, Göttingen, Germany). Persistence time is the length of time before the cell changes its direction of movement significantly (15, 16). The 'average speed' of the cell and 'persistence time' are the parameters used commonly to analyze the cell migration on a particular substrate.

2.7 In vivo implantation of E-SFCS scaffolds

Rat was anesthetized by administering standard rat cocktail consisting of ketamine (100 mg/cc), xylazine (20 mg/cc), and atropine (0.4 mg/cc) at a dosage of 0.1 cc/100grams, intramuscularly. After anesthesia takes effect, the rat's abdomen was shaved from the costal margin to the pubic area and from flank to flank. A depilatory agent (Nair) was applied to the shaved skin for 7 minutes and then wiped clean to remove all hair shafts from the skin. The animal was placed on an operating table maintained at 37 ^{0}C and the abdomen was prepped with betadine solution and sterilely draped. A small 2 cm midline incision was made and a loop of bowel with its mesentery was pulled up out of the abdomen and draped across a saline moistened sponge. The operating microscope was positioned and a 10x10 mm SFCS and E-SFCS were positioned on top of the mesentery, near one of the blood vessels of the vascular arcade radiating

to the bowel (n=3 animals). Each corner of the implant is sutured to the mesentery with a 9-0 nylon suture (Figure 2). The bowel with implant was returned to the abdominal cavity and the abdomen was closed using 5-0 nylon suture.

After 2 weeks, the animals were euthanized with CO_2 followed by thoracotomy and explantation of the implants. The explants were fixed in 10% formalin overnight, paraffin embedded and 4μm sections were cut and mounted on glass slides, immunostained for Factor VIII (source of the antibody), and imaged with polarized light microscopy with polarizer, analyzer and red retardation plate in order to observe the endothelial cells in conjunction with the aligned SF fibers (17, 18). Further analysis of the 4 μm sections was conducted with JSM-590 scanning electron microscope (JEOL, USA, Inc., Peabody, MA) imaging.

2.8 Statistical analysis

The data was compared statistically SigmaStat program. The level of significance was chosen as $p<0.05$. Two-way ANOVA was performed with scaffold type as factor 1 and cell type/culture as factor 2 to analyze the *in vitro* results. Also, post hoc Tukey test was used for pair-wise comparisons. All data was represented as mean ± SEM (standard error of mean).

3. Results

Model of self assembly of SF fibrils

If a rod-shaped particle is placed in an inhomogeneous alternating electric field, it will experience a time-averaged, translational dielectrophoretic force due to induced dipolar effects (19-22) given by

$$\vec{F}_{DEP} = \frac{\pi a^2 b}{3} \varepsilon_m f_{CM} \nabla \left| \vec{E}^2 \right|, \qquad \text{(i)}$$

Where, 'a' is the radius of the rod and 'b' is its length. ε^*_p and ε^*_m are the complex permittivities of the particle and its suspending medium, respectively, and $\nabla \left| \vec{E}^2 \right|$ is the gradient of the magnitude of the electric field squared. f_{CM} is the so-called Clausius-Mossotti factor which describes the frequency-dependent dielectric characteristics of the particle and its suspending medium,

$$f_{CM} = \mathrm{Re}\left\{ \frac{\varepsilon^*_p - \varepsilon^*_m}{\varepsilon^*_p + 2\varepsilon^*_m} \right\}. \qquad \text{(ii)}$$

Quadrupole and higher dielectric terms, ignored here, may be included if required (20-22). Equation (ii) shows that the dielectrophoretic force is attractive or repulsive depending on whether the polarizability of the particle is greater or less than that of its suspending medium, respectively. The complex permittivity of a particle may be expressed in terms of core dielectric (ε_p), core conductivity (σ_p), and surface (interfacial) conductivity (K_s) properties as $\varepsilon^*_p = \varepsilon_p - \frac{j}{\omega}(\sigma_p + \frac{2K_s}{a})$, where $j = \sqrt{-1}$ and ω is the angular frequency of the applied electric field [Arnold et al., 1987]. Even when the particle core is less polarizable than the suspending medium, the surface conductivity term will overwhelm the intrinsic particle properties and lead to attractive dielectrophoretic forces below some crossover frequency at which $\mathrm{Re}(f_{CM}) = 0$. Solving equation (ii) for this condition yields

$$\omega = \left[\frac{\left(\frac{2K_s}{a} + \sigma_p - \sigma_m \right)\left(\frac{2K_s}{a} + \sigma_p + 2\sigma_m \right)}{(\varepsilon_m - \varepsilon_p)(\varepsilon_p + 2\varepsilon_m)} \right]^{\frac{1}{2}} \qquad \text{(iii)}$$

Of significance to the molecular assembly work proposed here for elongating silk proteins is that the radius of the particle, a, affects the contribution made by surface conductivity to the

magnitude and sign of the dielectrophoretic force. To illustrate this, the crossover frequency is plotted at right for aqueous solutions of 1 to 16 mS/m conductivity, a core protein dielectric constant of $4\varepsilon_0$, and a surface conductivity of 2 nS, as a function of particle radius (Figure 3). The plot shows that small radius (<100 nm) molecules experience dielectrophoretic attraction to electrode tips even at high frequencies. However, the crossover frequency decreases sharply and becomes negative if molecular assembly into solid fibers of sufficiently large radius occurs. The threshold radius for which the crossover frequency drops off rapidly is determined by the suspension medium conditions. This shows that it should be possible to concentrate and orient small radius, elongate molecules by strong attractive dielectrophoretic forces at the electrode tips yet repel larger radius assembly products towards low field regions between the electrodes. Once focused and oriented in low field regions, additional assembly to form much larger structures can proceed. The advantages of this scheme are that a continuous assembly process is enabled in which the electrode tips remain clear of assembled material and in which very large fibers can be assembled in extensive, oriented "bay" regions between rows of electrode tips. In this way, the scale of the assembled fibers may be significantly larger than the scale of the electrode tips. This methodology provides the possibility of creating oriented fiber assemblies in three dimensions through repulsion from two-dimensional electrode planes because, while positive dielectrophoresis depends on high field regions that can only be produced at localized structures, negative dielectrophoresis can concentrate matter away from structures and surfaces.

Assessment of fiber alignment

SF fibril and polymer chain alignment within the fibril has been studied using polarized light microscopy using a polarizer, analyzer, and a red retardation plate {Mathur, 1997 #36}.

Under the polarizer-analyzer the SF fibril alignment is seen as white fibrils embedded in the unaligned regions, which appear black. Fibrils showed distinct alignment at 45° angle to the electrode bars (Figure 4A). Under the red retardation plate, SF polymer chains distinctly reflect blue showing that polymer chains within the fibrils aligned primarily parallel to the fibril direction (Figure 4B). As fiber assemblies begin to grow in thickness and length, their dielectric properties change and they are repelled into the gaps between electrodes where they assemble into larger fibers (~50 μm) that are aligned along the negative dielectrophoretic regions (Figure 4C). Moving along the z-axis of the assembled scaffold, it was observed that the E-SFCS was composed of layered sheets of aligned fibers. However, SFCS scaffold showed no such alignment of fibrils as seen in E-SFCS {Gobin, 2005 #4} as previously studied. SEM images of SFCS show that sheet surfaces were smooth with micro-fiber projections at the edges as has been shown previously {Gobin, 2005 #4}. However, the surfaces of E-SFCS sheets were textured with nano-fibers (97.2 ± 2.7 nm) and ridges (0.51 ± 0.03 μm) (Figure 5A).

Endothelial and Stem Cell Adhesion to SFCS and E-SFCS Scaffolds

Both HUVEC and hASCs adhere to SFCS and E-SFCS scaffolds as can be seen in SEM images (Figure 5). While the cells have an opportunity to interact with the nano-features of E-SFCS, the larger microfibrils of the SFCS capture the relatively smaller cells. The surface of HUVEC appears to be smoother than the porous and hairy surface of hASCs. In the co-culture of HUVEC and hASC, HUVEC-HUVEC and HUVEC-hASC interact via cellular extensions. More than 85% cells adhere to the scaffolds within 30 minutes of incubation (Figure 6). Percentage adhesion of hASC on SFCS (98.7% ± 0.3%) and E-SFCS (96.3% ± 0.7%) scaffolds

was significantly higher ($p<0.05$) than HUVEC on SFCS (91.7% ± 1.8%) and E-SFCS (89.7% ± 2.7%).

Endothelial and Stem Cell migration and Kinetics on SFCS and E-SFCS Scaffolds

Cells migrate on both SFCS and E-SFCS scaffolds as a function of time. Cell movement was tracked over time (give the amount of time) as shown in Figure 7 and the video can be viewed at http://video.google.com/videoplay?docid=4866859754121817448.

Table 1 shows the cytokinetic data collected after cell tracking. The average speed was highest for single-culture hASC on SFCS (18.5 ± 9.3 μm/hr) and was significantly different from single-culture HUVEC ($p<0.001$) and co-culture HUVEC ($p<0.001$) or hASC ($p<0.001$) on SFCS scaffold. Similarly on the E-SFCS scaffold single-culture hASCs had higher average speed ($p<0.1$) than co-culture hASCs. Interestingly, the speed of single culture hASCs was higher ($p<0.05$) on SFCS than E-SFCS. Persistence times of the cells were comparable on either type of scaffolds except for co-culture HUVEC, which was significantly lower ($p<0.05$) on E-SFCS than SFCS scaffold.

Percentage of moving cells in each image frame during 4 hours of imaging time was also calculated. The percentage of moving cells was highest for single-culture hASC on SFCS (40.3 ± 5.6%) and was significantly different from single-culture HUVEC ($p<0.05$) and co-culture HUVEC ($p<0.05$) or hASC ($p<0.001$) on SFCS scaffold. There was no significant difference for moving cells between single or co-culture seeded HUVEC and hASCs on E-SFCS scaffolds. However, percent of moving cells for single-culture hASCs ($p<0.01$) and co-culture HUVEC ($p<0.05$) were significantly lower on E-SFCS as compared to SFCS scaffold.

When both cell types were grouped together for data analysis in two-way ANOVA, persistence time was significantly higher ($p<0.05$) on SFCS (34.9 ± 3.2 minutes) as compared to E-SFCS (27.7 ± 3.6 minutes) (Figure 8A). Similarly, the percentage of moving cells was significantly higher ($p<0.05$) on SFCS (10.4 ± 2.4%) as compared to E-SFCS (4.1 ± 1.9%) (Figure 8B). However, even after grouping the cell type, average speed was not significantly different between SFCS and E-SFCS (Figure 8C).

E-SFCS and SFCS Remodeling post-*in vivo* Implantion

E-SFCS and SFCS scaffolds explanted at 2 weeks showed that the implants remodeled and integrated within the mesentery. Histological evaluation of the immunostained samples under the polarized light microscope shows that the explants may be similarly characterized by cellular infiltration, degradation of scaffold, and deposition of new matrix within the SF fibrils (appear as blue). E-SFCS scaffolds directionally remodeled with vascular structures forming in the direction of the fibrils (Figure 9A) similar overall orientation has been observed in the native rat mesentery between the native fibers and blood vessels (Figure 9B). SFCS scaffolds showed similar cellular interactions with the SF fibrils but less uniform. Some alignment of the SF fibrils was noted, possibly due to remodeling and contraction of the scaffold. Endothelial cells of the vasculature were observed to be attached to the SF fibrils (Figure 10).

In order to deduce any sub-structural contribution in cellular interactions of scaffold that was not visible via polarized light microscopy of the histological sections, SEM imaging was conducted of the histological sections. SEM images showed that the remodeled SFCS scaffold explants consisted of stacked sheets of smooth surface, an architectural feature similar to pre-implant SFCS (Figure 11 A and B). On the other hand, the E-SFCS scaffold sheets were

interconnected with nano-fibrous structures (141 ± 19 nm) (Figure 11 C and D). There were both small and big parallel fibers with diameter range of 121 ± 12 nm and 252 ± 15 nm. Also, cells can be seen interacting with nano-fibers (51 ± 6 nm) on the matrix, which provide anchoring surface to cells (Figure 12).

4. Discussion

In this study, the technique of dielectrophoresis was used for the first time to engineer SFCS scaffolds with aligned fibrils and nano-featured architecture self assembled in 3-dimensions. *In vitro* endothelial cell and stem cell migration study showed that the nano-fibrillar architecture of the E-SFCS surface promoted adhesion and slower migration of stem cells. Additionally, endothelial cells in co-culture with stem cells on E-SFCS or SFCS slowed the migration of stem cells regardless of the scaffold architecture. *In vivo* results show that the nanofibrous architecture of the E-SFCS and smooth surface architecture of the SFCS sheets is retained during remodeling of the scaffolds over two weeks. The directional growth of the vasculature and remodeling of the cells was similar in SFCS and E-SFCS, although less consistent in the SFCS.

Cellular adhesion was enhanced on the E-SFCS as compared to the SFCS surface. Nano-fibrous substructures on the E-SFCS surface may provide a fertile anchoring surface to the cells. HUVEC express more adhesion molecules such as β1-integrin on nano-fibrous silk fibroin nets compared to micro-fibrous net scaffolds (23). Although cells prefer to adhere to the nanostructured surface of the E-SFCS, the ones that migrate tend to change their directions faster on nano-fibers than on the smooth surface of SFCS as evidenced by the lower persistence time on E-SFCS.

Human endothelial cells on polystyrene surface coated with 1% gelatin have been shown to migrate at the cell speed of 30 μm/hr (30), which is much higher as compared to that found on SFCS scaffolds (1.3 μm/hr) and E-SFCS (5.1 μm/hr). SFCS scaffolds provide 3-dimensional anchoring surface to cells, which might have slowed down the cell speed. Various other cell types on different surfaces have been shown to have speed in the range of 10-138 μm/hr and persistence time in the range of 27-300 minutes (12). The persistence time for cells in this study was within the range of 13-47 minutes for single and co-cultures but the average speed was comparatively lower (1.3-18.5 μm/hr). The 3-D scaffolds as compared to 2-D polystyrene surface may provide higher affinity surface to HUVEC and hASCs hence relatively lower migration speed as is evident in the difference between fewer percentage of moving cells on E-SFCS than SFCS scaffolds, with E-SFCS perhaps providing a more adhesive surface (16).

The migration speed was found to be highest for hASCs on SFCS scaffold. But in the presence of HUVEC (co-culture), the migration speed reduced significantly. HUVEC are known to be quiescent cells unless activated by an extracellular signal such as hypoxia [reference]. We observed in SEM and confocal microscopy images that HUVEC interact with hASCs actively. In co-culture, inter-cellular signaling may allow HUVEC to communicate with hASCs and reduce their speed of migration. The interaction of HUVEC and hASCs can further be explored in future studies, which will help understand their interaction on these scaffolds.

SEM images from both *in vitro* and *in vivo* studies confirm that the surface of E-SFCS was textured with nano-fibers, whereas the surface of SFCS scaffolds was very smooth with micro-

projections on the edge of the sheets as has been found previously (2). Also, it was found previously that more hASCs attach to the micro-projections on SFCS compared to smoother sheet surface (12). Similarly, we also observed that more cells attach to nano-fibrous surface of the E-SFCS scaffold (data not shown- why??). Percent of adherent cells in 30 minutes was higher for hASCs than HUVEC on either type of scaffolds probably due to the higher surface area of hASCs provided by its rough surface imaged under the SEM. HUVEC probably take longer time to adhere on scaffolds due to their relatively smoother surface and that is why their adhesion in 30 minutes is lower. Interestingly, the overall cellular adhesion of HUVEC and hASC was similar on SFCS and E-SFCS, regardless of structural differences. This may be because the chemistry of SFCS contributes more for cell adhesion than the structural features of the scaffolds.

Endothelial cells have been shown to preferentially utilize the fibers of the extracellular matrix in the native mesentery to extend cellular projections for migration (3). This *in vivo* study shows that the scaffolds implanted in the mesentery of silk fibroin-chitosan chemistry also allow for cellular invasion and guidance of endothelial cell neo-vasculature. Regardless of the SFCS or E-SFCS surface characteristics histological markers and polarized light microscopy indicated that the aligned fibrils of silk fibroin supported endothelial cell attachment leading to neo-vascularization at 2 weeks. Perhaps, short term study at implant times of 1-4 days may be more indicative of the initial effect of substructures such as nanofeatures, as is evident in the *in vitro* study that shows that less percentage of cells are moving on nano-featured E-SFCS than SFCS.

This study had a few limitations and one of them was the shorter time capture (only up to 4 hours) of cytokinetic data due to the leaching and bleaching of fluorescent dyes. Also, many focus areas (frames) during time-lapse confocal microscopy did not show moving cells leading

to low number of migrating cells. To overcome this problem we tried to capture more than one frame on a single sample.

Another limitation of the study was the thin E-SFCS scaffold. Increasing the thickness of the scaffold compromised with the alignment of fibers as electrode for the dielectrophoresis align the fibers on the surface only. In the future a 3-dimensional electrode can be developed to make thicker aligned scaffolds. Also, different castellation can be used to align the fibers in specific directions.

Dielectrophoresis was successfully used to engineer the SFCS scaffolds with aligned nano-fiber morphology. Both SFCS and E-SFCS scaffolds facilitates hASCs and HUVEC adherence, migration and interactions. More cells migrate with higher persistence time on SFCS than E-SFCS. HUVEC appear to slow the speed of hASC migration on scaffolds due to cell-cell interactions. Also, *in vivo* study shows that cells attach to the nano-fibers of E-SFCS scaffolds and blood vessels align with silk fibroin fibrils regardless of E-SFCS or SFCS due to remodeling of the scaffolds after two weeks. Hence, guidance of cells in complex tissues formation may require cellular interactions at the nanoscale and E-SFCS may provide such a scaffold for tissue regeneration but cell-cell interactions such as endothelial cell-stem cell interactions play a larger role as well. Therefore, a balance of sub-structural features and cell-cell interactions has to be inter-played when dealing with stem cells *in vivo* to reach complete control of the regenerative process, where a regulated regeneration is reached and unregulated growth such as tumors is minimized in tissue engineered scaffolds.

Acknowledgements

Funding support for this work was provided by the Department of Defense, Telemedicine and Advanced Technology Research Centers. We would like to thank Dr. Jared K. Burks for helping in cytokinetic data capture, Arnie Jimenez for immunohistochemistry and Kenn Dunner for processing the SEM samples. Also, the help of Tom Anderson in designing the micropattern for engineered scaffolds is gratefully acknowledged. Micropattern electrodes were prepared at the Microelectronics Research Center at UT Austin of National Nanofabrication Infrastructure Network supported by National Science Foundation under award # 0335765.

References

1. Rios CN, Skoracki RJ, Miller MJ, Satterfield WC, Mathur AB. In vivo bone formation in silk fibroin and chitosan blend scaffolds via ectopically grafted periosteum as a cell source: a pilot study. Tissue Engineering: Part A. 2009;accepted Feb 2009.
2. Gobin AS, Froude VE, Mathur AB. Structural and mechanical characteristics of silk fibroin and chitosan blend scaffolds for tissue regeneration. J Biomed Mater Res A. 2005 Sep 1;74(3):465-73.
3. Anderson CR, Ponce AM, Price RJ. Immunohistochemical identification of an extracellular matrix scaffold that microguides capillary sprouting in vivo. J Histochem Cytochem. 2004 Aug;52(8):1063-72.
4. Gascoyne PR, Vykoukal J. Particle separation by dielectrophoresis. Electrophoresis. 2002 Jul;23(13):1973-83.
5. Wang XB, Yang J, Huang Y, Vykoukal J, Becker FF, Gascoyne PR. Cell separation by dielectrophoretic field-flow-fractionation. Anal Chem. 2000 Feb 15;72(4):832-9.
6. Chou CF, Tegenfeldt JO, Bakajin O, Chan SS, Cox EC, Darnton N, et al. Electrodeless dielectrophoresis of single- and double-stranded DNA. Biophys J. 2002 Oct;83(4):2170-9.
7. Morgan H, Hughes MP, Green NG. Separation of submicron bioparticles by dielectrophoresis. Biophys J. 1999 Jul;77(1):516-25.
8. Krupke R, Hennrich F, Lohneysen H, Kappes MM. Separation of metallic from semiconducting single-walled carbon nanotubes. Science. 2003 Jul 18;301(5631):344-7.
9. Venugopal J, Ramakrishna S. Applications of polymer nanofibers in biomedicine and biotechnology. Appl Biochem Biotechnol. 2005 Jun;125(3):147-58.
10. Smith LA, Ma PX. Nano-fibrous scaffolds for tissue engineering. Colloids Surf B Biointerfaces. 2004 Dec 10;39(3):125-31.
11. Altman AM, Yan Y, Matthias N, Bai X, Rios CN, Mathur AB, et al. IFATS Series: Human adipose-derived stem cells seeded on a silk fibroin-chitosan scaffold enhance wound repair in a murine soft tissue injury model. Stem Cells. 2008;Sept 25 Epub.

12. Altman AM, Rios CN, Alt EU, Mathur AB. A silk fibroin-chitosan matrix fosters attachment and migration of human tissue resident mesenchymal stem cells. 2008;submitted.
13. Norrby K. In vivo models of angiogenesis. J Cell Mol Med. 2006 Jul-Sep;10(3):588-612.
14. Bai X, Ma J, Pan Z, Song YH, Freyberg S, Yan Y, et al. Electrophysiological properties of human adipose tissue-derived stem cells. Am J Physiol Cell Physiol. 2007 Nov;293(5):C1539-50.
15. Lauffenburger DA, Linderman JJ. Receptors: Models for Binding, Trafficking, and Signaling. New York: Oxford University Press; 1993.
16. Palsson B, Bhatia SN. Tissue Engineering: Pearson Prentice Hall; 2003.
17. Leong AS-Y, Cooper K, Leong FJW-M. Manual of Diagnostic Antibodies for Immunohistology. 2nd ed: Greenwich Medical Media Ltd., London, England; 2003.
18. Gobin AS, Butler CE, Mathur AB. Repair and regeneration of the abdominal wall musculofascial defect using silk fibroin-chitosan blend. Tissue Eng. 2006 Dec;12(12):3383-94.
19. Pohl HA. Dielectrophoresis: the behavior of neutral matter in nonuniform electric fields: Cambridge University Press., Cambridge, England 1979.
20. Wang XJ, Wang XB, Gascoyne PRC. General expression for dielectrophoretic force and electrorotational torque derived using the Maxwell stress tensor method. Journal of Electrostatistics. 1997;39:277-95.
21. Jones TB, Washizu M. Multipolar dielectrophoreticand electrorotation theory. Journal of Electrostatistics. 1996;37:121-34.
22. Clague DS, Wheeler EK. Dielectrophoretic manipulation of macromolecules: the electric field. Phys Rev E Stat Nonlin Soft Matter Phys. 2001 Aug;64(2 Pt 2):026605.
23. Bondar B, Fuchs S, Motta A, Migliaresi C, Kirkpatrick CJ. Functionality of endothelial cells on silk fibroin nets: comparative study of micro- and nanometric fibre size. Biomaterials. 2008 Feb;29(5):561-72.
24. Murugan R, Ramakrishna S. Nano-featured scaffolds for tissue engineering: a review of spinning methodologies. Tissue Eng. 2006 Mar;12(3):435-47.
25. Nakayama S, Nozaki R, Senna M. Refinement of nano-structured fibroin thin films by near-IR pulsed laser deposition from targets consolidated with autogenous binder. J Biomater Sci Polym Ed. 2008;19(7):915-24.
26. Woo KM, Jun JH, Chen VJ, Seo J, Baek JH, Ryoo HM, et al. Nano-fibrous scaffolding promotes osteoblast differentiation and biomineralization. Biomaterials. 2007 Jan;28(2):335-43.
27. Venugopal J, Ramakrishna S. Biocompatible nanofiber matrices for the engineering of a dermal substitute for skin regeneration. Tissue Eng. 2005 May-Jun;11(5-6):847-54.
28. Karuri NW, Porri TJ, Albrecht RM, Murphy CJ, Nealey PF. Nano- and microscale holes modulate cell-substrate adhesion, cytoskeletal organization, and -beta1 integrin localization in SV40 human corneal epithelial cells. IEEE Trans Nanobioscience. 2006 Dec;5(4):273-80.
29. Scott JE, Parry DA. Control of collagen fibril diameters in tissues. Int J Biol Macromol. 1992 Oct;14(5):292-3.
30. Stokes CL, Lauffenburger DA, Williams SK. Migration of individual microvessel endothelial cells: stochastic model and parameter measurement. J Cell Sci. 1991 Jun;99 (Pt 2):419-30.

Table 1. Cytokinetic data for cell-seeded SFCS and E-SFCS scaffolds.

Scaffold Type	Cell Type and Culture	Average Speed (μm/hr)	Persistence Time (minutes)	% of moving cells (image frames)
SFCS	Single-culture HUVEC (n=3)	1.3 ± 0.7*	46.7 ± 6.7	3.6 ± 2.2† (3)
	Single-culture hASC (n=12)	18.5 ± 9.3	41.4 ± 24.7	40.3 ± 5.6 (3)
	Co-culture HUVEC (n=18)	3.1 ± 0.5*	35.2 ± 4.7	11.5 ± 3.8† (23)
	Co-culture hASC (n=8)	2.0 ± 0.3*	23.9 ± 2.7	5.8 ± 3.0* (23)
E-SFCS	Single-culture HUVEC (n=4)	5.1 ± 2.2	28.9 ± 8.7	6.0 ± 2.3 (4)
	Single-culture hASC (n=6)	11.1 ± 3.7†	37.9 ± 5.2	5.4 ± 3.0$^{\varphi}$ (3)
	Co-culture HUVEC (n=3)	3.6 ± 0.6	13.4 ± 0.8‡	0.74 ± 0.74‡ (15)
	Co-culture hASC (n=3)	1.8 ± 0.6	19.8 ± 1.8	6.7 ± 4.5 (15)

Data is represented as mean ± SEM. *$p<0.001$ vs. single culture hASC on SFCS, $^{\dagger}p<0.05$ vs. single culture hASC on SFCS, $^{\ddagger}p<0.05$ vs. co-culture HUVEC on SFCS, $^{\varphi}p<0.01$ vs. single culture hASC on SFCS.

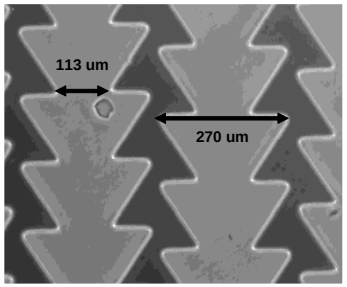

Fig. 1. Image of the triangular castellations on micropatterned electrode used for *in vivo* study.

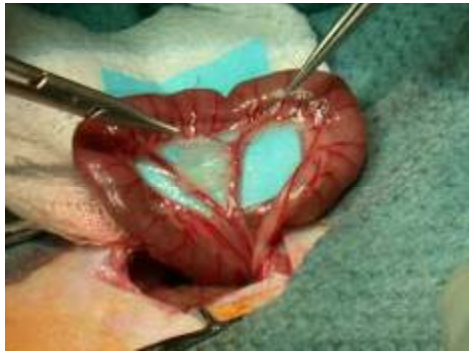

Figure 2

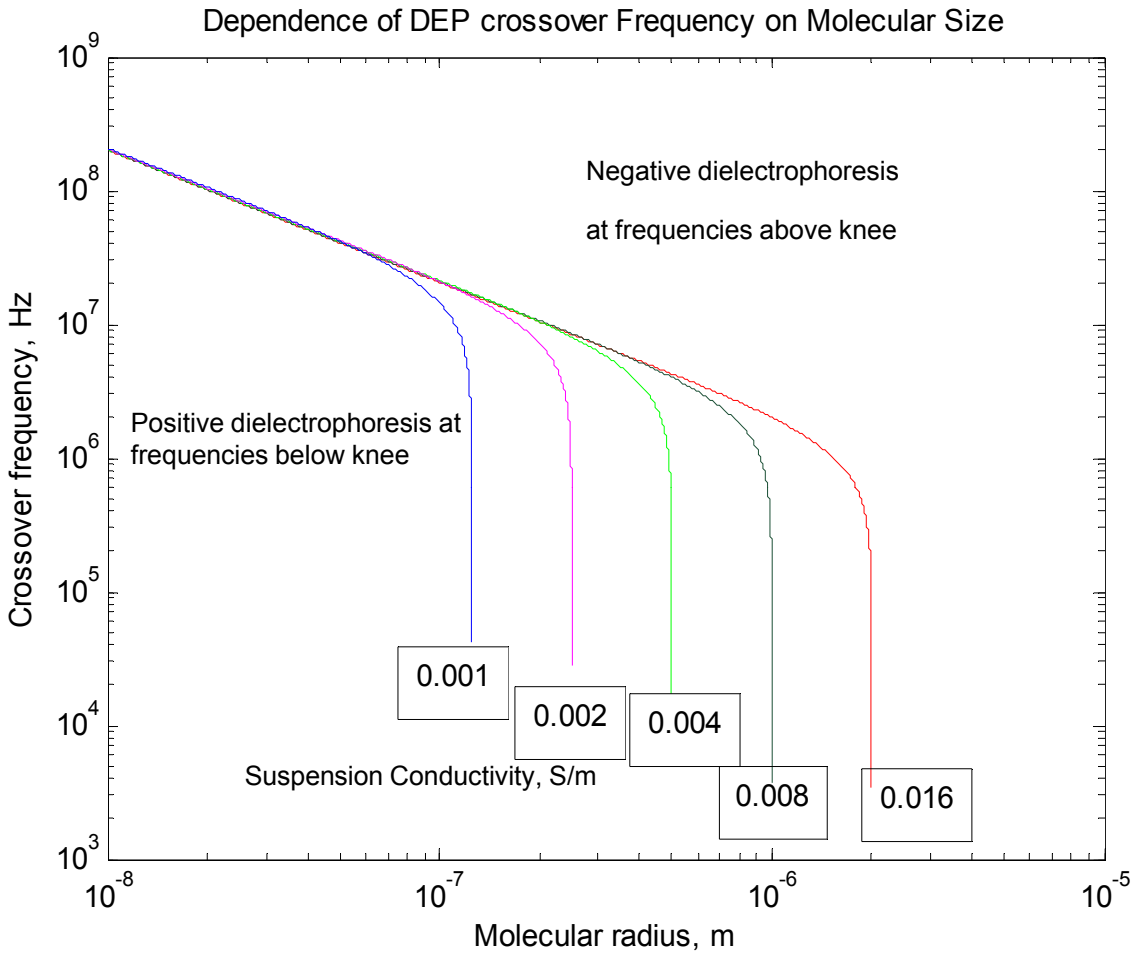

Fig. 3. Plot of crossover frequency versus particle radius for aqueous solutions of 1 to 16 mS/m conductivity, a core dielectric constant of 4, and a surface conductivity of 2 nS in order to illustrate the self-assembly of silk fibroin and chitosan polymers in to fibrils under dielectrophoretic forces.

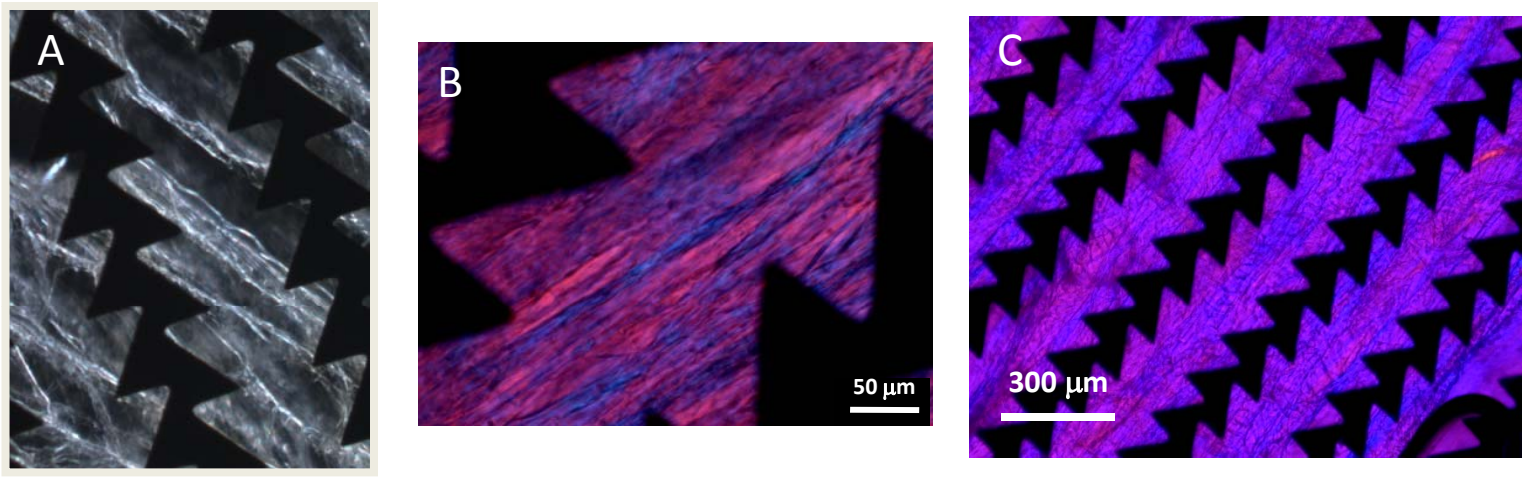

Figure 4

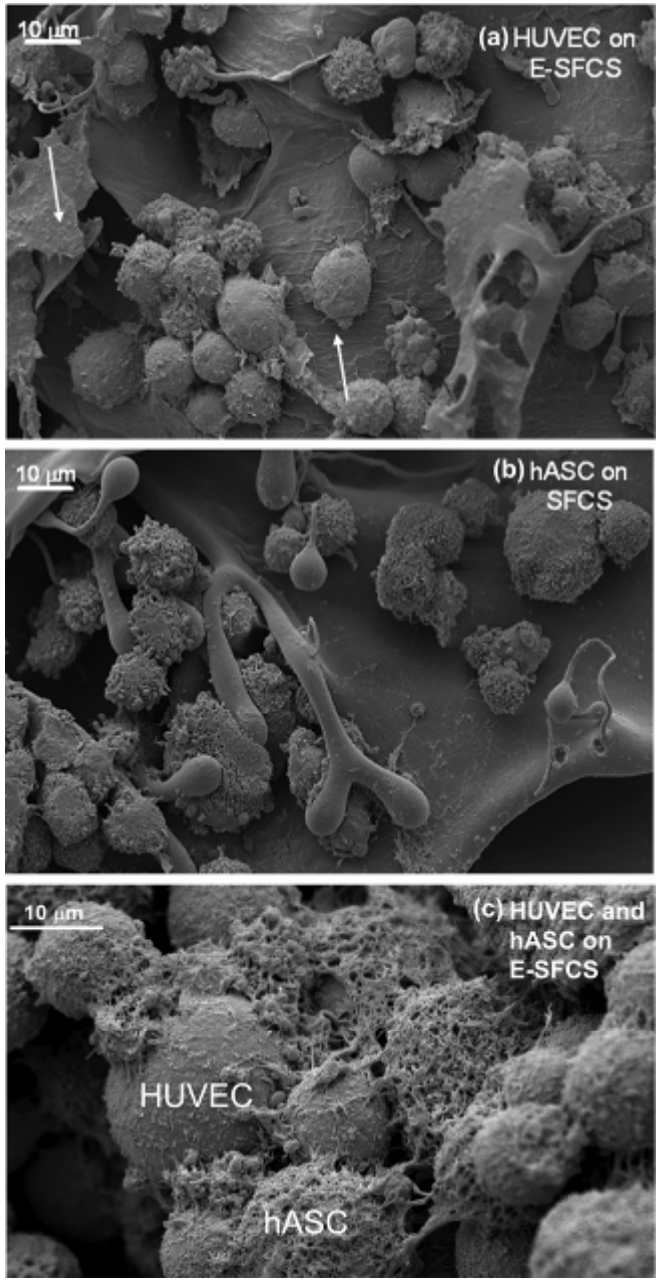

Figure 5. Representative SEM images of cell-seeded scaffolds. (a) Single-culture HUVEC seeded on top of E-SFCS, arrow indicates the nanofibers and ridges on scaffold surface. (b) Single-culture hASC seeded on top of SFCS. (c) Co-culture of HUVEC and hASC seeded on E-SFCS scaffold showing the interactions of HUVEC-HUVEC and HUVEC-hASCs through cell extensions.

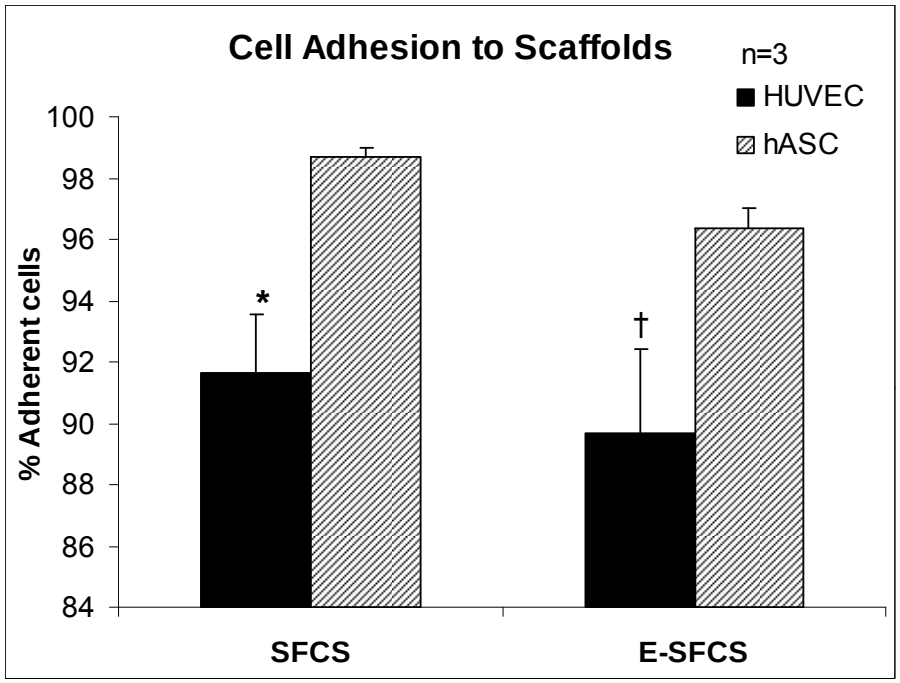

Fig. 6. Percentage adherence of HUVEC and hASC on SFCS and E-SFCS scaffolds after 30 minutes of seeding. Data represented as mean ± SEM. *p<0.05 vs. hASC on SFCS, †p<0.05 vs. hASC on E-SFCS.

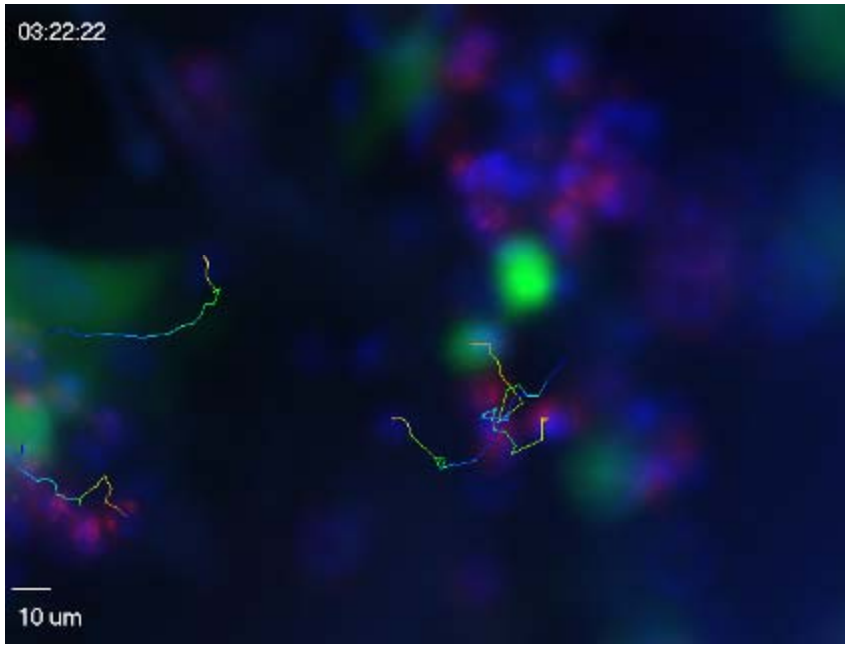

Figure 7. Confocal fluorescence microscope image of cells moving on top of SFCS scaffold. hASC are labeled green and HUVEC as blue with red cell membrane. The movement of cells was tracked as shown by the lines.

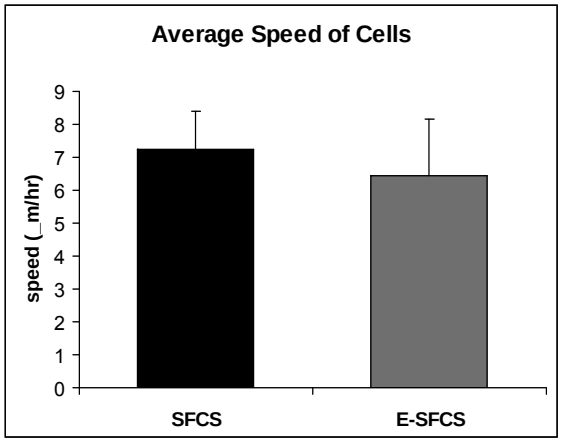

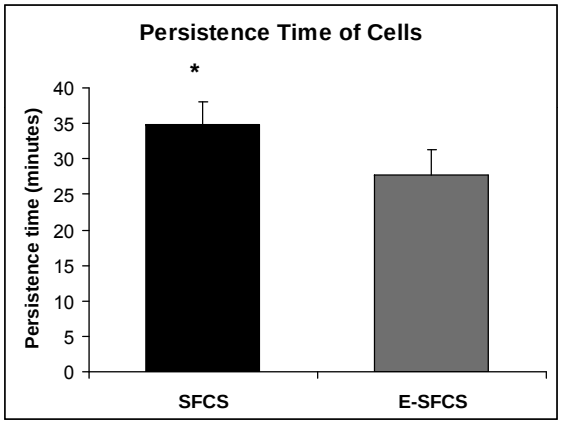

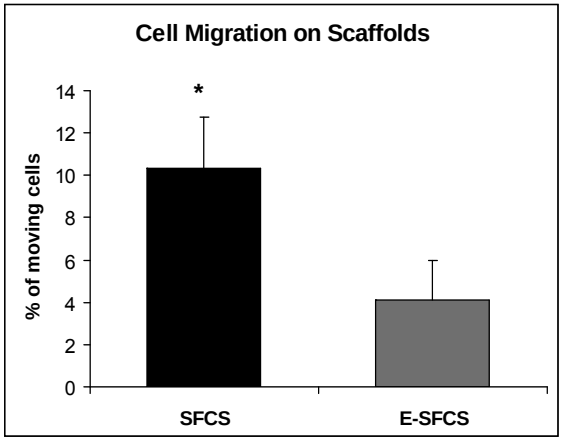

Figure 8. Cytokinetic data after combining hASC and HUVEC both in single and co-culture on SFCS and E-SFCS scaffolds during 4 hours of fluorescence imaging. Data represented as mean ± SEM. *$p<0.05$ vs. E-SFCS.

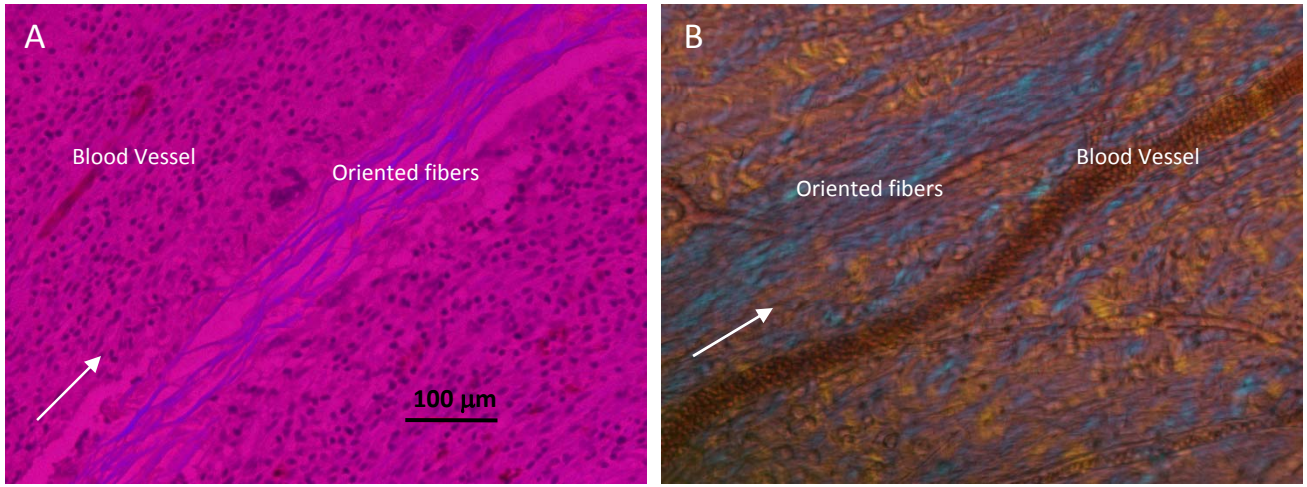
A
Blood Vessel
Oriented fibers
100 µm
B
Oriented fibers
Blood Vessel

Figure 9

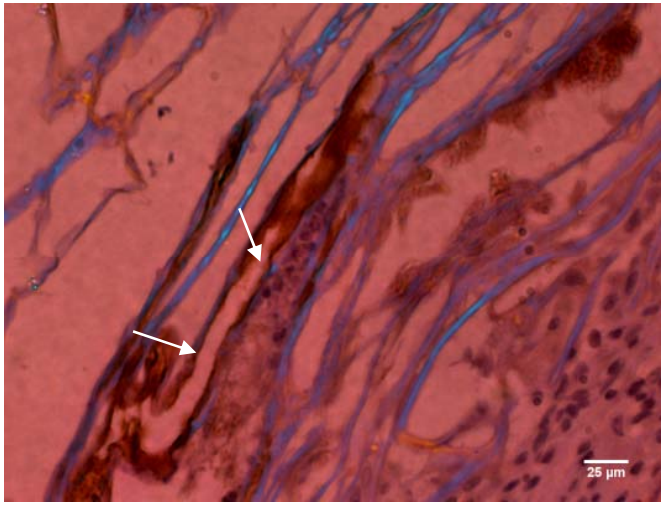

Figure 10. Microvascular Endothelial cells immmunostained for Factor VIII were imaged with polarized light microscopy with red retardation plate. Ecs attach to Silk Fibroin Fibrils (blue) and form a vessel between two fibrils. Arrows indicate the elongated morphology and raised nuclei of the endothelial cells is visible with Factor VIII staining.

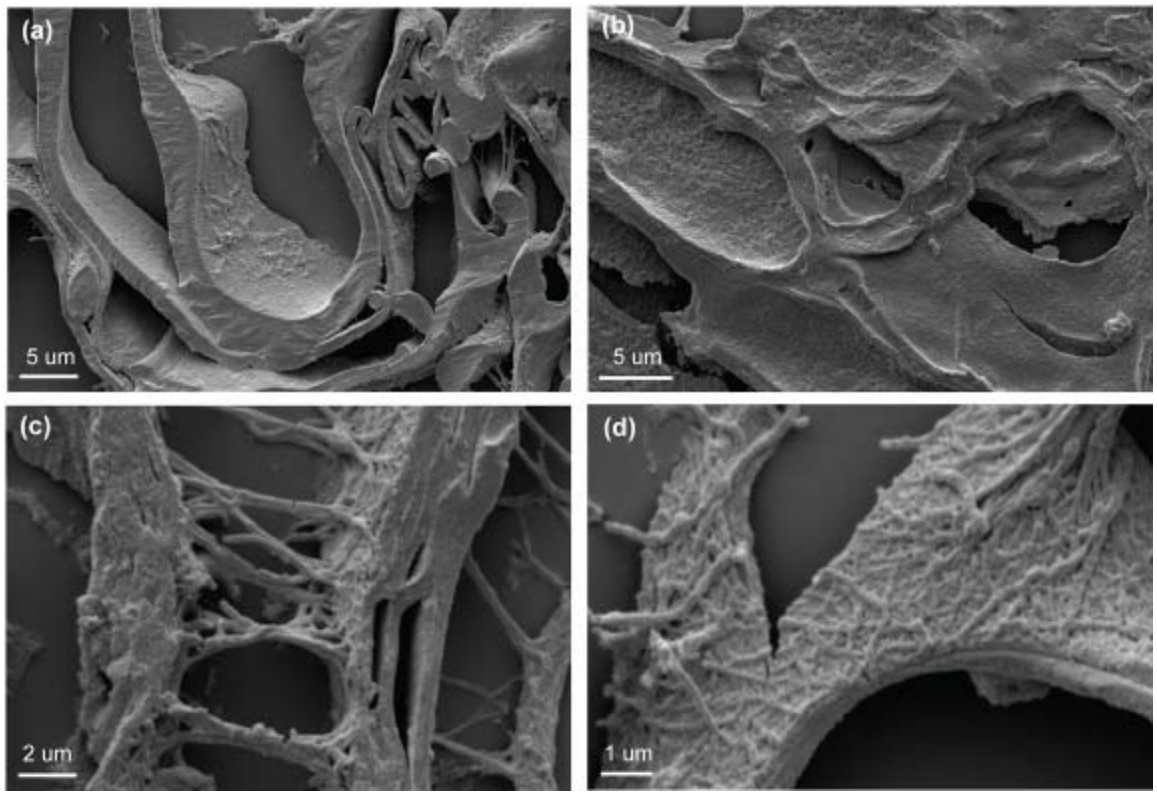

Fig. 11. SEM images of SFCS (a, b) and E-SFCS (c, d) scaffolds after 2 weeks of *in vivo* implantation in the rat mesentery. (a) and (c) show side of sheet view. (b) and (d) show top of sheet view. E-SFCS scaffolds show the nano-fibers on the surface and even parallel fibers connecting two scaffolds sheets.

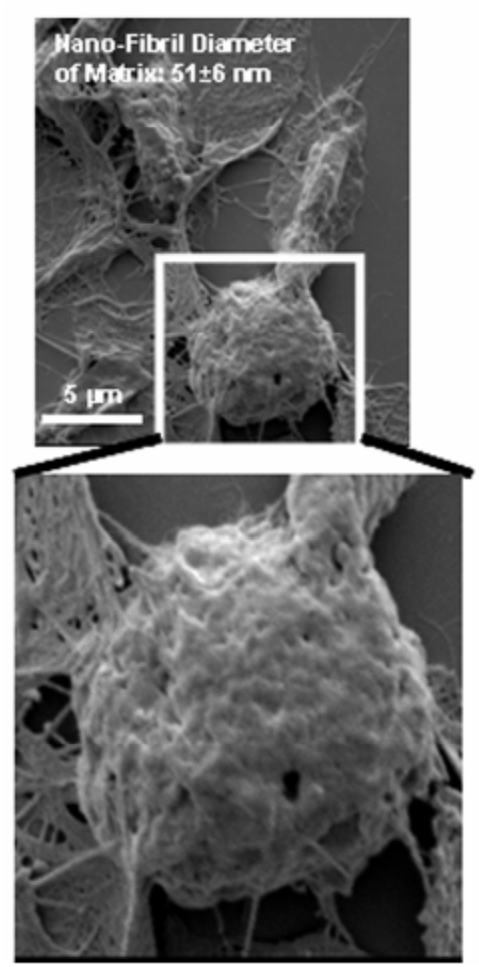

Figure 12. SEM images of E-SFCS scaffold with nano-morphology in 3-dimensions showing interaction of a cell with the nanofibril structures after 2 weeks of *in vivo* implantation in the rat mesentery. Bottom image is the zoomed in view of the top image.

Development of Nanotherapeutics to Enhance Wound Healing

Joan Nichols, PhD (University of Texas Medical Branch)

Roberto Advincula, PhD (University of Houston)

A report for Dr. Nichols' project was never filed with our office despite repeated attempts to contact the Principal Investigator.

Self-Asembling Peptide-Amphiphile Nanofiber Networks for the Controlled Growth and Differentiation of Dental Stem Cells

Jeffrey Hartgerink, PhD (Rice University)

Rena D'Souza, DDS, PhD (UT Health Science Center at Houston)

Drs. Hartgerink and D-Souza finished their seed project during the original performance period (June 20, 2006 – September 20, 2007) and therefore did not carry out experiments or incur expenses during the performance period being reported in this Annual Report.

Alliance for NanoHealth Seed Grant

Title: Feasibility of selective laser elimination of leukemia cells targeted with gold and silver nanorods.

Final Progress Report 02-28-2009

Principal Investigator: Marina Konopleva, M.D., Ph.D.
Assistant Professor
Department of Blood and Marrow Transplantation
The University of Texas M.D. Anderson Cancer Center
1515 Holcombe Blvd., Unit 448
Houston, Texas 77030
Tel. 713-794-1628; Fax. 713-794-4747
Email: mkonople@mdanderson.org

Co-Investigator: Jason Hafner, Ph.D.
Associate Professor of Bioengineering,
Rice University
6100 Main Street
Houston, Texas 77005
Tel. 713-737 5870
Email: hafner@rice.edu

Co-Investigator: Alexander Oraevsky, Ph.D.
Vice President for Research and Development
Fairway Medical Technologies, Inc.
Houston, Texas 77099
Tel. 713-772-7867
Email: aoraevsky@fairwaymed.com

Background:
Despite recent advances in the chemotherapy of hematologic malignancies, a large proportion of patients remain incurable. ASCT is potentially curative treatment strategy, which is limited by the risk of re-infusion of residual tumor cells in the graft. While numerous purging methods have been developed, no existing method removes 100% of the tumor cells from the transplant. The nanotechnology of fabricating gold and silver nanorods has only recently become available. This project is based on the patented method of LANTCET, which uses gold NRs to enable selective *ex vivo* purging of tumor cells from a mixture with normal cells. Gold and silver nanorods (NR) possess very strong optical absorption tunable in the near-infrared spectral range (650 nm to 1100 nm) by changing their aspect ratio (of length to diameter). NPs can be targeted specifically to tumor cells using monoclonal antibodies (MAB). The cells loaded with gold NR can be detected using photothermal imaging and destroyed by laser-generated microbubbles (LMB) of vapor that emerge around the optically absorbing gold NRs. The proposed collaboration is aimed at developing an image-guided Laser Assisted NanoThermolysis Cell Elimination Technique (LANTCET) for purging of leukemia cells from autologous bone marrow or apheresis grafts.

AIMS:
1. Evaluate efficacy and safety of LANTCET technology with gold nanorods in model K562 cells based on protocols established earlier for spherical gold nanoparticles
2. Develop optimized protocol of conjugation, protocol of cell targeting, and protocol of laser treatment, methods for analysis of treated cells (dead and live).

Cells: Tumor model: K562, HL-60
MAB: CD33
Nanoparticles: Gold nanorods with aspect ratio of 3.6 (wavelength approximately 750-800 nm).
Laser: Pulsed laser 680-850 nm, energy of 100 mJ to create microbubbles around NR clusters

Methods

1. NR detection in individual cells: Flow Cytometry, Fluorescence Microscopy, SEM, Light

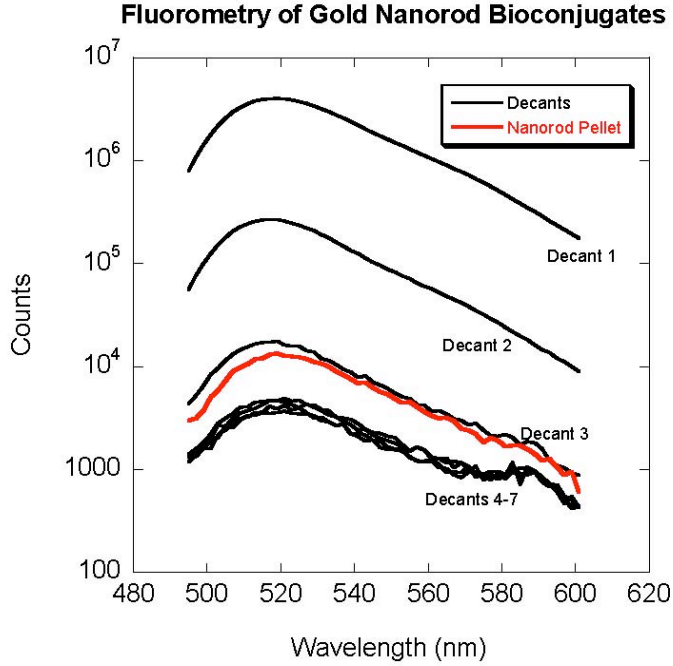

Figure 2. Fluorometry of nanorod conjugates after rounds of centrifugation

Scattering Microscopy, silver stain

2. Cell damage detection: Concentration count (hemocytometer), Flow Cytometry Viability Count (live/dead fluorescence assay)

Results

1. Developed a method of reliable fabrication of gold nanorods (GNR) with narrow distribution of aspect ratio to accurately match the GNR absorption peak with the laser wavelength.
2. Developed conjugation of GNR with PEG to produce “stealth” nanoparticles invisible by the immune system.
3. Developed a method of covalent conjugation of gold nanorods with monoclonal antibodies and demonstrated stability of these conjugates in blood.

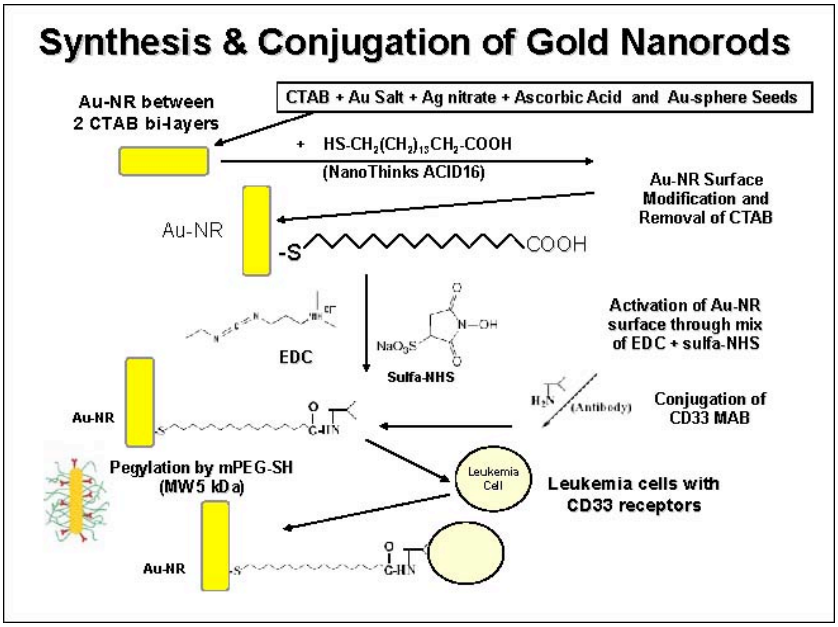

4. Demonstrated high specificity and good efficiency of accumulation of such conjugates in cultures of leukemia cells: K562 and HL60

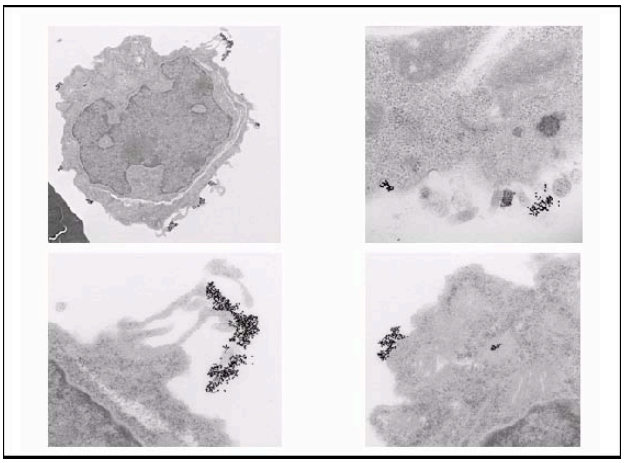

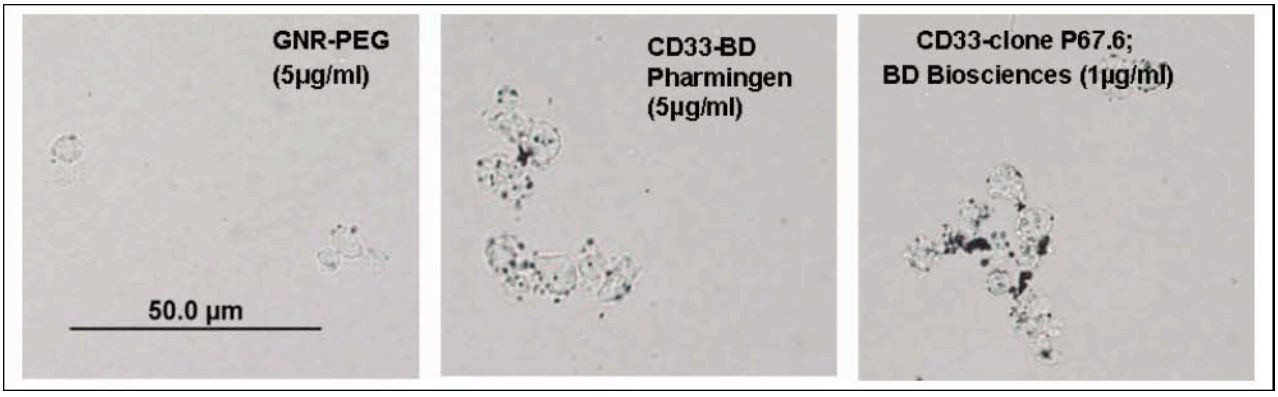

5. Performed successful laser ablation experiments in HL60 and K562 cell cultures and mixtures of primary AML with normal cells, thereby demonstrating feasibility of LANTCET (laser assisted nano-thermolysis as cell elimination technology).

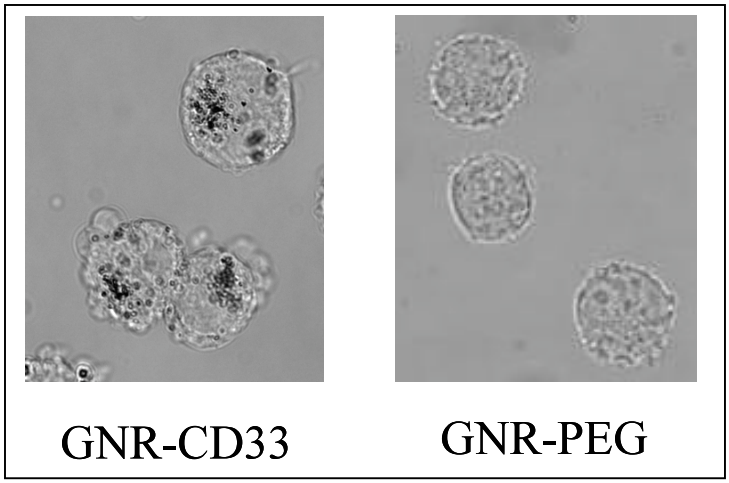

6. Reported the results at DoD retreat meeting with Program Director

D) Conclusions

In the course of the ANH/DoD project we made the following two main accomplishments: (1) developed and tested an improved gold nanorod conjugates with poly(ethylene-glycol) and monoclonal antibody against leukemia cells that can be effectively used for targeting these cells *in vivo*, and (2) improved the design of our laser irradiation system to enable LANTCET procedure in a static and flow cuvettes. The laser beam homogeneity was also improved to provide equal irradiation conditions to all cells in the treatment area, which in turn improves selectivity of the treatment.

The significance of our first accomplishment is that we can now begin targeting specific molecular receptors in live primary cells. We tested stability of our conjugates in live blood and concluded that the immune system of a live animal does not destroy out GNR conjugates keeping them biologically active for targeting tumor cells. The mechanism of the covalent conjugation for gold nanorods we developed and PEG protection can be applied to any monoclonal antibody.

The significance of our second accomplishment is that we can now begin statistically significant experimental work in suspensions of primary cells, with the goal to achieve highest possible efficacy and specificity of the laser treatment.

The nano-technological contrast (therapeutic) agent and the selective technology for laser treatment of cells being developed by our project promises to deliver in future highly effective method of elimination of abnormal cells from human tissues, such as bone marrow and blood.

E) Translation to Military Medicine

Leukemia is one of the prevalent types of cancer in the military personnel that works in the hazardous environment and high radioactivity zones. Our project is intended to improve the state of the art methods of bone marrow and blood transplantation by eliminating tumor cells from the grafts. If commercialized, our technology will save lives of leukemia patients. In addition, our platform technology can be potentially applied for elimination of other cells from human blood and other tissues.

F) Scientific Publications, Abstracts, & Presentations

1. D. Lapotko, E. Lukianova, P. Mitskevitch, V. Smolnikova, M. Potapnev, M. Konopleva, M. Andreeff, A.A. Oraevsky: Photothermal and photoacoustic processes in laser activated nano-thermolysis of cells, *Proc. SPIE* 2007; **6437**: 6437031-6437037.
2. D.O. Lapotko; E.Y. Lukianova-Hleb; S.A. Zhdanok; J.H. Hafner; B.C. Rostro; P. Scully; M. Konopleva; M. Andreeff; C. Li; E.Y. Hanna; J.N. Myers; A.A. Oraevsky: LANTCET: laser nanotechnology for screening and treating tumors ex vivo and in vivo, *Proc. SPIE* 2007; **6735**; 673516.
3. D.O. Lapotko, E.Y. Lukianova-Hleb, A.A. Oraevsky: Clusterization of nanoparticles during their interaction with living cells. *NanoMed*. 2007, **2**(2): 241-253.
4. D. Lapotko, E. Lukianova-Hleb, S. Zhdanok, B. Rostro, R. Simonette, J. Hafner, M. Konopleva, M. Andreeff, A. Conjusteau, and A.A. Oraevsky: Photothermolysis by laser-induced microbubbles generated around gold nanorod clusters selectively formed in leukemia cells, *Proc. SPIE* **6856**, 68560K, 9p (2008).
5. Hleb, E. Y., Hu, Y., Drezek, R. A., Hafner, J. H., Lapotko, D. O. Photothermal bubbles as optical scattering probes for imaging living cells, *NanoMed*. 2008; **3**(6): 797-812.
6. Kathryn M. Mayer, Seunhyung Lee, Hongwei Liao, Betty C. Rostro, Amaris Fuentes, Peter T. Scully, Colleen L. Nehl, Jason H. Hafner, "A label-free immunoassay based upon localized surface plasmon resonance of gold nanorods" ACS Nano 2008, **2**(4), 687-692.
7. Betty C. Rostro, Lissett R. Bickford, Courtney M. Payne, Emily S. Day, Seunhyung Lee, Kathryn M. Mayer, Tomasz Zal, Liana Adam, Colin P. N. Dinney, Rebekah A .Drezek, Jennifer L. West, Jason H. Hafner, "Stabilization and Targeting of Surfactant-Synthesized Gold Nanorods", Bioconjugate Chemistry, submitted.

G) Funding Received as a result of the seed funds

An R21CA129872 grant application was submitted to NCI, however, not funded. We will improve our application by adding new results and resubmit in 2009.

Photothermolysis by laser-induced microbubbles generated around gold nanorod clusters selectively formed in leukemia cells

Dmitri Lapotko[*a], Ekaterina Lukianova-Hleb[a], Sergei Zhdanok[a], Betty Rostro[b], Rebecca Simonette[b], Jason Hafner[b], Marina Konopleva[c], Michael Andreeff[c], Andre Conjusteau[d], Alexander Oraevsky[d]

[a]Lykov Heat and Mass Transfer Institute, 15 P. Brovka St, Minsk 220072, Belarus;
[b]Rice University, 6100 Main St., Houston, TX, 77005;
[c]University of Texas M.D. Anderson Cancer Center, 1515 Holcombe Blvd, Houston, TX, 77030;
[d]Fairway Medical Technologies, Inc, 9431 W. Sam Houston Parkway South, Houston, TX 77099.

ABSTRACT

In an effort of developing clinical LANTCET (laser-activated nano-thermolysis as cell elimination technology) we achieved selective destruction of individual tumor cells through laser generation of vapor microbubbles around clusters of light absorbing gold nanorods (GNR) selectively formed in target tumor cells. Among all gold nanoparticles, nanorods offer the highest optical absorption in the near-infrared. We applied covalent conjugates of gold nanorods with targeting vectors such as monoclonal antibodies CD33 (specific for Acute Myeloid Leukemia), while GNR conjugates with polyethylene-glycol (PEG) were used as nonspecific targeting control. GNR clusters were formed inside the tumor cells at 37 ^{0}C due to endocytosis of large concentration of nanorods accumulated on the surface of tumor cells targeted at 4 ^{0}C. Formation of GNR clusters significantly reduces the threshold of tumor cell damage making LANTCET safe for normal cells. Appearance of GNR clusters was verified directly with optical resonance scattering microscopy. LANTCET was performed *in vitro* with living cells of (1) model myeloid K562 cells (CD33 positive), (2) primary human bone marrow CD33-positive blast cells from patients diagnosed with acute myeloid leukemia. Laser-induced microbubbles were generated and detected with a photothermal microscope equipped with a tunable Ti-Sa pulsed laser. GNT cluster formation caused a 100-fold decrease in the threshold optical fluence for laser microbubble generation in tumor cells compared with that in normal cells under the same targeting and irradiation conditions. Combining imaging based on resonance optical scattering with photothermal imaging of microbubbles, we developed a method for detection, image-guided treatment and monitoring of LANTCET. Pilot experiments were performed in flow mode bringing LANTCET closer to reality of clinical procedure of purging tumor cells from bone marrow grafts.

Keywords: gold nanoparticle cluster, cell damage, tumor cell, laser-induced bubble, purging.

1. INTRODUCTION

Gold nanospheres (GNS) that absorb strongly in the visible spectral range and gold nanorods (GNR) that absorb very strongly in the near-infrared spectral range hold a significant potential as diagnostic and therapeutic contrast agents [1-5]. These nanoparticles (NPs) were found non-toxic to normal cells [6,7]. Recently, possibility of selective destruction of tumor cells without damage of normal cells was demonstrated through selective laser nanothermolysis based on absorption properties of GNS and GNR [1,8-17]. Natural process of endocytosis aimed at protection of living cells from foreign bodies on their surfaces is known to result in accumulation of gold nanoparticles inside the cells. We manipulated with temperature of cell environment to increase accumulation of nanoparticles conjugates on the membrane surface, then to increase uptake and form nanoparticle clusters (NPC) inside the cells. Formation of small and large groups of nanoparticles linked though specific vectors to membrane receptors on cellular surfaces was noticed in earlier experiments that dealt with nanoparticle-cell interactions [8,18-22]. The goal of our experiments was to achieve effective internalization and formation of large clusters inside the target cells. We found that after internalization at 37 ^{0}C large groups of nanoparticles can aggregate in specific cellular compartments (endosomes) inside the cell [18-22].

* ld@hmti.ac.by, phone: (+375)172842483; fax: (+375)172842483; aoraevsky@fairwaymed.com, phone: 17137727867

Photons Plus Ultrasound: Imaging and Sensing 2008: The Ninth Conference on Biomedical Thermoacoustics, Optoacoustics, and Acousto-optics, edited by Alexander A. Oraevsky, Lihong V. Wang, Proc. of SPIE Vol. 6856, 68560K, (2008) · 1605-7422/08/$18 · doi: 10.1117/12.771660

NPCs were intentionally produces in tumor cells with the goal to improve selectivity of pulsed laser nano-thermolysis of tumor cells [14-16,22-24]. Advantages of nanoparticles clusters over single NPs for medical diagnostics and therapy using optical methods include greatly increased total volume, which allows effective photo-thermo-mechanical interactions under conditions of relatively slow heat diffusion. Formation of NPCs in target cells permits significant reduction of the laser fluence threshold for selective pulsed laser thermolysis of tumor cells with simultaneous enhancement of safety of this treatment for normal cells.

Three years ago we introduced laser-activated nano-thermolysis as cell elimination technology (LANTCET), a new method for selective killing of tumor cells [14]. This method utilizes vapor microbubbles generated by laser pulses selectively around superheated clusters of gold nanoparticles [14-16, 22-24]. This selective nanothermolysis was demonstrated for variety of tumor cells using similar cell targeting protocols that resulted in formation of nanoparticle clusters. In the present work we experimentally demonstrated that gold nanorods strongly absorbing in the NIR spectral range can significantly improve the efficacy, selectivity and safety of optical diagnostics and therapy [10].

2. MATERIALS AND METHODS

2.1 Principle of laser-activated nano-thermolysis as cell elimination technology (LANTCET).

The method for selective elimination of target tumor cells from a mixture with normal cells includes three steps: (a) administration of gold NP conjugates nontoxic to cells unless irradiated with laser pulses, followed by selective accumulation of the conjugates in target tumor cells through cell receptor affinity to tumor-specific monoclonal antibodies (MAB) or peptide vectors conjugated to NP, (b) endocytosis of NPs with subsequent formation of NP clusters, and (c) selective destruction of tumor cells by pulsed laser-induced microbubbles (LMB) generated around NPC in target cells (Figure 1) [14-16,23,24].

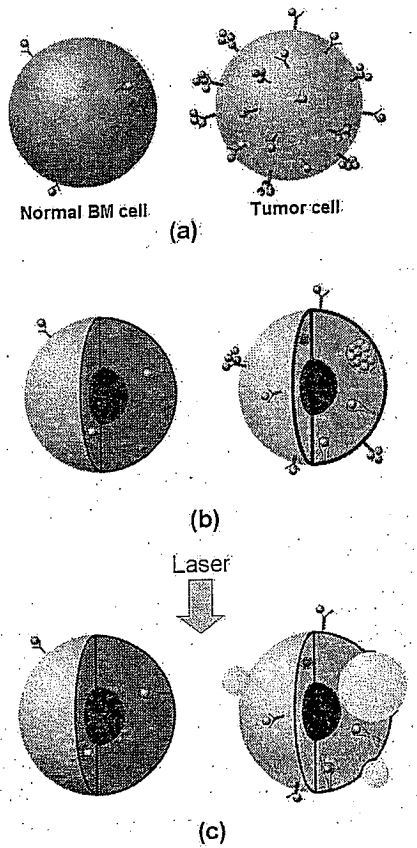

Figure 1. Graphic diagram explaining three steps of LANTCET: (a) membrane targeting with NPs, (b) formation of NPCs selectively in target cells, (c) laser-induced vapor bubbles resulting in the cell damage.

In the present set of experiments we achieved high selectivity of NPC formation in the target tumor cells, however, the targeting efficiency was greatly variable, especially in the primary human cells. We used two different cell incubation protocols. At this time, we can not give preference to one or the other protocol described below.
In one set of experiments, single stage incubation was performed at 37 ^{0}C using gold nanorods conjugated with specific monoclonal antibody. In another set of experiments we used a two-stage incubation procedure, in which the first stage targeting was done at 4 ^{0}C followed by the second stage performed at 37 ^{0}C [22]. In the first stage NPs were selectively coupled to the membranes of target cells using specific MAB (Figure 1a). MAB can provide strong selective coupling to membrane receptors and for tumor cells there are established MABs that are diagnosis-specific. At 4 °C most cell membrane receptors are located on the very surface with active sites facing outside the cell, so that maximum number of NPs could be accumulated at the surface of cell membrane. To stimulate uptake by cells at the second stage, the temperature was increased to physiological level of 37 °C. The second stage was intended to create maximal size NP clusters inside the target cells (Figure 1b). The incubation time set to 30-60 minutes was sufficient for complete internalization of NPs through endocytosis. Endocytosis is a universal and fast biological mechanism that delivers NPs and small clusters of NPs from the cell membrane into the cytoplasm where NPs are concentrated into larger clusters inside endosomes.
At the end of the incubation procedure large NP clusters were formed only in those cells with high initial levels of membrane-bounded NP, i.e. the target tumor cells [22, 23]. After that, tumor cells destruction could be effectively achieved through generation of laser-induced microbubbles around NPCs strongly absorbing short laser pulses at a specific wavelength in the NIR (Figure 1c). The laser fluence was set at the minimal level above the threshold that provides bubble generation only around the biggest NP clusters (>200 nm) and does not induce any bubbles around single NPs. In the previous reports we showed that the optical fluence threshold for generation of microbubbles around single NPs is more than an order of magnitude higher than that for generation of microbubbles around NPCs [24, 25]. The fine tuning of the optical fluence provides high selectivity of tumor cell killing and safety for normal cells, which accidentally uptake only single NPs.
As depicted in Fig.2, left panel, LANTCET protocol can be complemented by a stage of tumor cell detection using resonance optical scattering at the wavelength of NPC scattering (strong scattering driven by plasmon resonance in large gold nanoparticles was reported by several groups [2, 26, 27]. Selective destruction (nanothermolysis) of individual tumor cells by pulsed laser-induced microbubbles can conveniently monitored with photothermal microscopy [28]. A distinct feature of vapor microbubbles is that they have high optical refraction contrast (Fig.2, right panel). Therefore, real-time optical monitoring of cell damage through detection (imaging) of laser-induced microbubbles can be used as a guiding tool for LANTCET.

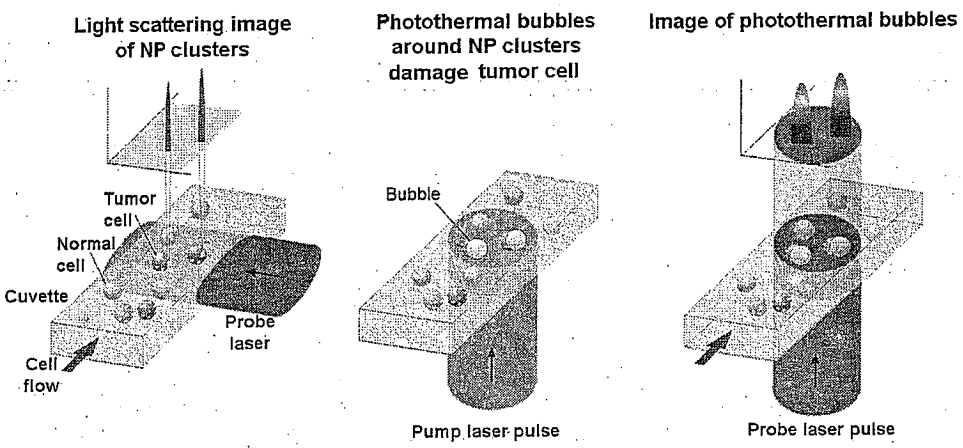

Figure 2. LANTCET stages: light-scattering imaging of NP clusters in individual targeted cells (left); damage of targeted cells with microbubbles that are induced by a high-fluence laser pulse (middle); detection of cell damage by recording images of microbubbles (right).

2.2 Cells

To understand mechanisms of laser generation of microbubbles we have used water suspension of gold NPs and NP clusters. Water suspensions of NP were prepared using gold nanorods with dimensions of approximately 15x54 nm and

absorption maximum at ~760-780 nm. 10 μl of GNR suspension was placed into a standard 9 mm diameter culture well (#C24765, Molecular Probes, Inc., Eugene, OR) and sealed with a glass cover slip. The concentration of GNR was adjusted so to provide average distance between them to be much greater than 1μm. This excluded any possible collective thermal effects during absorption of short laser pulses. NPCs were formed from the suspension of these GNR by adding 50% acetone. Transition from single GNR to aggregation was verified by the broadening optical absorption peak. Then GNR clusters were resuspended in water.

Anti-leukemia application of LANTCET was tested first in suspensions of cultured K562 cells, which have high level of expression of CD33 antigens. Then experiments were conducted using primary samples of human bone marrow (BM) were taken either from normal donors or patients with the diagnosis of acute myeloid leukemia (AML). All AML samples consisted mainly of tumor cells (the level of B-lymphoblasts was 94 to 98% in samples from different patients). Leukemia cells overexpress CD33 diagnosis-specific genes that were determined using standard flow cytometry.

We used conjugates of gold nanorods (GNR) with and without antibodies CD33. As a nonspecific targeting control, GNR were conjugated with polyethylene-glycol (PEG), through one end functionalized by thiol group [10]. For specific targeting experiments, AML and K562 cells were incubated with GNR-MAB conjugates as described above. Then live and fixed cells were used as suspensions for microbubble generation and detection.

2.3 Generation and detection of laser-induced microbubbles.

In this study we applied photothermal (PT) microscope shown in Fig. 3 for generation and detection of laser-induced microbubbles in individual cells [25, 28]. Each cell was illuminated with 3 collinear focused laser beams: pulsed high fluence beam tunable from 720 nm to 840 nm for microbubble generation, and low-power continuous (633 nm, 0.1 mW) and pulsed (532 nm, 0.1 mJ) probe beams for detecting microbubbles in tumor cells in real time. A microbubble-related change of refractive index causes a phase shift (refraction) of the probe beam that influences beam intensity at the input of the photodetector. The output of the photodetector was measured as a digital PT response by a standard data acquisition board with a fast analog-to-digital converter. When microbubble is generated in a cell, PT response has a specific shape, providing convenient means for detection of microbubbles in the course of pulse laser irradiation of individual cells. Each individual cell (total of 90 for each sample) was irradiated one by one with single focused laser pulse of the same fluence at 720-840 nm. PT image and a time-resolved signal from each cell were simultaneously recorded. The image was recorded using delayed pulsed probe laser, while the response signal was recorded using CW probe laser beam. This monitoring method allowed (1) detection of the bubbles and (2) measurement of the microbubble lifetime that characterizes maximum bubble diameter. After sequential irradiation of all cells in the sample and registering PT images and signal responses from each cell we measured the probability P_{MB} of microbubble generation at specific laser fluence as:

$$P_{MB} = N_2 / N \tag{1}$$

where N is the number of irradiated cells, and N_2 is the number of cells with a bubble-specific PT response. The microbubble generation threshold fluence for specific pump laser wavelength was defined as the fluence that corresponds to P_{MB} level of 0.5.

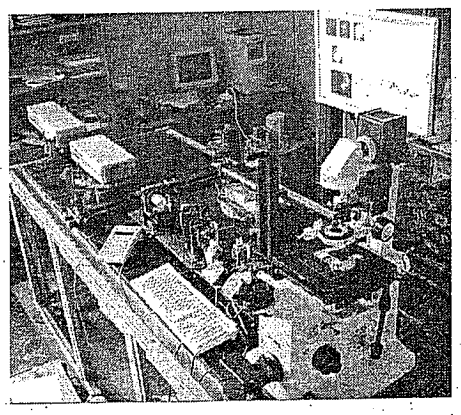

Figure 3. Photograph of a photothermal microscope used in the microbubble monitoring experiments.

For time-resolved imaging of microbubbles in individual cells we used 10-ns pulsed pump laser beam. CCD-camera used as an image detector captured pulsed laser images so that only events that occurred during the pulse duration were visualized. This high temporal resolution method permitted analysis of microbubble location and diameter.

2.4 Light-scattering microscopy

Gold NPs are known not only as excellent light absorbers, but also for their strong optical scattering in the NIR spectral range [2, 5, 26, 27]. Fraction of right angle (90°) scattering of incident light due to surface plasmon resonance is size-dependent, the wavelength of maximal scattering increases with increasing NP dimensions. The same optical microscope as used in PT microscopy experiments, was also employed in resonance scattering measurements. As the source of light we used white light continuous source filtered through a NIR band-pass filter. Light was directed with optical fiber at the glass slide with the sample at the angle 70-80 deg. Optimal angle was adjusted to achieve maximal intensity of scattered light. Optical scattering measurements use the same source of signals, gold nanoparticles. Scattering properties of gold NPs are very different from those of any endogenous cellular components.

3. RESULTS AND DISCUSSION

3.1 Generation of photothermal bubbles around NP in suspension.

Single GNR and GNR clusters were imaged with optical scattering microscopy (Fig. 4). Average size of GNR clusters was estimated to be in the range of 200-400 nm. Water suspension of non-aggregated GNRs was irradiated and imaged as additional control to study generation of microbubbles around single nanoparticles. Optimal concentration of GNR provided about 10 GNRs within a volume of NP suspension covered by the laser beam. The averaged distance between GNR particles was about ten micrometers. This excluded any collective effects during interaction of laser pulse with these NPs. We scanned pulsed pump laser beam across the cuvettes with samples of GNR and GNR clusters without the cells. Pump pulse wavelength was tuned to the maximum of NP absorbance at 760 nm, and the fluence varied from 0.5 to 20 J/cm2. Thus the thresholds of microbubble generation were determined for the suspensions of single NPs and for their clusters. The optical fluence threshold of laser-induced microbubbles was >3 J/cm^2 for single GNR and <0.3 J/cm^2 for GNR clusters, which is an order of magnitude lower. Fig. 4 shoes images of NP suspensions obtained by pulsed probing the cuvettes 500 ns after irradiation with the pump laser having an optical fluence of 1.1 J/cm^2. No microbubbles were detected at this fluence level around single NPs, while GNR clusters produced microbubbles with the diameters of 1-10 μm (Fig. 4). Such big bubbles are sufficient for mechanical destruction of the cell membranes. The difference in the optical fluence threshold for generation of vapor bubbles around single GNR and GNR clusters demonstrate the selectivity of LANTCET method. With sufficiently low optical fluence only the biggest GNR clusters can serve as sources of laser-induced bubbles and result in selective cell nano-thermolysis.

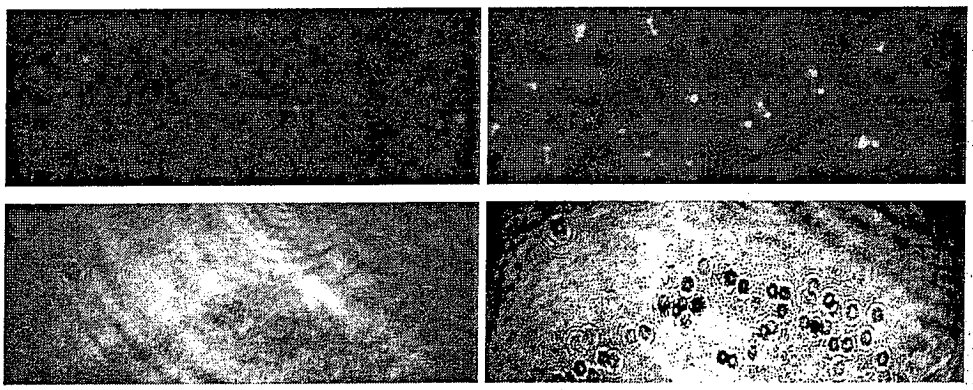

Figure 4. Optical scattering images (top) of the layers of GNR (left) and clusters of GNR (right) in suspension in water and time resolved images (bottom) of the layers of GNR (left) and clusters of GNR (right) in suspension in water during they scanning with pump pulsed laser (740 nm, 1.1 J/cm^2); pump laser can path through GNR clusters show microbubbles, while no bubbles were generated at this laser fluence around single GNR.

3.2 Optical scattering images and spectra of NP clusters in cells

Formation of NP clusters was verified directly with optical scattering microscopy and microspectroscopy. GNR-treated and control (untreated) K562 cells were imaged using photothermal microscopy. We obtained images of individual cells with resolution of about 0.5 μm (Figure 5). Those images revealed two common features in both AML and K562 cells: (1) NPC-related signals were detected in 90-95% of targeted cells and (2) spatial distribution of NPC-related signals within the cell was highly heterogeneous with apparent local peaks. On the other hand, no NPC-related signals were found in the images of control cells. This indicates that regardless of targeting method used the NPs aggregate into clusters during interaction with living cells. However, increased concentration of accumulated nanoparticles on the cell membrane and increased temperature around physiological level can substantially enhance probability of cluster formation in the target cells. Amplitudes of scattering signals were 1230±580 for intact control cells and 3980 ±1170 for GNR targeted K562 and AML cells. Scattering images were recorded with continuous white light source through a NIR filter and no photobleaching effects occurred. GNR, therefore are well suitable for molecular imaging and quantitative studies. Untreated (control) cells also produced some optical scattering though with much lower amplitudes and without strong local peaks (Figure 5a). Optical scattering sensitivity may be improved by using a monochromatic light source at the wavelength that matches the wavelength of plasmon resonance scattering peak for GNR clusters. Spectral studies of the cells were performed with a microspectrometer. Scattering spectra of a local zone with diameter not bigger than 1 μm were measured for both, the control and GNR targeted cells (Figure 5c). For the targeted cells the spectra were measured in areas occupied by GNR clusters. Cluster-related spectrum has yielded resonant nature of scattering and is very close to that obtained for the water suspension of GNR: their peak almost coincide (680 nm for GNR water suspension and 670 nm for GNR clusters in cells). This allowed us to conclude that local scattering signals represent clusters of gold nanorods.

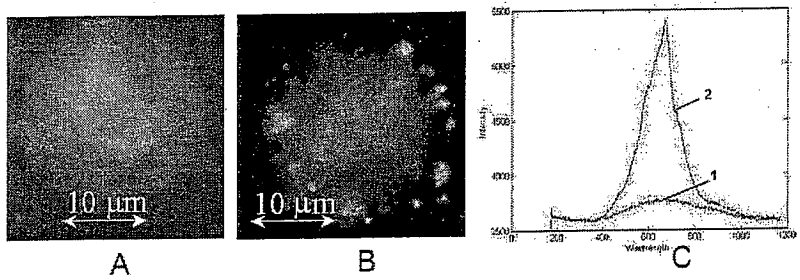

Figure 5. Images and spectra of K562 myeloid culture cells obtained with optical scattering microscope: (A): cell without NP, (B): cell with cytoplasm-located clusters of gold nanorods, and (C): optical scattering spectra for intact cells (1) and for nanorod cluster in cell (2).

3.3 Photothermal bubbles around single NP and in cells around gold NP

A typical bubble-specific PT response image and signal are shown in Fig. 6b and Fig. 6c. These results were obtained in individual AML cells with GNR clusters at different laser fluencies. Peripheral location of the bubble-specific signals in the PT image of the tumor cell shows that the bubbles were generated in the cytoplasm and likely not in the nucleus.

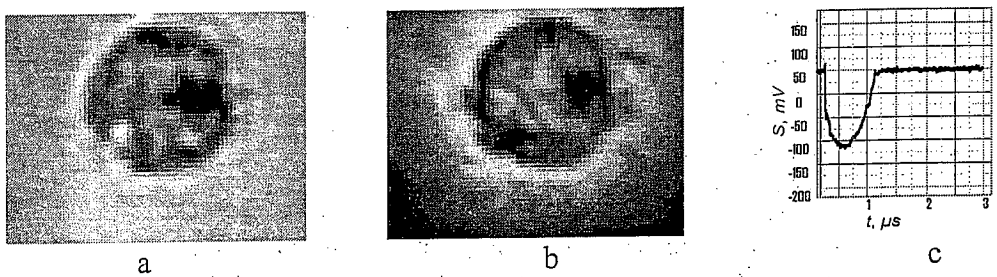

Figure 6. Optical microscopic images of AML cell 0.5 μs after pulsed laser irradiation with single laser pulse (10 ns, 780 nm) showing laser-induced microbubble in this cell (a), and 5 s after the laser irradiation showing damaged membrane (b), and photothermal response signal indicative of laser-induced microbubble (c).

For all types of studied cells (including cultured and primary tumor cells) we discovered that a single laser pulse accompanied by a laser-induced microbubble caused cell lysis through mechanical damage of cytoplasmic membrane. Unlike continuous wave heating, laser-induced microbubble can be precisely localized within one cell and therefore can produce damage only to the cell in which it is generated. In our experiments no damage was observed to surrounding cells. Cell membrane damage can be seen in its optical image as a plume of ejected subcellular material (Fig. 6b). Even the smallest bubbles with lifetimes of 20-40 ns caused cell damage as determined by the trypan blue assay. An advantage of photothermal microscopy for guiding LANTCET is that the cell damage can be detected by observing microbubbles in the cell in real time immediately after the laser pulse. Each individual damaged cells can be monitored this way, thus eliminating the need for post-irradiation cytometric studies. Even in optimized experimental conditions of laser irradiation, PT-microscopy might be useful as image-guidance technique for mixed single cells and cell suspensions.

Table 1. Bubble generation thresholds for AML cells (780 nm, 10 ns).

Samples	Bubble generation thresholds, F_{th} J/cm^2
Intact cells	>50
Cells with GNR (4°C)	>1.5
Cells with GNR (37°C)	~0.32

Analysis of the cell damage probability as a function of the optical fluence as shown in the Table 1 indicates that probability of vapor microbubble generation gradually increases to 100% along with increasing optical fluence. This means that all cells in the sample population accumulated GNRs, however, the size of clusters naturally varies. Also such dependence allows one to determine the bubble generation threshold, F_{th} as one value for all cells. We found that increasing the temperature during the incubation of the cells with GNR from 4°C (when only chemical reactions in cells occur) to 37°C (when all physiological reactions including endocytosis occur) caused significant increase of P_{MB}, the microbubble size and corresponding 5-fold decrease of the bubble generation threshold. This allows us to conclude that GNR clusters can be formed in cells targeted at either 4oC or physiological temperature, but GNR clusters formed under 37°C were much larger. The cell damage threshold measured at 4 °C and 37 °C was much lower than that obtained in suspension of single GNR in water.

We measured spectral dependence of microbubble lifetime and probability of microbubble generation around single GNR in their water suspension and after their clusterization in human bone marrow CD33+ AML cells (Figure 7). The microubble generation probability (P_{MB}) was measured at several NIR wavelengths at fixed laser fluence levels that was 7.5 J/cm^2 for single NR in water and 0.75 J/cm^2 for the cells treated with the same GNR conjugates. The spectrum of P_{MB} for single GNR closely matches its absorption spectrum, while formation of GNR clusters has broadened the spectrum of P_{MB} obtained for cells (Figure 7).

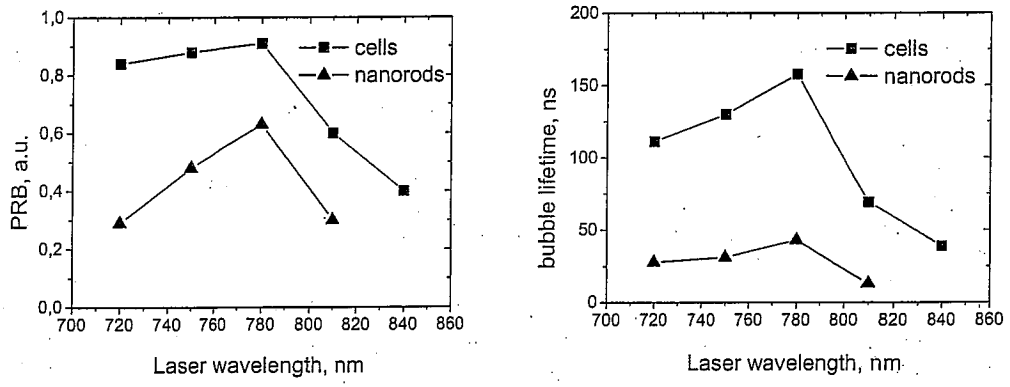

Figure 7. Bubble generation probability spectra (left) and bubble lifetime spectra (right) for single gold nanorods and human bone marrow tumor cells.

First, we found that P_{MB} spectra for GNR in water matches optical absorption spectra of the same GNR suspension with peak P_{MB} and optical density at 780nm. This means that bubbles were generated due to absorption of laser energy. Second, cell spectrum for P_{MB} also has a peak around 750-780 n, which matches the spectrum of P_{MB} for GNR suspension. Besides we did not discovere significant broadening of P_{MB} spectrum as was found for optical absorption spectrum of aggregated GNR in water. It is important to point out that optical absorbance spectra and P_{MB} spectra of GNR suspension in water match each other in terms of width of peak. However, in case of cells no match was found between the two spectra: absorbance spectrum of suspension of GNR clusters is very broad, but P_{MB} spectrum of cells that apparently have GNR clusters is not so broad, and the width of its peak is closer to the width of peak of P_{MB} spectrum obtained for individual GNR in water.

In summary, our experiments demonstrated that upon optimal targeting conditions tumor cells can form large clusters of gold nanorods resulting in a 100 fold decrease of the optical fluence threshold for microbubble generation and, in turn, of the tumor cell damage threshold relative to the untreated tumor cells or treated normal cells.

4. CONCLUSIONS

This study demonstrated that:
- GNR clusters can be selectively formed in tumor cells, a phenomenon that was verified by corresponding widening of the absorption spectrum and increased optical scattering;
- incubation of live normal cells with gold nanorods conjugated with tumor-specific antibodies did not result in formation of GNR clusters and did not cause toxicity to the normal cells;
- slightly above the threshold laser fluence for laser generation of microbubbles around GNR clusters no bubbles were detected around single nanorods;
- gold nanorods, nanoparticles with extremely strong absorption in the near-infrared spectral range (where biological cells are transparent) help to achieve maximum efficacy and selectivity of laser nano-thermolysis for elimination of tumor cells.

Advantages of LANTCET for selective destruction of tumor cells compared with other laser methods based on photo-activated chemical reactions or photothermal effects include better clinical efficacy and safety as defined by the following parameters: (1) low toxicity of GNR compared with dyes and drugs, (2) low absorbance of NIR laser excitation wavelengths by respiratory chain proteins and NADH, (3) low probability of normal cell damnage due to spatial confinement of laser damage to cells loaded with GNR clusters. These features might be imprtant in the application of LANTCET to highly heterogeneous cellular tissues such as bone marrow or blood.

5. ACKNOWLEDGMENTS

This research was sponsored through a DoD grant received through the Alliance for NanoHealth (Texas). Dmitri Lapotko would like to thank Scholar Rescue Fund (New York, NY) for personal financial support. Authors also would like to acknowledge staff of Laser Cytotechnology Laboratory at Lykov Heat and Mass Transfer Institute where photothermal microscopy experiments were performed.

REFERENCES

1. X. Huang, I. H. El-Sayed, W. Qian and M. A. El-Sayed, "Cancer cell imaging and photothermal therapy in the near-infrared region by using gold nanorods," *J Am Chem Soc* **128**(6), 2115-2120, 2006.
2. A.A. Oraevsky, A.N. Oraevsky, "Plasmon resonance in ellipsoid nanoparticles," *Quant Electron* **32**(1), 79-82, 2002.
3. D.V. Guzatov, A.A. Oraevsky, A.N. Oraevsky, "Plasmon resonance in ellipsoidal nanoparticles with shells," *Quantum Electronics* **33**(9), 817-822, 2003.
4. J.L. West, N.J. Halas, "Engineered nanomaterials for biophotonics applications: improving sensing, imaging, and therapeutics," *Annu. Rev. Biomed. Eng.* **5**, 285-292, 2003.
5. H. Liao, C. Nehl, J. Hafner, "Biomedical applications of plasmon resonant metal nanoparticles," *Nanomedicine* **1**(2), 201-208, 2006.
6. G. Oberdorster, E. Oberdorster, J. Oberdorster, "Nanotoxicology: an emerging discipline evolving from studies of

ultrafine particles," *Environ Health Perspect* **113**(7), 823-39, 2005,).
7. E. Connor, J. Mwamuka, A. Gole, C. J. Murphy, M.Wyatt, "Gold nanoparticles are taken up by human cells but do not cause acute cytotoxicity," *Small* **1**(3), 325 – 327, 2005.
8. C.M. Pitsillides, E.K. Joe, X. Wei, R.R. Anderson, C.P. Lin, "Selective cell targeting with light absorbing microparticles and nanoparticles," *Biophys. J.* **84**(6), 4023-432, 2003.
9. D.P. O'Neal, L.R. Hirsch, N.J. Halas, J.D. Payne, J.L. West, "Photo-thermal tumor ablation in mice using near-infrared absorbing nanoparticles," *Cancer Lett.* **209**(2), 171-176, 2004.
10. J.A. Copland, M. Eghtedari, V.L. Popov, N. Kotov, N. Mamedova, M. Motamedi, A.A. Oraevsky: Bioconjugated gold nanoparticles as a molecular based contrast agent: Implications for imaging of deep tumors using optoacoustic tomography, *Molecular Imaging and Biology* 2004; **6**(5): 341-349.
11. L.R. Hirsch, R.J. Stafford, J.A. Bankson, S.R. Sershen, B. Rivera, R.E. Price, "Nanoshell-mediated near-infrared thermal therapy of tumors under MR guidance," *Proc Natl Acad Sci* **100**(23), 13549–13554, 2003.
12. M. Everts, V.Saini, J. L. Leddon, *et.all*, "Covalently linked Au nanoparticles to a viral vector: potential for combined photothermal and gene cancer therapy," *Nano Lett* **6**(4), 587 – 591, 2006.
13. I. El-Sayed, X. Huang, M. El-Sayed, "Selective laser photo-thermal therapy of epithelial carcinoma using anti-EGFR antibody conjugated gold nanoparticles," *Cancer Letters* **239**(1), 129-135, 2005.
14. D. Lapotko, E. Lukianova, A. Shnip, G. Zheltov, M. Potapnev, V. Savitsky, O. Klimovich, A.A. Oraevsky, "Laser activated nanothermolysis of leukemia cells monitored by photothermal microscopy," *Proc. SPIE* **5697**, 82-89, 2005.
15. D. Lapotko, E. Lukianova, M. Potapnev, O. Aleinikova, A. Oraevsky, "Elimination of leukemic cells from human transplants by laser nano-thermolysis," *Proc. SPIE* **6086**, 135-142, 2006.
16. D. Lapotko, E. Lukianova, M. Potapnev, O. Aleinikova and A. Oraevsky, "Method of laser activated nanothermolysis for elimination of tumor cells," *Cancer Lett.* **239**(1), 36-45, 2006.
17. A.R. Lowery, A. M. Gobin, E. S Day, N. J Halas, J. L West, "Immunonanoshells for targeted photothermal ablation of tumor cells," *Int J of Nanomedicine* **1**(2), 149-154, 2006.
18. J.M. de la Fuente, C.C. Berry, M.O. Riehle, A.S. Curtis, "Nanoparticle targeting at cells," *Langmuir* **22**(7), 3286-3293, 2006.
19. O. Siiman, K. Gordon, A. Burshteyn, J. Maples, J. Whitesell, "Immunophenotyping using gold or silver nanoparticle-polystyrene bead conjugates with multiple light scatter," *Cytometry* **41**(4), 298–307, 2000.
20. B.D. Chithrani, A.A. Ghazani, W.C. Chan, "Determining the size and shape dependence of gold nanoparticle uptake into mammalian cells," *Nano Letters* **6**(4), 662-668, 2006.
21. A. Tkachenko, H. Xie, Y. Liu, D. Coleman, J. Ryan, W. Glomm, M. Shipton, S. Franzen, D. Feldheim, "Cellular trajectories of peptide-modified gold particle complexes: comparison of nuclear localization signals and peptide transduction domains," *Bioconjug. Chem.* **15**(3), 482-490, 2004.
22. D. Lapotko, E. Lukianova-Hleb, A. Oraevsky, "Clusterization of nanoparticles during their interaction with living cells," *Nanomedicine* **2**(2), 241–253, 2007.
23. D. Lapotko, E. Lukianova, A. Oraevsky, "Selective laser nano-thermolysis of human leukemia cells with microbubbles generated around clusters of gold nanoparticles," *Lasers Surg. Med.* **38**(6), 631-642, 2006.
24. A. Conjusteau, S.A. Ermilov, D. Lapotko, H. Liao, J. Hafner, M. Eghtedari, M. Motamedi, N. Kotov, A.A. Oraevsky: Metallic nanoparticles as optoacoustic contrast agents for medical imaging, *Proc. SPIE* **6086**: 155-165, 2006.
25. D. Lapotko, E. Lukianova-Hleb, P. Mitskevich, V. Smolnikova, M. Potapnev, M. Konopleva, M. Andreeff, A. Oraevsky, "Photothermal and photoacoustic processes in laser activated nano-thermolysis of cells," *Proc. SPIE* **6437**, 64370C, 2007.
26. X. Huang, Jain PK, El-Sayed IH, M.A. El-Sayed, Gold nanoparticles: interesting optical properties and recent applications in cancer diagnostics and therapy, *Nanomed.* **2**(5):681-93, 2007.
27. C.J. Murphy, A.M. Gole, S.E. Hunyadi, J.W. Stone, P.N. Sisco, A. Alkilany, B.E. Kinard, P. Hankins, Chemical sensing and imaging with metallic nanorods, *Chem Commun (Camb)* 7(5): 544-57, 2008.
28. D. Lapotko, G. Kuchinsky, "Photothermal Microscope," In: *Photoacoustica and Optothermal Phenomena*, F. Scudiery, M. Bertolotti, eds.(AIP, Rome,1998), p. 184-186.

Photothermal and photoacoustic processes in laser activated nano-thermolysis of cells

Dmitri Lapotko*[a], Ekaterina Lukianova[a], Pavel Mitskevich[b], Viktoriya Smolnikova[c], Michail Potapnev[c], Marina Konopleva[d], Michael Andreeff[d], and Alexander Oraevsky[e]

[a]Lykov Heat and Mass Transfer Institute, 15 P. Brovka St, Minsk 220072, Belarus;
[b] Republican Center of Transplantology and Cells Biotechnology, 8 Semashko St, Minsk 220116, Belarus;[c]Research Institute of Hematology & Transfusiology, 160 Dolginovskyi Tract, Minsk 220053, Belarus;
[d]The University of Texas M.D. Anderson Cancer Center, 1515 Holcombe Blvd, Houston, TX 77030;
[e]Fairway Medical Technologies, Inc, 9431 W. Sam Houston Parkway South, Houston, TX 77099.

ABSTRACT

Laser Activated Nano-Thermolysis was recently proposed for selective damage of individual target (cancer) cells by pulsed laser induced microbubbles around superheated clusters of optically absorbing nanoparticles (NP). One of the clinical applications of this technology is the elimination of residual tumor cells from human blood and bone marrow. Clinical standards for the safety and efficacy of such procedure require the development and verification of highly selective and controllable mechanisms of cell killing. Our previous experiments showed that laser-induced microbubble is the main damaging factor in the case cell irradiation by short laser pulses above the threshold. Our current aim was to study the cell damage mechanisms and analyze selectivity and efficacy of cell damage as a function of NP parameters, NP-cell interaction conditions, and conditions of bubble generation around NP and NP clusters in cells. Generation of laser-induced bubbles around gold NP with diameters 10-250 nm was studied in Acute Myeloblast Leukemia (AML) cultures, normal stem and model K562 human cells. Short laser pulses (10 ns, 532 nm) were applied to those cells in vitro and the processes in cells were investigated with photothermal, fluorescent and atomic force microscopies and also with fluorescence flow cytometry. We have found that the best selectivity of cell damage is achieved by (1) forming large clusters of optically absorbing NP in target cells and (2) irradiating the cells with single laser pulses with the lowest fluence that can generate microbubble only around large clusters but not around single NP. Laser microbubbles with the lifetime from 20 ns to 2000 ns generated in individual cells caused damage and lysis of the cellular membrane and consequently cell death. Laser microbubbles did not damage normal cells around the damaged target (tumor) cell. Laser irradiation with equal fluence did not cause any damage of cells without accumulated NP clusters.

1. INTRODUCTION

After rapid improvement of the results of leukemia treatment (including targeted therapy with monoclonal antibodies (MAB) in the past 2 decades, a limit for further intensification of chemotherapy appears to be reached in acute and chronic forms of leukemia]. Results of autologous stem cell transplantation (ASCT) demonstrated the potential for achieving molecular remissions, but these are not durable. Contamination of transplants (grafts) with residual tumor cells seriously limits the efficacy of autologous transplantation. Residual cells may be partially removed from graft with purging methods that were recently developed for in *vivo* and *ex vivo* applications [1]. Current methods for purging do not provide sufficient clinical efficacy and safety [1-3]. Development of new efficient and safe purging methods may help to improve the survival rate for leukemic patients treated with ASCT.

Laser ablation (destruction) of leukemia cells may be applied for elimination of leukemia cells from the transplant. After pioneering works of early 1980s [4], there is a significant and growing interest in developing laser therapy methods for treatment of cancer at the level of single cells. It was recently established that laser-induced local heating of cellular structures (through photothermal (PT) mechanisms), using either pulsed or continuous laser radiation and mediated by

* ld@hmti.ac.by; phone: (+375) 172-842483; fax: (+375) 172-842483

Photons Plus Ultrasound: Imaging and Sensing 2007: The Eighth Conference on Biomedical Thermoacoustics, Optoacoustics, and Acousto-optics, edited by Alexander A. Oraevsky, Lihong V. Wang,
Proc. of SPIE Vol. 6437, 64370C, (2007) · 1605-7422/07/$18 · doi: 10.1117/12.713082

optically absorbing nanoparticles and microparticles, may provide precisely localized damage that can be limited to single cells [5-8]. Accumulation of strongly absorbing nanoparticles in relatively transparent cells may enhance their optical absorption up to several orders of magnitude, making cells detectable by various imaging methods [9-11]. Thus nanoparticles (NR) act as localized sources of laser-induced heat that can cause cell damage. Even greater potential for selective damage of target (e.g. tumor) cells exists through integration of nanoparticles and cell-specific MAB or other vectors that may allow specific targeting of the cells [5, 11-13]. Gold nanorods and nanoshells that absorb strongly in the near-infrared, hold the greatest potential as photothermal agents that are also non-toxic to normal organs [7, 11-14]. PT effects of continuous wave (CW) radiation (such as hyperthermia) are most effectively used in damaging relatively large areas of abnormal tissues [15]. Spatial selectivity of CW irradiation methods is relatively poor. Pulsed PT interactions were shown effective for selective damage of single cells [5, 8, 11, 16]. This method referred as nano-thermolysis has been successfully applied *in vitro*. Despite apparent advantages of the laser nano-thermolysis, the full potential of this method has not been realized yet. Previous studies yielded insufficient efficacy, selectivity and safety, the main clinical criteria of successful treatment. Reported results were experimentally obtained only for model cultured cells [5, 8, 11, 16]. The next step is to provide the efficacy and safety of laser nanothermolysis for real human cells and tissues. Heterogeneous nature of human cancer cells prevented successful targeting of NPs to these cells in the past. The main problems of all previously reported methods of laser nano-thermolysis are as follows: heterogeneity of real human cancer cells may compromise efficacy of NP coupling to tumor cells; absence of a highly specific MAB may cause non-specific coupling of NPs to normal (non-target) cells; mechanisms of NP-mediated damage depend not only upon the parameters of NP and laser radiation, but also upon the properties of cells making heat deposition and bubble generation hard to control in a heterogeneous cell population. Thus, safety (also referred to as laser-induced non-specific toxicity) can be considered as the main obstacle for the progress of laser nano-thermolysis technology towards its clinic application. The current state of nano-thermolysis can be described as "good in the lab though poor in the clinic".

We recently introduced laser-activated nano-thermolysis as cell elimination technology (LANTCET), i.e. a method for selective cell killing. This method utilizes vapor microbubbles generated by laser pulses around superheated clusters of gold nanoparticles [14, 17, 18]. In our study we demonstrated for cultured tumor cells that a cell targeting protocol that results in formation of nanoparticle clusters can significantly improve the efficacy, selectivity and safety of laser-activated nano-thermolysis [14, 17, 18]. Further development of LANTCET required its evaluation in *ex vivo* treatment of real human cells in suspensions. Real tissues differ from model tissues due to their high heterogeneity of cell types and properties. The heterogeneous cells affect the efficacy and safety of the laser nanothermolysis. The major *ex vivo* application of laser nanothermolysis is anticipated in selective elimination of residual tumor cells from bone marrow and blood transplants. Autologous transplantation of bone marrow and stem cells extracted from blood is one of the modern methods for treatment of leukemia [1]. The tasks of our work described below, included: development of a method for selective cell targeting with nanoparticles; optimization of the cell killing procedure with the goal to improve its efficacy and safety for real human cells and experimental evaluation of the developed technique in real bone marrow samples.

2. MATERIALS AND METHODS

2.1 Samples

Our selection of the cells for experimental study of LANTCET was aimed at obtaining realistic results that would allow evaluation of the clinical potential of this method. Therefore, primary human cells were chosen for the experiments. The primary human cells are quite heterogeneous in their physiological properties. As a result real tissue of bone marrow responds in a way different from cultured homogeneous cells to the nanoparticle targeting and to the laser treatment. For that reason we have excluded culture cells from the experiments and used primary human cells derived from leukemia patients and healthy donors.

Leukemia cells reside mainly in the bone marrow and blood in the form of suspension, not solid tissue. Leukemia is a type of cancer that can be treated using extracorporal methods. Thus, studies of laser ablation mechanisms using real tumor cells *ex vivo* do not compromise safety of human patients. Availability of diagnosis-specific MAB for targeting NP to most human leukemia cells enables research in the experimental conditions very close to clinical situation.

Fresh samples of human bone marrow (BM) taken either from normal donors or patients with the diagnosis of acute myeloid leukemia (AML) were used in experiments. Suspensions of normal and tumor cells were studies separately without mixing them. Normal BM samples had no tumor cells, and AML (tumor) samples consisted mainly of tumor cells (the level of B-lymphoblasts was 94 to 98% in samples from different patients. We used 3 normal and 3 tumor samples, all obtained from different patients. Normal and tumor samples were prepared and analyzed as separate

samples though they were treated with one and the same protocol (see below). Leukemia cells express diagnosis-specific genes that were determined individually for each AML patient by using standard clinical protocols [19]. Specific MAB, raised against cell membrane receptors corresponding to specific genes, have been used for each sample of tumor cells. Phenotyping was performed with flow cytometry. As a result diagnosis-specific (primary) monoclonal antibodies were determined (MAB1) as CD 33.

2.2 Principles and experimental protocol of laser-activated nano-thermolysis as cell elimination technology

The method for selective killing (elimination) of target cells includes two main steps: the delivery of NPs into the cells and laser treatment of the sample. The purpose of the first step is to create light absorbing clusters of NP that can be activated to generate vapor microbubbles that can damage target cells. Desirably, accumulation of NP occurs only in target cells. Even more desirable is to form clusters of NPs in the target cells in order to reduce the laser fluence thresholds for generation of vapor bubbles. The purpose of the laser treatment is to activate NP clusters and generate bubbles in target cells using minimal laser fluence, so that normal cells will not be damaged. In our earlier work we proposed that clusters of light-absorbing NPs could serve as centers of heat deposition for effective generation of vapor microbubbles that kill individual cells [14]. Advantage of the clusters relative to single NP is that clusters allow significant decrease of optical energy required for bubble generation and produce bigger bubbles [17].

We have achieved high selectivity of formation of clusters of NPs in the target tumor cells through a two-stage incubation procedure (Figure 1 a). In the first stage NP have been selectively coupled to the membranes of target cells using MAB. To enhance coupling of multiple NP to one cell surface receptor, we used so called sandwich method with the primary MAB1 and secondary MAB2 [14]. MAB1 can provide strong selective coupling to membrane receptors and for leukemia there are established MABs that are diagnosis-specific [19].

At the first stage the samples (normal and tumor) were separately incubated for 30 min at 4^0C with diagnosis-specific MAB1 (for each tumor sample we have used corresponding MAB1: mouse anti-human CD33) that selectively attach mainly to blast cells. Then both samples were separately incubated for 30 min at 4^0C with 30 nm gold spherical NP that were conjugated with secondary MAB2 (#15754, Ted Pella, Inc, Redding, CA). NP-MAB2 comes as a factory-made complex, and MAB2 (goat anti-mouse IgG(H+L)(AH)) has high coupling efficiency for MAB1. Thus we attached gold nanoparticles to cell membranes (Figure 1 b) through the chain of bonds: cell receptor-MAB1-MAB2-NP. All operations during the stage1 were performed at 4^0C. This temperature minimizes any physiological processes and allows efficient MAB-receptor or MAB-MAB interactions. Selectivity of the targeting after the stage 1 is good, however not sufficient from the clinical point of view. First, MAB1-specific receptors may be in some cases expressed in minor levels also in some normal cells. Second, MAB2 may directly couple through different uncontrollable mechanisms directly to membranes of normal (non-target) cells. As a result small amount of NPs will attach to membranes of normal cells. This may cause undesirable death of normal cells during exposure to laser radiation.

To improve the targeting selectivity (and safety of LANTCET) we used the second incubation stage (Figure 1 a) with the goal to create maximal clusters of NP inside the target cells. For this we set the temperature at 37 ^{0}C and time of incubation to 30 – 120 min, so to stimulate internalization of NPs through endocytosis (Figure 1 c). Endocytosis is a universal and fast biological mechanism that delivers NPs and small clusters of NP from the cell membrane into the cytoplasm where NPs are concentrated into larger clusters inside endosomes. At the end of the stage 2 large NP clusters were formed only in those cells with high initial level of membrane-bounded NP, i.e. the target cells. Due to a much lower level of NP at the membranes of normal cells, the clusters either were not formed at all or had much smaller dimensions. The bigger the cluster size, the lower the laser fluence threshold of bubble generation. An explanation for such reduction of the laser fluence threshold comes from combination parameters responsible for vapor bubble formation: larger NP volume increases heat accumulated in the vapor, longer heat diffusions time increases effectiveness of laser interaction with light-absorbing clusters, reduced surface tension and dynamic viscosity allows expansion of vapor nuclei into microbubbles [18].

Next, normal and tumor cell suspensions were injected into separate sample chambers with diameter of 2.5 mm (S-24737, Molecular Probes, OR), then exposed to single laser pulses at the wavelength of 532 nm matching peak of light absorbance for spherical 30-nm gold NP (Figure 1 d). The laser pulse duration was 10 ns, which approximately matches the heat diffusion time from a 200 nm cluster of gold NPs into water. We set laser energy (fluence) at the minimal level that provides bubble generation only around the biggest NP clusters (>200 nm) and does not induce any bubbles around smaller clusters or around single NPs (which have higher threshold for bubble generation, Figure 1 d). Such fluence level provides high selectivity of cell killing: no bubbles can be generated in normal cells even if they accumulated some NP. The two experimental modes were studied: (1) single cell irradiation and (2) simultaneous irradiation of many cells in suspension. Tumor and normal samples were exposed to laser pulses with equal fluence. In a single-cell mode each

individual cell (total of 150) was irradiated one by one with single focused laser pulse at 532 nm (LS 2132, Lotis TII, Minsk, Belarus). This mode was used for investigation of laser-induced bubbles in cells. Biological damage to irradiated cells was studied in the suspension mode (Figure 2 b) through simultaneous irradiation of 4,000 to 20,000 cells in a sample chamber with a wide laser beam (3 mm diameter, 532 nm, 10 ns). After exposure to laser pulses the samples were collected from the chambers and analysed for cell viability.

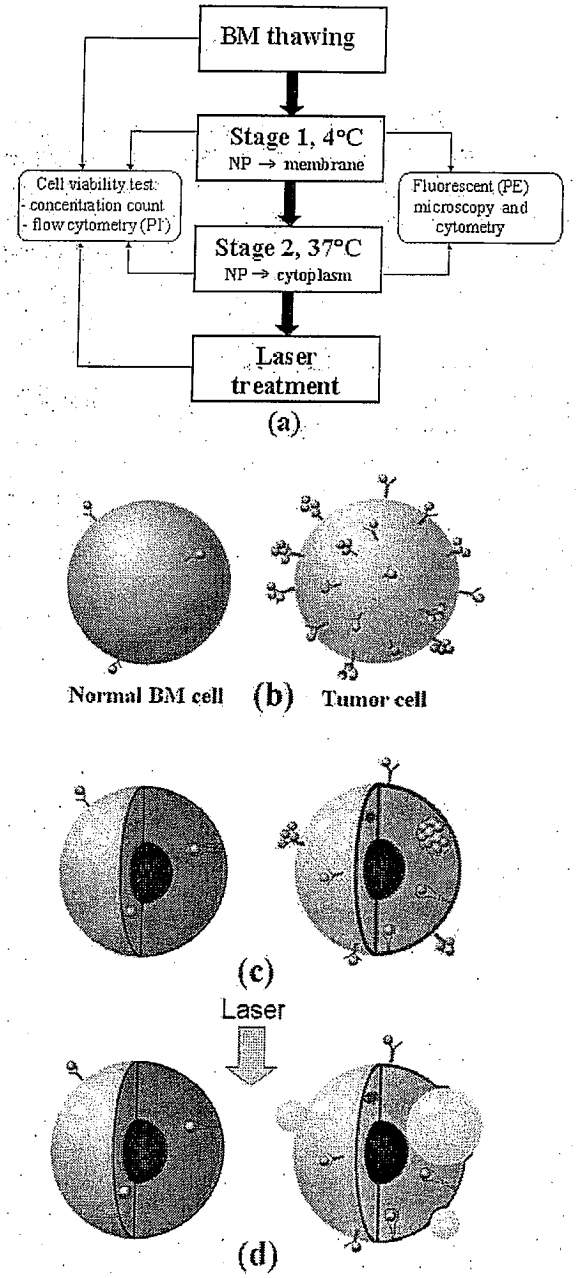

Figure 1. Block diagram of the experimental protocol for LANTCET (a) and a graphic diagram explaining steps of LANTCET: (b) membrane targeting with NP - stage 1, (c) clusterization of NP - stage 2, (d) laser-induced vapor bubbles and cell damage.

2.3 Light-scattering microscopy

Gold NPs are known not only as excellent light absorbers but also for its light scattering [6]. Side (90°) scattering of incident light due to surface plasmon resonance is size-dependent: the wavelength of maximal scattering increases with increase of NP diameter [6]. We have used the same optical microscope as for PTM and LSM. As the source of light we

used white light continuous source. Light was directed with optical fiber at the glass slide with the sample at the angle 70-80°. Optimal angle was adjusted to achieve maximal intensity of scattered light. LSM and PTM use the same sources of signals – NPs – through their light absorptive and scattering properties that are very different from those of any endogenous cellular components.

2.4 Detection of laser-induced microbubbles in cells

We used photothermal (PT) microscope previously developed by us for detecting vapor bubbles in individual cells [20, 21]. Each cell was illuminated with three collinear focused laser beams: pulsed beam for bubble generation, and two low-intensity continuous (633 nm, 0.1 mW) and pulsed (640 nm, 8 ns) probe beams for detecting the bubble in cell in a real time. Any bubble-related change of refractive index causes the shift of the phase of the probe beam that influences beam intensity in the input of photodetector. Output of the photodetector is measured as PT response by high-speed digitiser (Bordo-211, Auris Ltd., Belarus) and in case of the bubble PT response has specific shape so bubble generation can be detected during irradiation of individual cell with laser pulse. Each individual cell (total of 150) was irradiated one by one with single focused laser pulse at 532 nm (Lotis TII, Minsk, Belarus) and PT response from each cell was simultaneously recorded as time-response of probe laser intensity [20]. This mode allowed (1) detecting the bubbles and (2) measuring their lifetime that characterizes maximal bubble diameter. After sequential irradiating 150 cells with single pulse and registering PT response from each one we have measured the probability PRB of bubble generation at specific laser fluence as:

$$PRB = \frac{N_2}{N} \tag{1}$$

where N – amount of irradiated cells, N2 – amount of cells with bubble-specific PT responses. Bubble generation threshold fluence for specific pump laser wavelength was defined as the fluence that corresponds to PRB level of 0.5.

For time-resolved imaging of the bubbles in individual cells we have used dye pulsed probe laser beam at the wavelength of minimal light absorption by cell (640 nm, 8 ns), which was synchronized and delayed for 120 ns against the pump pulse. CCD-camera (an image detector) captured probe beam image so only events that occurred after this delay and during probe pulse duration were visualized. Thus we were able to analyse bubble location and diameter. Detailed description of time-resolved PT imaging can be found in [20].

2.5 Cell damage detection methods

Laser-induced damage was measured with microscopy (concentration counts in hemocytometer) and flow cytometry (outer membrane damage detection as Propidium Iodide (PI) positive stains) after each stage of sample preparation (Figure 1 a) and 2 hours after laser treatment. The former method detected the destruction of cells and the latter one detected necrotic death of those cells that were damaged but not destructed. Cells with compromised membranes that included PI were considered as damaged. The cells that were counted as PI-negative were considered as survived live cells. The level of survived live cells *LLC* was used as a measure of LANTCET efficacy and was analyzed experimentally for each normal and tumor sample as function of laser pulse fluence, number of laser pulses, type of MAB1 and incubation stage (1 and 2 – see Figure 1 a). This parameter describes relative change of the level of living cells in population due to (1) destruction and (2) cell death:

$$LLC = \frac{C_{al}}{C_{bl}} \times C_{PI-} \times 100\% \tag{2}$$

where C_{bl} is the initial concentration of all cells in the sample before laser treatment, C_{al} is the concentration of all cells in the sample after laser treatment (both counted in hemocytometer), C_{PI-} is the level of PI-negative (live) cells obtained with flow cytometer for MAB1-positive cells in the tumor sample and for all cells in the normal sample. We did not consider delayed cell death because bubble-related mechanism of cell damage acts very fast. The evidence for that was obtained earlier during similar experiments with selective laser nanothermolysis of leukocytes [5].

3. RESULTS

3.1 Light-scattering images of nanoparticles in cells

NP-treated and control cells were imaged with light scatter, photothermal microscopy. We have obtained the images of individual cells. Those images revealed two common features both K562 and AML cells: NP-related signals (1) were

detected in 90-95% of targeted cells and (2) spatial distribution of NP-related signals within the cell was highly heterogeneous with apparent local peaks (Figure 3, middle). Also we have not found NP-related signals in the images of control cells. This indicates that regardless targeting method used the NPs aggregate into clusters during interaction with living cells. (Figure 2). Amplitudes of LSM signals are 5 times higher that that for untreated cells. LS images were registered with continuous white light source and no photobleaching effects occurred. So they are more suitable for NP imaging and quantitative studies. Untreated (control) cells also produced LSM images though with much lower amplitudes and without strong local peaks. The signal-to-noise ratios were estimated using pixel amplitudes of the images of control cells. LSM sensitivity may be improved by using monochromatic light source at the wavelength that matches plasmon resonance wavelength for NPC.

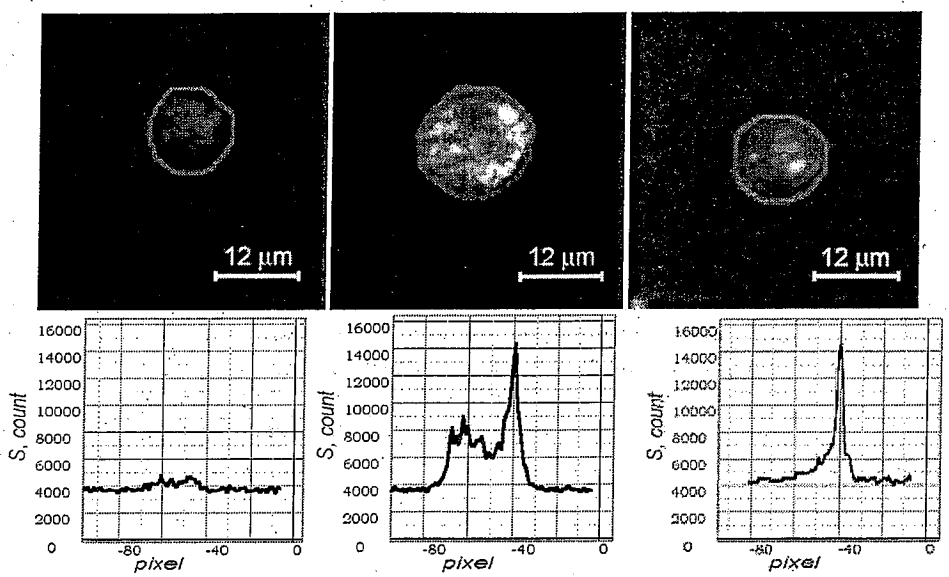

Figure 2. Images of AML human cells obtained with light scatter microscope: left: cell without NP, center: cell with membrane-located NP and their clusters, right: cell with cytoplasm-located clusters of NP.

3.2 Bubbles around NP in water

After measuring the threshold of bubble generation we have discovered its strong dependence upon NP diameter, especially for NP smaller than 100 nm (Figure 3). With increase of NP concentration (decrease of inter-NP distance) the threshold decreases, which means that several NP may produce the bubble at lower fluence than single NP. We refer this effect as cluster effect, which means that increase of NP local concentration is equal to increase of diameter of single NP in terms of bubble generation and allows lower fluence for bubble generation.

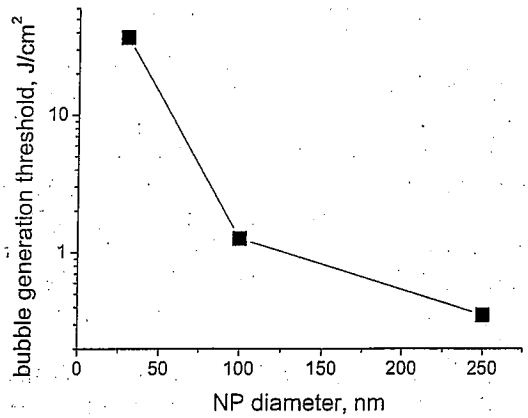

Figure 3. Bubble generation threshold as function of nanoparticle diameter.

Also we discovered that increase of laser pulse fluence leads to increase of the bubble lifetime.
NP of the same diameter may produce bubbles having various lifetimes despite the same fluence. This heterogeneity in bubble parameters indicates the dependence of bubble generation conditions upon local properties of surrounding media (viscosity, density). Cell is heterogeneous multi-component system where such properties may vary from point to point and therefore bubble parameters in cells may also vary for specific NP diameter and laser fluence. Single NP produce bubbles only during the first pulse and never generate bubbles during the next pulses – apparently NP are thermally destroyed because bubble generation around single NP requires highest fluencies and highest temperatures.

3.3 Bubbles in cells

First we have compared two phenomena: cell damage and bubble generation (Figure 4). We have found that cell damage correlates with generation of the bubbles: even trepan blue penetrated into the cells 10-20 min after they were irradiated with single laser pulse. Also cell membrane showed signs of distortion as imaged within 1 min after laser pulse. This correlation was the same for K562 and human myeloblasts. Earlier we have found the same correlation for a wide range of blood cells [20, 21]: red blood cells, lymphoblasts and neutrophils. Even smallest bubbles with lifetimes of 20-40 ns caused cell damage. Penetration of PI and trepan blue and visually detected changes of cellular membrane prove that the bubble damages the membrane and this is lethal for cell.

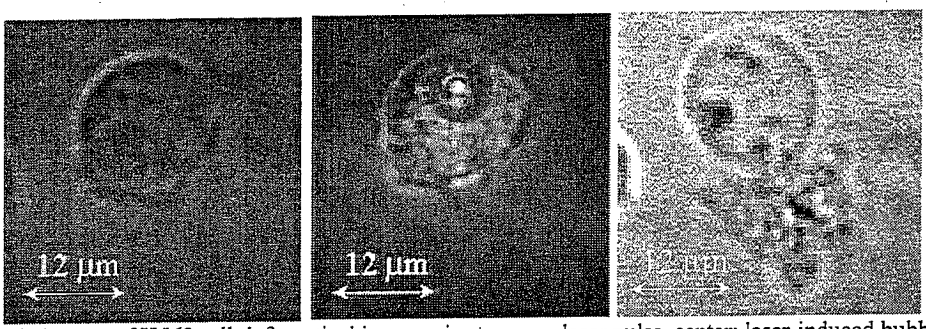

Figure 4. Microscopic images of K562 cell: left: optical image prior to pump laser pulse, center: laser-induced bubble, right: optical image of the cell 1 min after laser pulse with signs of the cell damage.

Additional result is that cell damage can be detected through the detection of the bubbles in cell and this can be done in real time (relatively to laser pulse) and for each individual cell thus eliminating post-irradiation cytometric studies. This allows to apply PT-microscopy for image-guidance of laser treatment of individual cells or cell suspension.
Second, we have found that bubble generation correlates to presence of NP in cells. NP-treated cells showed 10-100 times lower thresholds of bubble generation in comparison with the threshold for the same cells that were not treated with NP. The most important result is that the threshold of bubble generation in the cells that were targeted with NP and MAB were found to be much lower than the threshold for bubble generation around the same individual NP in water suspensions of NP! (Table 1)

Table 1. Parameters of laser-induced thermal bubbles in cells.

	K562		Human Myeloblasts (AML)	
	Threshold of generation, J/cm^2	**Generation probability at 0.7 J/cm^2**	**Threshold of generation J/cm^2**	**Generation probability at 0.7 J/cm^2**
Cells without NP	50-70	0	35-50	0
Single NP in water	37	0	37	0
Cells with incidental NP	5.0	3.0	2.1	7.5
Cells with NP clusters	0.3	93.0	0.3	82.0

This (together with the results of imaging the NP in cells that were obtained with independent 3 methods) means that the sources of laser-induced bubbles in NP-treated cells are not individual NP but their clusters. We define NP cluster as the

group of closely located particles that thermally act as one solid object: thermal fields and evaporated volumes around each single NP in cluster overlap so that cluster of NP produces one initial nuclei of the bubble, not many nuclei around each NP.

3.4 The influence of NP parameters and of targeting conditions on the bubble generation threshold and lifetime. We have studied bubble generation threshold and lifetime as function of NP diameters (10 and 30 nm) and of incubation time and temperature. Increase of incubation temperature from 4°C to 37°C caused increase of bubble lifetime from 79 ns to 216 ns – by 2.7 times. Bubble lifetime is roughly proportional to maximal diameter of laser-induced bubble. Increase of incubation time from 30 min to 60 min did not cause significant changes in the parameters of the bubbles (Figure 5). This means that cluster formation is completed mainly by 30 min of high-temperature incubation. Described effects were similar for K562 and AML cells.

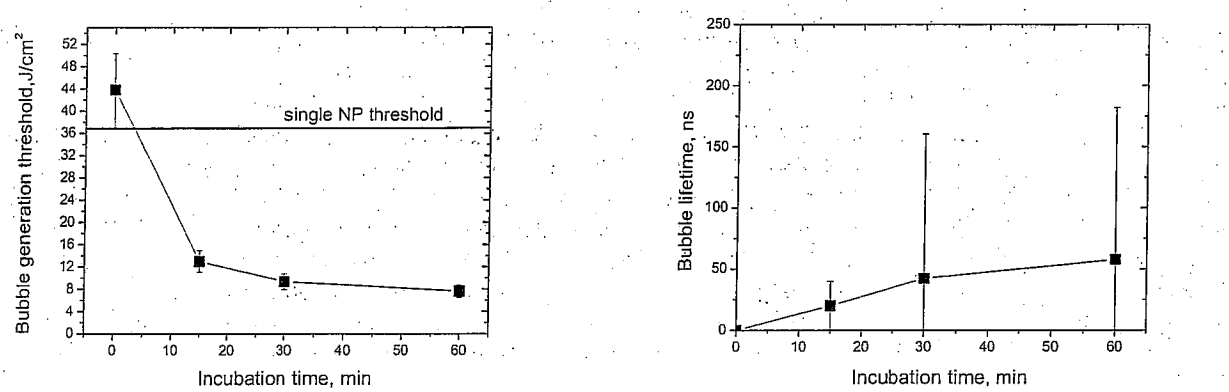

Figure 5. Time-course of the two NPC-related parameters obtained for K562 cells with photothermal microscopy: (A) the threshold of generation of laser-induced bubbles around NPC and (B) population-averaged lifetime of laser-induced bubbles around NPC (at 8 J/cm^2) as measured during the incubation at 37°C with 30 nm bare gold NP.

We have also applied direct physiological targeting as one-step procedure to the cells without their immunological pre-targeting and without using any MAB: *NP-cell*. This allowed (1) to monitor kinetics of endocytosis without influence of MAB-related effects and (2) to compare 3 targeting approaches: direct immunological and physiological targeting methods and combined immunological and physiological targeting. K562 cells were incubated with bare 30 nm gold NP during 0 (control sample), 15, 30 and 60 min at 37°C. After incubation was completed unbound NP were washed off with centrifuge, cells were fixed with 10% Paraformaldehyde solution and were analyzed with PT microscopy (as with most sensitive method). As NPC-related parameters we have measured the threshold and duration of laser-induced thermal bubbles as function of incubation time (Figure 4). Those parameters are most NPC-specific and do not depend upon endocytosis like fluorescence intensity (see above). We have found that after 15 min of incubation NP already aggregated into the clusters: at this stage the threshold of bubble generation in cells (13 J/cm^2) was 3 times lower than the threshold of bubble generation around individual 30 nm gold NP (37 J/cm^2). This difference in threshold levels means that the bubbles were generated around the structures that are bigger than single NP. Analysis of bubble lifetimes confirmed this conclusion: at laser fluence level of 8 J/cm^2 (Figure 5B) no bubbles were registered from single NPs but were registered in the cells. Further incubation till 30 min caused increase of NPC diameter in cells because bubble lifetime increased and bubble generation threshold decreased. Longer incubation of the cells with NP did not produce significant changes in NPC-related parameters (Figure 5) and may indicate saturation of internalization processes. This experiment confirmed that aggregation of NP into the clusters occurs even when bare NP without MAB are used and such clusterization is provided by natural physiological processes that include internalization of NP. These processes of NPC formation are quite fast and almost complete in 30 min at physiological temperature.

In this experiment we have used bare NP without any MAB being pre-conjugated to them. Therefore no specific coupling of NP to membrane occurred. To compare the efficiency of NPC formation we analyzed bubble generation threshold in K562 cells after targeting 30 nm gold NP with 3 procedures: immunological, physiological and combined methods. Immunological targeting with primary and secondary MAB (*NP-MAB2-MAB1-receptor-cell*) yielded threshold

of 0.49 J/cm^2, and follow- up application of physiological targeting improved this parameter down to 0.37 J/cm^2, which indicates an increase of NPC diameter to the maximal level. Direct physiological targeting (*NP-cell*) yielded the bubble threshold of 7-9 J/cm^2 (Figure 4A). Therefore the biggest NPC (corresponding to the lowest threshold of bubble generation) emerge as the result of combined immunological targeting with cell-specific MAB and follow-up physiological targeting.

Selectivity of bubble generation was estimated by comparing bubble generation threshold for the cells of one type though under different targeting conditions. Specifically targeted K562 cells (cell were targeted with primary cell-specific MAB) with follow-up high temperature incubation yielded the threshold level of 0.3 J/cm^2. Removal of primary MAB from targeting scheme caused non-specific targeting and bubble generation threshold increased by 30 times. Bubble lifetime decreased by 35 times from 216 ns to 6.1 ns. Therefore best bubble generation conditions require application of cell-specific MAB during initial targeting stage.

Bubble generation threshold significantly increased after 30 nm NP were changed by 10 nm NP. Under equal incubation conditions 30 nm NP yielded the threshold of 0.9 J/cm^2 and 10 nm NP yielded the threshold of 25 J/cm^2. Such difference may indicate that NP clusters of 10 nm NP have much smaller diameters though the total number of NP inside each cluster may be even higher than that for 30 nm NP.

Table 2. Influence of NP and incubation parameters on the parameters of laser-induced bubbles.

Bubble parameter	NP diameter increase	Incubation temperature increase from 4 to 37 °C	Incubation Time	
			at 4°C	at 37°C
Threshold of generation	decreases	decreases	no influence	slight decrease
Lifetime	increases	increases	no influence	slight increase
Location	no influence	relocation inside cells	no influence	no influence

4. DISCUSSION

4.1 Mechanisms of accumulation of nanoparticles.

Generally speaking the nanoparticles may get into the cells through specific and non-specific mechanisms. The former ones provide necessary for LANTCET selectivity while the latter ones ruin the selectivity. Furthermore we can never totally exclude non-specific mechanism such as phagocytosis for example. Therefore our efforts were aimed at creating NP structures that are highly specific for target tumor cells and that would not emerge in normal cells. Based on our hypothesis and obtained experimental results we may suggest that the solution is the clusters of NP. The clusters with maximal diameter (consisting of maximal number of NP) can be formed in controllable way by using the two-stage targeting (incubation) as described above. The first ("cold") stage provides accumulation of NP at cell membrane due to receptor-MAB1-MAB2 inteeractions. As a result the several NP may couple to one receptor at cell membrane (Figure 1 b). MAB-receptor and MAB-MAB interactions do not depend upon temperature and are performed at 4°C. This temperature slows all biological processes and thus (1) prevents uncontrollable internalization of NP and (2) preserves the cells (especially normal ones) from incidental damage and death. Then free (uncoupled) NPs are washed off from the cells. The second ("hot") stage forms NP clusters through endocytosis of NP. During endocytosis the endosomes concentrate NPs into relatively big clusters (Figure 1 c) that are larger than those at cell membrane. Our experimental results (maximal amplitudes of fluorescent peaks for 4°C 0.5 h (stage 1) and 37°C 1-2 hrs (stage 2)) allow to estimate the increase of cluster size (increase of the number of NP in one cluster) by 2-4 times. Such clusters with high peak signals were observed only in the cells being incubated at 37°C when endocytosis was enabled and were not observed in cells being incubated at 4°C when endocytosis was not possible.

Described two-stage mechanism of NP targeting is rather universal and can be applied to the different types of cells (not only tumor cell), and can be regulated through the control of cell incubation parameters - time and temperature - of each stage. This mechanism employs two biological processes (endocytosis and MAB-receptor interaction) and gold NP that do not affect cell viability.

4.2 Bubble generation conditions.

The cluster of 5-20 NP may have the diameter that is much larger (3-10 times) than the diameter of individual NP. During electron microscopy examination of NP distribution inside cells [14] we have found that inter-particle distance in the cluster is comparable to NP diameter (30 nm). The thickness of superheated fluid around NP for 10-ns laser pulse is about 20 nm in the water [5]. Therefore NP cluster with the diameter of 150 –250 nm acts a solid superheated volume of vapor and thus can be considered as nuclei of the bubble. Bubble expansion will occur when initial pressure in this volume overcomes surface tension pressure, which is inversely proportional to R_c. In our case the vapor pressure inside nuclei depends upon the laser pulse fluence. This explains why at specific fluence levels the bubbles may develop only around NP clusters with the size (or the number of NPs) being above some threshold and cannot develop around single NP. According to the obtained results we may use peak amplitude S of fluorescent signal as relative measure of the number of NP in the cluster. Therefore cytoplasmic (inner and bigger) clusters may generate laser-induced bubbles at the lowest fluencies. Even 2-fold increase of the diameter of NP cluster may cause dramatic decrease of bubble generation threshold fluence. In our experiments with big solid NP (their photothermal properties are similar to those of NP clusters of equal size) we have observed that increase of NP diameter from 30 nm to 250 nm caused the decrease of bubble generation threshold almost 100 times [18].

4.3 Generation of vapor microbubbles around clusters of nanoparticles

It was a surprising finding of our studies performed several years ago that vapor microbubbles could not be generated around single gold nanoparticles heated only slightly above 100 ^{0}C [22]. Three main possible reasons for such phenomenon are: refraction of light by a thin layer of vapor around nanoparticle heated above the evaporation temperature, surface tension preventing nanobubble to expand into a microbubble, and rapid heat diffusion in small nanoparticles making even 20 ns laser pulses to long for efficient interaction with small NPs. Our model of bubble generation matched the experiment, thereby revealing that in order to generate a microbubble around optically absorbing particle, the particle size must provide sufficient capacity of to store thermal energy required for evaporation of water layer and generation of a microbubble. Simultaneously we found that in order to generate a vapor bubble capable of expansion without continuous supply of thermal energy to a nanoparticle, initial superheating above temperatures exceeding that of evaporation (i.e. >100 ^{0}C) might be necessary. Using nanosecond laser pulses it is possible to superheat water around a cluster of nanoparticles to the critical temperature of 374 ^{0}C. The specific latent heat of vaporization at the critical temperature equals zero. Thus, the entire volume of water superheated to the critical temperature is immediately converted into vapor, and a microbubble can be formed thereby avoiding the reduction of efficiency of laser energy absorption by the nanoparticle due to light refraction by a thin layer of vapor (nanobubble). Based on consideration presented above and the fact that large submicron and micron size nanoparticles can not be effectively targeted to tumor cells, we proposed to form clusters of small nanoparticles in target cells, thereby satisfying condition for effective generation of destructive microbubbles in the cells at the lowest possible laser fluence threshold [14,18,19].

Our previous experiments demonstrated that a microbubble must have diameter of at least 1-2 μm in order to produce nonrepairable damage to a 10-20 μm size cell [20]. Quantitative analysis of vapor bubble generation upon pulsed laser heating of gold nanoparticles is discussed in a separate publication [23].

4.4 Cell damage mechanisms

Cell damage may be caused by several mechanisms that can be triggered by heated NP and vapor bubbles. The most universal is the mechanical damage (rupture) of vital cellular component –outer membrane – that will cause the necrosis and lysis in any cell. When the bubble reaches for the size being comparable to that of the cell it would definitely damage cellular membrane. We have shown previously [20, 21] that laser-induced bubbles damage various types of cells. We have also shown experimentally [20, 21] that damaging effect of the bubble is localized within the cell where bubble is generated: surrounding cells are not damaged. This feature provides very precise mechanism of individual cell damage.

In terms of efficacy of the killing of target cells (that can be rather heterogeneous) the more universal is the mechanism of cell damage the more efficient will be the method. In some cases the target cells that are the very small portion among normal cells must be totally eliminated or killed (minimal residual disease for example). Even if several tumor cells are left after laser treatment they may give a birth to new tumor [1]. Cell killing through bubble-induced lysis and necrosis seems to be a reliable mechanism that depends upon NP cluster and laser radiation properties and does not depend upon the properties of specific cells. We experimentally verified this feature by using the transplants of human bone marrow.

These cell samples (both normal and tumor) consist of many different types of cells – not like cultured cells. Despite such heterogeneity we have demonstrated that clusterization of NP, bubble generation and cell damage can be diagnosis-specific. This was done only for one type of cancer – acute lymphoblastic leukemia. In future new technology (LANTCET) will be evaluated for different diagnoses.

Comparing LANTCET with other laser methods for cell killing (based on photo-activated chemical reactions or photothermal effects not confined by individual cells) we may point out several potential advantages (table 1), which would provide better clinical efficacy, safety and applicability of laser nano-technologies. LANTCET uses (1) non-toxic agents (NP are non-toxic in comparison with dyes and drugs), (2) can use longer laser excitation wavelengths (far red and near-infrared) with better safety for normal cells due to lower light absorption at these wavelengths, (3) minimal amount of expensive nano-material (PDT requires about 10^6 molecules per one cell and LANTCET can be done with 10^{2-3} nanoparticles) and (4) universal and precise mechanism of cell damage. All these features would help in application of LANTCET highly heterogeneous tumor tissues. Combining light-scattering imaging with bubble imaging we may suggest new image-guided mode of the LANTCET operation (Figure 6) that may provide detection and elimination of 1 tumor cell among 100 million normal cells.

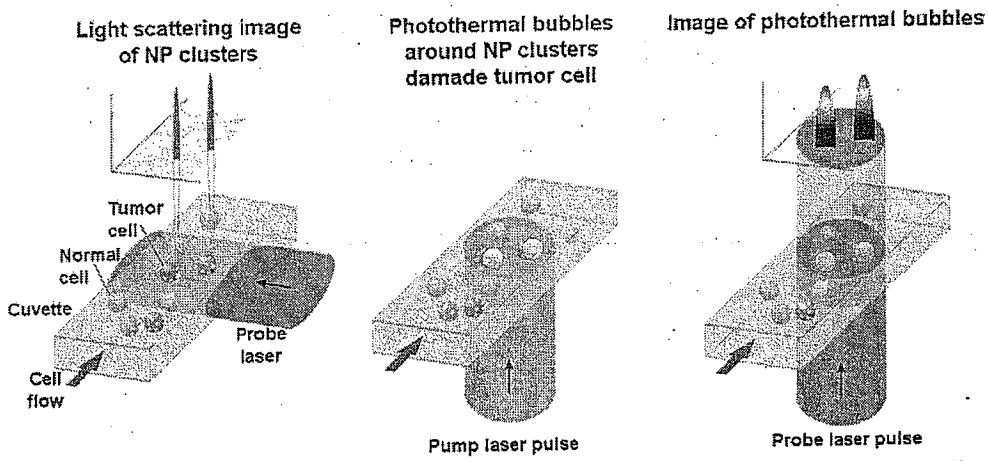

Figure 6. LANTCET stages: light-scatter imaging of NRC in individual targeted cells (left); damage of targeted cells with LIMB that are induced by a high-fluence laser pulse (middle); detection of cell damage according to images of LIMB (right).

5. CONCLUSIONS

Absorption of short laser pulse by nanoparticles leads to generation of vapor bubbles around nanoparticles.

Increase of NP diameter or aggregation on small NP into big cluster decreases bubble generation threshold.

Laser pulse usually thermally destroys individual NPs but not their cluster so that non-clustered NP cannot produce multi-pulse bubbles though the cluster can produce multi-pulse bubbles.

Bubbles that are generated around NP and their clusters in living cells damage those individual cells by destroying their membranes and causing cell lyses.

Parameters of laser-induced bubbles in cells – threshold of generation and the lifetime – do not depend upon cells properties and can be controlled through laser pulse fluence and NP diameter – thus making laser nano-thermolysis applicable to heterogeneous populations of cells with variable properties.

Lowest thresholds of bubble generation and cell damage was achieved for cells with biggest clusters of NP.

Application of specific cell targeting method provides good selectivity of nanothermolysis of target cells through generation of the bubbles only around big NP clusters that are selectively formed in target cells but not in other cells undergoing same treatment.

Laser-activated nano-thermolysis as cell elimination technology (LANTCET) looks promising for (1) detection of residual disease in the transplant and (2) chemical-free purging of residual tumor cells from blood and bone marrow grafts.

ACKNOWLEDGEMENTS

This work was supported in part by the Alliance for Nano-Health grant W81XWH-06-0067 from the Department of Defense. Authors thank Prof. Jason Hafner for useful discussions.

REFERENCES

1. J. C. Alvarnas and S. J. Forman, "Graft purging in autologous bone marrow transplantation: a promise not quite fulfilled," *Oncology* 18(7), 867-876 (2004).
2. S. Faderl and Z. Estrov, "The clinical significance of detection of residual disease in childhood ALL," *Crit. Rev. Oncol. Hematol.* 28(1), 31-55 (1998).
3. M.J. de Lima, E.J. Shpall, "Ex-vivo purging of hematopoietic progenitor cells," *Curr. Hematol. Rep.* 3(4), 257-264 (2004).
4. R.R. Anderson, J.A. Parrish, "Selective photothermolysis: precise microsurgery by selective absorption of pulsed radiation," *Science* 220(4596), 524-527 (1983).
5. C.M. Pitsillides, E.K. Joe, X. Wei, R.R. Anderson and C.P. Lin, "Selective cell targeting with light absorbing microparticles and nanoparticles," *Biophys. J.* 84(6), 4023-432 (2003).
6. J.L. West and N.J. Halas, "Engineered nanomaterials for biophotonics applications: improving sensing, imaging, and therapeutics," *Annu. Rev. Biomed. Eng.* 5, 285-292 (2003).
7. D.P. O'Neal, L.R. Hirsch, N.J. Halas, J.D. Payne and J.L. West, "Photo-thermal tumor ablation in mice using near-infrared absorbing nanoparticles," *Cancer Lett.* 209(2), 171-176 (2004).
8. C.P. Lin, M. Kelly, S. Sibayan, M. Latina and R. Anderson, "Selective cell killing by microparticle absorption of pulsed laser radiation," *IEEE J. Select Topics Quant. Electron.* 5(4), 963-968 (1999).
9. A. Oraevsky, A. Karabutov and E. Savateeva, "Enhancement of optoacoustic tissue contrast with absorbing nanoparticles," *Proc. SPIE-Int. Soc. Opt. Eng.* 4434, 60-69 (2001).
10. J.A. Copland, M. Eghtedari, V.L. Popov, N. Kotov, N. Mamedova, M. Motamedi, A.A. Oraevsky: Bioconjugated gold nanoparticles as a molecular based contrast agent: Implications for imaging of deep tumors using optoacoustic tomography, *Molecular Imaging and Biology* 6(5): 341-349 (2004).
11. C. Loo, A. Lowery, N. Halas, J. West and R. Drezek, "Immunotargeted nanoshells for integrated cancer imaging and therapy," *Nano Lett.* 5(4), 709–711 (2005).
12. A.A. Oraevsky, A.N. Oraevsky: Plasmon resonance in ellipsoid nanoparticles, *Quant. Electron.* 2002; **32**(1): 79-82.
13. D.V. Guzatov, A.A. Oraevsky, A.N. Oraevsky: Plasmon Resonance in ellipsoidal nanoparticles with shells, *Quantum Electronics* 33(9): 817-822 (2003).
14. D. Lapotko, E. Lukianova, M. Potapnev, O. Aleinikova and A. Oraevsky, "Method of laser activated nanothermolysis for elimination of tumor cells," *Cancer Lett.* 239(1), 36-45 (2006).
15. X. Huang, I. H. El-Sayed, W. Qian and M. A. El-Sayed, "Cancer cell imaging and photothermal therapy in the near-infrared region by using gold nanorods," *J. Am. Chem. Soc.* 128(6), 2115-2120 (2006).
16. V. Zharov, R. Letfullin and E. Galitovskaya, "Microbubbles-overlapping mode for laser killing of cancer cells with absorbing nanoparticle clusters," *J. Phys. D, Appl. Phys.* 38(15), 2571–2581 (2005).
17. C. Jennings and K. Foon, "Recent advances in flow cytometry: application to the diagnosis of hematologic malignancy," *Blood* 90(8), 2862-2892 (1997).
18. D. Lapotko, E. Lukianova, A. Shnip, G. Zheltov, M. Potapnev, V. Savitsky, O. Klimovich, A.A. Oraevsky: Laser activated nanothermolysis of leukemia cells monitored by photothermal microscopy, *Proc. SPIE* 5697, 82-89 (2005)
19. D. Lapotko, E. Lukianova, M. Potapnev, O. Aleinikova, A. Oraevsky, "Elimination of leukemic cells from human transplants by laser nano-thermolysis," *Proc. SPIE* 6086, 135-142 (2006).
20. D. Lapotko, A. Shnip, E. Lukianova, "Photothermal detection of laser-induced damage in single intact cells," *Lasers Surg. Med.* 33(5), 320–329 (2003).
21. D. Lapotko, "Laser-induced bubbles in living cells," *Lasers Surg. Med.* 38(3), 240-248 (2006).
22. A. Conjusteau, S.A. Ermilov, D. Lapotko, H. Liao, J. Hafner, M. Eghtedari, M. Motamedi, N. Kotov, A.A. Oraevsky: Metallic nanoparticles as optoacoustic contrast agents for medical imaging, *Proc. SPIE* 2006; **6086**: 155-165.
23. S. Ermilov, D.V. Huzatau, V.V. Klimov, A.P. Kanavin, A.A. Oraevsky, Vapour bubbles generated around laser irradiated gold nanoparticles: Theoretical model and optoacoustic experiments. *J. Appl. Phys.* **103** (2007) (pending).

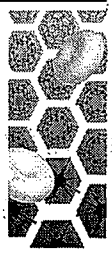

Clusterization of nanoparticles during their interaction with living cells

Dmitri O Lapotko[1†], Ekaterina Y Lukianova-Hleb[1] & Alexander A Oraevsky[2]

[†]Author for correspondence
[1]Laser Cytotechnology Lab, AV Luikov Heat and Mass Transfer Institute, 15 P Brovka Street, Minsk 220072, Belarus
Tel.: +37 517 284 2483; Fax: +37 517 284 2483; E-mail: ld@hmti.ac.by
[2]Fairway Medical Technologies Inc., 9431 W Sam Houston Parkway, South, Houston, TX 77099, USA

Aims: Clusters of nanoparticles may significantly improve the sensitivity of diagnostics and the safety and efficacy of therapeutic nanotechnologies in medicine. We report methods for the formation of nanoparticle clusters and for monitoring their accumulation in cancer cells. **Methods:** The accumulation of gold nanoparticles in tumor cells was studied using flow cytometry, optical scattering and fluorescent, atomic force, photothermal and scanning electron microscopy. **Results:** Incubation of cells at 37°C for 30 min or more with 10–30-nm nanoparticles resulted in the formation of clusters of nanoparticles as large as 20 nanoparticles or more. **Conclusions:** Specific targeting using a monoclonal antibody as a vector increases the concentration of nanoparticles on the surface of target cells compared with nonspecific nanoparticle accumulation. In turn, an increased concentration of nanoparticles on the target surface yields larger nanoparticle clusters inside the cells due to endocytosis. Photothermal and scattering microscopy were found to be the most sensitive methods for imaging nanoparticle clusters in living cells.

Biomedical applications of nanoparticles (NPs) involve their interactions with living cells through various mechanisms. These interactions may result in the formation of NP clusters (NPCs) on the surface and inside the cells. Formation of NPCs in cells was noticed in experiments involving NP–cell interactions [1–5]. Particularly, it was noted that NPCs may emerge at the surface of a cell membrane as groups of NPs linked though specific vectors to membrane receptors. After internalization of NPs, they may aggregate in specific cellular compartments (endosomes) inside the cell [2–5]. However, the properties of NPCs in cells have not been studied and cell-specific formation of NPCs has not been addressed.

In our previous studies, we intentionally generated NPCs in tumor cells with the goal of improving the selectivity of laser-pulsed nanothermolysis of tumor cells [6–9]. Clusterization of NPs may also allow the use of smaller NPs for cell targeting owing to their better coupling efficiency and permeability compared with larger NPs. One large NPC may be more efficient in diagnostic and therapeutic terms than a much higher number of individual NPs that are distributed over the whole cell surface or volume. Thus, NPC-based diagnostic and therapeutic methods may require much fewer NPs per cell to achieve the desired effect.

With the realization of the importance of NPCs in methods of cancer diagnostics [10,11], as well as of therapy [6–9], in this study, we aimed to quantitatively analyze cluster formation in live cells and evaluate various microscopy techniques for sensitive detection of NPCs. We hypothesized that the process of NPC formation in cells can be controlled through the conditions of NP–cell interactions (i.e., use of cell-specific vectors, temperature and time of incubation of cells with NPs).

The methods used currently for the detection and imaging of NPs at the cellular level include various types of microscopies (electron transmission [4,5,12], scanning [3,13], fluorescent (FM) [2,12,14–16] and atomic force (AFM) [17]), flow cytometry (FC) [3,13,14,18,19] and some other indirect methods [20]. However, those methods had not been used earlier for detecting NPC-specific signals in living cells. Our goal was also to determine the optimal experimental conditions for the formation of large NPCs in target cells. We determined the most effective microscopy methods for visualization of NPCs on the surface and inside cells.

Materials & methods

Nanoparticles

Gold NPs have attracted significant and growing attention of biomedical researchers owing to their favorable properties for medical diagnostic and therapeutic applications [21], especially taking into account the possibility of tuning the peak of the plasmon resonance by changing the shape of gold NPs [1,10,22–25]. Relatively small gold spherical NPs were chosen for targeting cells owing to the following reasons:

Keywords: antibody, cluster, endocytosis, microscopy, nanoparticle, tumor cell

future medicine part of fsg

- In our preliminary studies, we found that small NPs can be targeted and attached to the cell surface receptors with efficiency approximately inversely proportional to NP size;
- The cell membrane has greater permeability to smaller NPs compared with larger NPs;
- A large number of small individual NPs does not decrease the optical fluence threshold of microbubble generation, so that selectivity of laser nanothermolysis of cells with clusters of NPs can be significantly improved [9,11].

Silver NPs possess stronger optical absorption and scattering owing to plasmon resonance [26,27]. Nevertheless, our experiments were performed with gold NPs because:

- Gold NPs are nontoxic to cells [28];
- Gold NPs can be functionalized covalently (through the dating S= bond) with antibodies and other cell-specific vectors, which allows selective targeting;
- Gold NPs and their bioconjugates are available commercially;
- The optical properties of gold NPs owing to plasmon resonance in the near-infrared spectral range provide high contrast and efficiency of optical absorption and scattering, which in turn increases sensitivity of NP detection.

We used 10 and 30 nm gold nanospheres, including bare (#15706, Ted Pella, Inc, Redding, CA, USA) and conjugated with goat anti-mouse IgG(H + L)(AH) antibody (#15754 and #15751, Ted Pella, Inc, Redding, CA, USA).

Cells

Tumor cells represent the most interesting subject of NP-related studies owing to the potential usefulness of NPs in cancer diagnostics and therapy. We have used a model culture myeloid cell line K562 and primary human leukemia cells. Membranes of those cells express the myeloid tumor-specific antigen CD33 that can be used for NP coupling through related surface protein receptors. Human cells are different from cultured cells due to the heterogeneity of their properties. This prevents the direct association of results obtained in cultured cells with real human cells. We have used myeloblasts, leukemia cells obtained from bone marrow of primary patients with diagnoses of acute myeloblast leukemia (AML). Those cells also express tumor cell antigen CD33, which is specific to this diagnosis.

In vitro *incubation models*

Interaction of NPs with living cells was studied *in vitro* under two types of experimental conditions. These conditions were designed to study the mechanisms of NP coupling to the cell outer membrane and the mechanisms of NP internalization by the cell. We employed low-temperature immunotargeting of cells with NPs conjugated with monoclonal antibodies (MABs) against CD33 receptors to accumulate gold NPs on the surface of cells (Figure 1A). This procedure was performed at low temperature (4°C) to prevent any physiological processes in a cell that may influence NP coupling. This method of targeting is based on well-established interactions between membrane receptors and matching antibodies. In order to perform our experiments with commercial conjugates, we used a well-known sandwich method for targeting specific receptors on cell membranes. Target cells were first incubated for 30 min with a tumor cell-specific anti-CD33 antibody (MAB1) and then the cells were incubated for 30 min with NPs conjugated to secondary MAB2 raised against MAB1. Thereby, we used commercial conjugates NP + MAB2 for coupling NPs to primary cell-specific MAB1 (anti-CD33). Cells were incubated with a NP concentration of 15000 NP/cell. As a result, the link NP + MAB2–MAB1 receptor was formed.

After NPs were accumulated at the cell membranes, we used the universal biological mechanism of endocytosis under physiological temperature (37°C) for the uptake of NPs into the cells. We allowed sufficient incubation time for endocytosis and phagocytosis to take effect and deliver NPs into the cell. We observed that ingestion of NPs gradually results in coalescence of NPs into clusters inside specific cellular compartments – endosomes (Figure 1B). By performing experiments with and without primary MAB1 (CD33), we verified that accumulation of NPs in cells occurs much more effectively under specific immunological targeting, which in turn results in formation of larger NPCs. We estimated the selectivity of NP–cell interactions by detecting NPCs in targeted cells. The cells were incubated at 37°C for 15–120 min to allow sufficient time for endocytosis.

All NP–cell interaction experiments were performed with live cells. After the targeting procedure, the cells were washed off twice to remove unbound NPs from solution. The cells were then fixed with 10% paraformaldehyde solution and prepared for imaging. Fixation was performed to prevent any incontrollable NP–cell interactions during cell imaging.

Figure 1. Interaction of nanoparticles with target (brown) and nontarget (blue) cells.

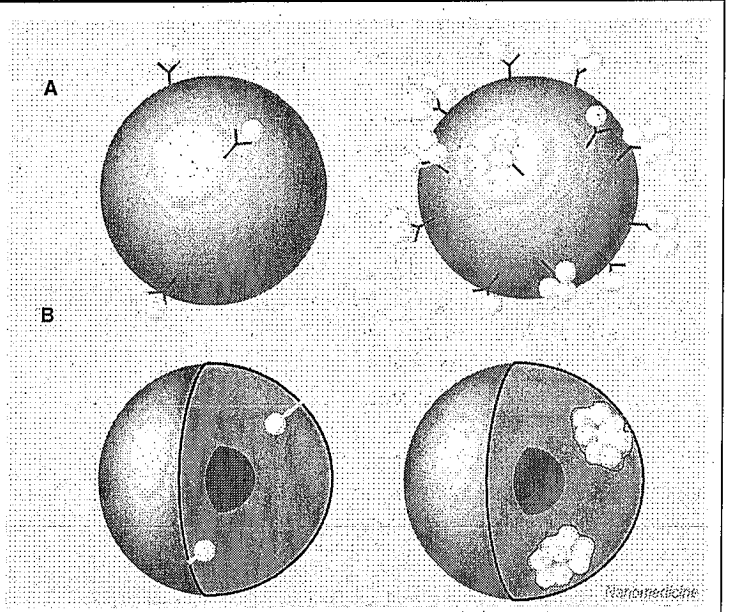

(A) Nanoparticle clusters (NPCs) at the cell membrane after immunological targeting at 4°C. **(B)** NPCs in the cytoplasm after incubation at physiological temperature of 37°C.

Imaging methods

Currently, there is no preferred approach for imaging NPs in living cells. Furthermore, it is not clear what method is the best for detection and imaging of NPCs. For those reasons, we applied six different methods. This combination of methods provided comprehensive information about NPCs and allowed comparison of the applicability of these methods for this specific task.

Fluorescent microscopy & flow cytometry

FM and FC are based on the ability of NPs to carry the molecules of specific fluorophores. R-phycoerythrin (PE) molecules were attached to NPs using anti-goat IgG antibodies (#P9787, Ted Pella, Inc, Redding, CA, USA). NPs of 10–100 nm in size, which is lower than the optical diffraction limit of any optical devise (~300 nm), cannot be imaged directly. Fluorescence from markers bound to single NPs can be detected with an image sensor as a diffraction-limited image of a fluorescing spot. Providing that each NP has the same amount of fluorescent molecules, the amplitude of detected fluorescence signal can be used as a relative measure of the amount of NPs that contribute to the fluorescence signal. This principle was realized with FM for imaging of NPs and their location in individual cells and with FC for measuring the total fluorescent signal from each cell for estimating the total amount of NPs accumulated by individual cells [8]. We used FACScanto™ flow cytometer (BD Biosciences, CA, USA) and Leika DMLA fluorescent microscope (Leica Microsystems GmbH, Germany).

Atomic force microscopy

AFM has sufficient spatial resolution (several nanometers) and sensitivity for the detection of single NPs at the surface of the cell membrane. This is a direct method that allows imaging of NPs and their clusters at the surface of cells and also makes it possible to measure the diameter of NPCs. However, AFM is inefficient in detecting NPs located inside the cells because the cell membrane acts as a shield between NPs and the AFM probe. We used the NT-206 (Microtest Machines Ltd, Belarus) AF microscope and prepared dried cell samples on microscope slides.

Photothermal microscopy

Another optical method used in our experiments is photothermal microscopy (PTM) in the bubble mode, in which laser-induced microbubbles around NPs were used to substantially increase image contrast [29,30]. The principle of PTM is based on irradiation of a cell with a short laser pulse that is absorbed selectively by NPs, causing their immediate superheating with consequent evaporation of surrounding media and the generation of thermal bubbles around the NPs. These bubbles provide good contrast based on optical refraction index as their diameter exceeds this limit and they can be imaged with time-resolved optical microscope regardless of their location (i.e., at the cell membrane or inside the cell). PTM was applied to living cells in suspension. We used a previously developed PT microscope that provides 10 ns temporal resolution and may detect laser-induced bubbles in individual cells and around single light-absorbing NPs with a diameter as small as 10 nm [31,32]. The pump laser pulse wavelength was 532 nm, duration was 10 ns and fluence was adjusted in each experiment. Laser-induced bubbles were imaged with pulsed and continuous wave laser beams at 657 and 633 nm. We measured two parameters of laser-induced bubbles:

- Microbubble lifetime
- Energy threshold of the bubble generation

As we found earlier [6–9], these parameters of laser-induced bubbles depend upon the diameter of optically absorbing NPs or NPCs. Increase of the NP or NPC diameter causes a corresponding increase in the microbubble lifetime and decrease in the bubble generation threshold.

Resonant scattering microscopy

Gold NPs are known not only as excellent optical absorbers but also for their strong optical scattering due to plasmon resonance interaction [26,27,33–35]. Right-angle (90°) scattering of incident light owing to surface plasmon resonance is size dependent: the wavelength of maximal scattering increases with increase in NP diameter [36]. We used the same optical microscope as in our PTM for resonant scattering microscopy (RSM) studies. As the source of light, we used a white light continuous wave lamp. Light was directed with optical fibers to the glass slide with the sample at an angle adjusted in the 70–80° range. Optimal angle was used to achieve maximal intensity of scattered light.

RSM and PTM use one and the same sources of signals (i.e., gold NPs). However, RSM employs the optical scattering properties of NPs, whereas PTM employs their strong optical absorption. Contrast in these methods is very high due to a large difference between optical absorption and scattering of NPs, NPCs and endogenous cellular components.

Figure 2. Flow cytometry histograms of the amplitudes of NP-specific fluorescence (PE dye).

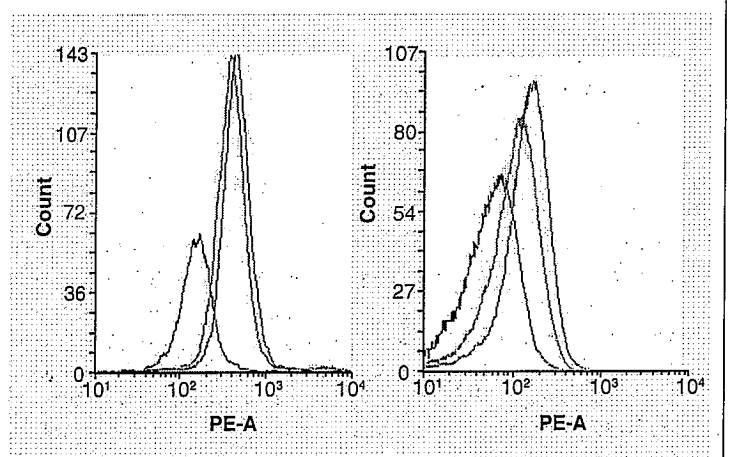

Control cells (black), after immunological targeting at 4°C (blue) and additional incubation at physiological temperature of 37°C (red) obtained for **(A)** model K562 cells and **(B)** human AML cells.
AML: Acute myeloblast leukemia; NP: Nanoparticle; PE: Phycoerythrin.

Scanning electron microscopy

Scanning electron microscopy (SEM) was applied to cells fixed on a glass slide and spin coated with 10-nm gold or carbon films. Spatial resolution of CamScan-4 electron microscope (Oxford Instruments Ltd, UK) is 40 nm in imaging mode and 100 (lateral) or 1500 nm (axial) in spectroscopy mode with energy-dispersed microspectral analyzer INCA 350 (Oxford Instruments Ltd, UK). Spectroscopy mode was used for verification of the presence of gold in cluster-like structures detected with EM. SEM spatial resolution is not sufficient for imaging individual NPs with 10–30-nm diameter, although it does provide direct visualization of NPCs located at the cellular membrane.

Results & discussion

Accumulation of NPs in cells

Accumulation of NPs in the cells was studied with FC for untreated (control) and NP-targeted cells. Amplitudes of NP-specific fluorescence (related to PE dye) were obtained for each cell sample and presented as FC histograms (Figure 2). According to FC, 97–99% of K562 and human AML cells incubated with 30-nm NPs (specific immunological targeting was applied) yielded 2.6–5.0-times stronger fluorescence of 605 counts for K562 cells and 164 counts for AML cells compared with 195 counts for K562 cells and 63 counts for AML cells in control samples of the same cells that were not treated with NP conjugates. It is assumed that the amplitude of FC signal correlates with the total amount of NPs in individual cells. Thus, obtained data show clearly that NPs attach to almost every $CD33^+$ AML and K562 cell. The histograms indicate that populations of cells with NP-positive signals are homogeneous. Therefore, we may conclude that the total amount of NPs in cells does not vary significantly within one cell population and that there are almost no NP-negative subpopulations among targeted cells.

Further incubation at physiological temperature (37°C) of the cells pre-incubated with NPs at 4°C and then washed to remove uncoupled NPs caused 1.4-times the decrease of PE fluorescence amplitude (Figure 2 & Table 1) in both cell types, AML and K562. Providing that this follow-up physiological targeting procedure does not remove attached NPs from cells, but stimulates their internalization and relocalization inside the cell, we may conclude that internalization of NPs modifies the properties of fluorescent dye

attached to these NP conjugates. Therefore, the fluorescent method does not allow direct quantitative measurement of the concentration of NPs located on the surface and inside cells.

The FC approach seems to be most useful for estimating the general efficiency of NP targeting for a specific population of cells because the FC signal is defined by the total level of NPs in each cell. However, FC cannot differentiate NPCs from single NPs and cannot determine the location of NPCs in the cell. These were therefore studied with five microscopy methods.

Detection of NPCs in cells

NP-treated and control cells were imaged using five techniques:

- FM
- Resonant optical scattering
- PTM
- AFM
- SEM

With all five methods we obtained images of individual cells. These images revealed two common features in K562 and AML cells: NP-related signals were detected in 90–95% of targeted cells and spatial distribution of NP-related signals within the cell was highly heterogeneous with apparent local peaks (Figure 3ii). None of the methods yielded the signals that showed spatially homogenous distribution of individual NPs on the surface and inside the cells. This indicates that NPCs can be formed at both temperatures of incubation, 4 and 37°C. However, only small clusters can be formed at the cellular surface. These small NPCs were detected directly with SEM and AFM at cellular membranes (Figures 3Aii & Bii). We have not found NP-related signals on the images of control cells. Combined application of SEM and spatially resolved energy-dispersed spectroscopy (spatial resolution is 100 nm) confirmed that local bright structures at the cell membrane (Figure 3Aii) contain gold with the mass being much higher than the mass of single NPs. Therefore, we believe that detected structures represent small gold NPCs. The diameter of NPCs located at the cell membrane was measured as 100–200 nm (as determined from SEM and AFM). We further found that NPs aggregate into large clusters after internalization with living cells. We have estimated signal:noise ratios for these two methods (Table 1) using their corresponding values of spatial resolution.

Optical methods also yielded localized NPC-related signals in targeted cells (Figures 3C–E, compare ii & iii). These signals are much stronger than those obtained from untreated control cells (Table 1). Amplitudes of FM and RSM signals were five-times higher that those for untreated cells presented in Figures 3Ci & Di. Also providing that resonant optical scattering and fluorescence signals were registered using different charge-coupled device cameras with different sensitivity, it should be noted that the intensity of scattered light was almost one order of magnitude higher than that for fluorescence light. Registration of FM images required maximum exposure time

Table 1. NPC parameters for CD33 + AML human cell samples.

Method	Fluorescent flow cytometry	Fluorescent microscopy	Atomic force microscopy	Light scattering microscopy	Photothermal microscopy	Scanning electron microscopy
Size-sensitive parameter	*Fluorescent intensity (counts)*	*Maximal pixel amplitude (counts)*	*NPC size (nm)*	*Maximal pixel amplitude (counts)*	*Bubble lifetime (ns)*	*NPC size (nm)*
Cells without NPCs	63 ± 46	110 ± 47	0	620 ± 110	0	0
Cells with NPCs at membrane (immunological targeting)	164 ± 78	564 ± 127	300–600	3450 ± 1650	79.0 ± 91	100–400
Signal:noise ratio	2.6	5	5	5.6	>10	2–8
Cells with NPC in cytoplasm (immunological and physiological targeting)	121 ± 83	832 ± 592		9200 ± 4770	216 ± 322	100–600
Selectivity	0.74	1.5		2.7	2.7	1.5

AML: Acute myeloblast leukemia; NPC: Nanoparticle cluster.

Figure 3. Images of human AML cells.

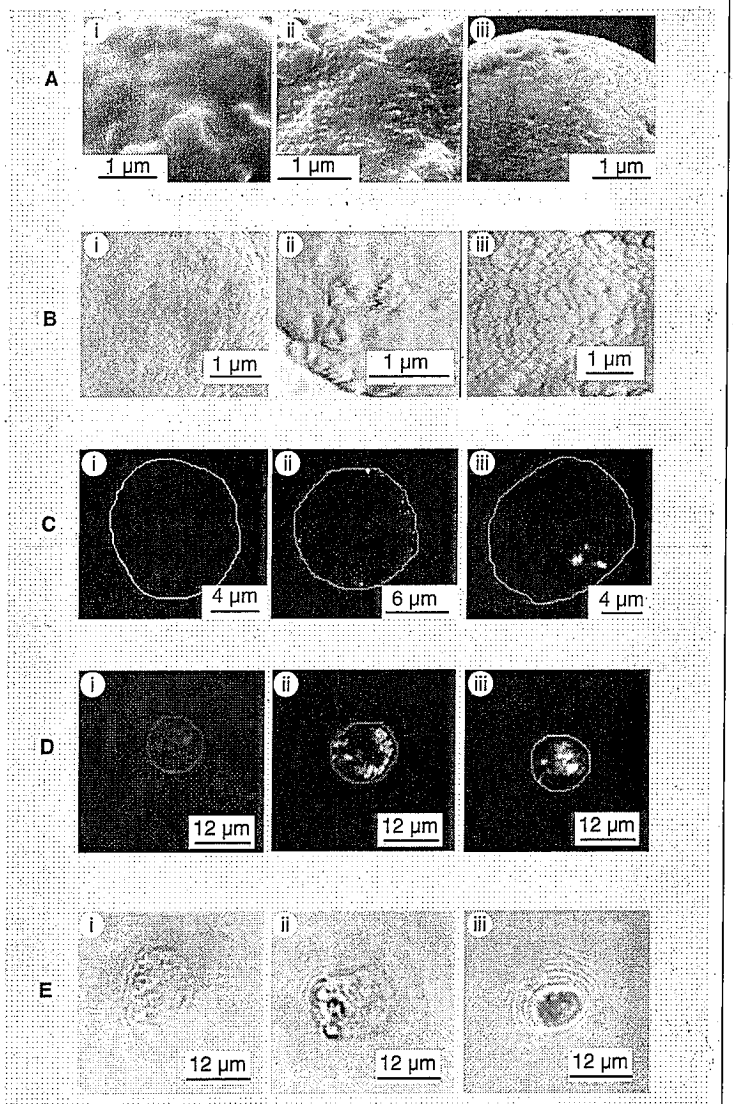

Control (i), after immunological targeting with 30-nm gold NPs at 4°C (ii) and after immunological targeting with 30-nm gold NPs followed by incubation at physiological temperature (37°C) (iii) obtained with scanning electron **(A)**, atomic force **(B)**, fluorescent **(C)**, resonance optical scattering **(D)** and photothermal **(E)** microscopies.
AML: Acute myeloblast leukemia; NP: Nanoparticle.

due to the lowest light levels. Besides, PE fluorescence does not last longer than 1 s owing to photobleaching of PE molecules and this requires a pulsed excitation source and synchronized image detection. These features, together with the dependence of fluorescence quantum yield of PE on the conditions of incubation and location of NPC (as discovered with FC) that we determined, make FM imaging rather complicated and not suitable for quantitative measurements. RSM images were registered with a continuous white light source and no photobleaching effects occurred. Thus, the resonant optical scattering method is more suitable for NP imaging and quantitative studies.

Untreated (control) cells also produced FM and RSM images, although with much lower amplitudes and without strong local peaks. The signal:noise ratios for these two methods were estimated using pixel amplitudes of the images of control cells. RSM sensitivity may be further significantly improved by using a monochromatic light source at the wavelength that accurately matches plasmon resonance wavelength for NPC.

PTM imaging of NP-targeted cells revealed laser-induced bubbles in NP-treated cells at the pump laser pulse fluence of 0.7 J/cm^2, whereas no bubbles at all were detected in untreated cells (Figure 3E). Also at this fluence, no bubbles were detected in water suspensions of single NPs with a diameter of 30 nm. This proves that the bubbles were produced only around NPCs that are larger heat sources compared with single NPs or with optically transparent untreated cells. Figure 3Eii shows the localized character of laser-induced microbubbles that correlates with the location of NPCs formed after endocytosis of NPs into the cells. The lifetime of laser-induced bubbles around a NPC can serve as a quantitative measure of NPC size. The lifetime is proportional to the maximal diameter of the bubble and can be measured with better accuracy. This parameter was equal to zero for control cells (no bubbles) at the laser pulse fluence of 0.7 J/cm^2. Laser-induced bubbles can be distinguished easily from any cell without NPs. Accurate control of the incident laser fluence (as carried out in these experiments) may provide conditions in which laser-induced bubbles are generated only around NPCs and not single NPs. Therefore, the PTM method possesses the best signal:nose ratio for NPC detection among all five microscopy methods.

Summarizing the results obtained independently with five different methods, we may conclude that aggregation of NPs into clusters as NP–MAB–receptor–cell complexes occurs at the cell membranes after incubation of the cells at 4°C with MAB-conjugated NPs.

Influence of incubating conditions on NPC size & location

Role of cell-specific vector

We also studied the effect of cell-specific MAB (CD33) on NPC formation. Two cell samples were analyzed with FC, FM and PTM: the first one was prepared using specific immunotargeting

(NP + MAB2–MAB1–cell) and the second sample was targeted nonspecifically using a single-stage targeting protocol that did not include pre-incubation of the cells with CD33 as MAB1 (NP + MAB2–cell).

The total amount of NP accumulation was measured with FC. Application of cell-specific MAB1 resulted in an increase in intensity of NP-specific fluorescence from 43 counts (for nonspecifically targeted AML cells), which is the same as the background level of PE fluorescence obtained from control cells (Table 1), to 166 counts for specifically immunotargeted cells. Therefore, removal of cell-specific MAB1 (anti-CD33) significantly decreased coupling of NPs to the cells at 4°C. Brightness of NPC-related fluorescence of AML CD33+ cells on FM images increased 2.5-times from 110 counts (nonspecifically targeted cells) to 565 counts for specifically immunotargeted cells. This result demonstrates that an increase of cluster size (the number of NPs in the cluster) occurs. Lifetimes (in nanoseconds) and thresholds (in J/cm^2) of laser-induced bubbles around NPCs were found to be 40 ns and 0.49 J/cm^2, respectively, for immunotargeted cells with MAB1 and 0 ns and 5.1 J/cm^2 for nonspecifically targeted cells without the primary MAB1. The latter threshold is lower than that for untreated control cells (45 J/cm^2) and this indicates the presence of a small concentration of NPs or even of small NPCs in nonspecifically targeted cells. These NPs and NPCs can produce relatively small laser-induced bubbles in the nonspecifically targeted cells, although at much higher fluence of laser pulse.

The results obtained in our experiments mean that no NPCs or very small NPCs appeared in AML CD33+ cells after nonspecific targeting and without cell-specific primary MAB1. Therefore, the interaction of membrane receptors with matching anti-CD33 MAB1 is important for effective NP coupling to the cell membrane, which in turn stimulates aggregation of NPs into the clusters inside the cells. We may further conclude that cluster formation in target cells makes interaction of laser pulses with the cells more selective compared with the situation when only single NPs are bound to the surface of the same cells.

Influence of incubating temperature & time: two-stage targeting

The main discovered features of two-staged targeting are:

- 4°C incubation, washing off uncoupled NPs
- Incubation at physiological temperature increased the size of NPCs and relocation of NPCs from the cellular membrane into the cytoplasm

In AML cells, NPC-related signals increased (Figure 3ii & Table 1) from 564 to 832 counts (1.5-times, FM), from 3450 to 9200 counts (2.7-times, RSM), from 79 to 216 ns (2.7-times, PTM) and, according to SEM, the maximum diameter of detected NPCs increased from 400 to 600 nm (1.5-times). Similar results were obtained for K562 cells. Relocation of NPCs was registered directly with SEM and AFM. The number of NPCs located at the cell membrane significantly decreased and numerous pores (holes) appeared as black spots with a diameter of approximately 100 nm in the membrane (Figure 3Aiii). By contrast, the membrane surfaces of control and immunotargeted cells were smooth and without any pores (Figure 3i & ii). A limitation of AFM is that this method cannot directly detect subsurface NPCs, whereas SEM is capable of imaging gold structures within a depth of 1–1.5 µm below the cell surface. SEM and AFM showed directly that NPs and NPCs are internalized by the cells within 30–120 min. This effect was similar in both K562 and AML cells.

Internal NPCs are much larger targets for optical methods owing to transparency of cells in the visible and near-infrared spectrum of light. Cells that were incubated at 4°C exhibited the strongest local signals at their outer membranes (Figure 3ii) and the cells that were preincubated at 4°C, washed and then incubated at 37°C for 30 min exhibited the strongest local signals in their cytoplasm (Figure 3iii). We consider this as evidence of large NPC formation in the cytoplasm. The cytoplasmic NPCs are much larger than NPCs located at the cell membrane. NPCs at the cell membrane may be distributed circularly and in a more uniform fashion than NPCs inside the cells. RSM and FM showed that the amount of NPC decreased, whereas the amplitude of their signals increased (Figures 3Ciii & Diii). A similar result was obtained with PTM. The number of laser-induced bubbles decreased, although their diameter and lifetime increased (Figure 3Eiii & Table 1). These data indicate an increase of NPC diameter and a change of NPC location from membrane to cytoplasm. It should be noted that NP-related signals were never observed in the nuclei area of the cells of either type. It seems that NPs cannot penetrate through the nuclear membrane.

We have analyzed histograms of NPC size-related signals obtained with FM and PTM for control and for AML cells immunotargeted (incubated with NP conjugates at 4°C), as well as immunotargeted at 4°C and then incubated at 37°C (Figure 4). For FM, we used maximum pixel amplitude in the cell images and, for PTM, we used microbubble lifetime as the parameter of NPC formation. Immunotargeted cells at 4°C showed homogenous distribution of FM and PTM signals, which correlates with the results obtained with FC (Figure 2). Zero bar in the PTM histogram for control means that no bubbles were detected. However, after incubation of immunotargeted cells at 37°C for 30 min, NPC signals divided into two subpopulations: one with smaller signals, typical of incubation at 4°C, and the second one with the signals having 2–3-times (FM) or 3–10-times (PTM) higher amplitude, representing the cells with the biggest NPCs inside. This result shows that immunotargeting followed by incubation at 37°C:

- Produces the biggest NPCs that are located in the cytoplasm
- Increases the heterogeneity of the NPC diameters and locations

This heterogeneity may be caused by the variation in the speed of internalization and clusterization of NPs within one cell.

Physiologically formed NPCs were found to be stable. We did not find (with PTM) any changes in the cells when they were kept at room temperature for 4 h after physiological targeting. Similar results (coupling to cell membrane, internalization into cytoplasm and concentration into endosomes) were obtained earlier for nanosize viruses, which can be considered as biological nano-objects [36].

Influence of incubating temperature & time: one-stage nonspecific physiological targeting

We also applied a nonspecific targeting at physiological temperature as a one-step procedure to the same cells. In this case, no immunotargeting (no MAB) was used, that is, the cells were incubated with bare NPs to bring the NPs to the cell surface. This experiment allowed:

- Monitoring of kinetics of endocytosis without the influence of MAB-related effects
- Comparison of the nonspecific targeting with previously studied specific targeting approaches:
  - Specific immunological targeting at 4°C
  - Immunotargeting followed by the incubation at 37°C

Living K562 cells were incubated with bare 30-nm gold NPs for 0 (control sample), 15, 30 and 60 min at 37°C. After this incubation, unbound NPs were washed off by centrifugation, cells were fixed with 10% paraformaldehyde solution and were analyzed with PTM (the most sensitive method). As NPC-related parameters, we measured the threshold and lifetime of laser-induced microbubbles as a function of incubation time (Figure 5). Those parameters are the most NPC-specific and do not depend upon endocytosis like fluorescence intensity, described above.

We have found that, after 15 min of incubation, NPs aggregated into clusters. At this stage, the threshold of bubble generation in cells (F_{NPC} = 13 J/cm^2) was three-times lower than the threshold of bubble generation around individual 30-nm gold NPs (F_{NP} = 37 J/cm^2). This difference in threshold

Figure 4. Histograms of NPC-related parameters for human AML cells.

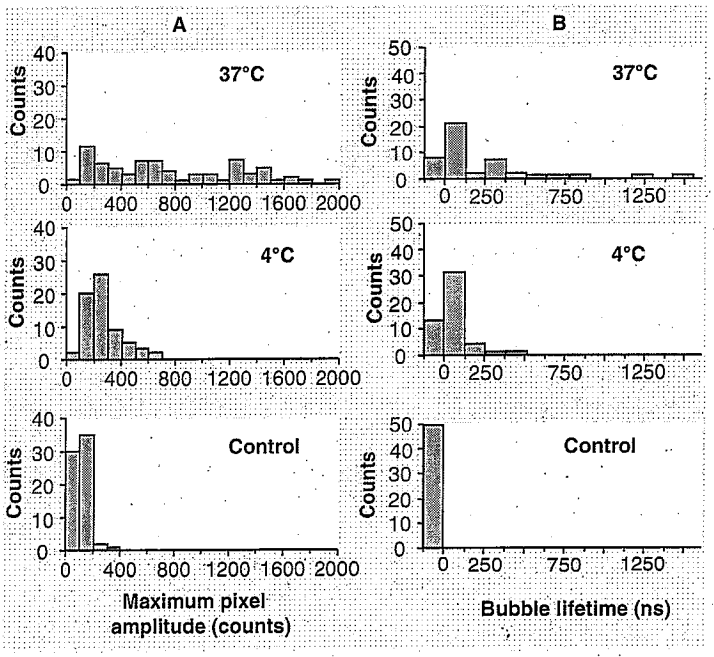

(A) Maximal pixel amplitude of fluorescent microscopy image. **(B)** Lifetime of laser-induced bubbles as measured with photothermal microscopy (bar to the left of zero point indicates cells without bubbles) for control cells and after immunological targeting procedure and after additional incubation at physiological temperature.
AML: Acute myeloblast leukemia; NPC: Nanoparticle cluster.

Figure 5. Time-course of the two NPC-related parameters obtained for K562 cells with photothermal microscopy.

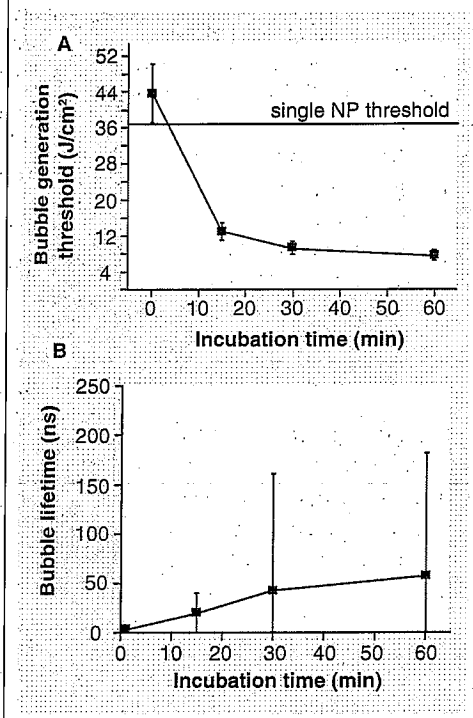

(A) The threshold of generation of laser-induced bubbles around NPCs and **(B)** population-averaged lifetime of laser-induced bubbles around NPCs (at 8 J/cm²) as measured during incubation at 37°C with 30 nm bare gold NPs.
NP: Nanoparticle; NPC: Nanoparticle cluster.

levels means that the bubbles were generated around clusters that are significantly bigger than single NPs. Analysis of the microbubble lifetimes confirmed this conclusion. At the laser fluence level of 8 J/cm² (Figure 5B), no bubbles were detected from single NPs but the bubbles were detected in the cells. Further incubation for 30 min resulted in a substantial increase of NPC diameter in cells, indicated by the increased bubble lifetime and decreased bubble generation threshold. Longer incubation of the cells with NPs did not produce significant changes in NPC-related parameters (Figure 5), which may indicate saturation of the internalization processes. The large spread in the microbubble lifetimes, as indicated with error bars in Figure 5B, reflects heterogeneity of the cell properties in one population. This means that younger and older cells possibly have different endocytosis activity, so that NPCs formed in these cells may vary in their diameters. As a result, the bubbles around such clusters will also be of different diameters, and measured lifetimes will also be very different.

This experiment confirmed that aggregation of NPs into clusters occurs even when bare NPs without MAB are used and such clusterization is provided by endocytosis – natural physiological processes. NPC formation due to endocytosis is fast and is almost completed in 30 min at physiological temperature. In this experiment, no specific coupling of NPs to the membrane could occur. To compare the efficiency of NPC formation, we analyzed bubble generation threshold in K562 cells after targeting 30-nm gold NPs using the three protocols described above. Immunotargeting with primary and secondary MAB (NP–MAB2–MAB1–receptor–cell) and incubation at 4°C a yielded threshold of 0.49 J/cm². Similar immunotargeting followed by incubation at physiological temperature (two-staged targeting) decreased the laser fluence threshold to 0.37 J/cm², which indicates an increase of NPC diameter to the maximum level. Direct nonspecific targeting at physiological temperature (NP–cell) yielded the laser fluence threshold for bubble generation of 7–9 J/cm² (Figure 5A). Therefore, the biggest NPC (corresponding to the lowest threshold of the bubble generation) can be formed as a result of two-stage targeting with cell-specific MAB followed by incubation at physiological conditions.

Also, as our experiments demonstrated, nonspecific targeting without tumor-specific MAB but using NP–MAB2 conjugates (NP + MAB2–receptor–cell) yielded the threshold of 5.1 J/cm². This confirms that nonspecific antibodies result in a greater probability of NP accumulation at the cell membrane compared with bare nonconjugated NPs.

The results obtained for cells incubated at 37°C allow one to conclude that, during this incubation, NPs and small NPCs disappear from the cell membrane and appear in the cellular cytoplasm as large NPCs. The biological mechanism responsible for the above described processes is endocytosis. Low temperature (e.g., 4°C) disables endocytosis and, therefore, during incubation of cells with NPs at 4°C, no NPCs can be formed inside the cells. Activation of endocytosis at 37°C results in internalization from the membrane into the cytoplasm and further concentration into NPCs located in endosomes within 30 min. Also, endocytosis alone (without preliminary specific immunological

targeting) is not efficient in the formation of large clusters because only an insufficient concentration of NPs can be accumulated without a specific MAB at the cell membrane.

Influence of NP diameter

The influence of the NP diameter was studied by comparing the effects of 30- and 10-nm NPs that were applied at concentrations with equal mass of gold as per one cell. This study was performed with FC, FM and PTM. Immunological targeting was analyzed with FC and yielded the following average levels of NP accumulation at cell membranes (as mean amplitudes of NP-specific fluorescence): K562 cells – 888 counts for 10-nm NPs and 801 for 30-nm NPs; AML cells – 621 count for 10-nm, 572 count for 30-nm NPs. Providing that each 10-nm NP has seven-times less molecules of fluorescent dye (PE) and that PE-signal amplitude is proportional to the total quantity of molecules that contribute into the signal from one cell, we may estimate that both types of cells took seven- to eight-times more 10-nm NPs than 30-nm NPs during immunological targeting. However, the level of total mass and volume of 10-nm NPs coupled to cell membranes was three- to four-times lower than those for 30-nm NPs. The level of NP uptake by K562 cells is higher than for AML cells (Figure 2). The difference in NP uptake levels between model and real cells can be caused by different levels of the expression of CD33 receptors at their membranes. Follow-up physiological targeting of AML cells was studied with FC, FM and PTM (Table 2).

The FM study showed that the number of 10-nm NPs in the clusters is approximately seven-times higher than that for 30-nm NPs in NPCs. The possible physical diameter of a cluster formed from 10-nm NPs may be smaller compared with a cluster formed from 30-nm NPs. Assuming that cluster is densely and uniformly packed with NPs and the NPC has a spherical structure, we made FM-based and PTM-based estimations of NPC diameters (Table 2). According to FM and PTM data, smaller NPs under equal targeting conditions accumulate in one cluster in much larger quantities although the physical size of the cluster is smaller than that of the cluster formed from larger-diameter NPs. Also, no significant differences between 10- and 30-nm NPs were found for the kinetics of NP clusterization in all studied cells.

A PTM study of AML cells showed that 10-nm NPs require much higher laser fluence to generate microbubbles (20 J/cm^2) than 30-nm NPs (0.9 J/cm^2). This 21-fold difference in the bubble generation threshold can be explained by the difference in cluster diameters and in the optical absorption cross-section for 10- and 30-nm NPs. The cross-section of 10-nm NPs is nine-times smaller than that for 30-nm NPs. The diameter of a cluster formed from 10-nm NPs may be 0.2–0.7-times the diameter of a cluster formed of 30-nm NPs.

Viability of the cells

Viability of the cells was measured as a value inversely proportional to the number of propidium iodide dye-positive (PI$^+$) cells (which

Table 2. Influence of NP diameter on NPC parameters in AML cells after physiological targeting.

Method	Diameter of NP (nm)	
	10	*30*
Flow cytometry		
Amplitude of PE fluorescence (counts)	621 ± 252	572 ± 246
Amount of NP in cell (normalized by 30-nm NPC)	7.7	1.0
Fluorescent microscopy		
Maximal local amplitude of PE fluorescence (counts)	765 ± 768	1203 ± 804
Amount of NP in cluster (normalized by 30-nm NPC)	7.3	1.0
NPC diameter (normalized by 30-nm NPC)	0.33	1.0
Photothermal microscopy		
Bubble lifetime at laser pulse fluence 0.9 J/cm^2 (ns)	0	79 ± 91
Bubble generation threshold (J/cm^2)	20	0.9
NPC diameter (normalized by 30-nm NPC)	0.1–0.3	1

AML: Acute myeloblast leukemia; NP: Nanoparticle; NPC: Nanoparticle cluster; PE: Phycoerythrin.

indicates membrane damage) with FC before and after targeting procedures. Incubation at 4°C did not have any considerable negative effect on the cells. For K562 cells, the level of PI^+ cells changed from 2 (before targeting) to 2.8% after targeting; for AML cells, corresponding values were 1.8 and 5.5% after 1 h incubation. Follow-up incubation at 37°C resulted in additional damage of cells (K562: 3.4%, AML: 7–10%), dependent on the sample. These values indicate that targeting cells with NPs and the processes of NP clusterization do not significantly damage the cells. This is partly owing to the nontoxic nature of gold NPs that have negligible toxicity on living cells [23,28]. As for a long-term toxicity of gold NPs, we did not make such measurements because existing data [23,28] confirm that gold NPs induce no toxic effects at the cellular or tissue levels. We assume that low toxicity of immunotargeting is achieved by using a low temperature of incubation during the entire procedure, which preserves the cells. During targeting under physiological temperature where NPCs appear inside the cells, we also did not find measurable degradation of cell viability. However, it is possible that primary and secondary MAB that we used could cause a certain level of toxicity to cells. Therefore, we may conclude that NPC formation does not noticeably compromise the viability of the cells.

Conclusion

Analysis of various microscopy methods applied for NPC detection and imaging in cells allows direct comparison of these methods. Fluorescent techniques (FC and FM) are the most popular among cell biologists. However, we found that internalization of fluorescent molecules changes their emission properties. This, together with rather low spatial resolution and low amplitude sensitivity, does not allow quantitative applications of FC and FM. However, these methods can be used for the general control of NP coupling (FC). Another potential problem is the toxic nature of fluorescent dyes that influences cell physiology, including its ability for endocytosis. AFM and SEM provide the highest spatial resolution and direct imaging and measuring of NPCs on the cell membrane but these methods cannot image NPCs inside cells efficiently. In addition, preparation of samples for AFM and SEM is a complicated and time-consuming procedure. However, if real-time monitoring of cells is not required, SEM (especially in combination with energy-dispersed spectroscopy) is a reliable and powerful tool for NPC studies. Also, SEM may detect NPCs located at up to 1 µm depth in the cytoplasm.

As for the optical methods, we found that PTM and RSM can be tuned into a NPC-specific mode of operation when the NPC signal will differ from signals related to a single NP. For laser scanning microscopy (LSM), it is the spectral dependence of resonance wavelength upon object size that can be used for quantitative analysis. LSM can spectrally resolve NPCs from NPs. For PTM, these are the dependence of laser-induced bubble threshold and the lifetime on the size of the light-absorbing object that represent useful parameters for detection of NPCs. Optimization of the incident laser fluence allows detection of bubbles only around NPCs, while no bubble could be generated around single NPs at the same fluence. Neither method requires a specific sample preparation procedure and both can be applied in monitoring the amount of living cells in real-time. It is also important that PTM and RSM can be combined in one microscope. However, laser-induced bubbles and resonance optical scattering signals do not clearly show the location of NPCs. Further improvement of these two methods can be made by replacing a standard microscope with a confocal microscope. We may conclude that quantitative analysis of NP–cell interactions can be made efficiently using an optical microscope in light scattering and photothermal modes, with optional control experiments using SEM.

The main conclusion from the work presented here is that the interaction of a large number of NPs with a living cell, as a rule, creates clusters (NPCs) of closely located NPs, linked either by specific antibodies and/or by cellular structures, such as endosomes. Formation of maximum-size NPCs can be achieved by applying two stages of incubation. At the first stage of incubation, performed at low temperature, NPs conjugated with monoclonal antibodies raised against specific receptors on cellular membranes can be effectively coupled to the cell surface. At the second stage, performed at physiological temperature, endocytosis results in effective internalization of NPs and their coalescence into large clusters within endosomes in the cytoplasm. The advantages of large clusters (NPCs) over single

NPs for diagnostics and therapy based on optical methods include higher optical absorption and lower threshold of vapor microbubble generation.

The application of large NPs with diameters comparable to those of NPCs in cells (up to 800 nm) instead of small NPs is not possible because NPs of such large size will hardly attach to or accumulate in the cells. However, NPCs can be formed selectively at the membranes of specific cells by using relatively small NPs with diameters of 5–50 nm and a low-temperature incubation procedure based on cell-specific vectors (e.g., MABs) that are preconjugated to NPs. NPC diameter and selectivity of their formation in specific cells may be further improved by allowing sufficient time for endocytosis upon incubation at physiological temperature. Washing off uncoupled NPs and incubating the cells at 37°C for 30–60 min will produce approximately three-times as large NPs in the cellular cytoplasm compared with NPCs that can be formed at cellular membranes. These large NPCs cannot be formed in nonspecific cells with a minimal level of incidentally coupled NPs. Thus, the selectivity of NPC formation in specific target cells is much higher compared with the selectivity of single NP targeting.

Optimization of NPC formation protocols for cells requires monitoring of NPC parameters in individual live cells. This can be performed with a number of techniques based on optical microscopy and the most sensitive among them are resonant optical scattering and photothermal imaging.

Future perspective

Using NPCs instead of single NPs in cells may allow the enhancement of NP-related diagnostics: NPCs provide much stronger signals in comparison with single NPs so the sensitivity of detection of specific cells with NPCs can be very high. Cluster-based nanotechnology can be applied for rare cell studies, drug delivery and in any cytometric tasks in which NPCs are used as cell-specific labels.

In therapeutic nanotechnologies, NPCs will increase their efficacy and safety owing to much stronger local impact of NPCs on the cell compared with that of single NPs and much higher selectivity of cluster formation in target cells compared with selectivity of accumulation of single NPs.

Using gold nanorods as NPs with extremely strong absorption in the near-infrared spectral range (where biological cells are transparent) achieves maximum efficacy and selectivity of tumor cell targeting and formation of large NPCs only inside tumor cells, thereby realizing the full potential of laser nanothermolysis as a tumor cell elimination technology.

Acknowledgements

Authors thank Pavel Mitckevitc and Viktoria Smolnikova (Belarussian Center for Cell Engineering, Minsk, Belarus) for their help with fluorescent measurements, Sergey Chizhik (Lykov Heat and Mass Transfer Institute, Minsk, Belarus) for his help with atomic force microscopy measurements, D. Lapotko and A. Oraevsky received financial support from the Alliance for NanoHealth under US Army Medical Research and Material Command grant No. W8IXWH-06-2-0067.

Executive summary

- The interaction of bare and functionalized nanoparticles (NPs) with a living cell, as a rule, creates NP clusters (NPCs) of many closely located NPs that are linked through specific antibodies and/or by cellular structures, such as endosomes and vacuoles.
- Interaction of bare NPs with cells can also form clusters but of smaller size and with lower probability.
- Advantages of clusters over single NPs for medical diagnostics and therapy using optical methods include much greater volume, which allows effective photothermal interactions under conditions of relatively slow heat diffusion.
- Formation of NPCs in target cells permits significant reduction of the laser fluence threshold for selective pulsed thermolysis of tumor cells with simultaneous enhancement of safety of this treatment for normal cells.
- Formation of NPCs compromises the viability of the cells insignificantly.
- Plasmon resonant optical scattering and photothermal microscopy are the two most sensitive methods for the detection of NPCs in cells.

Bibliography

1. Pitsillides CM, Joe EK, Wei X, Anderson RR, Lin CP: Selective cell targeting with light absorbing microparticles and nanoparticles. *Biophys. J.* 84(6), 4023–4032 (2003).
2. de la Fuente JM, Berry CC, Riehle MO, Curtis ASG: Nanoparticle targeting at cells. *Langmuir* 22(7), 3286–3293 (2006).
3. Siiman O, Gordon K, Burshteyn A, Maples JA, Whitesell JK: Immunophenotyping using gold or silver nanoparticle–polystyrene bead conjugates with multiple light scatter. *Cytometry* 41(4), 298–307 (2000).
4. Chithrani BD, Ghazani AA, Chan WCW: Determining the size and shape dependence of gold nanoparticle uptake into mammalian cells. *Nano Lett.* 6(4), 662–668 (2006).
5. Tkachenko AG, Xie H, Liu Y *et al.*: Cellular trajectories of peptide-modified gold particle complexes: comparison of nuclear localization signals and peptide transduction domains. *Bioconjug. Chem.* 15(3), 482–490 (2004).
6. Lapotko D, Lukianova E, Shnip A *et al.*: Laser activated nanothermolysis of leukemia cells monitored by photothermal microscopy. *Proc. SPIE* 5697, 82–89 (2005).
7. Lapotko D, Lukianova E, Potapnev M, Aleinikova O, Oraevsky AA: Elimination of leukemic cells from human transplants by laser nano-thermolysis. *Proc. SPIE* 6086, 135–142 (2006).
8. Lapotko D, Lukianova E, Oraevsky AA: Selective laser nano-thermolysis of human leukemia cells with microbubbles generated around clusters of gold nanoparticles. *Lasers Surg. Med.* 38(6), 631–642 (2006).
9. Lapotko D, Lukianova E, Potapnev M, Aleinikova O, Oraevsky AA: Method of laser activated nanothermolysis for elimination of tumor cells. *Cancer Lett.* 239(1), 36–45 (2006).
10. Copland JA, Eghtedari MA, Popov VL *et al.*: Bioconjugated gold nanoparticles as a molecular based contrast agent: implications for imaging of deep tumors using optoacoustic tomography. *Mol. Imaging Biol.* 6(5), 341–349 (2004).
11. Conjusteau A, Ermilov SA, Lapotko D *et al.*: Metallic nanoparticles as optoacoustic contrast agents for medical imaging. *Proc. SPIE* 6086, 155–163 (2006).
12. Kaul G, Amiji M: Cellular interactions and *in vitro* DNA transfection studies with poly(ethylene glycol)-modified gelatin nanoparticles. *J. Pharm. Sci.* 94(1), 184–198 (2005).
13. Dinauer N, Balthasar S, Weber C, Kreuter J, Langer K, von Briesen H: Selective targeting of antibody-conjugated nanoparticles to leukemic cells and primary T-lymphocytes. *Biomaterials* 26(29), 5898–5906 (2005).
14. Kirpotin DB, Drummond DC, Shao Y *et al.*: Antibody targeting of long-circulating lipidic nanoparticles does not increase tumor localization but does increase internalization in animal models. *Cancer Res.* 66(13), 6732–6740 (2006).
15. Zhang Y, Kohler N, Zhang M: Surface modification of superparamagnetic magnetite nanoparticles and their intracellular uptake. *Biomaterials* 23(7), 1553–1561 (2002).
16. Panyam J, Labhasetwar V: Dynamics of endocytosis and exocytosis of poly(D,L-lactide-co-glycolide) nanoparticles in vascular smooth muscle cells. *Pharm. Res.* 20(2), 212–220 (2003).
17. Yang PH, Sun X, Chiu JF, Sun H, He QY: Transferrin-mediated gold nanoparticle cellular uptake. *Bioconjug. Chem.* 16(3), 494–496 (2005).
18. Bohmer RM, King NJC: Flow cytometric analysis of immunogold cell surface label. *Cytometry* 5(5), 543–546 (1984).
19. Festin R, Bjorklund B, Totterman TH: Detection of triple antibody-binding lymphocytes in standard single laser flow cytometry using colloidal gold, fluorescein and phycoerythrin as labels. *J. Immunol. Methods* 101(1), 23–28 (1987).
20. Garcia-Garcia E, Andrieux K, Gil S *et al.*: A methodology to study intracellular distribution of nanoparticles in brain endothelial cells. *Int. J. Pharm.* 298(2), 310–314 (2005).
21. Liao H, Nehl CL, Hafner JH: Biomedical applications of plasmon resonant metal nanoparticles. *Nanomedicine* 1(2), 201–208 (2006).
22. Loo C, Lin A, Hirsh L *et al.*: Nanoshell-enabled photonics-based imaging and therapy of cancer. *Technol. Cancer Res. Treat.* 3(1), 33–40 (2004).
23. O'Neal DP, Hirsch LR, Halas NJ, Payne JD, West JL: Photo-thermal tumor ablation in mice using near-infrared absorbing nanoparticles. *Cancer Lett.* 209(2), 171–176 (2004).
24. Loo C, Lowery A, Halas N, West J, Drezek R: Immunotargeted nanoshells for integrated cancer imaging and therapy. *Nano Lett.* 5(4), 709–711 (2005).
25. Huang X, El-Sayed IH, Qian W, El-Sayed MA: Cancer cell imaging and photothermal therapy in the near-infrared region by using gold nanorods. *J. Am. Chem. Soc.* 128(6), 2115–2120 (2006).
26. Yguerabide J, Yguerabide EE: Resonance light scattering particles as ultrasensitive labels for detection of analytes in a wide range of applications. *J. Cell Biochem. Suppl.* 84(S37), 71–81 (2001).
27. Guzatov DV, Oraevsky AA, Oraevsky AN: Plasmon resonance in ellipsoidal nanoparticles with shells. *Quantum Electronics* 33(9), 817–822 (2003).
28. Oberdörster G, Oberdörster E, Oberdörster J: Nanotoxicology: an emerging discipline evolving from studies of ultrafine particles. *Environ. Health Perspect.* 113(7), 823–839 (2005).
29. Lapotko D: Laser-induced bubbles in living cells. *Lasers Surg. Med.* 38(3), 240–248 (2006).
30. Lapotko D, Lukianova K: Laser-induced micro-bubbles in cells. *Int. J. Heat Mass Transfer* 48(1), 227–234 (2005).
31. Lapotko D, Shnip A, Lukianova E: Photothermal detection of laser-induced damage in single intact cells. *Lasers Surg. Med.* 33(5), 320–329 (2003).
32. Lapotko D, Lukianova K: Influence of physiological conditions on laser damage thresholds for blood, heart and liver cells. *Lasers Surg. Med.* 36(1), 13–21 (2005).
33. El-Sayed IH, Huang X, El-Sayed MA: Surface plasmon resonance scattering and absorption of anti-EGFR antibody conjugated gold nanoparticles in cancer diagnostics: applications in oral cancer. *Nano Lett.* 5(5), 829–834 (2005).
34. Sönnichsen C, Franzl T, Wilk T: Drastic reduction of plasmon damping in gold nanorods. *Phys. Rev. Lett.* 88(7), 077402 (2002).
35. Loo C, Lowery A, Halas N, West J, Drezek R: Immunotargeted nanoshells for integrated cancer imaging and therapy. *Nano Lett.* 5(4), 709–711 (2005).
36. Aronow R, Danon D, Shahar A, Aronson M: Electron microscopy of *in vitro* endocytosis of T2 phage by cells from rabbit peritoneal exudates. *J. Exp. Med.* 120, 943–954 (1964).

Betty C. Rostro, Lissett R. Bickford, Courtney M. Payne, Emily S. Day, Seunhyung Lee, Kathryn M. Mayer, Tomasz Zal, Liana Adam, Colin P. N. Dinney, Rebekah A .Drezek, Jennifer L. West, Jason H. Hafner

"Stabilization and Targeting of Surfactant-Synthesized Gold Nanorods",

Bioconjugate Chemistry, submitted for publication.

ABSTRACT

The strong CTAB surfactant responsible for the synthesis and stability of gold nanorod solutions complicates their biomedical applications. The critical parameter to maintain nanorod stability is the ratio of CTAB to nanorod concentration. The ratio is approximately 740,000 as determined by chloroform extraction of the CTAB from a nanorod solution. A comparison of nanorod stabilization by thiol-terminal PEG and by anionic polymers reveals that PEGylation results in higher yields and less aggregation upon removal of CTAB. A heterobifunctional PEG yields nanorods with exposed carboxyl groups which can be used for covalent conjugation to antibodies with the zero length carbodiimide linker EDC. This conjugation strategy leads to approximately 2 functional antibodies per nanorod according to fluorimetry and ELISA assays. The nanorods specifically targeted cells in vitro, and were visible with both two photon and confocal reflectance microscopies. This covalent strategy should be generally applicable to other biomedical applications of gold nanorods as well as other gold nanoparticles synthesized with CTAB.

Acknowledgement of ANH/DoD support was made.

A Label-Free Immunoassay Based Upon Localized Surface Plasmon Resonance of Gold Nanorods

Kathryn M. Mayer,[†] Seunghyun Lee,[‡] Hongwei Liao,[‡] Betty C. Rostro,[†] Amaris Fuentes,[†] Peter T. Scully,[†] Colleen L. Nehl,[†] and Jason H. Hafner[†,‡,*]

[†]Department of Physics & Astronomy and [‡]Department of Chemistry, Rice University, Houston, Texas 77005

ABSTRACT Robust gold nanorod substrates were fabricated for refractive index sensing based on localized surface plasmon resonance (LSPR). The substrate sensitivity was 170 nm/RIU with a figure of merit of 1.3. To monitor biomolecular interactions, the nanorod surfaces were covered with a self-assembled monolayer and conjugated to antibodies by carbodiimide cross-linking. Interactions with a specific secondary antibody were monitored through shifts in the LSPR spectral extinction peak. The resulting binding rates and equilibrium constant were in good agreement with literature values for an antibody–antigen system. The nanorod LSPR sensors were also shown to be sensitive and specific. These results demonstrate that given a sufficiently stable nanoparticle substrate with a well defined chemical interface, LSPR sensing yields similar results to the surface plasmon resonance technique, yet with much simpler instrumentation.

KEYWORDS: gold nanorod · biosensor · immunoassay · localized surface plasmon resonance · SPR · nanobiotechnology · nanophotonics

Gold and silver nanoparticles exhibit localized surface plasmon resonances (LSPR) at visible and near-infrared frequencies, leading to sharp peaks in their spectral extinction.[1] The dependence of the resonance condition on the local dielectric environment enables a simple form of molecular sensing in which analyte binding to the nanoparticles surface causes a shift in the spectral extinction peak.[2] LSPR sensing is therefore the nanoparticle analogue of surface plasmon resonance sensing (SPR), which similarly monitors the resonance condition for surface plasmons in thin gold films.[3] SPR is a powerful surface analytical technique since it can detect submonolayer quantities of analyte at the gold film surface. Furthermore, since SPR measures an inherent property of the analyte, it does not require further labeling or chemical amplification. SPR can therefore measure dynamic processes in real time such as binding kinetics of biomolecular interactions, rather than simply providing the end-points. These properties have led to widespread use of SPR in the study of biomolecular interactions, as well as antibody screening for diagnostic and therapeutic applications.[4,5] However, despite its analytical capabilities, SPR is not widely used in clinical immunoassays or other nonresearch applications owing to the complexity of the optical instrumentation and the need for precise temperature control. It has been suggested that LSPR sensing with nanoparticle substrates will preserve the virtues of SPR but greatly broaden the scientific and technological applications, since LSPR sensing is based on a simple optical extinction measurement, is not temperature sensitive, and requires only common laboratory equipment.[6] Furthermore, nanoparticles have a highly localized LSPR sensing volume which eliminates the need to trap the interacting molecules of interest in a polymer matrix to enhance the signal, as is often done in SPR measurements.

LSPR sensing has evolved through the research of several groups over the past decade. The principle was first demonstrated in 1998 with antibody-conjugated gold nanoparticles in solution.[7] To mitigate spurious spectral shifts due to aggregation, nanoparticles were conjugated to monoclonal antibodies specific for a single epitope on the target ligand. However, to completely remove the possibility of aggregation, others have worked with nanoparticles bound to a transparent substrate, as demonstrated with silver nanotriangles created by nanosphere lithography,[8] and gold colloid films on glass.[9] Since these initial studies, there have been many reports on the technique[10–29] including demonstrations of multiplexing,[20,30] the detection of medically relevant analytes in clinical samples,[31] and fiber-based sensors.[10,13]

Despite these successes, LSPR sensing is still not nearly as prevalent as SPR. Thus far,

See the accompanying Perspective by Odom and Nehl on p 612.

*Address correspondence to hafner@rice.edu

Received for review November 18, 2007 and accepted February 11, 2008.

Published online February 22, 2008.
10.1021/nn7003734 CCC: $40.75

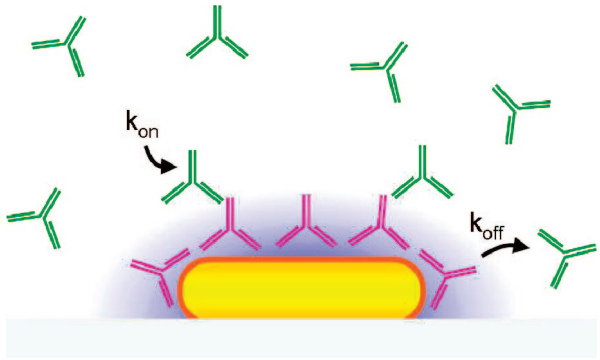

Figure 1. Schematic of the nanorod-based immunoassay. The nanorods are fixed to a glass surface *via* an APTES monolayer, and then coated with a self-assembled monolayer to which the capture antibody is coupled by carbodiimide cross-linking. The substrate is exposed to antigen (in this case secondary antibodies) and the binding is monitored *via* real-time absorption spectra.

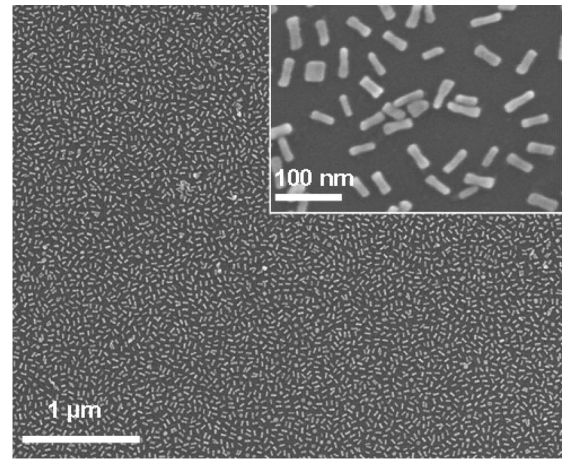

Figure 2. Scanning electron microscopy of films of gold nanorods. The coverage is uniform over large areas of the substrate. The individual nanorods are about 15 nm in diameter and 50 nm long.

biomolecular LSPR sensing studies have focused on biotin/streptavidin and antigen/antibody interactions, with a few exceptions.[14,16,22,32] All reports find a red shift as the ligand binds to the nanoparticles, but most do not observe the correct equilibrium binding constant (K_{eq}) when the interaction is studied in detail. A few reports have measured the correct K_{eq} value for antigen/antibody interactions,[12,20] but these were from endpoint assays rather than kinetics. Here we describe real-time analysis of antibody–antigen interactions by LSPR sensing with self-assembled gold nanorod substrates (Figure 1).[33] Through careful control of the substrate surface chemistry, we demonstrate the first successful measurement of binding constants by LSPR sensing.

RESULTS AND DISCUSSION

The gold nanorods for this report were produced by seed-mediated, surfactant directed synthesis,[34,35] which has been widely applied to generate homogeneous gold nanorods in high yield with LSPR resonances in the visible and near-infrared. Slight variations in the reactant ratios yield a variety of other anisotropic shapes.[34] However, further chemical manipulation of these nanoparticles is somewhat more complicated than that of classic citrate-stabilized gold colloid.[36] In surfactant directed synthesis, the CTAB acts as both the source of anisotropic growth and the stabilizer.[37] The 100 mM CTAB is thought to form a cationic bilayer around the nanoparticles, yet is clearly bound in a weak manner since a reduction of the CTAB concentration to below 1 mM causes aggregation. We previously reported a simple method to displace the CTAB stabilizer with a thiol terminated PEG.[33] Once PEGylated, the nanorods can be transferred to solutions devoid of PEG or other stabilizers. PEGylation allowed bioconjugation of the nanorods in solution and processing of nanorods into well-ordered films. Figure 2 displays such a film, demonstrating the uniformity of deposition.

Our initial attempts to use the PEGylation and bioconjugation protocols cited above for LSPR sensing produced shifts in response to binding, but did not yield the correct equilibrium binding constant for antigen/antibody interactions. Therefore, we adopted a surface chemistry based on self-assembled monolayers (SAMs).[38] First, the nanorod substrates were treated with oxygen plasma to remove the PEG and expose a clean gold surface. (The plasma presumably does not etch the APTES linkages holding the nanorods to the glass substrate.) Once cleaned, mixed SAMs of mercaptohexadecanoic acid and mercaptoundecanol were formed on the nanoparticles. Since SAMs on nanoparticles larger than 4 nm in diameter have been reported to exhibit behavior similar to those on planar surfaces,[39] the nanorods can be thought of as planar SPR surfaces in terms of their surface chemistry.

The sensitivity of the SAM-coated nanorod substrates to changes in the refractive index was checked by measuring the LSPR spectral extinction in air, water, ethanol (not shown), and formamide (Figure 3). This yielded a refractive index sensitivity of 170 nm per refractive index unit (RIU). While this sensitivity is not exceedingly high as compared to those in other reports,[40] the resonances are fairly narrow with a full width of 125 nm in water. The resulting figure of merit (sensitivity/line width)[41] for these sensors is 1.3, which is similar to other reports on nanoparticle ensembles.[40]

The nanorod substrates were tested as LSPR sensors in the flow cell by activating the carboxylic acid groups on the SAM *via* carbodiimide chemistry.[36] Rabbit IgG was coupled to the SAM to serve as a capture antibody, so that the binding of specific and nonspecific antibodies could be studied. The LSPR peak wavelength throughout such a reaction is displayed in Figure 4. First, the peak wavelength was allowed to stabilize against solvent annealing under a flowing buffer (not shown).[42] Exposure of the activated carboxy-terminal

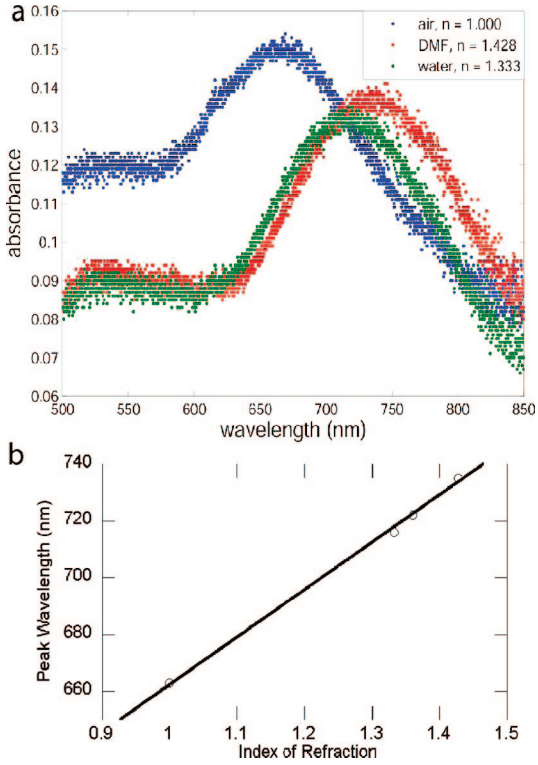

Figure 3. Characterization of the LSPR sensitivity to refractive index of the nanorod films: (a) Spectra of a nanorod film in three dielectric media. (b) The slope of the line yields a sensitivity of 170 nm/RIU.

nanorod SAM substrate to rabbit IgG produced the expected red shift of the LSPR peak wavelength due to IgG binding. The subsequent blue shift occurred during rinsing and was likely due to the removal of physisorbed rabbit IgG. Exposure to 30 nM goat antirabbit IgG caused a further red shift as the specific secondary antibody bound the capture antibody on the sensor.

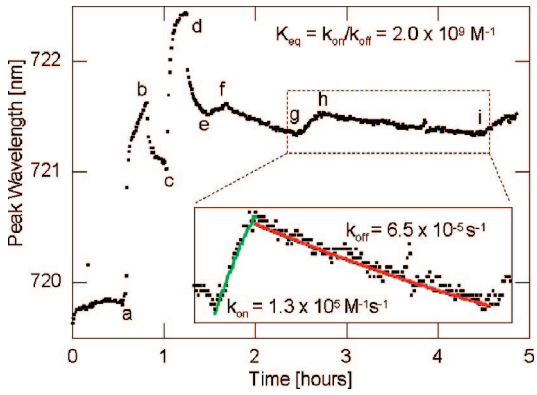

Figure 4. Immunoassay with kinetic data fits. The peak absorbance wavelength was measured *versus* time as the various solutions flowed over the substrate in a continuous experiment. Initially, the substrate was under a pH 6.1 buffer solution. At step a the substrate was exposed to a mixture of NHS and EDC, activating the SAM for protein binding. At step b, the substrate was rinsed with pH 6.1 buffer. At step c, rabbit immunoglobulin (IgG) was introduced. At step d, the substrate was rinsed with pH 7.6 buffer. At step e, it was exposed to 30 nM goat antirabbit IgG. At step f, it was again rinsed in pH 7.6 buffer. At steps g through i, these final steps were repeated twice more.

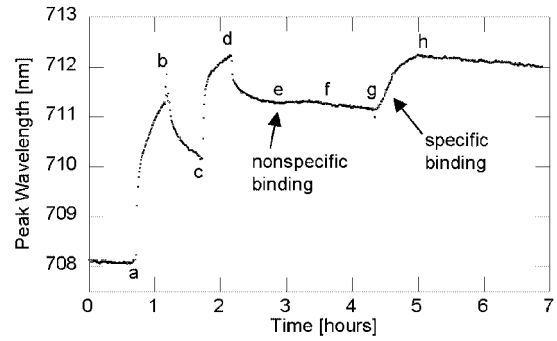

Figure 5. Demonstration of sensor specificity. Steps a through d are as in Figure 4. In step e, the substrate was exposed to 10 nM goat antimouse IgG, a nonspecific secondary antibody to the rabbit IgG. The binding is extremely weak. Step f is a buffer rinse. In step g, the substrate was exposed to 10 nM goat antirabbit IgG, and strong, specific binding was seen. Step h is a buffer rinse.

Then, the substrate was rinsed and unbinding of the secondary antibody was monitored *via* a blue shift. The final goat antirabbit IgG step was repeated three times to demonstrate substrate stability. The on and off rates for antibody binding were fit with a standard 1:1 binding model[43] which yielded the following:

$$k_{off} = 6.5 \times 10^{-5}\ s^{-1}$$

$$k_{on} = 1.3 \times 10^{5}\ M^{-1}\ s^{-1}$$

resulting in an equilibrium constant:

$$K_{eq} = 2.0 \times 10^{9}\ M^{-1}$$

This is a typical equilibrium constant for an antigen–antibody interaction,[43] and is the first measurement of the equilibrium constant from kinetic rates by LSPR sensing. This measurement was repeated several times, yielding equilibrium constants between $2 \times 10^8\ M^{-1}$ and $2 \times 10^9\ M^{-1}$. The additional data and fits can be found in the Supporting Information. The rates presented here match well to those observed for antigen–antibody binding in SPR.

Figure 5 illustrates a similar assay that tests the nanorod LSPR sensor's specificity. The nanorod conjugation with rabbit IgG was carried out exactly as described above, but the substrate was then exposed to 10 nM goat antimouse IgG as an analyte. As expected, there was very little binding of the nonspecific secondary antibody. When the specific secondary antibody was added in a subsequent step, significant binding was observed. This explicit demonstration confirms that the LSPR sensor retains the specificity of the capture antibody.

In addition, the detection sensitivity was measured. In Figure 6, the nanorod conjugation with rabbit IgG is again the same as in Figure 4, but in this case, the concentration of goat antirabbit IgG was raised in subse-

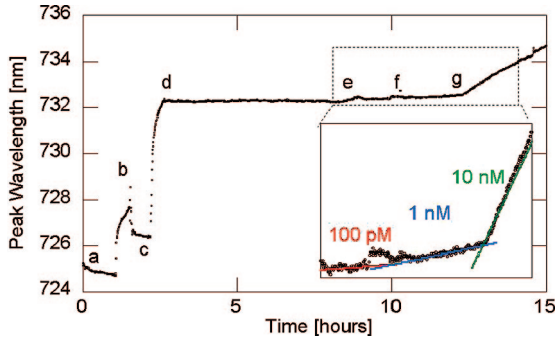

Figure 6. Test of sensor sensitivity. Steps a through d are as in Figure 4. In step e, the specific antibody (goat-anti rabbit IgG) was added at a concentration of 100 pM. The concentration was increased to 1 nM (at f) and 10 nM (at g). The inset shows linear fits to the binding curve.

quent steps. When the antibody was added at a concentration of 100 pM, there was no measurable response. When the concentration was increased to 1 nM, the peak began to redshift, with a slope of 0.076 +/−0.005 nm/hour. When the concentration was again increased to 10 nM, the slope, which should be proportional to concentration (to first order), also increased 10-fold, to 0.76 +/− 0.007 nm/hour. From this, we found that the limit of detection of this sensor over a reasonable time scale is about 1 nM.

Figure 7 illustrates the relationship between the LSPR shift due to the capture antibody binding and the LSPR shift due to analyte antibody binding over several experiments using different substrates. The linear relationship demonstrates that the results are reproducible and consistent from experiment to experiment, and that the variation in signal is most likely due to variation in the yield of capture antibody conjugation.

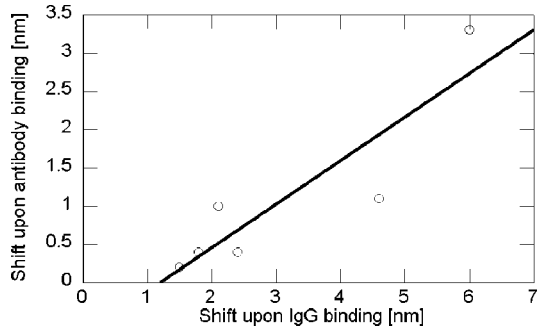

Figure 7. Comparison of LSPR shifts upon initial protein binding and specific antibody binding.

Most recent work on LSPR sensors has focused on maximizing the dielectric sensitivity by optimizing the nanoparticle shape.[40,44–46] While this is certainly advantageous, it is not a complete solution to extending LSPR applications in science and technology. More significant issues are the stability and availability of the sensor substrates, their chemical interface with the analyte, and the need for quantitative dynamic measurements. Here we have addressed these issues by fabricating LSPR substrates based on chemically synthesized gold nanorods with no lithographic steps and by exploiting standard techniques in self-assembly and bioconjugate chemistry. The resulting substrates are highly stable, as seen in the >15 h experiment in Figure 6. Also, the substrates can be plasma cleaned and reused, with some having undergone >20 such cycles in our laboratory. Although the nanorod substrates are not as sensitive as some other LSPR systems and geometries, their performance is comparable to dynamic SPR measurements in immunoassays. Such immunoassays may prove to be a significant application of LSPR sensing given the need for broadly available high throughput screening in fields such as proteomics, systems biology, and in vitro diagnostics.

CONCLUSIONS

Gold nanorod LSPR sensor substrates were fabricated by self-assembly for the study of biomolecular interactions. Through careful control of their surface chemistry, the nanorods were conjugated with capture antibodies which enabled immunospecific detection of secondary antibodies. Correct binding kinetics were measured, thus demonstrating that the nanorod LSPR sensor can monitor real-time dynamic interactions in a similar manner to SPR. In combination with recent reports on multiplexed nanorod LSPR sensors[30] and high throughput LSPR assays,[20] these substrates may help to expand LSPR sensing technology more broadly.

MATERIALS AND METHODS

Gold Nanorod Synthesis. Gold nanorods were prepared as described previously,[34] but the procedure was scaled up to increase the quantity.[33] All solutions were prepared fresh for each synthesis, except for the hydrogen tetrachloroaurate(III) (Sigma, no. 520918), which was prepared as a 28 mM stock solution from a dry ampule and stored in the dark. An aliquot of the stock solution was diluted to 10 mM immediately before use. Gold seed particles were prepared by adding 250 μL of 10 mM hydrogen tetrachloroaurate(III) to 7.5 mL of 100 mM cetyltrimethylammonium bromide (CTAB) (Sigma, #H9151) in a plastic tube with brief, gentle mixing by inversion. Next, 600 μL of 10 mM sodium borohydride (Acros, #18930) was prepared from DI water chilled to 2–8 °C in a refrigerator and added to the seed solution *immediately* after preparation, followed by mixing by inversion for 1–2 min. The pale brown seed solution was stable and usable for several hours.

The nanorod growth solution was prepared by adding the following reagents to a plastic tube in the following order and then gently mixing each by inversion: 425 mL of 100 mM CTAB, 18 mL of 10 mM hydrogen tetrachloroaurate(III), and 2.7 mL of 10 mM silver nitrate (Acros, #19768). Next, 2.9 mL of 100 mM ascorbic acid (Fisher, #A61) was added and mixed by inversion, which changed the solution from brownish-yellow to colorless. To initiate nanorod growth, 1.8 mL of seed solution was added to the growth solution, mixed gently by inversion, and left still for three hours. During this time, the color changed gradually to dark purple, with most of the color change occurring in the first hour.

Gold Nanorod PEGylation. One mL of CTAB-stabilized gold nanorods was centrifuged at 7000*g* to pellet the nanorods. The CTAB solution was decanted, and the pellet was resuspended in 2

mM potassium carbonate. This procedure leaves sufficient CTAB in the solution that the nanorods are stable for several hours. Twenty μL of 20 mM thiol terminated methoxypoly(ethylene glycol) (mPEG-SH, 5000 MW, Nektar Theraputics) was added to the solution and left overnight to displace the CTAB.[33] The nanorods were then taken through at least two more centrifuge/decant cycles, resuspending each time in deionized water, to further reduce the CTAB concentration.

Gold Nanorod Substrate Fabrication. Glass microscopic slides (75 mm × 25 mm) were cleaned in piranha solution (3:1 H_2SO_4/30% H_2O_2), thoroughly rinsed with deionized water, and dried. *WARNING: Piranha solution is very corrosive and must be handled with extreme caution; it reacts violently with organic materials*. They were then immersed in an ethanolic solution of 5 mM aminopropyltriethoxysilane (APTES) (Sigma, #440140) overnight, rinsed with water, and dried. The APTES coated slides were then immersed in a PEGylated nanorod solution overnight. Once rinsed and dried, a uniform layer of gold nanorods remained on the surface with an absorbance of approximately 0.1 at the LSPR peak wavelength. To remove the mPEG-SH and other contaminants, the substrates were processed in an oxygen plasma cleaner at low power for 30 s in 200 mT oxygen (model PDC-32G, Harrick Scientific) and immersed in an ethanolic solution of 50 μM mercaptohexadecanoic acid (Sigma, #448303) and 50 μM mercaptoundecanol (Sigma, #447528) for 2.5 h to form a mixed self-assembled monolayer (SAM). The plasma cleaning step has no significant effect on the nanorod structure as observed by atomic force microscopy and scanning electron microscopy. Plasma cleaning does cause a small LSPR blue shift consistent with the removal of a thin polymer coating.

Substrate Bioconjugation and LSPR Sensing Measurements. A closed flow cell was assembled consisting of two glass slides (one coated with nanorods covered with the mixed SAM and one clean) separated by a 1.5 mm thick polydimethylsiloxane (PDMS) seal with a 1 cm × 2 cm slot that served as the flow volume. The clean glass slide had two drilled holes to connect the input and output flows. This flow cell was mounted vertically on an optical bench in between a quartz−tungsten−halogen light source with collimating lens and a portable spectrometer (Ocean Optics, USB 4000). The 400 μL/minute flow rate was controlled by a syringe pump (NE1000, New Era Pump Systems).

At the start of an experiment, the substrate was exposed to 0.1 M 2-(*N*-morpholino)ethanesulfonic acid (MES) buffer (Sigma, #M-0164) at pH 6.1 until the LSPR peak wavelength stabilized. The carboxyl groups on the mixed SAM were then activated by exposure to a 1:1 mixture of 0.1 M *N*-hydroxysuccinimide (NHS) (Sigma #130672) and 0.05 M 1-ethyl-[3-dimethylaminopropyl]carbodiimide (EDC) (Sigma #1769) in the MES buffer, followed by rinsing in the MES buffer. Then, the substrate was exposed to rabbit IgG (Pierce, #31235)) at about 1 μM in the MES buffer, followed by a rinse with 0.05 M phosphate buffered saline (PBS) with 0.25 M NaCl at pH 7.6. Finally, either goat antirabbit IgG (Pierce, #31210) or goat antimouse immunoglobulin (IgG) (Pierce, #31160) was flowed at the desired concentration in PBS buffer followed by a PBS buffer rinse. The final step could be repeated more than once for successive tests of different secondary antibodies. Absorbance spectra were averaged for 30 s and recorded. Each spectrum was then analyzed in MATLAB with a Gaussian fit to monitor the peak wavelength, height, and width *versus* time.

Acknowledgment. K.M. acknowledges support from the NSF-funded Integrative Graduate Research and Educational Training (IGERT) program (DGE-0750843) in nanophotonics. This work was also supported by the National Science Foundation's Nanoscale Science and Engineering Initiative under award no. EEC-018007 and EEC-0647452, the U.S. Army Research Office under grant no. W911NF-04-1-0203, the Welch Foundation under grant C-1556, and the Alliance for NanoHealth under US Army Medical Research and Material Command grant no. W8IXWH-06-2-0067. The authors wish to thank Dr. Jennifer West, Dr. Rebekah Drezek, and Dr. James McNew for helpful discussions.

Supporting Information Available: Results for additional antibody−antigen kinetics experiments. This material is available free of charge *via* the Internet at http://pubs.acs.org.

REFERENCES AND NOTES

1. Hutter, E.; Fendler, J. H. Exploitation of Localized Surface Plasmon Resonance. *Adv. Mater.* **2004**, *16*, 1685–1706.
2. Willets, K. A.; Van Duyne, R. P. Localized Surface Plasmon Resonance Spectroscopy and Sensing. *Annu. Rev. Phys. Chem.* **2007**, *58*, 267–297.
3. Karlsson, R. SPR for Molecular Interaction Analysis: A Review of Emerging Application Areas. *J. Mol. Recognit.* **2004**, *17*, 151–161.
4. Fagerstam, L. G.; Frostell, A.; Karlsson, R.; Kullman, M.; Larsson, A.; Malmqvist, M.; Butt, H. Detection of Antigen-Antibody Interactions by Surface Plasmon Resonance. Application to Epitope Mapping. *J. Mol. Recognit.* **1990**, *3*, 208–214.
5. Safsten, P.; Klakamp, S.; Drake, A.; Karlsson, R.; Myszka, D. Screening Antibody-Antigen Interactions in Parallel Using Biacore A100. *Anal. Biochem.* **2006**, *353*, 181–190.
6. Haes, A. J.; Van Duyne, R. P. Preliminary Studies and Potential Applications of Localized Surface Plasmon Resonance Spectroscopy in Medical Diagnostics. *Expert Review of Molecular Diagnostics* **2004**, *4*, 527–537.
7. Englebienne, P. Use of Colloidal Gold Surface Plasmon Resonance Peak Shift to Infer Affinity Constants from the Interactions between Protein Antigens and Antibodies Specific for Single or Multiple Epitopes. *Analyst* **1998**, *123*, 1599–1603.
8. Haes, A. J.; Van Duyne, R. P. A Nanoscale Optical Biosensor: Sensitivity and Selectivity of an Approach Based on the Localized Surface Plasmon Resonance Spectroscopy of Triangular Silver Nanoparticles. *J. Am. Chem. Soc.* **2002**, *124*, 10596–10604.
9. Nath, N.; Chilkoti, A. A Colorimetric Gold Nanoparticle Sensor to Interrogate Biomolecular Interactions in Real Time on a Surface. *Anal. Chem.* **2002**, *74*, 504–509.
10. Cheng, S. F.; Chau, L. K. Colloidal Gold-Modified Optical Fiber for Chemical and Biochemical Sensing. *Anal. Chem.* **2003**, *75*, 16–21.
11. Frederix, F.; Friedt, J. M.; Choi, K. H.; Laureyn, W.; Campitelli, A.; Mondelaers, D.; Maes, G.; Borghs, G. Biosensing Based on Light Absorption of Nanoscaled Gold and Silver Particles. *Anal. Chem.* **2003**, *75*, 6894–6900.
12. Riboh, J. C.; Haes, A. J.; McFarland, A. D.; Yonzon, C. R.; Van Duyne, R. P. A Nanoscale Optical Biosensor: Real-Time Immunoassay in Physiological Buffer Enabled by Improved Nanoparticle Adhesion. *J. Phys. Chem. B* **2003**, *107*, 1772–1780.
13. Mitsui, K.; Handa, Y.; Kajikawa, K. Optical Fiber Affinity Biosensor Based on Localized Surface Plasmon Resonance. *Appl. Phys. Lett.* **2004**, *85*, 4231–4233.
14. Morokoshi, S.; Ohhori, K.; Mizukami, K.; Kitano, H. Sensing Capabilities of Colloidal Gold Modified with a Self-Assembled Monolayer of a Glucose-Carrying Polymer Chain on a Glass Substrate. *Langmuir* **2004**, *20*, 8897–8902.
15. Nath, N.; Chilkoti, A. Label-Free Biosensing by Surface Plasmon Resonance of Nanoparticles on Glass: Optimization of Nanoparticle Size. *Anal. Chem.* **2004**, *76*, 5370–5378.
16. Yonzon, C. R.; Jeoungf, E.; Zou, S. L.; Schatz, G. C.; Mrksich, M.; Van Duyne, R. P. A Comparative Analysis of Localized and Propagating Surface Plasmon Resonance Sensors: The Binding of Concanavalin A to a Monosaccharide Functionalized Self-Assembled Monolayer. *J. Am. Chem. Soc.* **2004**, *126*, 12669–12676.
17. Chen, H. H.; Suzuki, H.; Sato, O.; Gu, Z. Z. Biosensing Capability of Gold-Nanoparticle-Immobilized Three-Dimensionally Ordered Macroporous Film. *Appl. Phys., A: Mater. Sci. Process.* **2005**, *81*, 1127–1130.
18. Endo, T.; Yamamura, S.; Nagatani, N.; Morita, Y.; Takamura, Y.; Tamiya, E. Localized Surface Plasmon Resonance Based Optical Biosensor Using Surface Modified Nanoparticle

Layer for Label-Free Monitoring of Antigen-Antibody Reaction. *Sci. Technol. Adv. Mater.* **2005**, *6*, 491–500.
19. Kalele, S. A.; Ashtaputre, S. S.; Hebalkar, N. Y.; Gosavi, S. W.; Deobagkar, D. N.; Deobagkar, D. D.; Kulkarni, S. K. Optical Detection of Antibody Using Silica-Silver Core-Shell Particles. *Chem. Phys. Lett.* **2005**, *404*, 136–141.
20. Endo, T.; Kerman, K.; Nagatani, N.; Hiepa, H. M.; Kim, D. K.; Yonezawa, Y.; Nakano, K.; Tamiya, E. Multiple Label-Free Detection of Antigen-Antibody Reaction Using Localized Surface Plasmon Resonance-Based Core-Shell Structured Nanoparticle Layer Nanochip. *Anal. Chem.* **2006**, *78*, 6465–6475.
21. Fujiwara, K.; Watarai, H.; Itoh, H.; Nakahama, E.; Ogawa, N. Measurement of Antibody Binding to Protein Immobilized on Gold Nanoparticles by Localized Surface Plasmon Spectroscopy. *Anal. Bioanal. Chem.* **2006**, *386*, 639–644.
22. Kitano, H.; Anraku, Y.; Shinohara, H. Sensing Capabilities of Colloidal Gold Monolayer Modified with a Phenylboronic Acid-Carrying Polymer Brush. *Biomacromolecules* **2006**, *7*, 1065–1071.
23. Kreuzer, M. P.; Quidant, R.; Badenes, G.; Marco, M. P. Quantitative Detection of Doping Substances by a Localised Surface Plasmon Sensor. *Biosens. Bioelectron.* **2006**, *21*, 1345–1349.
24. Stewart, M. E.; Mack, N. H.; Malyarchuk, V.; Soares, J. A. N. T.; Lee, T. W.; Gray, S. K.; Nuzzo, R. G.; Rogers, J. A. Quantitative Multispectral Biosensing and 1D Imaging Using Quasi-3D Plasmonic Crystals. *Proc. Natl. Acad. Sci. U.S.A.* **2006**, *103*, 17143–17148.
25. Arai, T.; Kumar, P.; Rockstuhl, C.; Awazu, K.; Tominaga, J. An Optical Biosensor Based on Localized Surface Plasmon Resonance of Silver Nanostructured Films. *J. Opt., A* **2007**, *9*, 699–703.
26. Chen, C. D.; Cheng, S. F.; Chau, L. K.; Wang, C. R. C. Sensing Capability of the Localized Surface Plasmon Resonance of Gold Nanorods. *Biosens. Bioelectron.* **2007**, *22*, 926–932.
27. Gish, D.; Nsiah, F.; McDermott, M.; Brett, M. Localized Surface Plasmon Resonance Biosensor Using Silver Nanostructures Fabricated by Glancing Angle Deposition. *Anal. Chem.* **2007**, *79*, 4228–4232.
28. Marinakos, S. M.; Chen, S. H.; Chilkoti, A. Plasmonic Detection of a Model Analyte in Serum by a Gold Nanorod Sensor. *Anal. Chem.* **2007**, *79*, 5278–5283.
29. Miller, M. M.; Lazarides, A. A. Sensitivity of Metal Nanoparticle Surface Plasmon Resonance to the Dielectric Environment. *J. Phys. Chem. B* **2005**, *109*, 21556–21565.
30. Yu, C. X.; Irudayaraj, J. Multiplex Biosensor Using Gold Nanorods. *Anal. Chem.* **2007**, *79*, 572–579.
31. Haes, A. J.; Chang, L.; Klein, W. L.; Van Duyne, R. P. Detection of a Biomarker for Alzheimer's Disease from Synthetic and Clinical Samples Using a Nanoscale Optical Biosensor. *J. Am. Chem. Soc.* **2005**, *127*, 2264–2271.
32. Lin, T. J.; Huang, K. T.; Liu, C. Y. Determination of Organophosphorous Pesticides by a Novel Biosensor Based on Localized Surface Plasmon Resonance. *Biosens. Bioelectron.* **2006**, *22*, 513–518.
33. Liao, H.; Hafner, J. Gold Nanorod Bioconjugates. *Chem. Mater.* **2005**, *17*, 4636–4641.
34. Sau, T. K.; Murphy, C. J. Room Temperature, High-Yield Synthesis of Multiple Shapes of Gold Nanoparticles in Aqueous Solution. *J. Am. Chem. Soc.* **2004**, *126*, 8648–8649.
35. Nikoobakht, B.; El-Sayed, M. A. Preparation and Growth Mechanism of Gold Nanorods (NRs) Using Seed-Mediated Growth Method. *Chem. Mater.* **2003**, *15*, 1957–1962.
36. Hermanson, G. T. *Bioconjugate Techniques,* 1st ed.; Academic Press: San Diego, CA, 1996; Vol. 16, pp 9–177..
37. Gao, J. X.; Bender, C. M.; Murphy, C. J. Dependence of the Gold Nanorod Aspect Ratio on the Nature of the Directing Surfactant in Aqueous Solution. *Langmuir* **2003**, *19*, 9065–9070.
38. Lahiri, J.; Isaacs, L.; Tien, J.; Whitesides, G. M. A Strategy for the Generation of Surfaces Presenting Ligands for Studies of Binding Based on an Active Ester as a Common Reactive Intermediate: A Surface Plasmon Resonance Study. *Anal. Chem.* **1999**, *71*, 777–790.
39. Hostetler, M. J.; Wingate, J. E.; Zhong, C. J.; Harris, J. E.; Vachet, R. W.; Clark, M. R.; Londono, J. D.; Green, S. J.; Stokes, J. J.; Wignall, G. D.; Glish, G. L.; Porter, M. D.; Evans, N. D.; Murray, R. W. Alkanethiolate Gold Cluster Molecules with Core Diameters from 1.5 to 5.2 nm: Core and Monolayer Properties as a Function of Core Size. *Langmuir* **1998**, *14*, 17–30.
40. Liao, H.; Nehl, C. L.; Hafner, J. H. Biomedical Applications of Plasmon Resonant Metal Nanoparticles. *Nanomedicine* **2006**, *1*, 201–208.
41. Sherry, L. J.; Chang, S.-H.; Schatz, G. C.; van Duyne, R. P. Localized Surface Plasmon Resonance Spectroscopy of Single Silver Nanocubes. *Nano Lett.* **2005**, *5*, 2034–2038.
42. Malinsky, M. D.; Kelly, K. L.; Schatz, G. C.; Van Duyne, R. P. Nanosphere Lithography: Effect of Substrate on the Localized Surface Plasmon Resonance Spectrum of Silver Nanoparticles. *J. Phys. Chem. B* **2001**, *105*, 2343–2350.
43. Davies, C. Introduction to Immunoassay Principles. *The Immunoassay Handbook*, 3rd ed.; Wild, D., Ed.; Elsevier: Amsterdam, The Netherlands, 2005; pp 3–40..
44. Wang, H.; Brandl, D. W.; Le, F.; Nordlander, P.; Halas, N. J. Nanorice: A Hybrid Plasmonic Nanostructure. *Nano Lett.* **2006**, *6*, 827–832.
45. Bukasov, R.; Shumaker-Parry, J. S. Highly Tunable Infrared Extinction Properties of Gold Nanocrescents. *Nano Lett.* **2007**, *7*, 1113–1118.
46. Henzie, J.; Lee, M. H.; Odom, T. W. Multiscale Patterning of Plasmonic Metamaterials. *Nat. Nanotechnol.* **2007**, *2*, 549–554.